UNIVERSITY OF SOUTHAMPTON

FOG FORMATION IN RAPIDLY COOLED GAS – VAPOUR MIXTURES

ANDREW DAVID MILLER

SUBMITTED FOR THE DEGREE OF
DOCTOR OF PHILOSOPHY

FACULTY OF ENGINEERING AND APPLIED SCIENCE
DEPARTMENT OF MECHANICAL ENGINEERING

SPETEMBER 2000

UNIVERSITY OF SOUTHAMPTON

ABSTRACT

FACULTY OF ENGINEERING AND APPLIED SCIENCE

DEPARTMENT OF MECHANICAL ENGINEERING

Doctor of Philosophy

FOG FORMATION IN RAPIDLY COOLED GAS – VAPOUR MIXTURES

Andrew David Miller

Fog formation is often an undesired consequence of vapour recovery from gas- vapour mixtures inside industrial condensers. Such droplets, once formed, can be difficult to remove owing to their small size. A number of droplet recovery devices are commercially available, each of which operates most efficiently over a specific range of droplet sizes. Yet, to date, no work has been forthcoming to aid accurate estimation of droplet size ranges and allow chemical process engineers to identify the most appropriate droplet capture device.

Following a review of the literature concerning droplet formation and the supersaturation of gas-vapour mixtures, an experimental test rig was designed and manufactured with which to study fog formation during rapid cooling and partial condensation. On completion a large number of experiments were performed using water vapour- air mixtures with a wide range of temperatures, partial vapour pressures and velocities. During each test, measurements of the droplet sizes and number concentrations were performed and recorded using a Laser Doppler Anemometer. The measurements were carried out at a number of points between the condenser walls, as the fog exited the experimental condenser.

To complement the experimental program a theoretical study of fog formation within a partial condenser was completed. The resulting predictions of temperature drop along the condenser and bulk fog formation rates were used in conjunction with the experimental results and visual observations to present a clear description of the phenomena of fog formation within a partial condenser.

Fog formation was shown to occur inside a condenser for a wide range of temperatures and relative humidities of the initial gas vapour mixture, though in many cases the vast majority of droplets were confined to a narrow region close to the condenser walls. In all the experiments conducted that lead to a reasonable level of fog formation the total mass of liquid existing in the form of submicron droplets was insignificant (<< 1% of the total mass of fog). In general the extent of fog formation and the size of the droplets formed increased with increasing vapour pressure, coolant flow rate and condenser length, and with decreasing temperature and velocity. The presence of submicron droplets in the fog exiting the condenser was avoided completely by supersaturating the mixture by 15% or more prior to it entering the condenser.

ACKNOWLEDGEMENTS

The Author would like to thank Dr. Richard Bowen of the department of Mechanical Engineering, who supervised the project, for all the guidance given, and Professor Martin Thew, now of Bradford University, for his input into the initial stages of the study. Thanks must also go to Dr. Derek Colman of BP Chemicals for extending the sponsorship of the project, providing equipment and advice. In addition the author would like to thank all those in the Mechanical Engineering workshop who assisted in the manufacture of the experimental rig and who gave advice during the design process and those at the EPSRC loan pool and Dantec Ltd. for the loan and set-up of a replacement droplet-sizing device. Thanks must finally go to my friends at Southampton who kept me company through some long evenings in the laboratory and most importantly to my family and my wife Kate for all the support, financial and otherwise, throughout the course of the project, and particularly during the thesis write-up.

LIST OF CONTENTS

APPENDICES

NOMENCLATURE

dA	-	Differential condenser surface area (m^2)
c	-	Nuclei concentration (m^{-3})
c	-	Vapour mass fraction
c_p	-	Molar heat capacity (J/ mole K)
C_p	-	Specific heat capacity (J/ kg K)
C_c	-	Coefficient of contraction
C_D	-	Orifice discharge coefficient
C_o	-	Orifice coefficient
C_o	-	Ackermann correction factor
d	-	Diameter (m)
dA	-	Differential condenser surface area
D_{AB}	-	Diffusion coefficient in fluid (m^2/s)
D_h	-	Hydraulic diameter (m)
e_o	-	Saturation vapour pressure
e_r	-	Saturation vapour pressure of a pure liquid droplet of radius r
$e_r^{'}$	-	Saturation vapour pressure of a solution droplet of radius r
E_D	-	Eddy diffusion coefficient (m^2/s)
f	-	Friction factor
F	-	Mass velocity of fog (kg moles/ m^{2}s)
F_D	-	Drag (kg m/s^2)
$F^+(t)$	-	Saturated vapour pressure as a function of temperature
g_m	-	Mass transfer coefficient (kg/ m^{2}s)
G	-	Mass velocity of inert gas (kg moles/ m^{2}s)
$G^+(t)$	-	Calculated function of vapour pressure against temperature of mixture
Gr	-	Grashof number
ΔG	-	Free energy of a spherical embryo
ΔG_v	-	Free energy change when unit volume of liquid is formed without a change in surface area

h - Heat transfer coefficient (W/ m^2 K)

i - Van't Hoff factor

J - Nucleation rate

J_A - Flux density of A relative to plane of no net volume transport (kg moles/s m^2)

k - Thermal conductivity (W/ m K)

k_c - Time average mass transfer coefficient (kg/ m^2s)

k_g^* - Mass transfer coefficient $\left(= D_{AB}/RTy_o\right)$ (kg/ m^2s)

K_g - Mass transfer coefficient $\left(= D_{AB}P/RTy_o p_{BM}\right)$ (kg/ m^2s)

Kn - Knudsen number $\left(= l/r_d\right)$

l - Length (m)

l - Mean free path (m)

L - Mass velocity of condensate phase (kg moles/ m^2s)

Le - Lewis number $\left(= k/\rho c_p D_{AB}\right)$

m - Mass (kg)

$\dot{m}$ - Mass flow rate (kg/s)

M - Total molar mass velocity $\left(= G + V + F\right)$ (kg moles/ m^2s)

n^* - number of critical embryos

N - Molar flux (kg moles/ m^2s)

N_A - Avogadro's number (6.022×10^{23}/mole)

p - Partial vapour pressure (bar)

P - Total pressure (bar)

Pr - Prandtl number

q - Heat flux (W/ m^2)

r - Radius (m)

r_c - Critical droplet radius (m)

r_d - Droplet radius (m)

$r_{\min}$ - Minimum 'dry' particle size that will nucleate at a given supersaturation (m)

R - Pipe radius (m)

R - Gas constant (J/ kg K)

Re - Reynolds number

S - Supersaturation ratio
S_c - Critical supersaturation
S_{ext} - External supersaturation [value of the vapour away from the droplet surface]
$S_{\max}$ - Maximum supersaturation
Sc - Schmidt number, $\left(=\eta/\rho D_{AB}\right)$
t - Time (s)
t - Temperature (Celsius)
T - Temperature (Kelvin)
u - Component of velocity in the x-direction (m/s)
$\bar{u}$ - Average velocity of the fluid (m/s)
$\overline{U}_y$ - Velocity of the plane of no net volume transport (m/s)
U_m - Weighted mean velocity (m/s)
v - Induced velocity (due to mass transfer) (m/s)
$\overline{V}$ - Partial molal volume (m^3/ kg mole)
V - Mass velocity of condensable vapour (kg moles/ m^2s)
$\dot{V}$ - Volumetric flow rate (m^3/s)
W - Coolant flow rate (kg/s)
X - Constant in equation 7.10
y - Distance from bulk of gas towards interface (m)
y_o - Film thickness (m)
Y_A - Mole fraction of A

ε - Eddy viscosity
ρ - Density (kg/m^3)
ρ_m - Specific gravity
γ - Time (s)
τ - Shear Stress (N/ m^2)
λ - Latent heat of vaporisation (J/ kg mole)
η - Dynamic viscosity (Pa s)
μ - Viscosity (kg/ m s)

Θ - Film model correction factor

θ - Temperature excess (Celsius)

θ^{+} - Correction factor

ϕ - Dimensionless mass flux

ϕ - Relative humidity

σ - Molecular cross-sectional area (m^2)

υ - Kinematic viscosity

Subscripts

1 - at the interface

2 - in the bulk

a - air

A - water vapour

b - in the bulk

B - air

BM - logarithmic mean (for air)

c - diffusional

g - saturated vapour

i - at the interface

L - condensate

o - orifice plate

p - pipe

s - vapour

t - thermal

u - momentum

v - in the bulk

w - condenser wall

W - coolant

1. INTRODUCTION

1.1 *Introduction*

In a large number of chemical processes, liquid product is recovered from a flowing vapour stream using an industrial separator or condenser. The fluid is passed over a cold surface, well below its dew-point temperature. The vapour then condenses onto the surface and the resulting liquid is simply drained off. Often the fluid stream will contain a number of different vapours and/or an inert gas component, which builds-up near the cold walls. The presence of even a small amount of inert gas may cause a drastic reduction in the capacity of a condenser [1, 2]. Vapour moving towards the condensing surface has to diffuse through the noncondensable component [3], and the rate of condensation is considerably reduced. Nevertheless, large heat and mass transfer rates are produced inside such condensers, to ensure rapid recovery of the material and to keep plant sizes to a minimum. This combination of circumstances seemingly increases the probability of some vapour condensing to form liquid droplets within the bulk mixture, before the molecules are able to reach the cold surface, and a fog may form [4]. As the mixture proceeds through the condenser virtually all the vapour is removed, but the fog spreads, and the resulting cloud of liquid droplets may be carried out of the condenser.

Consequently, fog formation may result in the loss of valuable and/or hazardous material, a clear problem. Further problems may arise with equipment downstream of such condensers, through the rapid de-activation of any catalytic dryers etc. Hence it is generally very important to ensure the recovery of these droplets.

1.2 *Droplet size limits*

Fog formation may be initiated heterogeneously, upon condensation nuclei, or homogeneously within the main body of fluid. Liquid droplets formed during the cooling of initially saturated or superheated gas - vapour mixtures generally do so heterogeneously, since the high supersaturations required for homogeneous condensation are highly unlikely to be created. The droplets then grow by a mixture of further direct condensation, and coalescence with existing drops. The smallest droplets which may exist are therefore slightly larger than the smallest nuclei, ~0.001μm in diameter. (All droplets are roughly spherical because of the surface tension effects).

Theoretically the largest drops may grow indefinitely. However, in practise the maximum drop size is governed by the rate at which the large drops precipitate out of the fluid under the action of gravity. This may be evaluated via the terminal velocity of the drops. The drag on a spherical drop of between 3 and 100μm in diameter, is given by Stokes' Law as

$$F_D = 3\pi\mu uD \tag{1-1}$$

where μ is the fluid viscosity, u the velocity of the drop and D its diameter [5]. The terminal velocity, u_t, is then calculated by setting the drag equal to the force of gravity on the drop, i.e.

$$3\pi\mu u_t D = \pi/_6 D^3(\rho_L - \rho_G)g \tag{1-2}$$

hence

$$u_t = \frac{D^2(\rho_L - \rho_G)g}{18\mu} \tag{1-3}$$

where g is the acceleration due to gravity and ρ_L and ρ_G are the densities of the liquid drop and the fluid respectively. Using equation (1-3), the settling velocity of a 100μm drop with a specific gravity of 1.0 in air is approximately 0.3m/s. So drops of this diameter or larger may quickly precipitate out of a condenser. Equation (1-3) also indicates that the terminal velocity of a drop is proportional to its diameter squared. Therefore smaller droplets have a rapidly decreasing terminal velocity which soon becomes so small that, without a special effort being made to recover them, the droplets will remain suspended in the fluid. In fact, if the fluid flows vertically through a condenser, or the flow regime is highly turbulent, much larger drops may be temporarily suspended. The exact size of the largest drops is therefore dependent on a number of different factors, though typically the drops produced inside an industrial condenser are in the range 0.1 - 40μm [4].

1.3 *Droplet recovery*

The use of gravitational separation can be extended through the employment of large settling tanks, designed to substantially reduce the velocity of the fluid flow. However, this is still only a viable method of droplet collection for the larger drops (typically those ≥ 40μm). For recovery of droplets below this size it is necessary to use a different mechanism. The most commonly used devices utilise inertial separation. An obstruction is placed in the fluid stream to divert the flow. The entrained liquid droplets are carried forward by their large momentum relative to the gas flow, where they impinge upon a solid surface and are collected [6].

Yet there comes a size (~1μm in diameter), below which droplet recovery by inertial separation also becomes prohibitively difficult. A different technique is thus required for submicron droplets, and diffusional or electrostatic based separators exist for this purpose. A summary of the more widely employed industrial recovery devices is given in table 1.1, over the page.

1.4 *Choice of recovery device*

Steinmeyer suggests that whether fog formation is likely to occur inside industrial condensers is probably fairly well fixed by the entering gas-vapour-nuclei mix, and hence outside the control of the process design engineer [4]. This being the case, a droplet collection device is likely to be required, to recover liquid which would otherwise be lost. The most important factor to consider in choosing such a device is the average droplet size of the fog produced, since they operate most efficiently over a fixed range of sizes. The droplet size distribution is also of critical importance. The presence of larger droplets, having a much greater mass (since mass is proportional to diameter cubed), may well lead to an excessive loading, and the device becoming clogged and ineffective. Smaller droplets may be below the minimum droplet size recoverable (the cut-off diameter), and evade capture altogether. Consequently a number of droplet recovery devices are often used in series. For example, a cyclonic separator with a wire mesh upstream to remove the largest drops and prevent flooding, and a superfine glasswool filter downstream to collect the smaller drops down to 1μm in diameter.

Since the mass of a drop is proportional to its diameter cubed, a single 10μm drop contains as much material as 1000 1μm drops. Hence it is likely that by focussing on the largest drops the vast majority of material will be recovered. In addition, the smaller the droplets, the more difficult and costly it is to remove them, so it may well not be worthwhile including a device for the recovery of the smallest, submicron droplets.

Recovery device	Operating mechanism	Cut-off drop diameter	Typical loading	Remarks:
Settling tank knockout drum	Gravitational	D > 40μm	Heavy	A large tank, designed to slow the gas flow sufficiently that the settling velocity of the large drops is greater than the velocity of the gas. Poor efficiency, rarely used.
Impingement plates	Inertial	D > 10μm	Heavy	May take many forms, but essentially consist of a surface placed in the path of the flowing vapour, causing the larger droplets to impinge upon the plate, while the vapour and entrained smaller drops turn sharply through an angle from 90° to 180°.
Knitmesh de-misters	Inertial	D > 10μm	Up to 20 g/m^3	Simply consist of a wire mesh. As the fluid flows through the mesh, some of the droplets impact upon it. Again, the larger drops may be recovered in this way, but the smaller droplets tend to pass through and around the mesh, evading capture.
Cyclonic separators	Inertial	Typically D > 5μm	Up to 100 g/m^3	The fluid is introduced tangentially at the surface of the upper part of a cylindrical vessel, thereby causing the rotation of the fluid contained in the body. The centrifugal force pushes the gas to the centre and upwards, where it escapes through a central exit at the top. The droplets are thrown to the outside, and run down the wall, to be collected at the bottom. Cyclones are particularly useful for catching middle-sized droplets.
Superfine glasswool Filters	Inertial	D > 1μm	1 – 2 g/m^3	Made up of thousands of tiny fibres, each with a diameter of approximately 2 microns. Droplets impacting on the fibres drain off and are collected. Danger of clogging in high fog flows.
Candle de-misters	Diffusional	0 < D < 1μm	Very low	This works on the principle of diffusion collection, rather than inertial impacts. Hence candle de-misters require extremely small fluid velocities to operate efficiently. Candle de-misters are very effective for droplet sizes of 1 micron and below.

Figure1.1 Droplet recovery device summary [6, 7, 8].

However, this is not necessarily the case. The number of submicron droplets may be very much greater than those of a larger size. So a knowledge of the droplet size distribution of fogs formed inside industrial condensers is very important in designing droplet recovery systems for chemical plants. Very little information is currently available in the literature.

1.5 *Scope and objectives of work*

The aim of this study then, was to analyse fog formation arising from the condensation of gas - vapour mixtures, in order to predict the droplet size distributions produced in industrial chemical plants. The main objective was the design and construction of a test rig facility with which to study the rapid cooling of a gas - vapour mixture and the many factors which may influence fog formation. Tests were then performed on a wide range of water vapour – air mixtures, under steady-state conditions. In addition, a theoretical model was employed to estimate the propensity of fog formation from the different initial mixtures. A computer program was subsequently written with which to predict fog formation rates for any mixture, provided its condition on entry to the condenser is known. The results were used with the experimental data and analysis to explain the observed fog densities and droplet size distributions.

To summarise, the ultimate goal of this investigation was to increase our understanding of fog formation, highlight those factors crucial to the determination of fog droplet size distributions and quantify the effect each has. This was all in an attempt to enable predictions to be made of the droplet size distributions generated inside industrial condensers. Such information should prove very useful in balancing the need to recover the vast majority of such droplets against the associated increases in costs, equipment size etc.

1.6 *Structure of thesis*

In the following chapter the conditions required for condensational droplet formation are assessed using the available literature and the critical variables identified. The importance of foreign particles to fog formation is discussed as well as the abundance of such particles, their size range, size distribution and composition. The ease with which droplets form on the different particles is then assessed, allowing those particles most likely to produce droplets to be identified. The rate of droplet growth is then examined. Finally a number of recent experimental investigations into atmospheric droplet formations are reviewed and the relevance of the results to fog formation inside partial condensers is discussed.

In chapter 3 fog formation within partial condensers is assessed by examining the radial and axial variation of the mixture properties. First the onset of supersaturation and droplet formation within a partial condenser is studied. It is demonstrated that the vapour pressure and temperature gradients perpendicular to the cold wall can lead to the establishment of a fog forming region near the wall while the mixture in the remainder of the condenser remains superheated and fog free. This phenomenon is known as film fog, and a method for calculating the range of bulk mixture properties that will result in film fog at a specific axial location within the condenser is discussed. Attention is then focussed upon the variation of bulk mixture properties with distance along the condenser and the significance of the axial bulk temperature and vapour pressure profiles is discussed. It is demonstrated that by performing mass and energy balances over a differential section of a partial condenser, a set of differential equations is derived with which the rate of fog formation within the condenser may be predicted.

The development of a computer program that solves these equations is detailed in chapter 4. The program is subsequently applied to a range of water vapour – air mixtures to examine the effect of a number of variables on predicted bulk fog formation rates. The program was then adapted to allow hydrocarbon mixtures to be considered and the differences between the ensuing results and those for the water vapour mixtures are highlighted.

Chapter 5 describes in detail the design, manufacture and assembly of the experimental rig. After first designating the range of conditions over which the rig was to operate, the necessary constituent mass flow rates and condenser dimensions etc. were chosen accordingly. The manufacture of the numerous sections comprising the test rig is then described, and photographs included where appropriate.

The associated instrumentation incorporated into the experimental rig is detailed in chapter 6. The range of values of the most important measurable quantities, laid out in chapter 5, is used to identify suitable measurement instruments. The most appropriate device is then chosen, taking account also of what was readily available in the laboratory and from the project sponsors, the associated cost, accuracy and ease of use.

In chapter 7 the commissioning, operation and modification of the test rig is detailed. This section begins with a description of the initial problem encountered with the test rig, followed by the steps taken to resolve them. The method used to calculate the vapour and gas flow rates, required to produce the desired mixture conditions at condenser entry is then laid out. This is followed by the presentation of the rig operating procedure used throughout the experimental program. Finally, the ongoing problems with temperature control within the rig and the malfunction of the droplet sizing equipment and its eventual replacement are described.

A number of preliminary tests were performed with the experimental rig and these are summarised in chapter 8. These tests involved the measurement of the velocity and temperature profiles within the condenser. The results are shown to be in good agreement with those expected for fully developed turbulent flow, and the heat transfer coefficient for the condenser is calculated.

A large amount of experimental data was collected during the investigation and a selection of the most interesting experimental results and a discussion of their significance is presented in chapter 9, accompanied by further analysis where appropriate. This section commences with an account of the visual observations during the experiments and is accompanied by a number of photographs of the fogs produced, taken at condenser exit. This is followed by the presentation of the results obtained during experiments into the effects of a series of variables relating to the gas – vapour mixture and the condenser upon fog formation. The measurements presented focus primarily upon the mean droplet sizes, droplet size distributions and the associated droplet number concentrations. The interpretation of these results makes use of both work published regarding the processes of droplet formation, supersaturation and heat and mass transfer, presented in the chapters 2 and 3, and the theoretical calculations and predictions presented in chapter 4.

Chapter 10 outlines a programme for further work. The results of the experimental and theoretical studies are used to identify areas that require additional investigation. The applicability of the results obtained during this investigation to cases of fog formation in industrial process plants is also discussed.

The key results of the investigation are summarised in the concluding comments in chapter 11.

2. Principles of fog formation

2.1 *Sources of fog formation*

A fog (or mist) is a cloud of liquid droplets suspended in a gas. Such droplets may be produced in a number of different ways, for example during the expansion of a vapour [9, 10], the cooling of a vapour [11, 12], the mixing of vapour streams [13], or the spraying of a liquid through a nozzle (atomization) [6]. Whether the droplets remain suspended in the vapour and so may be classified a fog, is dependent upon the drops being of a sufficiently small size to avoid precipitation (see section 1.2), and the condition of the vapour being such as to ensure the drops do not immediately evaporate.

Here the focus will be restricted to the more pertinent and interesting cases of the spontaneous formation of droplets within a vapour, as opposed to droplet production from nozzles etc. The causes of this type of fog formation will now be addressed.

2.2 *Thermodynamics of fog formation*

To determine the thermodynamic state of a system, information about its properties is required. In most of what follows the two most readily obtainable properties of an open system, temperature and pressure, will be used.

If a vapour is cooled it will eventually reach a temperature at which it condenses. The temperature at which this takes place (corresponding to the given vapour pressure) is called the *saturation temperature* [14]. By plotting the saturation temperatures for all vapour pressures on a temperature-pressure graph (the data is widely available for most vapours) a *saturated vapour line* or saturation curve is obtained. The saturation curve for water vapour, obtained from steam tables [15], is shown in Figure 2-1.

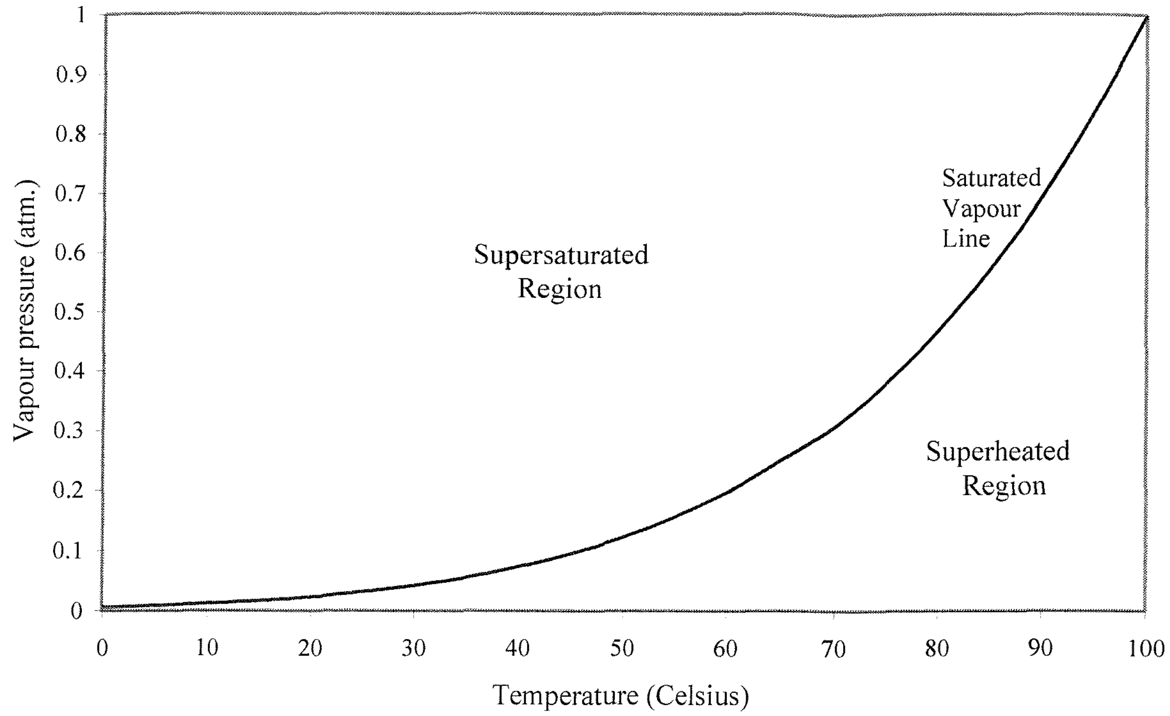

Figure 2-1. Saturated vapour line (saturation curve) for water vapour.

The different regions of Figure 2-1 equate to different states of the substance. A substance whose conditions correspond to a point below, or to the right of the saturation curve is referred to as a superheated vapour. A substance above or to the left of the saturation curve is described as supersaturated. The supersaturated state of a vapour / condensable gas is unstable thermodynamically [16, 17] containing more vapour than a stable, saturated vapour. The 'excess' vapour may condense into liquid droplets to form a fog, reducing the free energy of the system. The vapour pressure thus falls to the equilibrium value [18], i.e. until the vapour state of the resulting two-phase mixture is saturated.

A state of supersaturation is a necessary condition for fog formation [9]. However, supersaturation is not a sufficient condition for fog formation [5, 19]. The vapour may remain in a metastable supersaturated state. Whether a phase change occurs and a fog forms is dependent upon a number of factors, the most important of which are the presence of foreign particles and the degree of subcooling, or the supersaturation ratio, S, defined [20] as

$$S = \frac{\text{Partial pressure of vapour}}{\text{Saturated vapour pressure at gas-phase temperature}} = \frac{p_v}{p_s} \qquad \textbf{(2-1)}$$

These conditions apply equally if the substance is a vapour – gas mixture or a pure vapour. The presence of an inert gas component does not affect the saturation condition of the vapour.

2.3 *Liquid droplet formation from the vapour phase*

The molecules of a vapour make relatively frequent encounters with each other and have ample opportunity for becoming associated into groupings of more than one molecule – dimers, trimers, etc. – which may exist for a time before being broken up into smaller fragments or completely back to unassociated molecules. Alternatively they may combine with other associated groups or single molecules, or both, and there is always a finite, if often very small, probability that a grouping of n molecules will be found.

The energetics of these molecular groupings (involving typically many thousands of molecules) can be simplified, using what is often known as the "liquid drop" model [21]. The almost infinite number of positions which a molecule can take within a grouping of n molecules is confined to three (i) an "interior" position, (ii) a "surface" position, and (iii) a "vapour" position in which the molecule has escaped beyond the influence of the intermolecular forces. This reduces the free energy of a grouping of n molecules to a sum of two terms, one proportional to volume and the other proportional to surface area. This then, is essentially a continuum description, lacking any detail of structure, molecular position, or orientation. However, it is very useful and effective, and in many situations gives better agreement with experiment than more detailed treatments.

2.3.1 Energy changes associated with drop formation

Classical nucleation theory for the free energy of a spherical embryo of a condensed phase [22] gives:

$$\Delta G = \tfrac{4}{3}\pi r^3 \Delta G_v + 4\pi r^2 \sigma \qquad \textbf{(2-2)}$$

where r is the radius of the embryo, σ its surface tension and ΔG_v is the free energy change produced when unit volume of the liquid is formed without a change in surface area. Now using the substitutions

$$a = \tfrac{4}{3}\pi \Delta G_v \qquad \textbf{(2-3)}$$

and $b = 4\pi\sigma$ **(2-4)**

equation (2-2) may be written

$$\Delta G = ar^3 + br^2 \tag{2-5}$$

The surface tension, σ, and hence the term b, is always positive. A positive value for ΔG_v, and hence a, implies that work must be done to bring a molecule from the vapour phase into the condensed phase, so the reverse process, evaporation, is energetically favoured. Therefore $a > 0$ implies the vapour is superheated. Accordingly, $a = 0$ equates to equilibrium between vapour and liquid, i.e. saturated conditions, while supersaturation is indicated by $a < 0$. Now, the behaviour of ΔG with embryo radius can be readily obtained from equation (2-5). For supersaturated vapours ($a < 0$), $\Delta G = 0$ when

$$r = 0, \quad r = -b/a \tag{2-6}$$

and possesses stationary points when

$$\frac{d\Delta G}{dr} = 3ar^2 + 2br = 0 \tag{2-7}$$

i.e.

$$r = 0, \quad r = -2b/3a \tag{2-8}$$

Since

$$\frac{d^2\Delta G}{dr^2} = 6ar + 2b \tag{2-9}$$

$r = 0$ is a minimum, $r = -\frac{2b}{3a}$ is a maximum, and due to the dominance of the r^3 term, $\Delta G \rightarrow -\infty$ as $r \rightarrow \infty$.

The free energy of an embryo in a superheated vapour ($a > 0$) however has only one zero, at $r = 0$, and has no stationary points for real positive values of the embryo radius r. Its value increases monotonically with increasing radius, and the larger the embryo the greater the work which must be done to produce it. Since work must be done to bring a molecule from the vapour phase into the condensed phase: the reverse process, evaporation, is energetically favoured in superheated mixtures.

The results are illustrated in Figure 2-2 below.

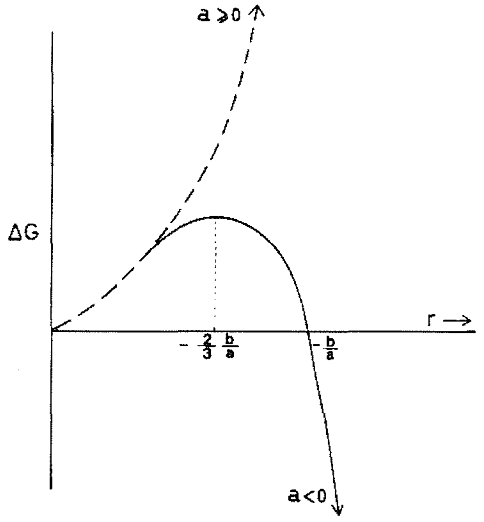

Figure 2-2. Free energy of a droplet embryo as a function of embryo radius [21].

Focussing on the supersaturated case ($a < 0$) pertinent to fog formation, a number of interesting features become evident. ΔG attains a maximum at $r^* = -2b/3a$ after which it decreases rapidly as the embryo radius increases. This demonstrates that the supersaturated state is unstable, the free energy of the system is reduced if the vapour can condense. The maximum of ΔG represents an energy barrier between the lower energy all-vapour state and the still lower energy all-condensed state. It is the surmounting of this energy barrier that constitutes nucleation.

2.3.2 The rate of nucleation

Classical nucleation theory relies on fluctuations to overcome this energy barrier. It invokes the possibility of random associations of molecules in energetically unfavourable combinations as a means of forming embryos of the critical size r^*. Kinetic theory is then used to calculate how many critically sized embryos experience a molecular collision in unit time, giving the nucleation rate.

Now, in order to calculate the size, number, and free energy of the critical embryos, and subsequently the nucleation rate, in terms of known quantities, Boltzmann statistics are employed. The number of embryos of a given size is proportional to $\exp(-\Delta G/kT)$, so the number of critical embryos n^* may be written

$$n^{*} = N\exp\left(-\Delta G/kT\right) \qquad \textbf{(2-10)}$$

where $r^{*} = -\tfrac{2}{3}b/a$, and $\Delta G^{*} = ar^{*3} + br^{*2} = \tfrac{4}{27}b^{3}/a^{2}$.

Therefore, calculation of the nucleation rate requires a knowledge of the quantities denoted by N and a. The required procedure is presented in standard texts [21]. The radius of the critical embryos may then be shown to be given by the following equation, known in its various forms as the Kelvin [23] , Kelvin-Helmholtz [24, 25], or Gibbs-Thomson [21] equation:

$$r^{*} = \frac{2\sigma M}{\rho RT\ln(S)} \qquad \textbf{(2-11)}$$

where σ is the surface tension of the embryo, M its molar mass and ρ its density.

The free energy of the critical embryos is subsequently given by

$$\Delta G^{*} = \frac{16\pi\sigma^{3}M^{2}}{3\rho^{2}R^{2}T^{2}}\frac{1}{\left[\ln(S)\right]^{2}} \qquad \textbf{(2-12)}$$

and the number of critical embryos by

$$n^{*} = N\exp\left[-\frac{16\pi\sigma^{3}M^{2}N_{A}}{3\rho^{2}R^{3}T^{3}}\left(\frac{1}{\ln(S)}\right)^{2}\right] \qquad \textbf{(2-13)}$$

The nucleation rate is finally calculated on the assumption that every critical embryo colliding with a vapour molecule surmounts the energy barrier and becomes a permanent condensation nucleus, thus the nucleation rate is

$$J = \alpha\cdot 4\pi r^{*2}\cdot n^{*}vN \qquad \textbf{(2-14)}$$

v being the kinetic coefficient $\sqrt{RT/2\pi M}$ and α an accommodation factor.

Written in full the equation for J is:

$$J = c\frac{16\pi\sigma^{2}M^{2}}{\rho^{2}R^{2}T^{2}\left[\ln(S)\right]^{2}}\frac{p^{2}}{kT\sqrt{2\pi m}}\exp\left[-\frac{16\pi N_{A}\sigma^{3}M^{2}}{3\rho^{2}R^{3}T^{3}\left[\ln(S)\right]^{2}}\right] \qquad \textbf{(2-15)}$$

where c is a constant of proportionality ≤ 1, and m molecular mass M/N_{A}.

Though many improvements to the classical theory have been proposed [26, 27], mostly involving the addition of terms to the free energy equation (2-2), they have resulted in greater discrepancies with experimental results for all but a few vapours, and have yet to become widely acknowledged. As a result, the classical theory is still the only accepted method for predicting the nucleation behaviour of the majority of real substances.

2.3.3 Quantitative deductions

A number of important points may be deduced from the above equations, the first of which is the typical size of critical embryos. For water at a temperature of ~20°C (293K), $\rho \approx 1000\text{kg/m}^3$, $R = 8.314$ J/mole K, $M = 18.015\times10^{-3}$ kg/mole, and $\sigma = 7.23\times10^{-2}$ N/m, r^* is approximately $1.1\times10^{-9}/\ln(S)$ metres. Thus, collecting some interesting values the following table is produced:

S (saturation ratio)	Supersaturation	r^* (critical radius - μm)
1.001	1×10^{-3}	1.07
1.01	1×10^{-2}	1.075×10^{-1}
1.1	1×10^{-1}	1.12×10^{-2}
2	1.0	1.54×10^{-3}
11	10.0	4.46×10^{-4}
1001	1×10^{3}	1.55×10^{-4}

Table 2-1. The critical radius of water droplets at a range of saturation ratios.

Hence r^* decreases rapidly with increasing supersaturation at relatively small values. At very large supersaturations, e.g. $S \sim 1000$, the critical radius size is of molecular dimension implying that a grouping of only a few molecules will grow into a liquid droplet.

For other liquids the quantity $\sigma M/\rho$ in equation (2-11) often differs significantly from that of water. For benzene, for example, $\sigma = 28.88 \times 10^{-3}$ N/m, $M = 78.108 \times 10^{-3}$ kg/mole, $\rho = 901$ kg/m^3, resulting in a critical embryo radius approximately $\frac{1}{500}$ that of water.

The most interesting information comes from the form of the nucleation equation (2-15). The exponential term dominates the expression for J so completely that a graph of J against $\ln(S)$ is very steep. The nucleation rate therefore increases from a very small value to a very large value for a small change in the supersaturation, as illustrated in Figure 2-3.

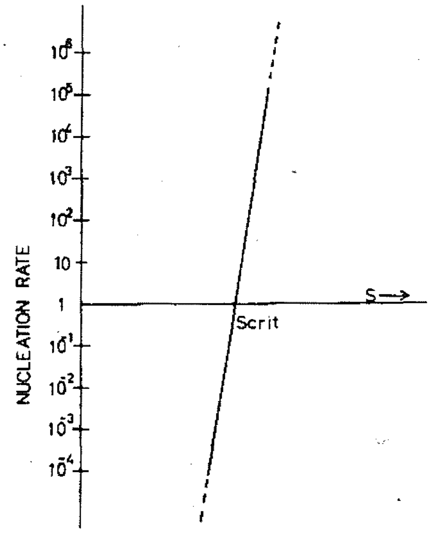

Figure 2-3. The phenomenon of critical supersaturation [21]

The fact that the nucleation rate increases so rapidly as supersaturation increases is used to define a critical supersaturation. This is defined as the value at which droplet formation becomes appreciable and is generally taken to be $J = 1$, i.e. the formation of one droplet per cubic centimetre per second. Though this value appears a little contrived, the corresponding critical supersaturation changes little if the criterion $J = 1000\,\text{cm}^{-3}\text{s}^{-1}$ is used because of the gradient of J against S, Figure 2-3.

The critical supersaturation for the nucleation of water vapour is approximately 340% $(S = 4.4)$ [21]. However, in the atmosphere cloud formation occurs at much lower supersaturations, and often almost as soon as the air becomes saturated. This apparent anomaly is attributed to the presence of suspended particles, lowering the energy required for droplet formation. The results presented so far in this section were based upon the assumption of droplet formation directly from the vapour phase, away from any solid surfaces and in the absence of such particles. This type of droplet formation is known as *homogeneous nucleation*. Homogeneous nucleation may be studied experimentally using cloud chambers, inside which saturated vapour is subjected to an abrupt expansion in the absence of any foreign nuclei. This cools the vapour very rapidly and produces almost instantaneous supersaturations. In these experiments no droplet formation is observed until a well-defined value of supersaturation is reached. At this point even a slight increase of supersaturation leads to immediate copious fog formation. Good agreement has been obtained between the critical supersaturations predicted by the classical model and those recorded during these experiments, validating the theory.

2.4 *Heterogeneous nucleation*

It is clear from cloud chamber experiments that foreign nuclei play an important role in fog formation. Droplet formation upon such nuclei is known as *heterogeneous nucleation*. Heterogeneous nucleation begins at very low supersaturations, and the formation and subsequent growth of the liquid drops then acts to reduce the supersaturation further. Thus, under normal circumstances, provided sufficient nuclei are present, the high supersaturations required for homogeneous nucleation are extremely unlikely. Indeed, during a series of experiments in which organic vapour – nitrogen mixtures were cooled, Peters and Altmann [28] demonstrated that only by reducing the nuclei number concentration could a transition from heterogeneous to homogeneous nucleation be observed, indicated by a great increase in the droplet concentrations. A knowledge of the number concentrations of foreign nuclei, their characteristics and source of origin is therefore extremely important.

2.4.1 Foreign Nuclei

The foreign nuclei present in the atmosphere comprise a number of different substances. These include sea salt, dust, ions and pollutants including sulphur, ammonia and carbon [21]. In section 2.3.1 it was demonstrated that for a liquid droplet to be in equilibrium or continue to grow, it must attain a critical size, or diameter. Hence, the obvious way to categorise the nuclei upon which droplets form is in terms of their size. Many of the nuclei will not be spherical in shape, though for simplicity the particles are still generally assigned a single diameter, often based upon their mass, assuming a density value and a spherical shape. Thus a particle size distribution may be obtained for the condensation nuclei present in the air. Atmospheric particle number size distributions are often trimodal [29], the modes consisting of nuclei $\left(< 0.1\mu m\ diameter\right)$, accumulation $\left(0.1\mu m < diameter < 2.0\mu m\right)$ and coarse particles $\left(> 2.0\mu m\right)$, translating to one of three modes in the corresponding volume size distribution. [Note that the term nuclei is also used to refer to the entire range of dry atmospheric particles, owing to all being potential sites for nucleation, and it is this convention which shall generally be adhered to here.] An example atmospheric particle size distribution is presented below. Note that the number of particles of a given size appears to increase rapidly below about $0.5\mu m$, despite the logarithmic scale on which the particle size axis is plotted. Yet the volume size distribution is dominated by the coarse particle mode, even though the number of particles in this category fails to register on the number size distribution.

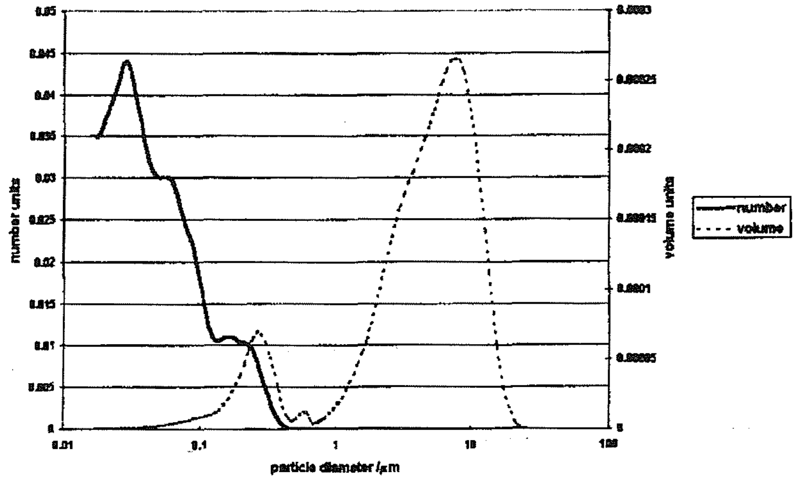

Figure 2-4. Normalised modified background particle number and volume size distributions. Obtained in a forest park, 15km west of Brisbane, Australia [29].

Such particle size distributions fluctuate from day to day [30], indeed from one moment to another, and vary to a greater degree with different environments, e.g. marine, forest, urban, industrial etc. Example distributions are presented below.

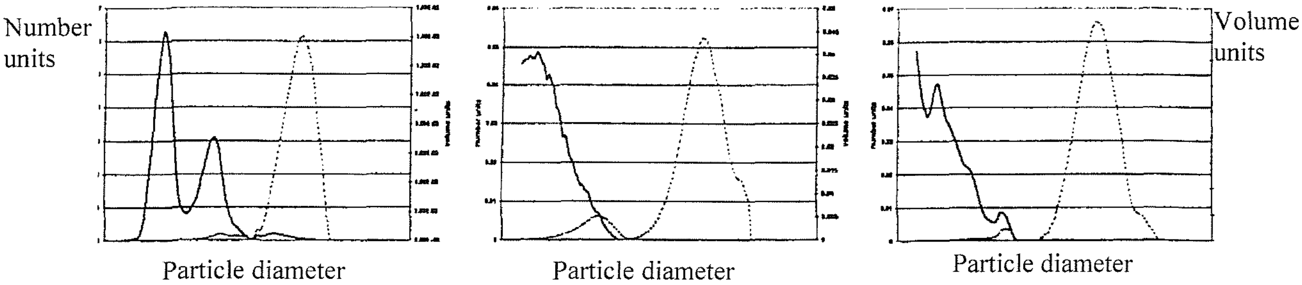

Figure 2-5. Normalised particle size (solid line) and volume (dotted line) distributions, averaged over a minimum of 100 measurements, in a number of different environments, namely oceanic, suburban and urban [29].

Though such variations exist in the nuclei distributions, atmospheric air contains always sufficient small particles for heterogeneous condensation [19]. Typical number concentrations are in the range $10^3 - 10^6$ particles per cm^3. Furthermore, in industrial processes high concentrations of fine particles are generated in addition to natural condensation nuclei. Therefore, providing extremely high initial supersaturations are avoided, heterogeneous nucleation will always be the dominant mechanism of fog formation inside partial condensers.

2.4.1.1 Insoluble nuclei

Now since condensation nuclei come in a variety of different sizes and substances, it may be expected that nucleation occurs more readily on some particles than others. Indeed, in natural condensation producing clouds and fogs only a few out of all the nuclei present are grown into drops [21]. Thus an understanding of the dependence of nucleation efficiency on the size and surface properties of the nucleating particles is very important and is necessary for predicting the magnitude of droplet concentrations.

When a given volume of liquid is formed on a surface it possesses a lower surface area than the same volume would have as an isolated sphere. The energy associated with its formation from the vapour phase is therefore reduced. Fletcher [31] theoretically investigated the effect of nuclei size on embryo formation. He calculated that for a spherical nucleating particle, its condensation nucleation efficiency is highly influenced by its size only when its radius is less than about 0.02μm (200A) for water. The increasing curvature of the nucleating particle at such small sizes increases the energy required for nucleation. Above 0.02μm however, the particle size is far less important, and the energy of formation approaches the result for a flat surface (i.e. the minimum value). Note that concavity of the nucleating surface, provided by steps or pits, may initially allow nucleation to proceed more readily, but once the pits are filled the conditions for further growth would be that of the surrounding geometry, i.e. flat or convex. Condensation on concave surfaces cannot alone produce drops that are larger than the original nucleus.

Another variable affecting the energy required for stable droplet formation upon an insoluble nucleus, is the contact angle between the condensate and the nucleus surface. The smaller the angle the lower the energy required. A contact angle of 0 degrees implies the nucleus is completely wet. The behaviour of such perfectly wetted nuclei is equivalent to that of pure water droplets of equal size. The Kelvin equation (2-11) can then be used to calculate the minimum nuclei radius required for nucleation at, for example, 1% supersaturation, typical of the upper level at which natural cloud formation occurs. Thus

$$r = \frac{2\sigma M}{\rho RT \ln(S_c)} \approx 1.1\times10^{-7} \qquad \textbf{(2-16)}$$

that is ~ 0.11μm for water. The concentration of such sized nuclei in the atmosphere is relatively low (see Figure 2-4 and Figure 2-5), and it is unlikely that many of them will be perfectly wetted or possess sufficiently small contact angles. In fact, water typically exhibits relatively large contact angles on common insoluble materials, so even larger nuclei would be required for the onset of fog formation at such low supersaturations. Nucleation upon insoluble particles is therefore not the means of forming the majority of droplets at atmospheric supersaturations $(< 1\%)$, and an alternative explanation is required.

2.4.1.2 Soluble nuclei

Experimental measurements suggest smaller sized nuclei, closer to 0.01μm are responsible for the majority of natural droplet formations. It can be shown theoretically [21] that soluble nuclei are much more conducive to droplet formation.

The two major soluble inorganic salts found in atmospheric aerosol collections are ammonium sulphate ($(NH_4)_2 SO_4$) and ammonium nitrate (NH_4NO_3), with ammonium sulphate dominating [32, 33]. As a result the properties of ammonium sulphate are often used in models of nucleation and hygroscopic growth [32].

Raoult's Law states that the vapour pressure of a solution is proportional to the mole fraction of the solute (e.g. inorganic salts) in the solution [21]. In calculating mole fractions a dissociated molecule which has dissociated into i ions is viewed as i molecules, where an undissociated molecule is counted only once. (Ammonium sulphate, nitrate, sodium chloride etc. are all highly dissociated in solution.) Therefore, for the solution as a whole an effective mole fraction, the van't Hoff factor, i, is used. This is a function of concentration, but is generally treated as a constant without introducing an appreciable error.

When vapour condenses upon a soluble particle of mass m, a solution droplet of radius r is formed. The mass of the droplet, $(4\pi/3)\rho_s r^3$, then consists of $\left[(4\pi/3)\rho_s r^3 - m\right]$kg of liquid, plus m kg of solute. The solute then produces im/M_N moles in solution while the liquid (solvent) present amounts to $\left[(4\pi/3)\rho_s r^3 - m\right]/M_W$ moles, where M_N is the molecular weight of the soluble particle material and M_W is that of the liquid condensing.

By Raoult's Law the saturation vapour pressure of such a solution droplet e_r', is related to the saturation vapour pressure e_r of a pure liquid drop of the same radius as follows:

$$\frac{e_r - e_r'}{e_r} = \frac{im/M_N}{\left(\frac{4\pi}{3}\rho_s r^3 - m\right)\Big/M_W + im/M_N} \qquad \textbf{(2-17)}$$

which is simply the ratio of moles of solute to the total moles in the solution drop. This may also be written

$$\frac{e_r - e_r'}{e_r} = \frac{imM_W/M_N}{\frac{4\pi}{3}\rho_s r^3 + mM_W\left(\frac{i}{M_N} - \frac{1}{M_W}\right)} \qquad \textbf{(2-18)}$$

in which, provided the droplets are at high relative humidities and are therefore quite dilute, the second term in the denominator can be neglected, reducing it to the form almost always used in cloud physics:

$$\frac{e_r^{'}}{e_r} = 1 - \frac{im_N}{(4\pi/3)\rho_s r^3} = 1 - \frac{b_N}{r^3} \qquad \textbf{(2-19)}$$

where m_N is an effective nuclear mass $(= mM_W/M_N)$. For ammonium sulphate $imM_W/M_N = 0.41m$. Now the equilibrium state and critical diameter of such a solution droplet is given by the Köhler equation which is obtained by combining Raoult's Law with the curvature effect of the droplets (Kelvin effect) [34].

The vapour pressure of a pure water drop of radius r, e_r, is written in terms of e_o, the saturation vapour pressure (of a flat liquid surface):

$$e_r = e_o \exp\left(\frac{2\sigma M}{\rho RT}\frac{1}{r}\right) \qquad \textbf{(2-20)}$$

which is equivalent to equation 2-11 introduced earlier. Thus, for a solution droplet of density ρ_s

$$e_r^{'} = \frac{e_r^{'}}{e_r} e_r = \left(1 - \frac{b_N}{r^3}\right) e_o \exp\left(\frac{2\sigma M}{\rho_s RTr}\right)$$

$$\approx e_o\left(1 - \frac{b_N}{r^3}\right)\left(1 + \frac{2\sigma M}{\rho_s RTr}\right) \qquad \textbf{(2-21)}$$

in which the exponential term has been linearised without introducing any serious error provided $r \geq 0.01\mu m$. It has also been assumed that b_N/r^3 and $2\sigma M/\rho_s RTr$ are small so their product can also be neglected, therefore

$$\frac{e_r^{'}}{e_o} = 1 + \frac{a}{r} - \frac{b_N}{r^3} \qquad \textbf{(2-22)}$$

which is known as the Köhler equation, and may also be written in terms of percentage supersaturation

$$S = \frac{a}{r} - \frac{b_N}{r^3} \qquad \textbf{(2-23)}$$

The variable represented by a is $2\sigma M/\rho_s RT$ where, assuming dilute solutions, $\rho_s \approx \rho$. Hence only b_N is dependent upon the size and the nature of the nucleus. The maximum of equation 2-23 is attained when $dS/dr = 0$, which occurs when the droplet achieves the critical radius r_c, hence

$$r_c = \sqrt{\frac{3b_N}{a}} \qquad \textbf{(2-24)}$$

$$S_c = \frac{2}{3}\frac{a}{r_c} = \frac{2}{3\sqrt{3}} a^{3/2} b_N^{-1/2} \qquad \textbf{(2-25)}$$

For a given nucleus the supersaturation can be plotted against droplet radius to produce a Köhler curve. A series of such curves for ammonium sulphate nuclei of various dry particle radius are plotted in Figure 2-6 below.

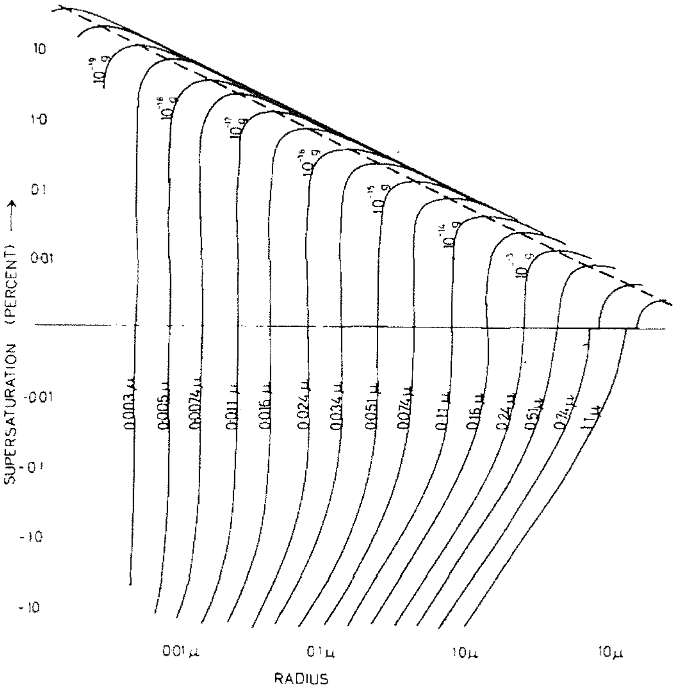

Figure 2-6. Köhler curves, relating equilibrium supersaturation to radius of droplet for ammonium sulphate nuclei. Each curve relates to a particular size of nucleus (and therefore mass of solute) indicated on the curves themselves. The broken line joins the maxima of all such curves [21].

Thus, referring to Figure 2-6, a 0.016μm radius nucleus in an environment of 0.1% supersaturation will grow to a size of approximately 0.04μm radius by direct condensation whereupon it will exist in an equilibrium state as a concentrated solution droplet. In fact, even in a sub-saturated environment such nuclei will take up a little water. If the supersaturation increases to 1% however, which is slightly greater than S_c, the critical supersaturation of an ammonium sulphate nucleus of this size, nucleation will occur and the droplet will grow much larger. Indeed, if the supersaturation remains greater than S_c, the nucleus is "activated" and will continue to grow indefinitely. Moreover, once activated the supersaturation with which the drop would be in equilibrium falls as the drop grows (Figure 2-6). Hence the growth of activated nuclei may continue even if the prevailing supersaturation is subsequently reduced due to the removal of vapour by condensation.

The minimum size particle which can nucleate at supersaturation S_c is given by the general formula [21]

$$r_{\min} = \left(\frac{32\sigma^3 M_W{}^2 M_N}{27\rho_L{}^2 R^3 T^3 i \rho_N} \right)^{\frac{1}{3}} S_c{}^{-2/3} \quad \textbf{(2-26)}$$

with S_c in percent, which is essentially equation (2-25), and for ammonium sulphate approximates to

$$r_{\min} \approx 1.45 \times 10^{-8} \, S_c{}^{-2/3} \quad \textbf{(2-27)}$$

Values of $r_{\min}$ over a range of typical atmospheric supersaturations are detailed in Table 2-2 below.

$S_c(\%)$	0.05	0.1	0.25	0.5	0.75	1.0
$r_{\min}(\mu m)$	0.11	0.067	0.036	0.023	0.017	0.015

Table 2-2 Minimum radius of ammonium sulphate nuclei which may nucleate at a given supersaturation.

The simple equation (2-27) from which Table 2-2 was drawn up, was obtained using values specific to ammonium sulphate. However, the minimum nucleus size for nucleation upon other soluble compounds will not differ too greatly from the values for ammonium sulphate, and is generally in the hundredth-micron range. This is in agreement with the typical minimum nuclei size observed in natural clouds and fogs. Thus it is concluded that the majority of particles which nucleate at supersaturations below 1% are soluble, and comprise of ammonium sulphate, nitrate, and other soluble compounds.

2.5 *Activation*

Consider the effect of a given supersaturation upon a population of particles of different sizes. Nuclei of a sufficiently large size, such as nucleus A in Figure 2-7, having a critical supersaturation below the externally applied value, $S_c < S_{ext}$, are nucleated and become activated. Smaller nuclei with $S_c > S_{ext}$ grow only slightly to a stable equilibrium size, which for nucleus B is denoted by radius r_B. Such a droplet, being inactivated, is referred to as a haze droplet.

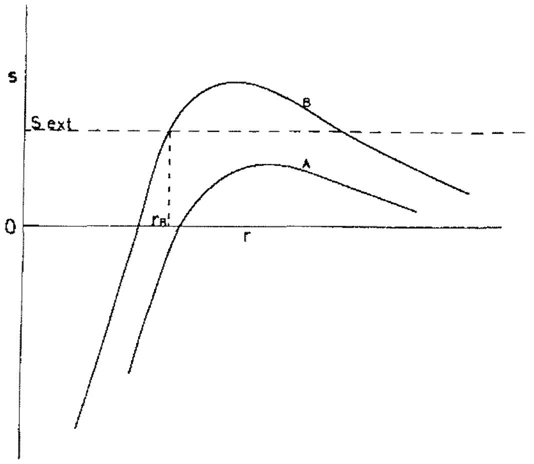

Figure 2-7. The effect of a given supersaturation on two different nuclei [21].

There is therefore a division of the nuclei into two classes, according to whether their critical supersaturation is smaller or greater than that of the fluid in which they are suspended. After a time, the activated nuclei will have grown into drops many times the size of the haze droplets, the growth being driven by the difference between the droplets' equilibrium supersaturation and that of the surrounding vapour. Though the activated nuclei are generally far fewer in number than the haze droplets, they constitute a much greater proportion of the total droplet mass. The haze droplets will generally be smaller than 0.01μm in radius, so the liquid mass (and volume) of 1 million such droplets will be less than that of just one activated 10μm drop.

Therefore, the effect of condensation upon haze droplets can be safely neglected in the present study.

2.6 *Critical Supersaturation*

In the preceding sections, atmospheric particles have been categorised largely in terms of their size. This is perfectly adequate for studying the behaviour of particles of a single compound. Under normal circumstances however, a wide range of particles of different characteristics and composition will be present. Thus, in an environment supersaturated with respect to water vapour, perfectly wetted insoluble particles larger than $\left(1.2\times10^{-7}S_c^{-1}\right)$m in radius will be activated, in addition to any ammonium sulphate nuclei larger than $\left(1.45\times10^{-8}\,S_c^{-2/3}\right)$m in radius, sodium chloride nuclei larger than $\left(1.606\times10^{-8}\,S_c^{-2/3}\right)$m in radius etc.

It is clear that categorising such particles in terms of just their size is insufficient when considering their behaviour as condensation nuclei. It is helpful only if used in conjunction with information about the composition of each particle. A more useful way to categorise such particles is in terms of their critical supersaturations, S_c, as it is this which determines an individual particles potential for nucleation. If the level of supersaturation of the system is known, those particles which will be activated can be readily identified, and an estimation of the resulting droplet number concentration obtained.

Experiments to measure the number of nuclei activated at a given, small supersaturation, within the range 0.1 - 2.0% may be conducted with a thermal diffusion cloud chamber. Inside these chambers a steady supersaturation is produced, allowing the activation of nuclei and their subsequent growth to a size at which they can be counted. This is then repeated for a number of different supersaturation levels, enabling the number of activated nuclei (droplet count per unit volume) to be plotted against supersaturation, giving the 'supersaturation spectrum'. The results of a series of such experiments upon atmospheric air from a number of different geographical locations are shown in Figure 2-8 below.

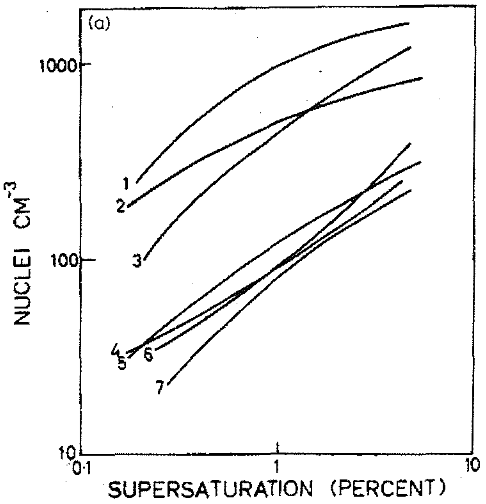

The numbers on the curves indicate the region, as follows:
1 - continental, Australia
2 – continental, US
3 – continental, Africa
4 – oceanic, South Pacific
5 – oceanic, North Atlantic
6 – oceanic, South Atlantic
7 – oceanic, North Pacific.

Figure 2-8. Experimentally measured supersaturation spectra from aircraft measurements in different geographic regions [21].

2.7 *Droplet number concentration*

In reality the supersaturation level varies with time. As the vapour cools and becomes supersaturated some nuclei become activated and grow, producing a fog. The growing droplets deplete the environment of water vapour and thereby act to reduce the supersaturation, while continued cooling acts to increase it. This interaction determines the maximum supersaturation, $S_{\max}$.

The experimentally determined spectra of Figure 2-8, are close to linear on the log-log scale on which they are plotted. This indicates a dependence which can be expressed to a good degree of approximation as

$$N \cong cS^{k} \qquad \textbf{(2-28)}$$

where N is the number of droplets activated per unit volume, c is the nuclei concentration and k is the gradient of N vs S (Figure 2-8), the median value of which, obtained from a large number of aircraft measurements is roughly $\frac{1}{2}$.

During cloud formation, a parcel of moist air ascends at a velocity V resulting in cooling and an increase in humidity, an upper bound can be placed on the resulting supersaturation, $S''_{\max}$, which can be shown [21] to be related to the rate of ascent and the nuclei concentration according to

$$S''_{\max} \propto c^{\frac{-1}{k+2}} V^{\frac{3}{2(k+2)}} \tag{2-29}$$

Thus, inserting the experimentally determined value for k,

$$N \propto c^{0.8} V^{0.3} \tag{2-30}$$

Hence, during natural cloud formation, the drop concentration is primarily determined by nucleus concentration, and to a lesser extent by the rate of ascent (or rate of cooling). Atmospheric nuclei concentrations may vary considerably throughout the day, as illustrated in Figure 2-9 below.

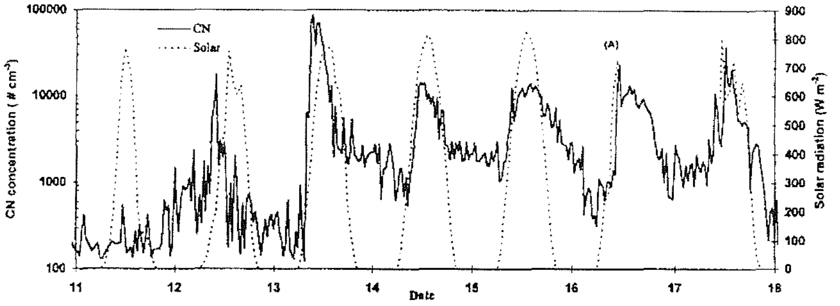

Figure 2-9. Time series of condensation nuclei and solar radiation data recorded at Mace Head, Ireland, between 11th and 18th April 1991 [30].

The nuclei concentrations presented above were obtained in a remote location. The large variations shown may be tempered significantly in industrial plants owing to the generation of a great number of additional nuclei during the process. Nevertheless, droplet concentrations are likely to be affected, though to a lesser extent.

2.8 *Condensational droplet growth*

The condensational growth of a liquid droplet suspended in a gas-vapour mixture may occur in one of three different regimes. The appropriate regime is determined via the Knudsen number, Kn, which is given by [23]

$$Kn = {}^{l}\!/_{r_d} \tag{2-31}$$

where r_d is the droplet radius and l is the mean free path of the surrounding medium. The mean free path is given by

$$l = \frac{M}{N_A \rho \sigma} \tag{2-32}$$

where M is the atomic weight, N_A is Avogadro's number (6.022x10^{23}/mole), ρ is the density and σ is the molecular cross-sectional area.

In the continuum regime, characterised by $Kn << 1$, the droplet growth rate is controlled by diffusive mass transfer, whereas when $Kn >> 1$, known as the free molecular regime, droplet growth rate predictions are based on kinetic theory. In the case of a droplet whose radius is of the order of the mean free path of the surrounding fluid the transport of mass and energy is partly under diffusion control and partly under kinetic control (transition regime) [19].

2.8.1 Continuum regime

The basis of the continuum theory $(Kn \to 0)$ was laid by J. C. Maxwell and is based on the assumption of thermodynamic equilibrium between the liquid surface and the vapour in direct contact with it [25]. In the continuum regime droplet growth is diffusion based. Diffusion is the process whereby matter is transported from regions of higher concentration to regions of lower concentration, and may alternatively be expressed in terms of densities or pressures. Hence, for a liquid droplet in a supersaturated environment, if the vapour pressure at the droplet surface, $p_{v,a}$ $(\propto S)$, is less than that of the surrounding fluid, $p_{v,\infty}$ $(\propto S_{ext})$, vapour molecules will diffuse towards the droplet where they will condense. The mass flux to the droplet has been presented in numerous equivalent forms [21, 23, 25], and may be written

$$\left(\frac{dm}{dt}\right)_{CR} = \frac{4\pi r D}{R_v T}\left(p_{v,a} - p_{v,\infty}\right) \tag{2-33}$$

where r is the droplet radius, D the diffusion coefficient, R_v the gas constant of the vapour and T is the droplet temperature. Droplets therefore remove vapour from their surroundings at a rate proportional to their radius. In fact, since the mass flux is also proportional to $(p_{v,a} - p_{v,\infty})$, or $(S - S_{ext})$, and the surface supersaturation, S, of activated droplets falls a little as radius increases (Figure 2-6), the mass flux increases slightly faster still as the droplet grows.

The relationship between mass flux and rate of droplet growth is given by

$$\frac{dm}{dt} = 4\pi r^2 \rho_L \frac{dr}{dt} \qquad \textbf{(2-34)}$$

hence, inserting this in equation (2-33) produces the droplet growth rate

$$\left(\frac{dr}{dt}\right)_{CR} = \frac{D}{\rho_L R_v T r}\left(p_{v,a} - p_{v,\infty}\right) \qquad \textbf{(2-35)}$$

which, to a first approximation, is proportional to the inverse of droplet radius. Thus droplets grow at a decreasing rate, the fastest relative growth occurring on the smallest droplets.

2.8.2 Transition regime

When the droplet size is comparable to the mean free path of the surrounding medium $(Kn \sim 1)$, equilibrium no longer exists between the vapour and liquid surface. A jump in vapour pressure and temperature occurs at the droplet surface which must be taken into account [23]. This is most easily achieved by the addition of a correction factor to the equations pertaining to the continuum regime (2-33) and (2-35) such that

$$\left(\frac{dm}{dt}\right)_{TR} = \left(\frac{dm}{dt}\right)_{CR} f(Kn_M) = \frac{4\pi r D}{R_v T}\left(p_{v,a} - p_{v,\infty}\right) f(Kn_M) \qquad \textbf{(2-36)}$$

where the Fuchs-Sutugin formula

$$f(Kn) = \frac{1 + Kn}{1 + 1.71Kn + 1.33Kn^2} \qquad \textbf{(2-37)}$$

is commonly used for $f(Kn)$ [23] and $Kn_M = {}^{l_v}\!/_{r}$. The droplet surface vapour pressure, $p_{v,a}$ may be obtained from equation 2-23, the Köhler equation for droplets forming on a soluble nucleus, which in expanded form is

$$S = \frac{p_{v,a}}{p_s} = \frac{2\sigma M}{\rho_s R T}\frac{1}{r} - \frac{i m_N}{(4\pi/3)\rho_s}\frac{1}{r^3} \qquad \textbf{(2-38)}$$

where the properties of ammonium sulphate may be used for the nucleus without appreciable error (see section 2.4.1.2). The droplet temperature, T, is greater than that of the surrounding fluid due to the latent heat released during condensation and may be calculated using [21, 23]

$$T_a = T_\infty - \frac{\frac{dm}{dt} L}{4\pi rkf\left(Kn_T\right)} \tag{2-39}$$

where L, k and Kn_T are the latent heat, the thermal conductivity and the Knudsen number as defined by $Kn_T = l_g / r$, respectively.

The mass flux to the droplet can then be obtained by the solution of the coupled equations 2-36, 2-38 and 2-39, and the rate of droplet growth from equation 2-34.

2.8.3 Free molecular regime

In the free molecular regime, it is assumed that the droplet surface is exposed to molecules with the properties of the surrounding vapour. The mass flux to the droplet is obtained by considering the difference between the molecular impingement and evaporation rates [10]. This regime $(Kn \to \infty)$, is only likely to be of interest in low pressure situations, or when the droplets are very small. Under these conditions equation 2-38 for determining the droplet surface vapour pressure, is no longer valid. Hence, droplet growth in this regime is to be neglected here.

2.9 *Droplet interactions*

Droplets have been shown to influence the vapour concentration and temperature profiles of a neighbouring droplet only if the distance between them is of the order of the droplet radius [23]. For a droplet concentration as high as 10^6 per cubic centimetre, assuming them to be equidistant, the distance between droplet centres is 100μm. Drops larger than 40μm quickly fall out of a system under the action of gravity (section 1.2). In addition droplets generally form on only a fraction of all the foreign particles present, for which 10^6 particles/cm^3 represents the upper end of observed concentrations (section 2.4.1). Thus the influence of neighbouring droplets on the vapour concentration and temperature profiles may be neglected. Interaction between the droplets cannot be excluded completely however, as in reality the droplets will not be equidistant and may approach or collide with one another, particularly in a highly turbulent field.

2.9.1 Droplet coalescence

Collisions between drops may result in coalescence leading, for example, to the formation of one 14μm drop from two 10μm drops. Coalescence thus affects both the droplet concentration and droplet size distribution. In fact, in natural cloud formation coalescence overtakes diffusional condensation as the dominant growth mechanism when a drop becomes large (>20μm), due to the $\frac{1}{r}$ dependence of condensational growth (section 2.8) and the larger drop falling more rapidly through smaller ones, thereby undergoing more collisions. Such gravitationally induced coalescence is likely to be of lesser relative significance inside industrial condensers due to the much greater cooling and condensation rates, narrower range of expected droplet sizes (section 2.10) than in clouds and smaller distances through which the drops may fall. Indeed, it is often assumed that there is no relative velocity between the droplets and the carrier gas inside condensers [19]. However, since the flow regime inside condensers is generally turbulent, some droplets will collide due to the eddy motion of the fluid. The greater the fluid velocity, the greater the Reynolds number associated with the flow and the greater the rate of droplet coalescence. The rate of coalescence will also increase with droplet number concentration and average droplet size.

2.9.2 Droplet break-up

Droplet break-up only occurs in very high velocity flows. For example, a flow velocity of 15m/s is required for the onset of instability in a 1mm droplet of water in air, and this velocity increases by the factor $\sqrt{10}$ for each order of magnitude of decrease in drop size [6]. Hence droplet break-up can be safely neglected here.

2.10 *Experimentally measured droplet sizes*

To date there has been no published work regarding droplet size distributions formed during the cold wall condensation of vapour or gas-vapour mixtures. However, a few papers have appeared in which experimentally measured droplet size distributions are presented. These measurements were all conducted upon systems in which the vapour cooling was not accomplished via contact with a cold wall. The cooling was achieved instead by natural convection, adiabatic expansion or radiation. A brief summary of the most important results and their relevance to the work undertaken here is now presented.

In 1994 a large field experiment was undertaken into natural fog formation. It was conducted in a polluted region of northern Italy, from which a number of interesting papers were published [32, 33, 34, 35, 36]. Fog formation of this kind was shown to be a slow process, occurring over a number of hours, and involving very low rates of cooling. The associated supersaturations were demonstrated to be extremely low, too low in fact for nucleation to occur. The simultaneous measurement of ambient droplet and corresponding 'dry' particle sizes, with the aid of the Köhler equation, proved that during the majority of fog events the droplets remained inactivated, being smaller than their critical size. This leads to continuous droplet size distributions from the lower size limit of the measurement apparatus, ~1 μm, to drops as large as 45μm. The largest drops formed on the largest particles (pollutants such as sulphates, black carbon etc. comprising the bulk of the largest particles [32]). This is also true of droplet formation in clouds [33].

Martinsson et al. [37] studied the formation of orographic clouds (i.e. clouds formed during the ascent of humid air over a mountain), where the rates of temperature decrease (-3 to 20mK/s) are significantly faster than those associated with natural fog formation, and exist over shorter time intervals (~ tens of minutes). From these experiments it appears that the droplet number density of orographic clouds is generally lower than that of natural fogs, whereas the mass concentration is greater. Almost all the cloud water was associated with activated droplets in a mode at 10-15μm diameter, which was formed on sub-micrometer particles. These differences between the two studies were highlighted by Frank et al. [34] in the figure below.

The droplet size distributions measured in orographic clouds show a large jump from the inactivated haze droplets / interstitial particles (< 0.5μm) and the activated cloud droplets (> 8μm), which is absent in the natural fog results. The main difference in conditions under which the droplet formations took place involves the rate of temperature decrease.

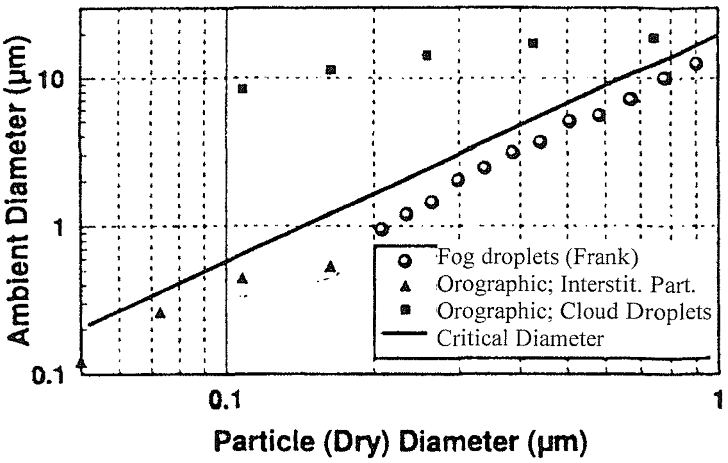

Figure 2-10. A comparison of the typical relationship between ambient and dry particle diameters measured during fog formation and orographic cloud formation.

Frank et al. [34] developed a closed parcel cloud model of fog formation, which was used to predict the influence of this rate of temperature decrease on droplet sizes. Though only low values (0.056 – 0.56mK/s) were used, the results predicted the appearance of activated droplets larger than 10µm as the cooling rate increased, the number of which also increased with increasing cooling rates. This is in broad agreement with the two studies discussed above, and is due to an increase in the resulting supersaturation. The nucleation rate does not follow the supersaturation rate immediately if it changes in time [38]. At small cooling rates, the excess water vapour continually condenses upon the soluble particles before large supersaturations have a chance to develop. As the rate of cooling increases however, greater supersaturations are realised before more nuclei are activated, as detailed in section 2.6, and equilibrium is reached between the rate of excess vapour production and its condensation upon growing droplets.

The largest cooling rates, and hence supersaturations, mentioned above, or which are associated with any natural droplet formation, are far below those produced inside partial condensers etc. Droplet formation over a range of large supersaturations has been studied experimentally by Heidenreich and Ebert [23], using the mixing of two virtually saturated air streams of different temperature. By this method, very high supersaturations of up to 80% were achieved almost instantly. This was designed to produce nucleation upon all foreign nuclei present with the aim of growing the resulting droplets to a size whereby they can easily be removed.

Modelling of the process predicted very narrow size distributions would result, with droplets of approximately 2.5μm in diameter existing upon all nuclei after very short growth times of only ~ 0.1s. The nearly single sized droplets are predicted due to the decrease of droplet growth rate with increasing size (as detailed in section 2.8). The corresponding experimental results presented show good agreement with the predicted mean droplet sizes, though droplet size distributions are not presented. It is acknowledged however that the measured distributions were wider than those predicted. This was attributed to the non-instantaneous nature of the supersaturation throughout the fluid, due to the complex mixing process.

2.10.1 Application to fog formation inside condensers

The experiments discussed above demonstrate the effect of rate of temperature decrease and degree of supersaturation upon heterogeneous droplet size distributions. At the cooling rates attained inside condensers, these results suggest reasonably large supersaturations and the activation and growth of large numbers of soluble nuclei. The resulting droplets will be far larger than the inactivated 'haze' droplets, and hence carry virtually all of the condensed liquid.

There is however one important difference between the formation of fog inside partial condensers and that occurring in the papers discussed. That is the additional complication of the simultaneous removal of vapour by surface condensation. The associated temperature and concentration changes take place over distances much larger than the scale of the fog droplets. These large scale fields are superimposed on the fine scale thermal and concentration fields [39]. Very little work has been done in this area. In studies involving the two processes in tandem it is customary to consider only the large scale problem in any depth, treating the fog as a simple sink of matter [39, 40].

Though all the work discussed above strictly applies only to the limiting case of very low large scale heat and mass transfer rates, the principles involved provide a useful insight into the processes of droplet formation and growth. They will allow qualitative analysis of the fogs produced inside condensers, and the prediction of the effects of conditional changes upon the size and concentration of the resulting droplets.

2.11 *Summary*

In summary, a fog is a cloud of liquid droplets, suspended in a gas / vapour. For droplets to form, the vapour must be supersaturated, the degree of supersaturation, S, being given by the ratio of actual vapour pressure to that of a saturated vapour at the gas-phase temperature. At sufficiently high supersaturations spontaneous droplet formation occurs, directly from the vapour phase. This process is known as homogeneous nucleation. Classical nucleation theory predicts the energy associated with this type of droplet formation, and the existence of a critical embryo size. Embryos achieving this critical size continue to grow, whereas the tendency for smaller embryos is to re-evaporate. The critical embryo size, r_c, is dependent upon the supersaturation. As supersaturation increases, r_c decreases until it is sufficiently small to allow critically sized cluster formation to occur readily. However, the supersaturations required for such homogeneous nucleations are very high, e.g. 340% for water vapour [21]. Under normal circumstances such high supersaturations do not occur because at very low levels, <1%, heterogeneous nucleation begins upon suspended particles. Normal air always contains a sufficient number of such particles, or nuclei, for droplet formation (between 10^3 and 10^6 per cm^3). The level inside industrial plants is generally even greater than that of the surrounding air.

Though these nuclei comprise many different compounds, soluble nuclei have been shown to lend themselves most readily to droplet formation. Of these, the salts ammonium sulphate and nitrate are the most common in atmospheric air. Even at high relative humidities, below saturation, some water will condense upon these particles and they will exist as concentrated solution droplets. Each particle dependent upon its size, composition, and surface characteristics has a critical droplet size, r_c, at which nucleation occurs. This takes place when the supersaturation reaches the critical value, S_c, which may be calculated for individual particles using the Köhler equation. Thus, given the external supersaturation, S_{ext}, those particles upon which nucleation will occur may be identified. As supersaturation increases the number of particles undergoing nucleation increases at an increasing rate. This acts in conjunction with the condensational growth of existing drops to deplete the vapour concentration until a maximum supersaturation, $S_{\max}$, is reached. This value determines the number of nucleated droplets. Those droplets with a surface vapour pressure (or supersaturation) below that of the surrounding vapour are said to be 'activated', and will then continue to grow indefinitely provided this remains the case.

If cooling produces the supersaturation, the rate of temperature decrease plays an important role in determining the droplet size spectrum. Very slow cooling rates, as observed during the formation of atmospheric fogs, result in very small supersaturations, an absence of activated nuclei, and a continuous size spectrum, with the largest drops forming on the largest condensation nuclei. Slightly larger rates of temperature decrease, typical of orographic cloud formation result in the production of higher supersaturations. This leads to the activation and rapid growth of those nuclei for which $S_c < S_{ext}$, while the remaining particles remain inactivated, as small concentrated solution droplets. In a short time a clear gap thereby develops in the droplet size spectrum. The condensed liquid contained in the inactivated droplets is then insignificant compared to that of the much larger activated drops, despite their greater number, and they can therefore be neglected.

The magnitude of the supersaturation and the length of time the droplets are subjected to it governs the size to which they will grow. As the drops grow they remove vapour from their surroundings at an increasing rate (approximately proportional to their radius r), but they grow at a decreasing rate $\left(\propto \frac{1}{r}\right)$. Thus provided the supersaturation is not later increased, once $S_{\max}$ has been reached and nucleation effectively terminated, there should be an effective narrowing of the droplet size spectrum.

The above description of droplet formation has been developed in the absence of the large-scale temperature and vapour concentration fields that exist inside industrial separators and condensers. Consequently, the results introduced are only strictly applicable for small bulk heat and mass transfer rates. However, many of the principles discussed will still be valid, and in any case will be very useful in providing qualitative explanations of experimentally observed phenomena.

3. Fog formation in partial condensers

3.1 Introduction

The previous chapter was concerned with the processes of droplet formation, from the foreign particles upon which the water condenses, to the processes of nucleation, activation and droplet growth. Focus was applied to individual droplets, concentrating on the small-scale diffusional and thermal fields to which they are subjected. These fields act over a distance comparable to the droplet size, i.e. $< 1 \times 10^{-4}$m. The properties of the surrounding fluid were assumed constant from one region to another.

Inside condensers and separators large-scale temperature and vapour pressure profiles are established [39]. Thus the factors influencing droplet formation vary from one point to another, both along the condenser, in the primary direction of fluid flow (axially), and perpendicular to this and to the cold condenser walls (radially/laterally). However, the local conditions required for fog formation at any location will be as described previously.

In this chapter the properties of a mixture flowing through a partial condenser will be studied. Following an initial consideration of the importance of heat and mass transfer rates upon the bulk mixture condition and the onset of bulk fog formation, attention is switched to the mechanisms of vapour flow towards the condensing surface and the temperature and concentration gradients established. In addition to the ordinary diffusion of vapour, a second flow, known as Stefan flow, is shown to exist in the case of surface vapour condensation. It is then illustrated how the resulting lateral temperature and concentration gradients may lead to supersaturation and hence fog formation being initially confined to a narrow region close to the wall, a phenomenon known as film fog. Techniques for predicting the onset of film fog are then discussed and employed in the case of water vapour – air mixtures.

Though the onset of fog formation is generally determined by localised conditions in the vicinity of the condensing surface, the general behaviour of the fluid, and its propensity for fog formation, is predominantly governed by the variation of bulk mixture conditions. This is in turn controlled by the relative rates of heat and mass transfer from the mixture. Hence, by performing a mass and energy balance over a differential section of a partial condenser, incorporating equations for the rates of heat and mass transfer (condensation), a set of differential equations is derived, describing the changes in the bulk mixture conditions. These may then be used to predict the temperature, vapour pressure, and vapour and fog flow rate throughout a partial condenser.

3.2 Supersaturation of the gas-vapour mixture

Along the length of a condenser the bulk temperature and the partial vapour pressure of the mixture fall due to heat and mass transfer respectively. The gas – vapour mixture entering the condenser may be assumed to be superheated with respect to the vapour, as is generally the case, in order to prevent the pre-existence of fog. Consider the bulk condition of the mixture, that is the 'mixing cup' average over the entire cross-sectional area, defined specifically for temperature within a pipe [3] as

$$t_b = \frac{\int_0^R \rho c_p 2\pi r t \, dA}{\int_0^R \rho c_p 2\pi r \, dA} \tag{3-1}$$

The transfer of heat tends to supersaturate the mixture, while the transfer of mass tends to superheat the mixture. This is illustrated in Figure 3-1 below.

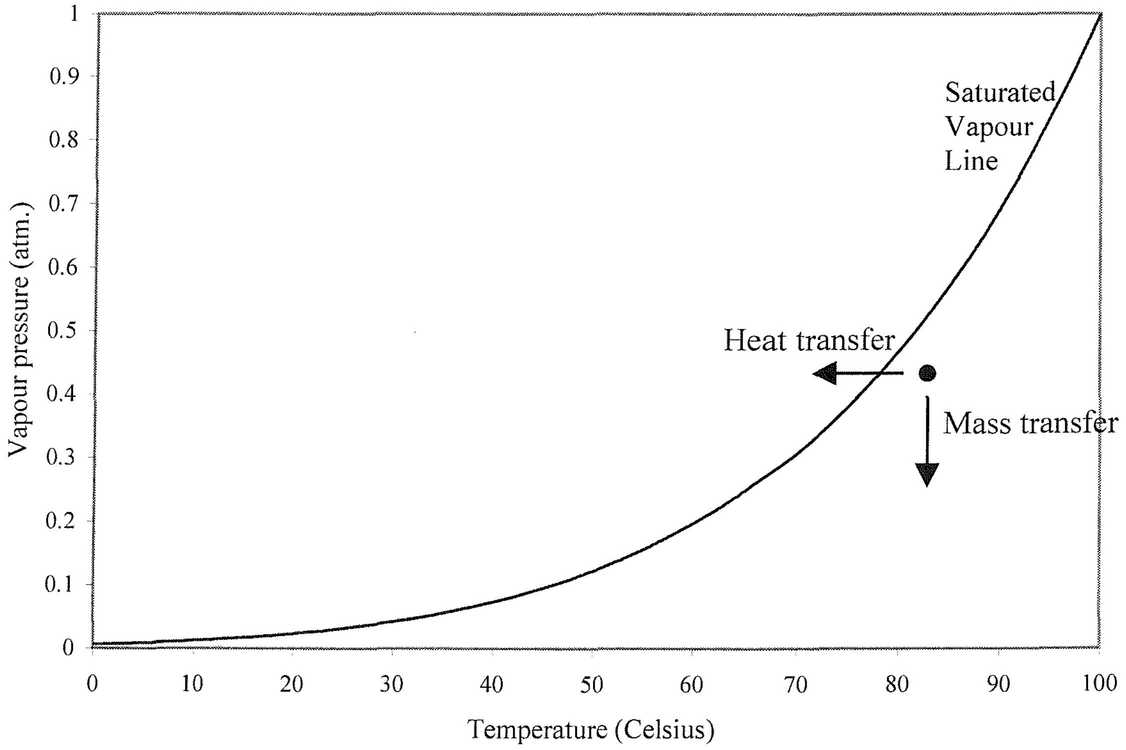

Figure 3-1. The effects of heat and mass transfer on bulk conditions during the flow of a gas – vapour mixture through a partial condenser.

The net effect upon the condition of the mixture will depend upon the ratio of heat transfer to mass transfer. If this ratio is sufficiently high, the bulk mixture will become supersaturated and fog formation will occur. Thus, bulk fog formation occurs by the simple cooling of a gas faster than condensable vapour can be removed by mass transfer [4].

Provided the initial condition of the mixture, the flow conditions, and condenser coolant temperature are known, it should be possible to estimate the heat and mass transfer rates, and thus predict the change of the bulk condition of the mixture. The axial location of the onset of any bulk fog formation can thereby be predicted. Such a technique shall be applied to the partial condensation of a gas – vapour mixture in section 3.8. However, fog formation may well begin before it is predicted by this method, because of its focus upon 'bulk' conditions. This ignores the possibility of supersaturation (and hence fog formation) in one cross-sectional part of the condenser and a superheated mixture in the remainder. Thus, to accurately predict the true onset of droplet formation within a condenser, it is also necessary to analyse the lateral variation of mixture conditions.

3.3 Vapour transport to the cold wall

Consider in detail the case of a mixture of a condensable vapour and a non-condensable gas, in contact with a cold wall below the dew point of the vapour. Any vapour in contact with the wall immediately condenses onto its surface resulting in a lowering of the vapour pressure in that region. The removal of vapour at the wall results in a bulk flow of both vapour and gas towards it, which is referred to as the 'convective velocity', 'bulk velocity' or 'Stefan flow' [17]. This results in an accumulation of non-condensing gas at the interface [41]. The partial pressure of gas at the interface therefore increases above that in the rest of the mixture, producing a driving force for gas diffusion away from the surface. This flow is exactly counterbalanced by that of the non-condensing gas in the opposite direction, associated with the Stefan flow [4, 42]. Hence, there is no net movement of gas perpendicular to the wall. The temperature and partial pressure profiles in the vicinity of the cold wall are of the form depicted in Figure 3-2, below.

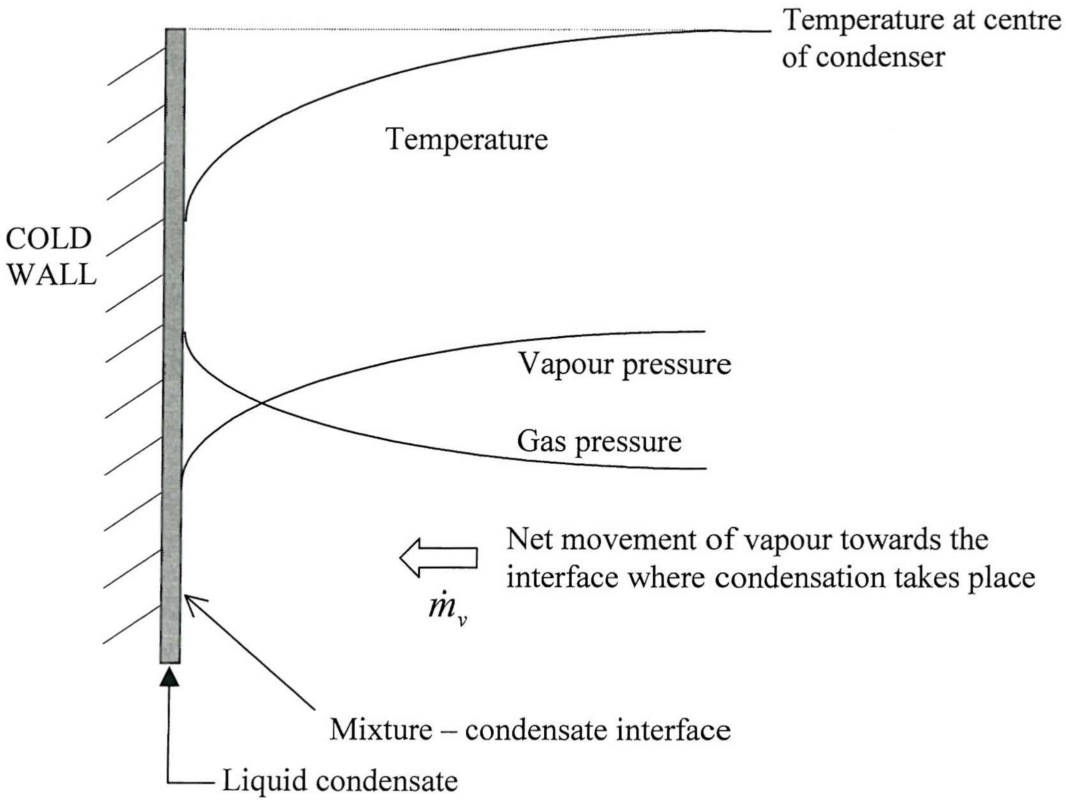

Figure 3-2. Temperature and pressure profiles during wall condensation in the presence of a non-condensable gas [43].

In summary, there is a diffusion of vapour towards the wall and non-condensable gas away from the wall. The gas flow is exactly counterbalanced by an additional bulk flow, or Stefan flow, towards the surface. This additional flow augments the rates of diffusional heat and mass transfer from the mixture.

3.4 Localised fog formation

The variation of partial vapour pressure with distance from the cold wall (Figure 3-2) raises the possibility of supersaturation first appearing in a restricted cross-sectional region of the condenser. Though the vapour pressure falls towards the wall, so does the mixture temperature. Thus, the saturation vapour pressure also falls. In order to assess whether supersaturation (and hence fog formation) will occur at a given location it is therefore necessary to compare the lateral saturation and actual vapour pressure profiles existing within the condenser. This was first discussed in detail by Johnstone, Kelley and McKinley [12], using the corresponding temperature profiles rather than those of vapour pressure. It is customary to follow their example [44].

A simple comparison may be conducted using a knowledge of conditions at the centre of the condenser and at the mixture – condensate interface. At the interface condensation is taking place, hence it is generally assumed that the mixture is saturated [12, 44, 45] and the saturation and actual temperature profiles are coincident. Considering initially the case of a highly superheated bulk mixture, the profiles are then of the form depicted in Figure 3-3.

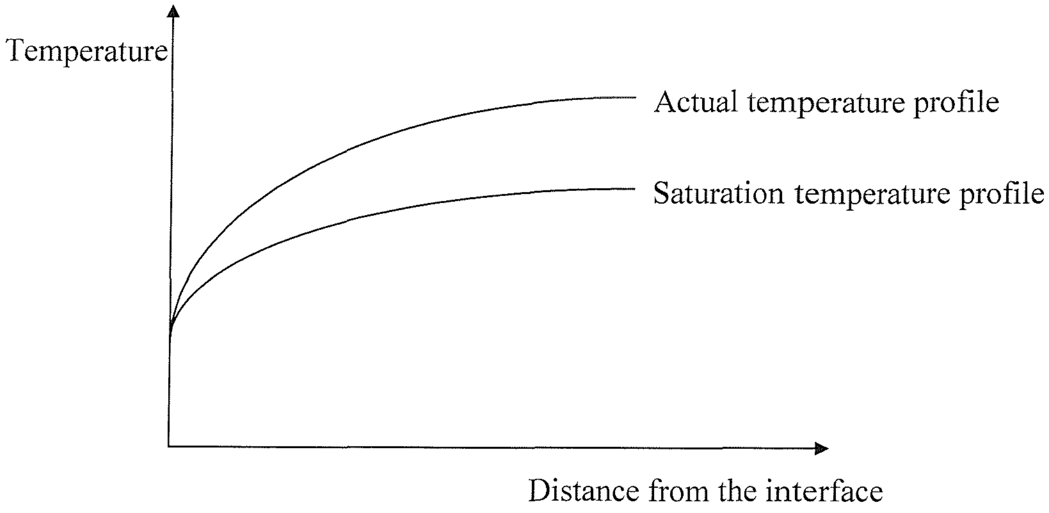

Figure 3-3. Saturation and actual temperature profiles perpendicular to the cold wall of a condenser for a highly superheated bulk mixture.

The actual temperature of the mixture is greater than the saturation temperature throughout the cross-section and hence no fog formation will take place. However, if the bulk mixture is only slightly superheated there is the possibility that the two profiles may cross. In this case the mixture between the interface and the point the profiles intersect will be supersaturated and a fog may form, see Figure 3-4 below.

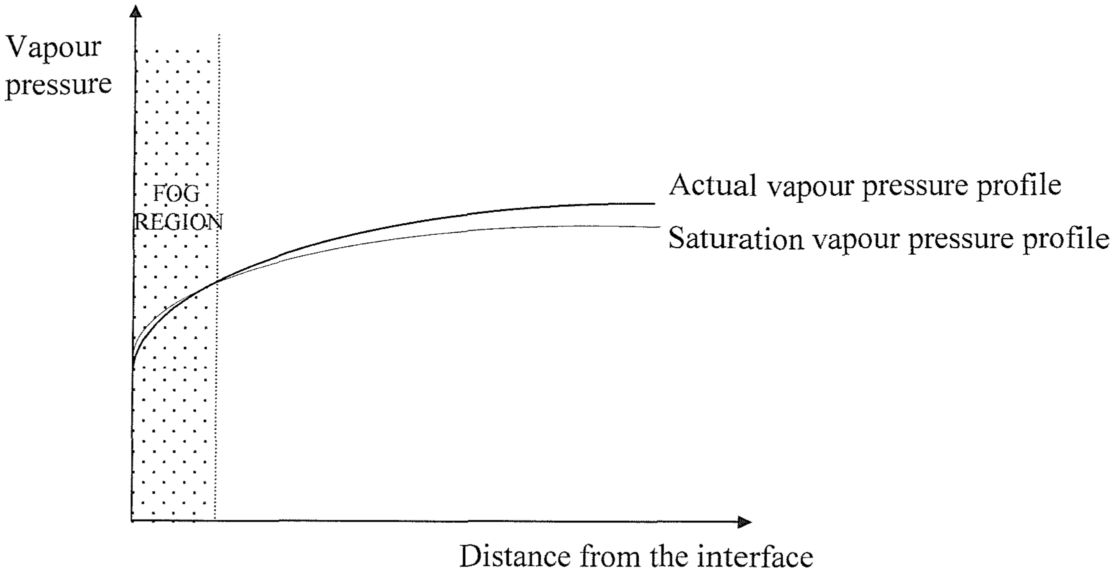

Figure 3-4. Temperature profiles during fog formation near the wall.

Fogs formed in this way are likely to be confined to a relatively thin region close to the wall, where the gradients are steepest and are often referred to as film fogs. The onset of fog formation will occur when the two profiles first intersect. The position exactly intermediate between the conditions of no fog and fog formation, as represented by Figure 3-3 and Figure 3-4 respectively, exists when the saturation and actual temperature profiles are tangent at the condensate – mixture interface, as first identified by Johnstone et al. [12]. This has become known as the 'tangency condition' and has been widely used to predict the onset of fog formation [16]. Thus, to accurately predict the conditions under which droplet formation will commence it is necessary to determine the interfacial derivatives of the two profiles.

3.5 Predicting localised fog formation

To compare the saturation and actual profiles, and allow easy interpretation of the results, the two values may be plotted on a graph of vapour mole fraction against temperature. If the total pressure inside the system is 1 atmosphere, the value of vapour mole fraction is equivalent to that of the partial vapour pressure (atmospheres). The location of the saturation curve is defined by the saturation function, $F^+(t)$. The function $G^+(t)$ describes the actual path of the mixture conditions, and is coincident with $F^+(t)$ at the interface where the mixture is saturated.

Figure 3-5 illustrates the three possible cases arising for a given interface temperature, i.e., $G^+(t) < F^+(t)$ [I], $G^+(t)=F^+(t)$ [II], and $G^+(t) > F^+(t)$ [III] at the interface.

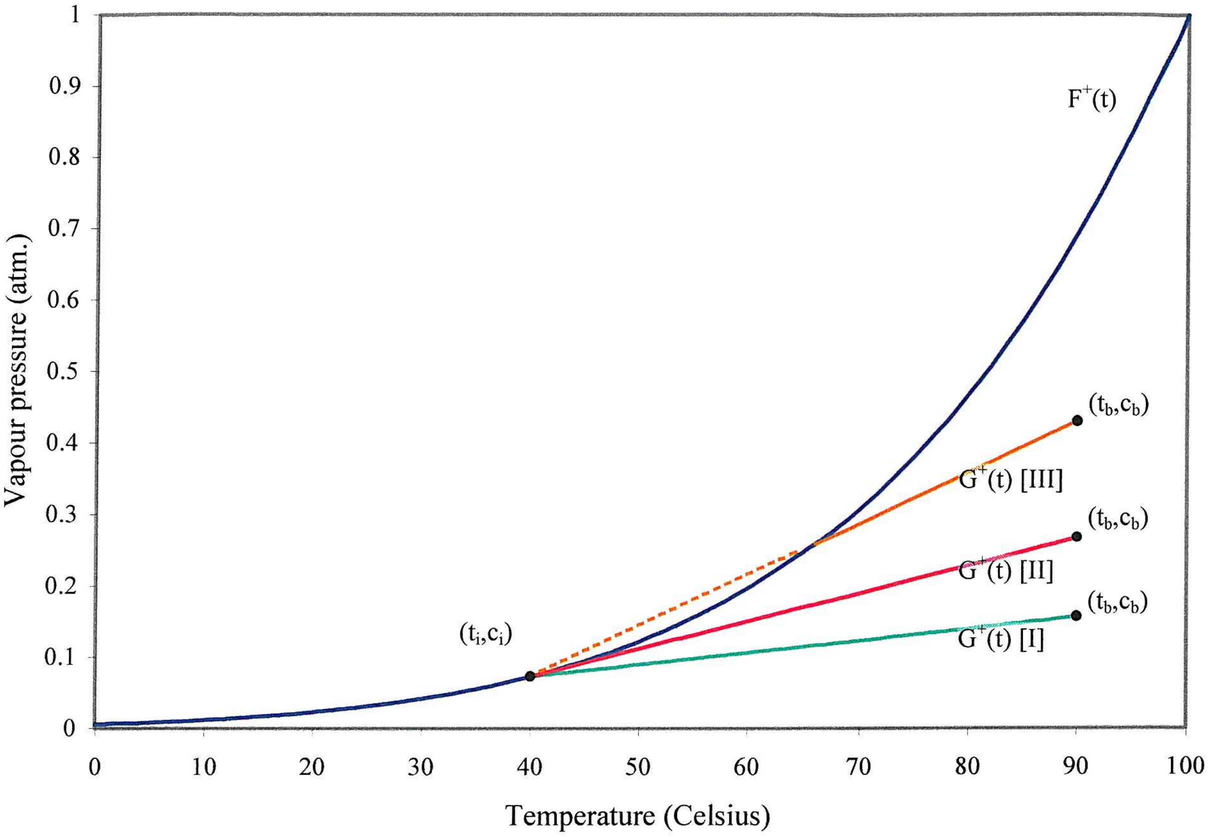

Figure 3-5. Distinguishing between fogging (case III) and fog free (case I) mixtures.

For simplicity, linear profiles of $G^+(t)$ are depicted, although this is not strictly true, being slightly convex for a water vapour – air mixture for example. In case I, $G^+(t)$ lies entirely in the superheated region, hence no fog is formed, whereas in case III $G^+(t)$ lies partially in the supersaturated region, implying fog formation near the wall. In case II, $G^+(t)$ and the saturation function are tangent.

The saturation function, $F^+(t)$, and hence its derivative, can be obtained for the majority of vapours from published tables [6, 46]. A procedure for calculating the derivative of $G^+(t)$ was first presented by Johnstone et al. [12], though Brouwers [47] later identified an erroneous assumption contained therein and produced a corrected derivation. Both results are presented in appendix A. These can be employed at any given axial condenser location where the bulk and interface conditions are known to predict the boundary between entirely superheated mixtures and those in which fog formation will occur at the axial location concerned. In the case represented in Figure 3-5 for example, film fog formation would be expected in mixtures with a bulk temperature of 90°C and a bulk vapour mole fraction, c_b, greater than that of case II. Such predictions for a water vapour – air mixture with interface temperatures of 20, 30 and 40°C, were calculated using the equations derived in both papers, and are presented in appendix A. The results are reproduced in Figure 3-6 below.

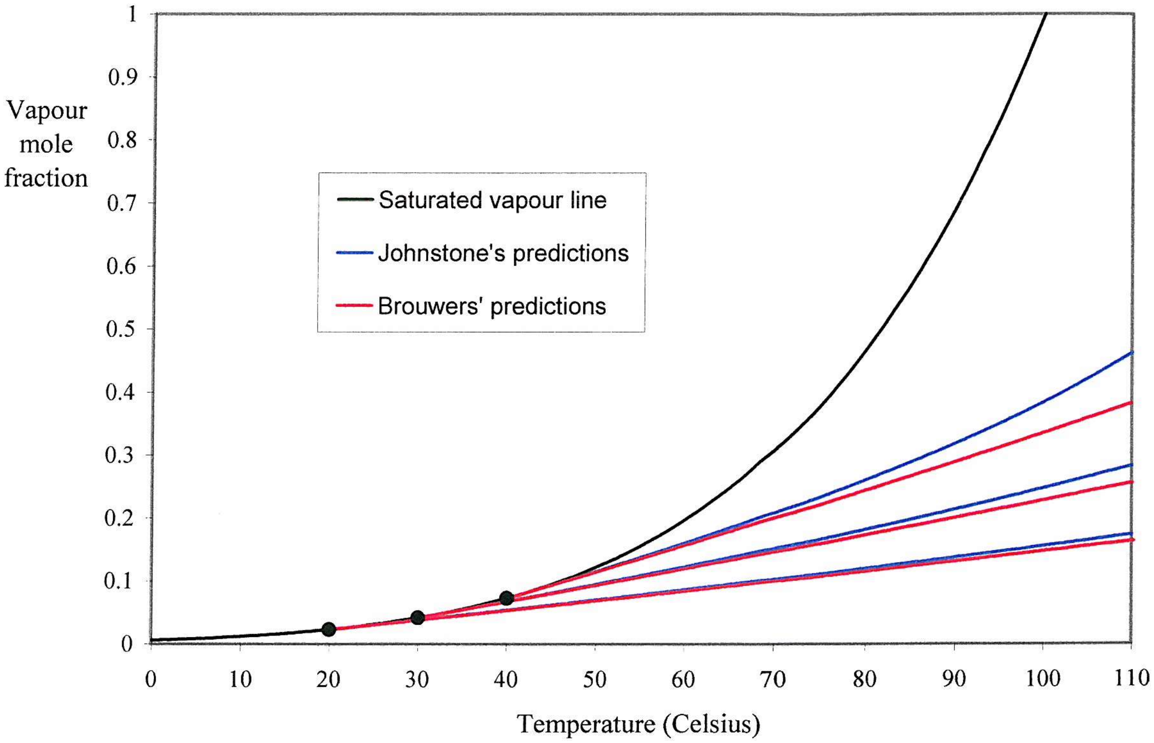

Figure 3-6. Determination of the critical conditions for fog formation when the interface temperature is 20°C, 30°C and 40°C.

Film fog is predicted to form near the wall in mixtures corresponding to a point lying above a given line. Below the line no fog is predicted. Generally better agreement is obtained with the experiments performed by Johnstone et al. using Brouwers' equation, particularly for water vapour – nitrogen mixtures. The few discrepancies that remain are attributed to the difficulty in determining the temperature at the interface. Figure 3-6 demonstrates how common droplet formation will be during the partial condensation of water vapour – air mixtures. With an interface temperature of 20°C (not unreasonable using cold water coolant) droplets will form in all mixtures for which the average temperature is below 100°C and the vapour mole fraction is greater than 0.2.

3.6 *Bulk mixture properties*

In the preceding sections the lateral temperature and vapour pressure profiles were shown to be critical in predicting the onset of fog formation inside a partial condenser from an initially superheated mixture. However, for the complete picture, the axial variations are of even greater importance. A sufficiently low heat to mass transfer ratio may lead to the evaporation of any film fog as the degree of superheating increases. Thus, droplet capture from the exit gases may be unnecessary despite fog formation occurring within the condenser. As in the previous section, the problem is most easily explained using a graph of vapour mole fraction (or partial vapour pressure) against temperature. Once again the most important points are the initial bulk mixture condition (t_{b1}, c_{b1}), and those at the cold wall (t_w, c_w), or allowing for a condensate film, the interface (t_i, c_i). Assuming a constant wall temperature, the bulk mixture condition will tend towards that at the wall, since the driving forces for heat and mass transfer, i.e. the temperature and concentration gradients $(t_b - t_i)$ and $(c_b - c_i)$ will tend to zero. However, the bulk condition will actually reach that at the wall only in an infinitely long condenser.

The path of the bulk mixture condition as it flows through the condenser determines its overall tendency to fog. Three distinct examples, in which the mixture tends to supersaturate, A, saturate, B, and remain superheated, C, are plotted in Figure 3-7 below.

The supersaturation predicted in case A will almost inevitably lead to fog formation, hence the actual path will follow the saturation line as the temperature falls below that indicated by point α, as discussed in section 2.2. The length of the condenser and the residence time of the mixture within it will determine how far along the appropriate line the condition passes. In industrial condensers the length and flow rates are generally set to ensure rapid removal of as much vapour as possible, providing the costs associated with the process do not escalate too greatly. Hence, the condition of the mixture usually approaches that of a saturated mixture at the temperature of the wall (t_w, c_w) quite closely.

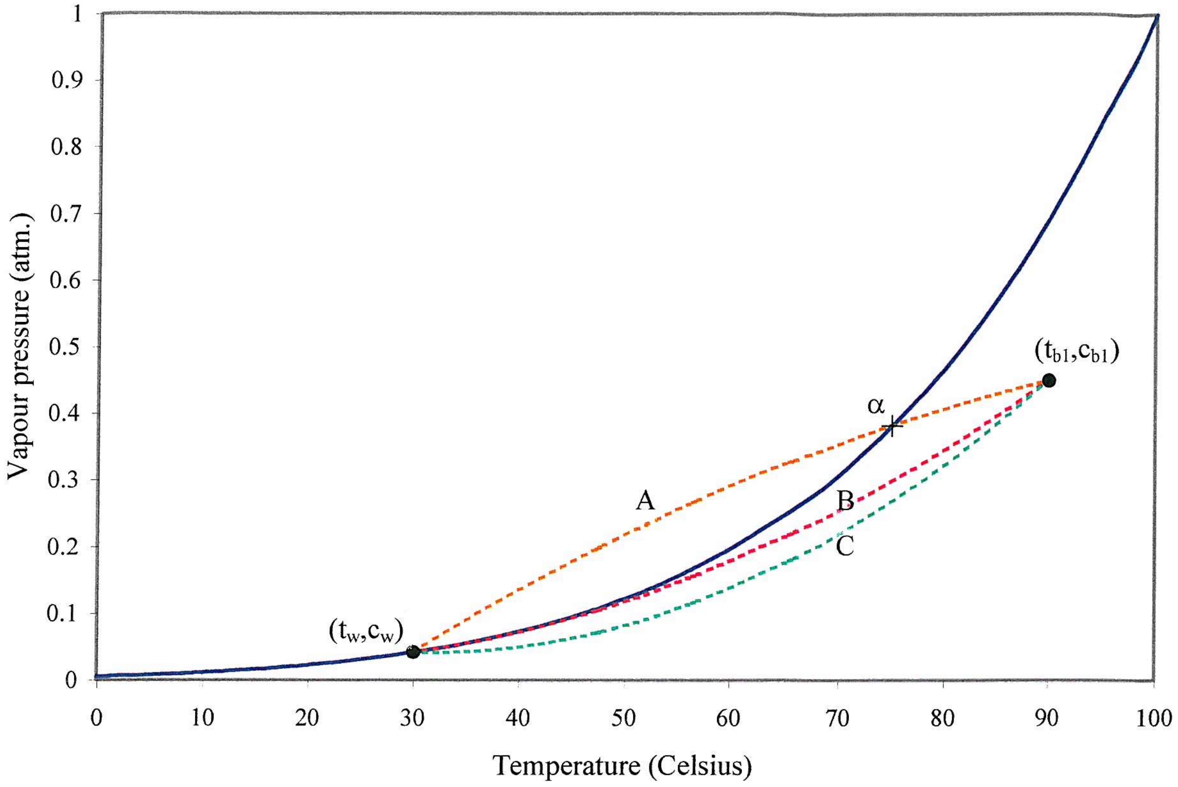

Figure 3-7. Potential paths of the bulk condition of a vapour – noncondensable gas mixture flowing through a partial condenser of constant wall temperature t_W.

3.7 *Heat and mass transfer*

In order to predict the condition of the mixture at condenser exit given the bulk entry condition, it is necessary to find a method of calculating the rates of cooling and vapour removal. These correspond to processes of heat and mass transfer respectively; the heat transfer rate being denoted by q [J/m^{2}s] and the mass transfer rate N_A [moles/m^{2}s].

The basics of mass transfer theory are laid out in appendix B, beginning with Fick's law, which, neglecting temperature gradients, pressure gradients and external forces (which are usually minor) is expressed by the simple differential equation

$$J_A = -D_{AB}\frac{\partial c_A}{\partial x} \tag{3-2}$$

This defines the diffusion coefficient, D_{AB}, for species A in a mixture of A and B, as the ratio of the unidirectional molar flux density, J_A, to the negative gradient of the molar concentration in the direction of diffusion [44]. It is negative because species A diffuses in the direction of decreasing concentration of A. Equation 3-2 may be rewritten in terms of the molar flux of A relative to a fixed point, N_A, as

$$N_A = -D_{AB}\frac{dc_A}{dy} + c_A N_A \overline{V}_A \tag{3-3}$$

in the case when species A only is diffusing. The first term on the right hand side is the flux resulting from diffusion, while the second term is the additional flux resulting from the molar bulk flow, i.e. the Stefan flow. To calculate the molar flux it is necessary to develop a model of the process. The three most commonly used models are the (stagnant) film model, the penetration model, and the turbulent boundary layer model, and they are summarised in appendix B also. The film model is used here because, despite being a gross oversimplification of the actual conditions near a phase boundary, it is widely used, easily applicable, and has proved sufficiently accurate for engineering applications [17]. The film model is based upon the idea of a thin stagnant film adjacent to the surface within which the resistances to mass transfer (and heat transfer) are confined. Within this stagnant layer, transport takes place by molecular diffusion only. Outside the film layer the fluid flow is turbulent. The film is of such a thickness y_o as to account for the experimentally observed magnitude of the mass-transfer resistance [44]. The situation is illustrated in Figure 3-8 below.

The molar flux is calculated by integrating equation 3-3 across the film. When the Stefan flow is negligible the rate of mass transfer, found by integrating equation 3-3 without the final term, is given by

$$N_A = \frac{D_{AB}P}{RTy_o}\left(Y_{A2} - Y_{A1}\right) \tag{3-4}$$

where Y_{A1} and Y_{A2} are the vapour mole fractions at the interface (phase boundary) and in the bulk mixture respectively, and are numerically equal to the volume fractions $c_{A1}V_{A1}$ and $c_{A2}V_{A2}$. When the rate of Stefan flow is significant the corresponding equation is

$$N_A = \frac{D_{AB}P}{RTy_o}\ln\left(\frac{1-Y_{A2}}{1-Y_{A1}}\right) \tag{3-5}$$

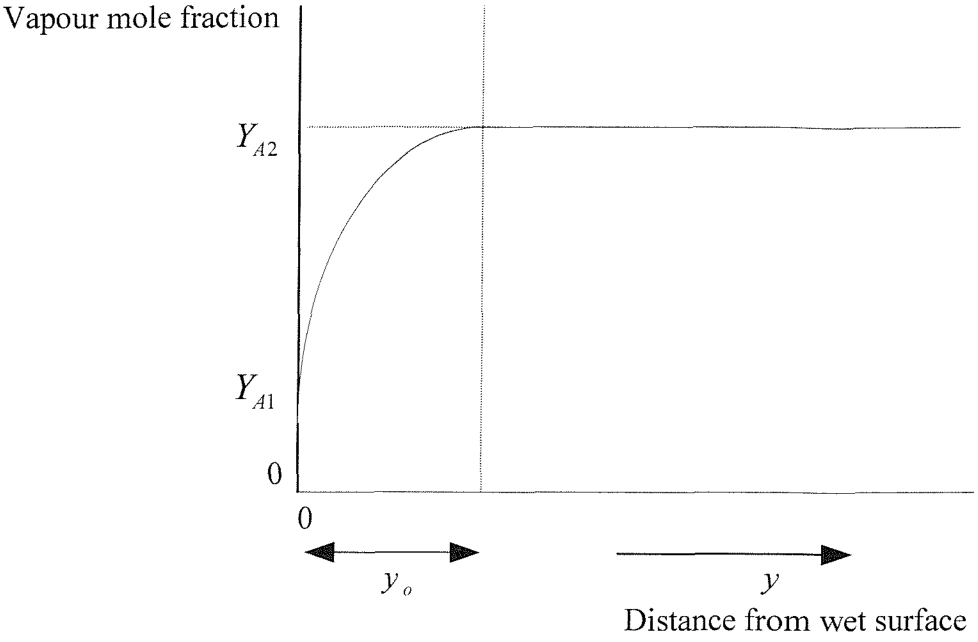

Figure 3-8. The film

Equation 3-5 is therefore often referred to as the Stefan equation [48]. The Stefan flow augments the overall rate of mass transfer in such cases, and consequently increases the rates of heat and momentum transfer also. These increases are commonly accounted for by the addition of correction factors to the usual transfer rate equations. For heat transfer the equations are then

$$q = hA\,\Delta t \tag{3-6}$$

i.e. that normally associated with heat transfer, when the Stefan flow is negligible, becoming

$$q = hA\Delta t\left(\frac{C_o}{1-e^{-C_o}}\right) \tag{3-7}$$

with the addition of the correction factor $\left(C_o/1-e^{-C_o}\right)$, when the Stefan flow is significant. [Note that $\left(C_o/1-e^{-C_o}\right)\rightarrow 1$ as $C_o \rightarrow 0$]. The term C_o is known as the Ackermann correction factor and may be expressed as

$$C_o = N_A C_{pA}/h \tag{3-8}$$

when species A only is diffusing. h is the heat transfer coefficient and C_{pA} is the specific heat of A. The equations of heat, mass and momentum transfer, and the associated correction factors for the effect of the Stefan flow are derived in appendix B.

3.8 *Mass and energy balances*

Equations 3-7 and 3-5 of the preceding section give the rates of heat and mass transfer that will arise during the surface condensation of a vapour from a gas-vapour mixture. Assuming the conditions at the interface and within the bulk mixture are known at a point within the condenser, and the relevant heat and mass transfer coefficients may be determined, then the rates of heat and mass transfer may be calculated. The values obtained are only valid at a single location however. Further along the condenser, lower bulk temperatures, t, and vapour pressures, p, are expected due to the removal of heat and liquid at the cold wall. For a near constant coolant temperature the conditions at the interface will change little, hence the heat and mass transfer rates will also fall along the length of the condenser, since from equation 3-7, $q \propto t - t_i$, and from equation 3-5, $N_A \propto \ln((1-p)/(1-p_i))$. The rates of heat and mass transfer will therefore both decrease asymptotically to zero in an infinitely long condenser. One of the simplest ways to incorporate this variation with position is to use the mean of the condenser entrance and exit values. However, for the purposes of predicting the variations of temperature, vapour pressure and fog formation with distance within the condenser, this method is insufficiently accurate. An improved method based upon calculating changes over a very short section of condenser, across which the rates of heat and mass transfer may be assumed constant without appreciable error, and then successively stepping along the entire condenser length in small increments is to be used here.

Such a differential condenser section is illustrated in Figure 3-9 below, in which the pertinent mixture properties and flow rates are noted. A material and energy balance may then be performed over the section [44], by summing and equating the mass (of inert gas, vapour, and liquid fog) and associated energy, entering and exiting the differential section. The loss of vapour due to condensation $(= N_A dA)$ and bulk temperature due to heat transfer $(= q\,dA)$ are also incorporated.

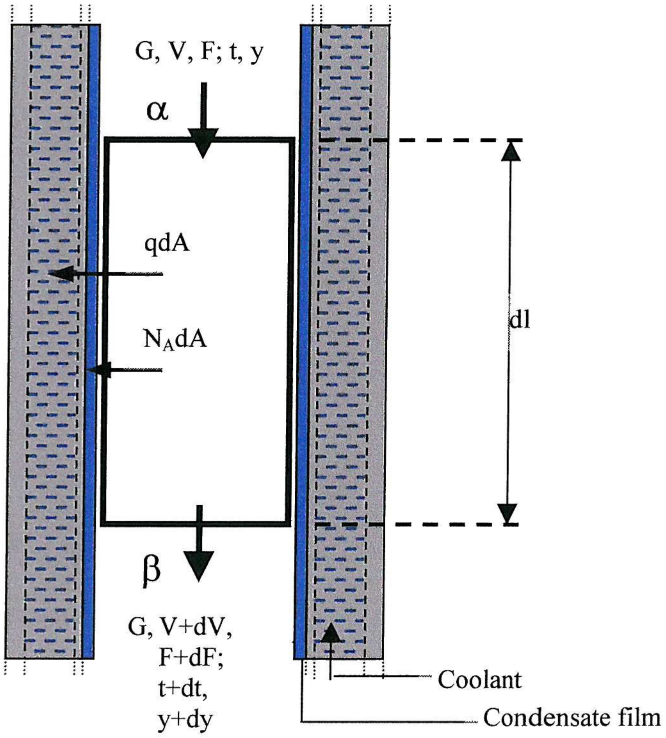

Figure 3-9. Differential section of a partial condenser (plan view).

Assuming steady-state flow conditions the mass (or material) balance is simply given by

$$N_A dA = -dF + dV \tag{3-9}$$

This states that the rate of condensation over the differential area of condenser selected, $N_A dA$ [kg/s or moles/s], given by equation 3-5, must be equal to the loss of vapour from the mixture, dV, less any change in the flow rate of fog, dF, over the section. The energy balance is somewhat more complicated, accounting for both the mass and temperature changes of all mixture constituents, in addition to any latent heat released, and the rate of heat transfer. The equation for the energy balance is

$$MC_{p,av}dt - \lambda dF + C_{pA}(t-t_i)(dV+dF) + qdA = 0 \tag{3-10}$$

where M is the total molar mass velocity, $C_{p,av}$ is the average specific heat of the mixture, λ is the latent heat of evaporation and C_{pA} the specific heat of the vapour phase.

Equation 3-10 is derived in appendix C, where a detailed analysis of the differential condenser section is laid out. This begins with the complete derivations of the material and energy balances over a differential section of a partial condenser, as discussed briefly above. The change in vapour flow rate appearing in these equations, dV, is then equated to a change in vapour partial pressure via Dalton's law, (section C-3), from which

$$dV = \frac{GP}{(P-p)^2}dp \tag{3-11}$$

This is used in conjunction with the material and energy balance equations (3-9) and (3-10), incorporating equations (3-7) and (3-5) for the heat and mass transfer rates, to calculate the changes in temperature, vapour pressure and vapour flow rate across the differential condenser section.

The prediction of fog formation is based upon the use of the 'saturation condition'. This assumes that as soon as the mixture becomes supersaturated, all 'excess' vapour condenses to form a fog. Though not strictly true (see section 2-11), this criterion has been widely used in theoretical fog formation studies in the past [16, 39, 49, 50] and appears reasonable inside industrial condensers where large condensation nuclei concentrations are likely to exist.

The predicted temperature and vapour pressure at differential condenser section exit are therefore of critical importance. Should these properties imply the bulk mixture is superheated, no fog formation is predicted (the possibility of film fog formation being ignored). However, as soon as the predicted values of temperature and vapour pressure imply supersaturation, the vapour pressure is assumed to fall to its saturation value at the predicted temperature, and the resulting reduction of vapour-phase mass is matched by that of fog formation.

The detailed analyses of Appendix C result in the derivation of two sets of differential equations. The first, pertaining to fog free mixtures is applicable to superheated mixtures. The relevant equations are then

$$\frac{dt}{dA} = -\left(\frac{h}{MC_{p,av}}\right)(t-t_i)\frac{C_o}{\left(e^{C_o}-1\right)} \tag{3-12}$$

$$\frac{dp}{dA} = -\frac{(P-p)^2}{GP} k_g^* P \ln \frac{1-Y_i}{1-Y} \tag{3-13}$$

$$\frac{dV}{dA} = -k_g^* P \ln \frac{1-Y_i}{1-Y} \tag{3-14}$$

$$\frac{dF}{dA} = 0 \tag{3-15}$$

As soon as the mixture becomes saturated however, a second set of equations allowing for the possibility of fog formation is required, specifically

$$\frac{dt}{dA} = -N_A \left(\frac{\lambda + \dfrac{C_{pA}(t-t_i)}{e^{C_o}-1}}{\dfrac{\lambda^2 p}{RT^2} \dfrac{GP}{(P-p)^2} + MC_{p,av}} \right) \tag{3-16}$$

$$\frac{dp}{dA} = -N_A \left(\frac{\lambda + \dfrac{C_{pA}(t-t_i)}{e^{C_o}-1}}{\dfrac{\lambda GP}{(P-p)^2} + MC_{p,av} \left(\dfrac{RT^2}{\lambda p} \right)} \right) \tag{3-17}$$

$$\frac{dV}{dA} = -N_A \left(\frac{\lambda + \dfrac{C_{pA}(t-t_i)}{e^{C_o}-1}}{\lambda + MC_{p,av} \dfrac{RT^2}{\lambda p} \dfrac{(P-p)^2}{GP}} \right) \tag{3-18}$$

$$\frac{dF}{dA} = N_A \left[\frac{\dfrac{C_{pA}(t-t_i)}{e^{C_o}-1} - MC_{p,av} \dfrac{RT^2}{\lambda p} \dfrac{(P-p)^2}{GP}}{\lambda + MC_{p,av} \dfrac{RT^2}{\lambda p} \dfrac{(P-p)^2}{GP}} \right] \tag{3-19}$$

Provided the initial condition of the mixture is specified, and the numerous parameters appearing in equations 3-12 to 3-19 are available the equations may then be solved iteratively, along the length of a condenser, to predict fog formation rates.

3.9 Concluding Remarks

Though it has been shown that fog formation will in fact commence before the bulk mixture becomes supersaturated [section 3.4], a widely accepted complete analysis is still currently absent from the literature, being extremely complicated, and is beyond the scope of this investigation.

Recently, a number of papers by Brouwers [17,49] have begun to address these problems, incorporating the film model correction factors due to Stefan flow in the heat and mass transfer rate equations, and allowing for superheated and saturated regions within the film. However, the predictions arrived at have not been compared to any experimentally obtained results. They are necessarily more difficult to employ and as Brouwers admits, the effect of fog formation within the film upon the overall heat and mass transfer inside condensers is likely to be small.

Thus the equations presented above are to be used to predict the mass of fog produced during partial condensation, while acknowledging the appearance of film fog well in advance of bulk supersaturation. The solution of the equations is presented in the following chapter and the ensuing results provide a means of identifying the critical variables involved, and their effects upon the levels of fog formation.

4. Theoretical predictions of fog formation rates

4.1 *Introduction*

In chapter 3 a number of equations were derived, describing the changing condition of a gas – vapour mixture as it flows through a partial condenser. The equations predict the rate of change with distance along the condenser of vapour flow rate, vapour partial pressure, temperature and the flow rate of any fog formed. These form two systems of four first order ordinary differential equations and will subsequently be referred to as the rate equations. The first system, comprising equations (3-12) to (3-15) is applicable to superheated mixtures and the second set, equations (3-16) to (3-19), is applicable to saturated mixtures. Provided the condition of the mixture on entry to the condenser is known, it becomes an initial value problem, of the form

$$\begin{aligned} y' &= f(t,y) \\ y(a) &= y_o \end{aligned} \tag{4-1}$$

where y, f and y_o are vectors of four dimensions [51]. Such problems may be solved numerically using a step-by-step method. Starting from the initial values, y_o (at $t = 0$), which are known, a sequence of points is generated t_1, t_2, ... at which the approximate solution to the differential equations (y_i) is calculated from the previous value. Runge-Kutta formulae are most frequently employed to generate the approximate solutions. Runge-Kutta methods are discussed briefly in appendix D, followed by the presentation of the relevant algorithm.

4.2 *Solution generation*

Obtaining solutions to the rate equations as described above and in appendix D involves the evaluation of the Runge-Kutta formula for each step along the length of the condenser, and hence involves a considerable amount of numerical calculation time. It is therefore necessary to write a computer program to perform these tasks. This may then be used to rapidly calculate approximate solutions to the sets of equations for any mixture, provided the initial conditions are specified, and tabulated data for the mixture constituents is available. It is necessary to assign values to the other parameters appearing in the rate equations, namely the interface temperature, t_i, the vapour mole fraction in the bulk mixture, Y and at the interface, Y_i , the heat transfer coefficient, h, the mass transfer coefficient, k_g^*, the molar flux of the condensing species, N_A, and the Ackermann correction factor, C_o. Each of these values will change as the bulk mixture properties change along the length of the condenser. Hence these parameters must also be evaluated at each step along the condenser.

The methods and equations used for determining the appropriate values are detailed in appendix E, which comprises the computational algorithm for the prediction of bulk mixture properties and fog formation rates at any axial point within a partial condenser. An example of the computer code used to generate numerical results (applied to a saturated water vapour – air mixture) is presented in appendix F.

4.3 *Validation*

Detailed experimental data regarding fog formation rates inside partial condensers with which to validate the computer program is absent from the literature. The majority of work published on partial condensation focuses on the calculation of heat and mass transfer rates and the size of condenser required to remove a given fraction of the vapour. The analyses that address condenser fogging, do so from a theoretical standpoint. These published theoretical predictions are restricted to a handful of cases for which comparisons are extremely difficult. The example used to verify the computer program is that presented by Sherwood et al. [44]. It is accompanied by graphical predictions of temperature, vapour pressure, vapour and fog flow rate variations with position within a condenser.

The example is that of a superheated benzene – air mixture with initial vapour mole fraction of 0.35. The problem is simplified greatly by the assumption of a constant interface temperature of 36.6°C. In addition, constant values were assigned to the mass transfer coefficient, gas, vapour and liquid specific heats, and the latent heat of vaporisation. The resulting solutions presented by Sherwood et al. are reproduced below in figures 4-1 and 4-2.

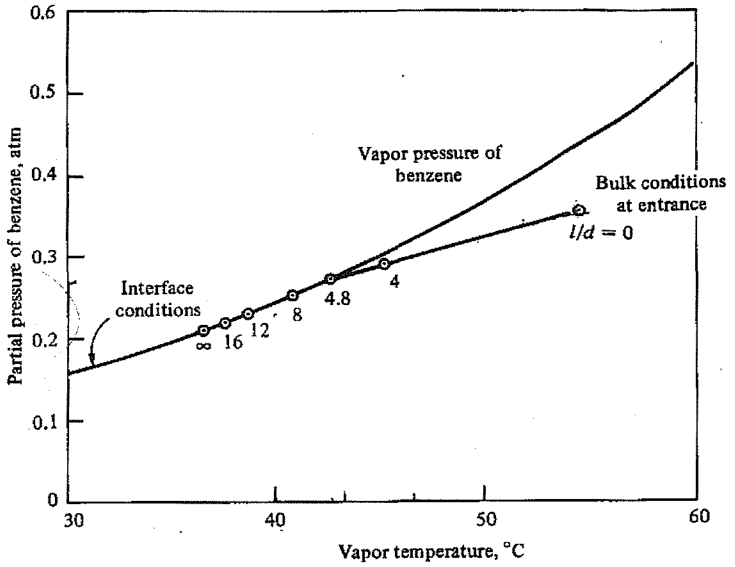

Figure 4-1. Predictions of partial vapour pressure and temperature with distance during the condensation of a benzene – air mixture (after Sherwood et al. [44]).

In order to compare these results with those produced by the computer program presented in appendix F, the associated parameters were modified accordingly. Initially the rate equations used in the program were replaced by those presented by Sherwood et al. However, upon saturation the mixture temperature and vapour pressure was predicted to fall almost immediately to the values at the interface. Such a rapid change is highly implausible and supports the deductions of appendix C (section C.6) where the erroneous nature of these equations was identified. Applying the corrected equations, namely (3-12) – (3-15) when the mixture is superheated and (3-16) – (3-19) when it is saturated produces the following results, presented in figure 4-3.

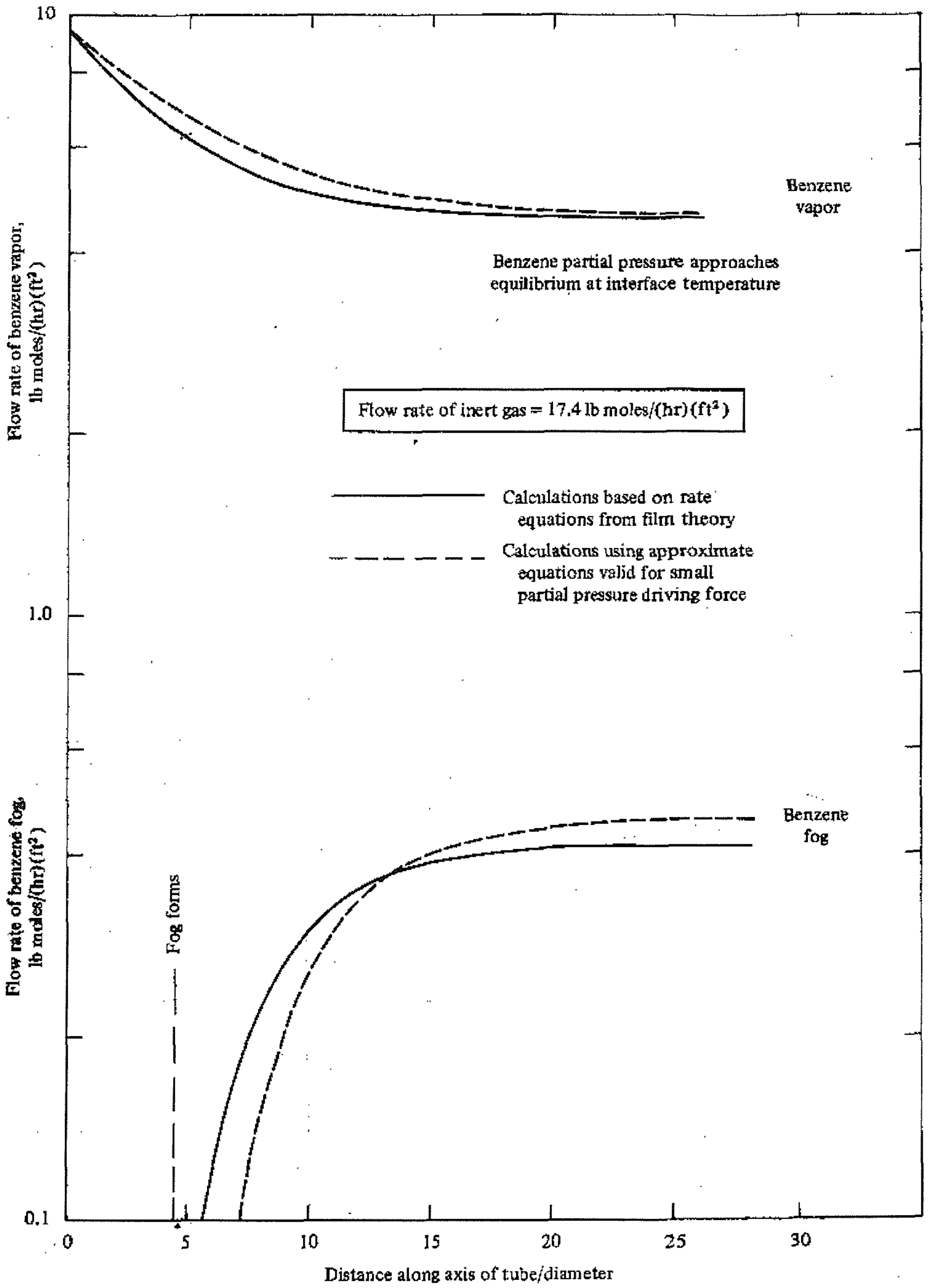

Figure 4-2. Sherwood et al.'s predictions of vapour and fog flow rates with distance during the condensation of a benzene – air mixture, corresponding to figure 4-1 [44].

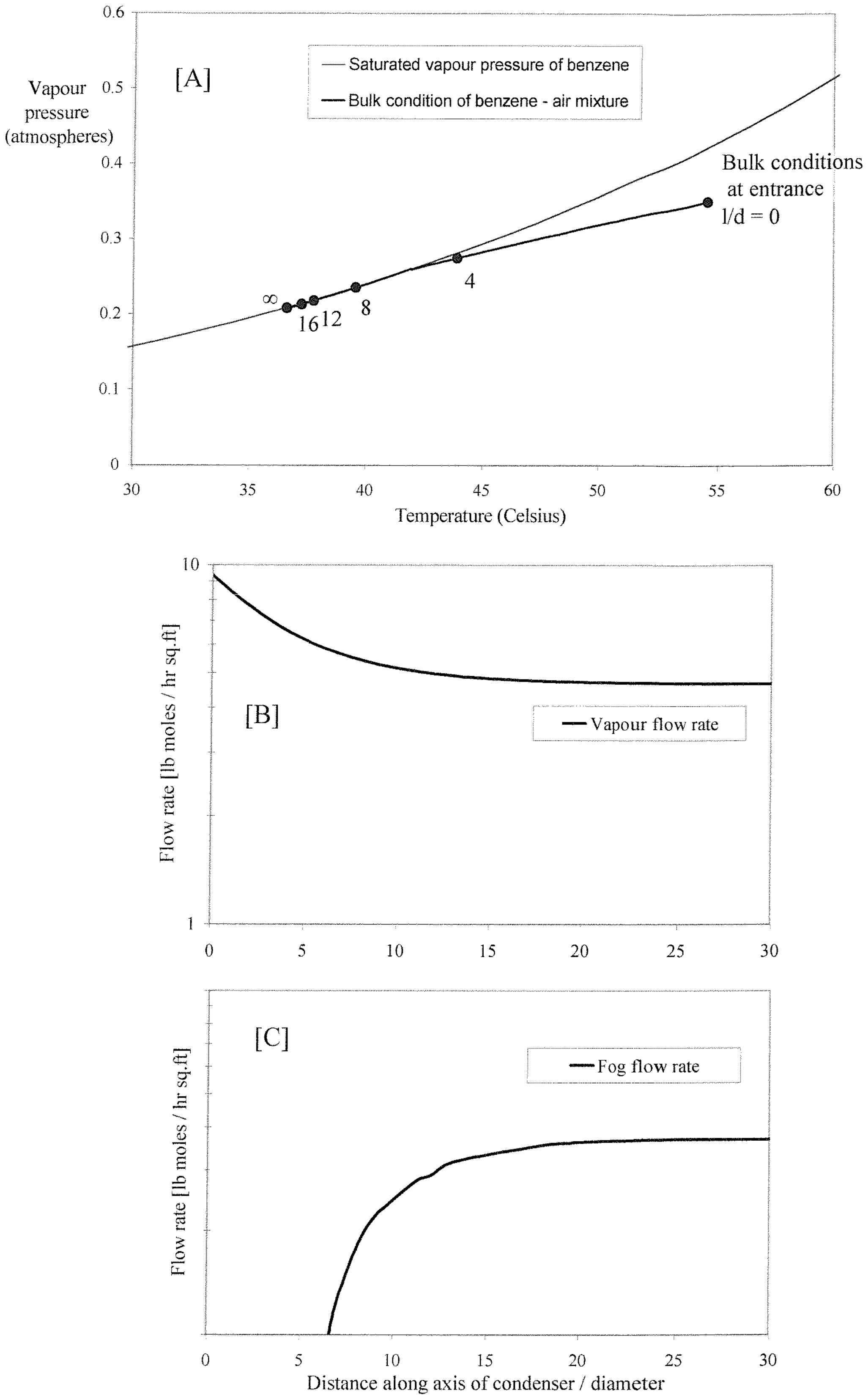

Figure 4-3. Computer program predictions of [A] vapour pressure and temperature (c.f. Figure 4-1), vapour flow rate [B], and fog flow rate [C].

The form of all three graphs is as expected, and concurs with the results of Sherwood et al. (c.f. Figures 4-1 and 4-2). The superheated mixture becomes saturated when the condenser length to surface area ratio is approximately 5 and its condition approaches that of the interface at a decreasing rate. The vapour flow rate falls to a constant value of approximately 4.5 lb mole/ft^2 hr [6.1 moles/m^{2}s], and the fog flow rate increases rapidly at saturation before also stabilising.

The values assigned to a number of variables required in the calculations were not specified by Sherwood et al. e.g., the heat transfer coefficient. Hence slight discrepancies between the two predictions may have arisen due to different methods being employed for their estimation to those used here. However, in general the results are in good agreement with the solution presented by Sherwood et al. in all aspects but for the quantity of fog formed. However, it should be noted that the final quoted value and apparent graphical value of fog to vapour flow rate in Sherwood et al.'s solution are inconsistent. There are clearly a number of errors within their work and hence perhaps not too great a significance should be attached to the disagreement in fog flow rate predictions.

4.4 *Computational results*

Having spent a considerable amount of time developing the computer program and attempting to validate it, it was then possible to generate results relatively quickly. These theoretical predictions were performed in conjunction with an experimental test program using water vapour – air mixtures, described in the following chapters of this thesis. The computer program was therefore initially run on water vapour – air mixtures, with the condenser diameter etc. set equal to that of the experimental test section. In each instance a series of runs were performed in which, as far as was possible, only one variable was altered from one run to the next.

4.4.1 Temperature

The first series of computational runs was designed to study the effect of initial entry temperature upon bulk fog formation rates. This was achieved by holding the condenser entry water vapour and air mass flow rates constant from one run to the next. A condenser length of 2m and coolant temperature of 15°C were used. The initial bulk vapour pressure was set at 0.468atm., giving a saturation temperature of 80°C. The initial temperatures matched those used experimentally, though the 85°C and 82.5°C results are added for illustrative purposes.

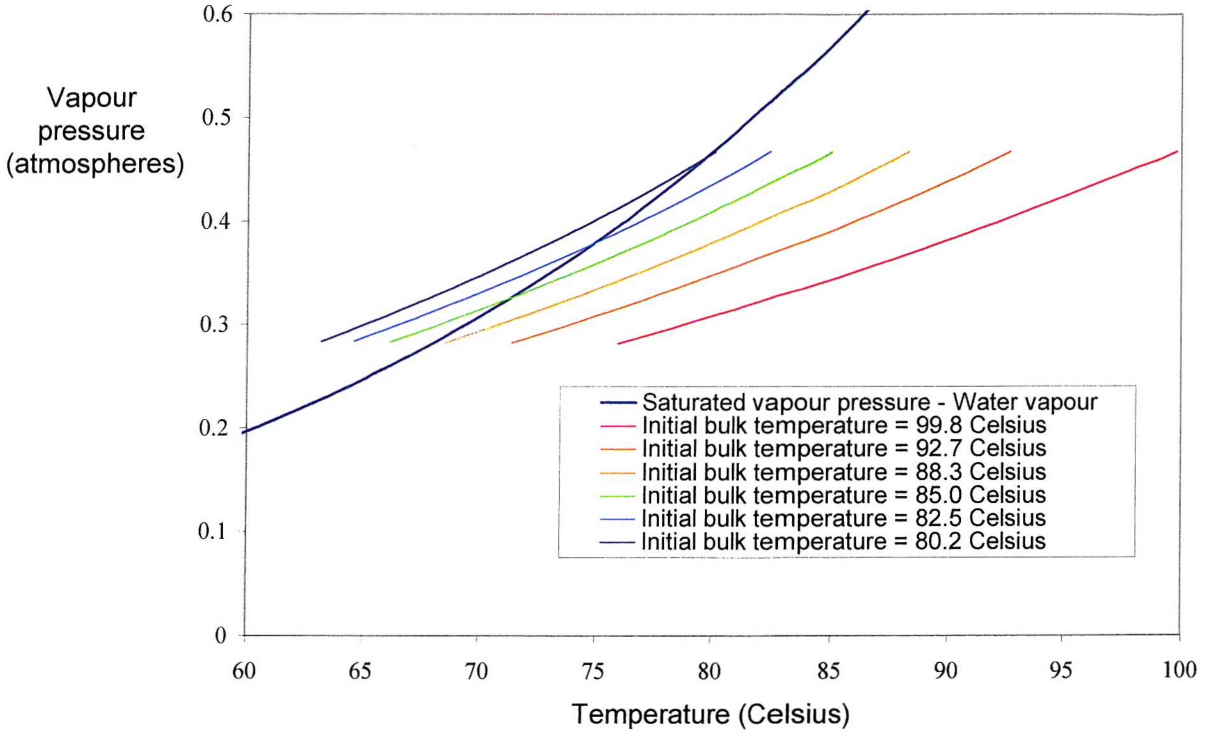

Figure 4-4. Predicted condition of mixtures of different temperature passing through a 2m long condenser when fog formation is neglected.

In each case the mixture tends towards supersaturation. The greater the bulk entry temperature, the greater the initial mixture superheat (and the lower the relative humidity) and the further along the condenser the mixture passes before it becomes saturated. The hottest mixtures remain superheated in a 2m long condenser, though all would become saturated were the condenser sufficiently long.

In reality, bulk fog formation begins as soon as the mixture becomes supersaturated. It is assumed that all excess vapour condenses in the form of fog (the saturation condition) and equations (3-12) to (3-15) are replaced by equations (3-16) to (3-19) in the computational calculations as soon as the mixture becomes saturated. Increasing the condenser length to 20m and using exactly the same initial mixture conditions as those used to produce Figure 4-4 above results in the following fog flow rate predictions.

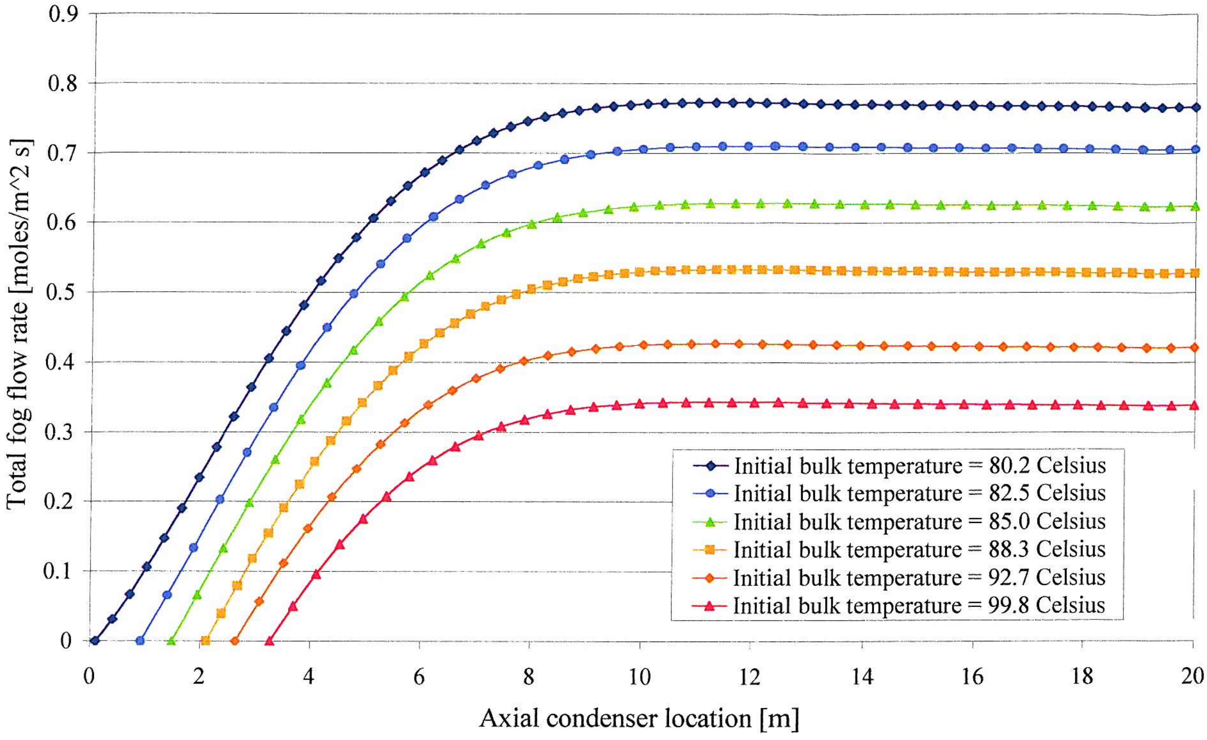

Figure 4-5. Fog flow rate predictions.

Fog formation begins further along the condenser the greater the initial mixture temperature, in agreement with the temperature pressure chart of Figure 4-4. The quantity of fog is greater the lower the bulk entry temperature of the mixture. This is true at all axial locations within the condenser and is also true of the final fog flow rates. Note also that the rate of fog formation is greatest when the mixture first becomes saturated, and tends to zero thereafter. At a distance of approximately 10m, the quantity of fog stabilises at a constant value. The greatest interface temperature predicted during the calculations was 40°C which, referring back to Figure 3-6 implies that film fog formation will occur in all mixtures as soon as they enter the condenser. However, this film fog will initially be restricted to a thin region near the interface, and will only comprise a small fraction of that formed upon bulk saturation.

The above results demonstrate the importance of the relative humidity of the initial mixture. The lower the relative humidity the lower the rates of fog formation, and in a condenser of fixed dimensions, if the relative humidity of the mixture is sufficiently low there will be no fog formation at all. Hence in subsequent calculations, designed to study the importance of other variables, the effects of relative humidity should be removed. This is most easily achieved by working with saturated mixtures, which also ensures that fog formation begins at condenser entry.

4.4.2 Saturation temperature

The effect of saturation temperature was studied using a series of saturated mixtures, of different temperatures, all entering the condenser section with the same mean velocity. Predictions of how the bulk temperature, partial vapour pressure, vapour flow rate and fog flow rate change with distance along the condenser are presented in Figure 4-6. Again the computational calculations were extended to 10m to illustrate more clearly the form of the solutions, and predict the effects of elongating the test section. The bulk temperature, vapour pressure and vapour flow rate all fall as the mixture flows through the condenser, due primarily to the transfer of transfer of heat through the condenser walls to coolant and the condensation of vapour on the walls. The rate of fog formation is predicted to be at its greatest at the beginning of the condenser, after which it falls until a steady fog flow rate is reached. The formation of fog further reduces the vapour pressure and vapour flow rates, but acts to counter the temperature drop with the release of latent heat. The graphs of Figure 4-6 show that the variables all change most rapidly at the start of the condenser when the driving forces for heat and mass transfer, the temperature difference between the mixture and the coolant and the corresponding saturation vapour pressures, are greatest. Thereafter the variables all approach steady values, denoting a steady flow of inert gas, vapour and fog at the temperature of the liquid coolant. Note that in general the higher the initial saturation temperature the greater the initial rate of fog formation and the greater the amount of fog formed. However, this was only true for saturation temperatures of below 80°C. At higher temperatures the predicted rate of fog formation falls to zero initially, the mixture remains saturated as the temperature falls until it drops to around 80°C and fog formation commences. It is not clear if this behaviour is to be expected in practice or is a result of a problem with the theoretical algorithm.

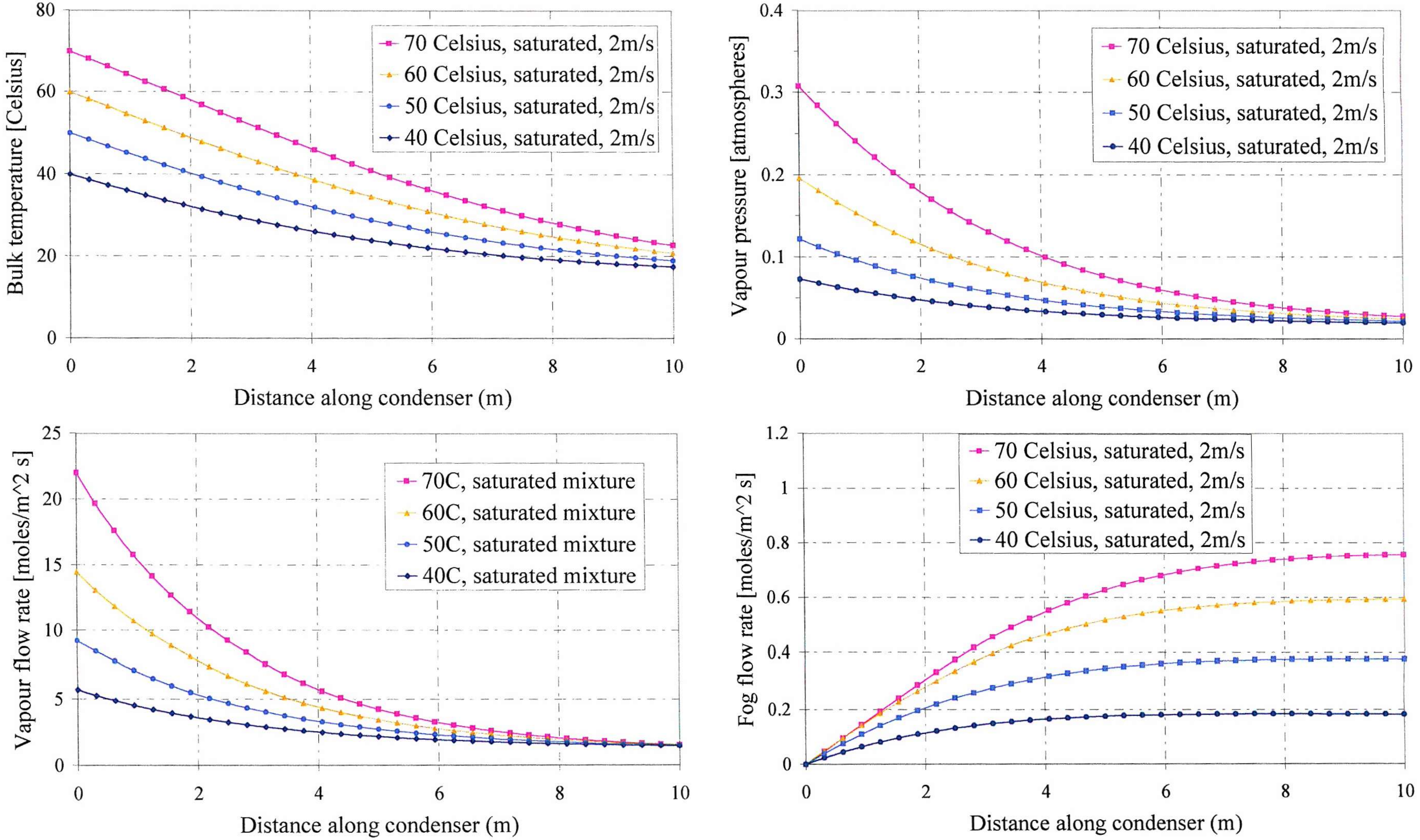

Figure 4-6. Computational predictions of temperature, vapour partial pressure, vapour flow rate and fog flow rate along the experimental condenser (extended to 10m).

This is because of two assumptions that exist within the numerical routine, both of which lead to inaccuracies in the calculations that increase with increasing vapour pressure (or saturation temperature). The first is the use of the ideal gas law to obtain both the vapour mole fraction at the interface from the interface temperature (and partial vapour pressure) and the relationship between vapour flow rate and vapour pressure (as discussed in appendix C). The second is the use of the Clausius-Clapeyron equation to calculate the relationship between temperature and vapour pressure for a saturated mixture. The inaccuracies contained therein increase with the temperature differences inside the condenser and therefore also with increasing saturation temperature.

It should be noted however that the majority of initial mixture conditions do not result in a saturated mixture of temperature greater than 80°C. Even those that enter the condenser at higher temperatures and vapour pressures may undergo sufficient cooling and / or condensation to ensure that when the mixture finally becomes saturated it does so at a temperature below 80°C.

4.4.3 Velocity

The effect of velocity on the rate of fog formation was initially investigated by examining the predicted drop in temperature and vapour pressure of four superheated mixtures of initial vapour pressure 0.1967 atm. (saturation temperature 60°C) and temperature 66°C, entering the condenser with mean velocities of 1, 2, 3, and 4 m/s. The results are plotted in Figure 4-7. Not only does the heat to mass transfer ratio decrease with velocity (signified by an increasing gradient of vapour pressure against temperature) but the temperature drop over a fixed condenser length also decreases, meaning that fog formation will be less likely and / or will be less profuse the greater the velocity of the fluid at condenser entry. In Figure 4-8 below, the temperature, fog flow rate and fog density predictions for three mixtures of the same initial condition, flowing at different velocities, are shown. The mixtures were all saturated and at a mean temperature of 60°C at entry to the condenser, ensuring that fog formation was predicted immediately.

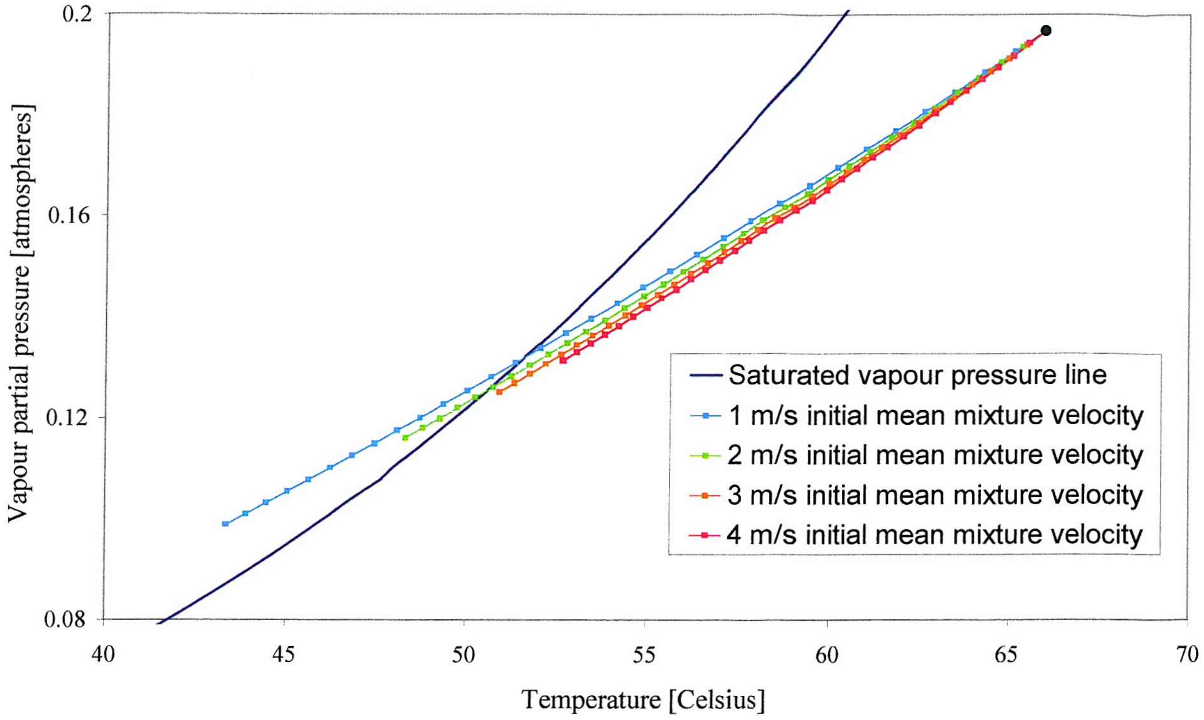

Figure 4-7. Predicted condition of mixtures of different mean velocity passing through a 2m long condenser when fog formation is neglected.

The fall in the mean temperature with distance along the condenser increases the lower the mean velocity of the mixture at entry to the condenser (Figure 4-8). Relations for the rate of heat transfer during forced convection, invariably predict an increase with increasing Reynolds number [3]. Hence, the greater the velocity of the mixture, the greater the rate of heat transfer, q. However the heat transfer increase with velocity is always less than the increased mass flow $(\dot{m} \propto U)$. Hence the bulk temperature change Δt, which may be calculated using $\Delta t = q/\dot{m}c_p$ always decreases as the flow velocity increases. Thus the graph of bulk temperature against condenser location is of the form expected.

The corresponding predictions of fog flow rate [moles/ m^2 s] initially appear to be the opposite of what was expected, i.e. the fog flow rate increases the greater the velocity of the mixture. However, the mass of fog per unit mass of mixture, i.e. the fog density [kg/m^3], increases as the initial fluid velocity decreases. The ratio of fog density to vapour density (or indeed fog flux to vapour flux) is also greater the lower the velocity of the mixture. This is true at all locations within the condenser, for all condenser lengths.

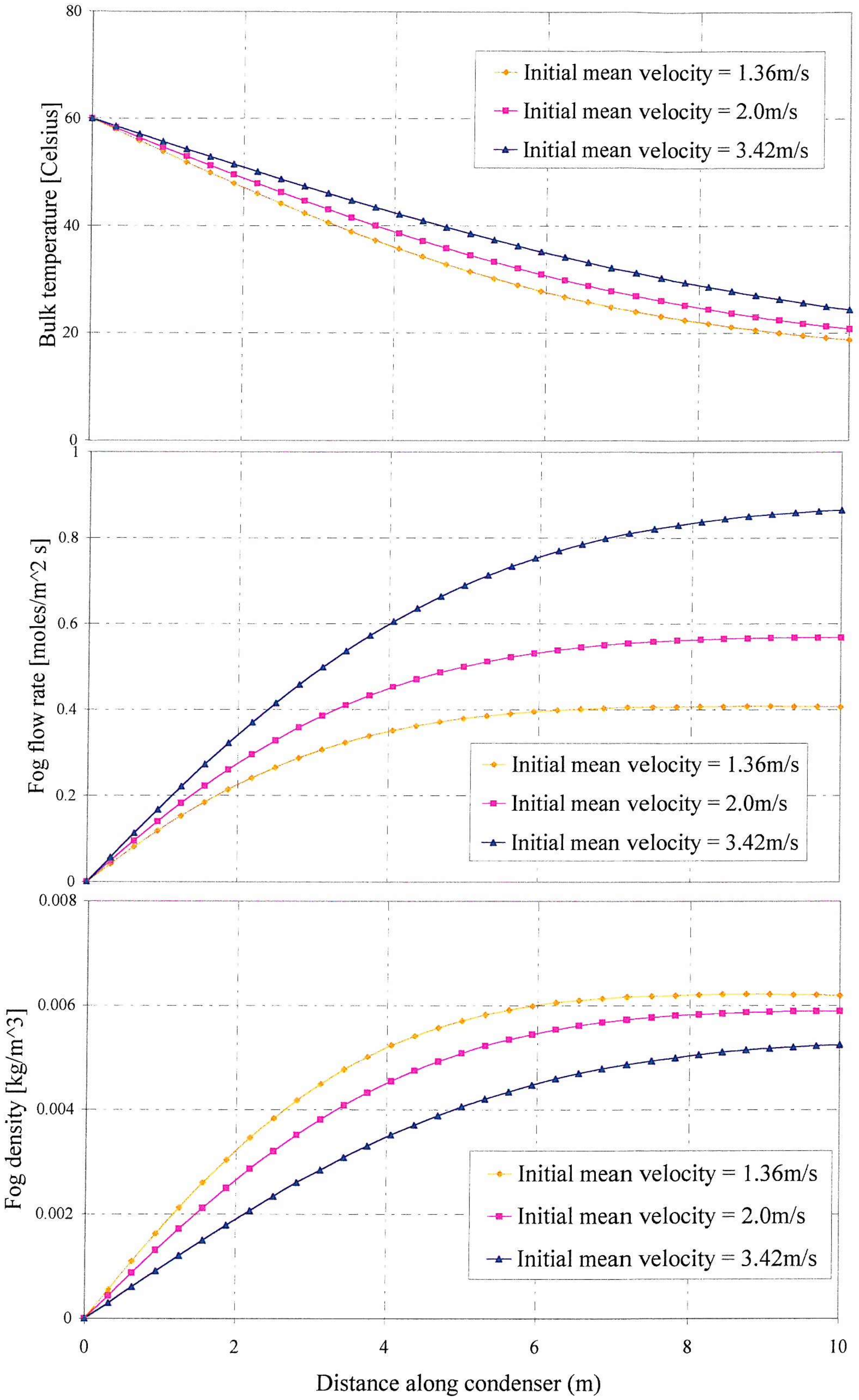

Figure 4-8. Computational predictions for 60°C saturated mixtures entering the experimental condenser (extended to 10m) with different velocities.

4.4.4 Mixture constituents

In industrial condensers where fog formation is a problem the vapours are usually hydrocarbons. Hence it was decided to run the computer program using a different vapour and inert gas. Benzene and nitrogen were chosen, a more realistic aromatic hydrocarbon – inert gas combination for which the required physical properties are readily available.

The first runs undertaken were designed to compare the relative propensity of the two mixtures (water vapour – air, and benzene – nitrogen) to fog. These could not be completed using identical starting conditions because of the different saturated vapour pressures of the two mixtures at equal temperatures. Instead, equal values were used for the initial differences in vapour pressure and temperature between the bulk and interface (the driving forces for mass and heat transfer respectively) were constant. The subsequent drop in vapour pressure and temperature were then calculated, neglecting the possibility of fog formation.

The results, presented in Figure 4-9, show that the path of the bulk mixture condition (dotted lines) is a lot closer to the straight line linking the initial bulk and interface conditions for the benzene – nitrogen mixture than for the water vapour – air one. Thus the heat to mass transfer ratio is smaller for benzene – nitrogen, and fog is more likely to form in such mixtures. Example fog formation rate predictions for a range of saturated benzene – nitrogen mixtures are presented in Figure 4-10. These are of the same form as those for water vapour – air mixtures, that is, the greatest rates of fog formation coincide with the onset of bulk fog formation, after which they steadily fall and a constant fog flow rate is approached. However, in general the rates of fog formation predicted are greater than those of water vapour – air mixtures at the same saturation temperatures and mixture velocities.

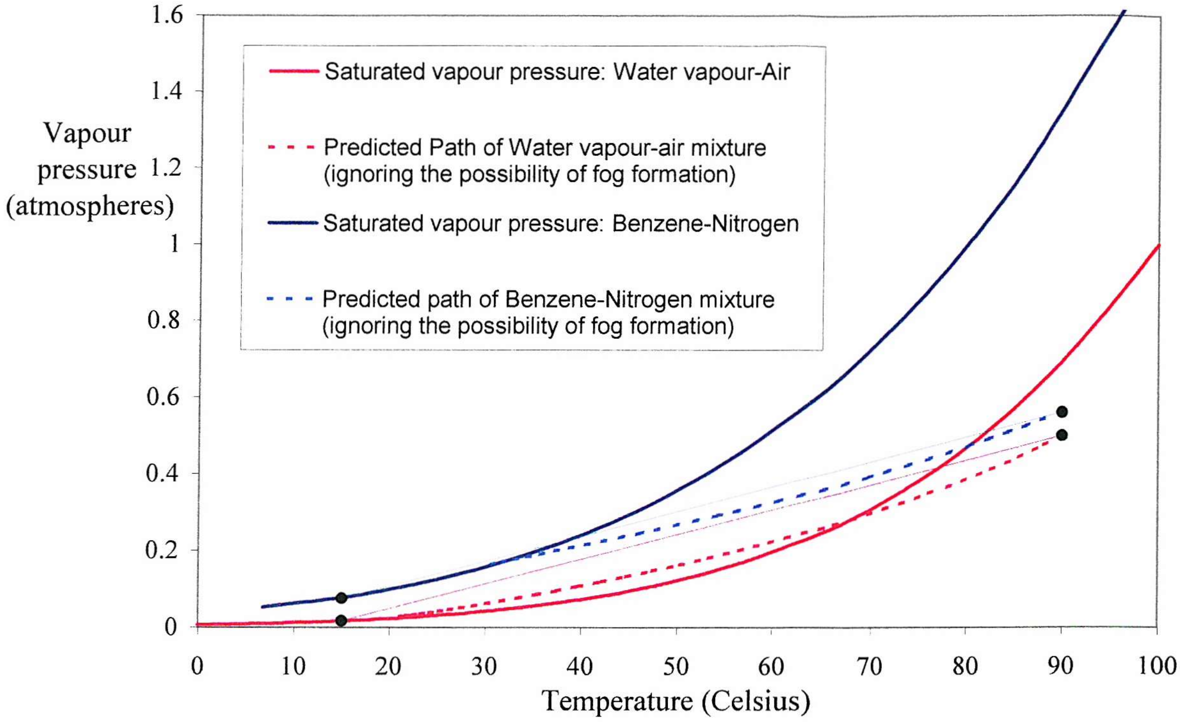

Figure 4-9. Theoretical predictions using different mixture constituents.

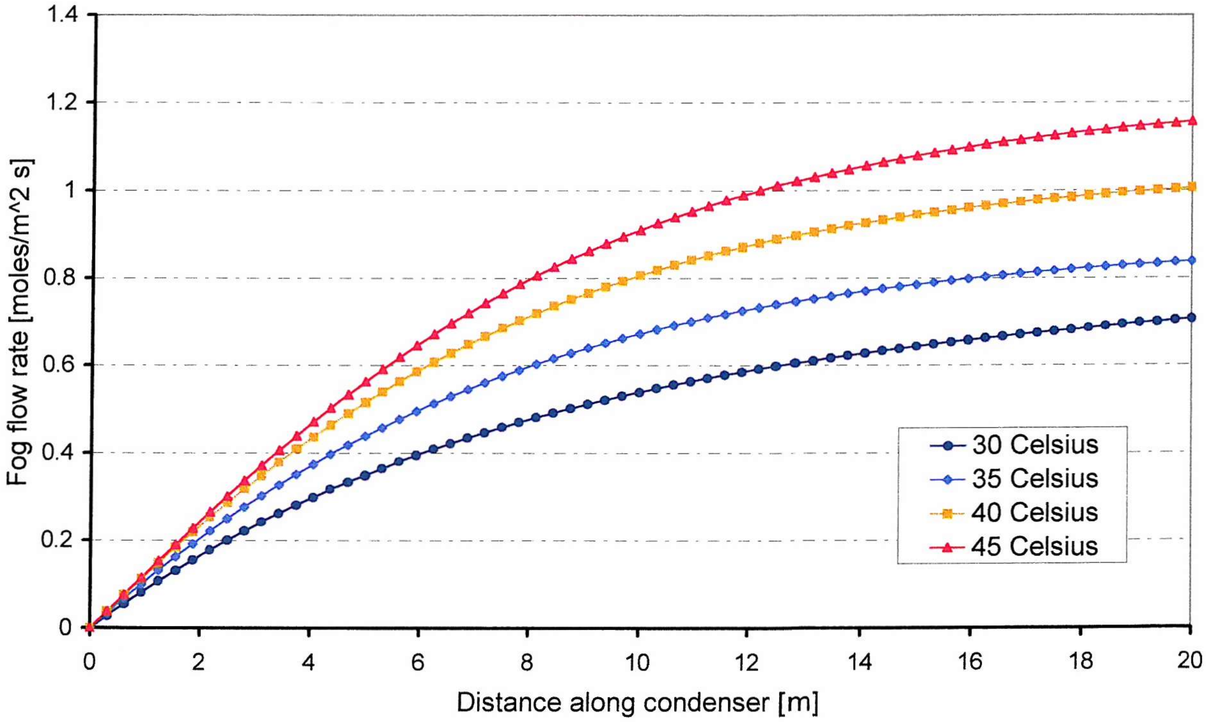

Figure 4-10. Example theoretical predictions of fog flow from a benzene – nitrogen mixture.

4.4.5 Overview

The predictions presented in this chapter provide a good indication as to the effect of changes in the temperature, velocity etc. of a mixture upon the overall rate of fog formation during partial condensation. However, possibly the most important point to note from the computational predictions is the form of the fog flow rate predictions. In each instance, provided the temperature at saturation is not too high, the greatest rate of fog formation occurs when the bulk mixture first becomes saturated. The rate of fog formation subsequently falls away to zero and the mass of the fog suspended in the mixture approaches a constant value.

This is a very interesting point. Since the rate of fog formation is greatest following the initial saturation of the mixture, the degree of supersaturation will also increase most quickly following saturation. This implies that droplet activation will also occur most rapidly during the onset of supersaturation and the initial phase of fog formation (see section 2.7). Thereafter, as droplet growth continues this raises the possibility of a peak in the supersaturation and the termination of droplet activation. Further droplet growth will result in the disappearance of all submicron droplets from the mixture.

The points raised above will be re-addressed in more detail during the analysis of the experimental results, in chapter 9.

5. RIG DESIGN AND MANUFACTURE

5.1 *Introduction*

An experimental rig was designed and manufactured with which to study fogs produced during the cooling and partial condensation of turbulent gas-vapour mixtures. In industrial chemical plants where fog formation is a problem the condensable component is generally a hydrocarbon vapour. However, since such materials are highly flammable and potentially hazardous it was decided that the rig would be designed to operate using water vapour - air mixtures. To simplify matters, and permit repeatability and reproducibility of results, it was intended that all experiments be performed under steady-state conditions, i.e. with constant flow rates, allowing pressure and temperature gradients within the rig to stabilise before any measurements were taken.

The rig comprised of three major parts, one for producing a constant supply of water vapour, one to deliver a constant air flow, and a third to mix and cool the air and water vapour (the main section). A diagram showing the general arrangement of the rig is presented in Figure 5-1. The design and manufacture of this rig is described on the following pages.

5.2 *Design Envelope*

Before designing the experimental rig it was first necessary to specify the range of conditions under which it would have to operate to allow a thorough study of fog formation from condensing water vapour - air mixtures.

5.2.1 Temperature and vapour pressure

In the preceding chapters it was noted that supersaturation is a necessary condition for fog formation, hence it is important to ensure that the water vapour – air mixture will become supersaturated within the condenser. The simplest way to achieve this would be to mix a large steam flow with a large air flow, at a low temperature, prior to condenser entry. However, this would lead to fog formation before the condenser is reached, and would not be the result of rapid cooling, the phenomenon it was intended to study. Hence the mixture should enter the test section saturated or superheated. In chapter 4 it was predicted that upon cooling

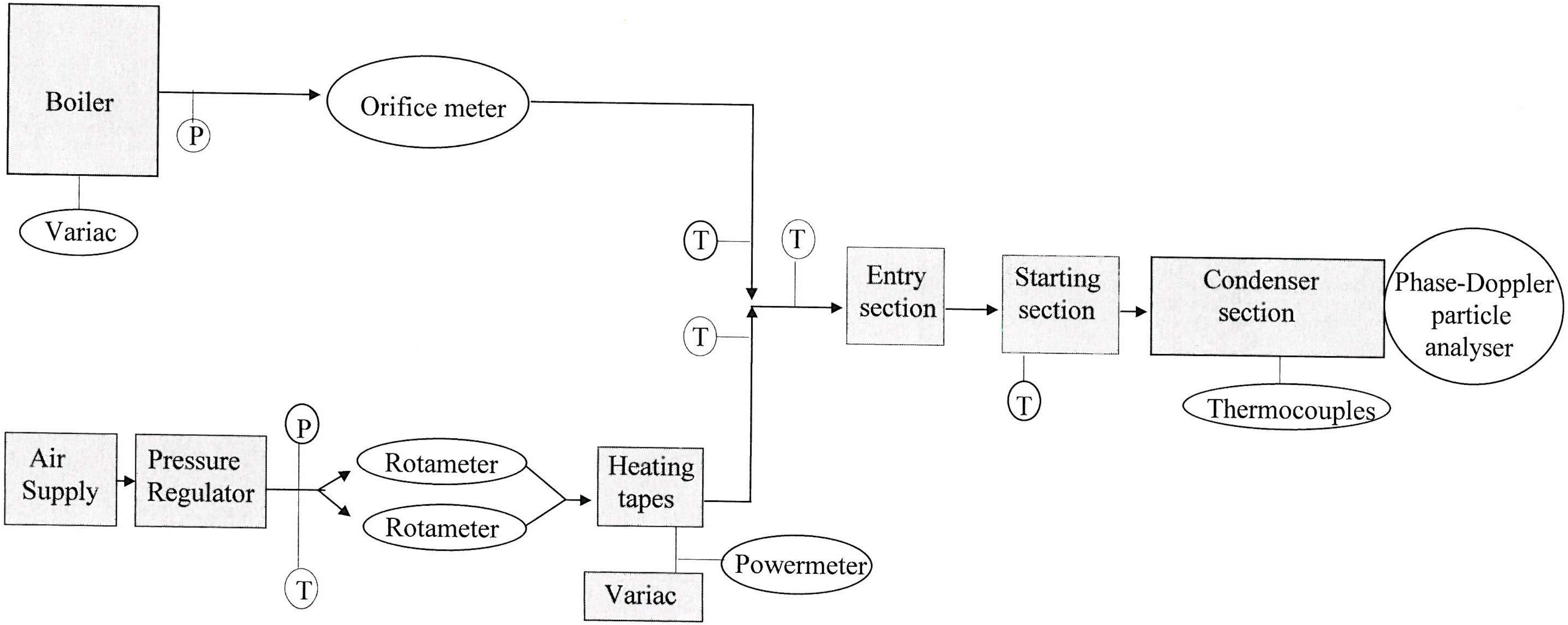

Figure 5-1. Block diagram showing the main components of the rig designed to study fog formation.

within the condenser a fog would form immediately within initially saturated mixtures and would form further along the condenser from initially superheated mixtures, provided the degree of superheat is not too great.

Upon exiting the condenser the mixture was to vent to atmosphere, allowing access to the droplets for measurement of their size etc. as they emerged. The total pressure inside the condenser would therefore be approximately equal to that of the surrounding atmosphere (~1.013bar). Since cold water was the obvious choice for the coolant, and this may range in temperature throughout the year from ~ 0 to 20°C, the water vapour – air mixtures would have to be significantly hotter than this. However, since the total pressure inside the condenser ~ 1 atmosphere, which is equal to the saturated vapour pressure of steam at 100°C, the water vapour – air mixture would have to be of a lower temperature if nearly saturated. The saturated vapour pressure increases rapidly with temperature such that above 80°C much greater flow rates would be required from the steam generating system. Hence the temperature range of mixtures to be studied was set at 40 – 110°C and the vapour pressure range was restricted to 0.074 (the saturated vapour pressure of steam at 40°C) to 0.474 bar (the saturated vapour pressure at 80°C).

5.2.2 Condenser dimensions

To calculate the water vapour and air flow rates required within the rig from the range of vapour pressures and temperatures, it was first necessary to set the internal dimensions of the condenser section, to specify the range of flow velocities required and thus the range of volumetric flow rates.

The condenser section was initially envisaged as a simple rectangular duct, with boxes attached to the outside through which cold water would flow, transferring heat out of the section. It was necessary to keep the cross-sectional area of the duct fairly small. This ensured that the steam and air flow rates achievable would give rise to turbulent flow (laminar flow being an industrially unrealistic case), with reasonably high mean velocities and Reynolds numbers. However, it was decided a minimum duct width of 4cm was necessary to allow any variations in fog density, droplet size and temperature with distance from the cold surfaces to be identified and also to allow film and bulk fogs to be distinguished. Finally, an aspect ratio of 5:1 was chosen, being roughly the lowest ratio with which it is possible to closely approximate 2d flow. Thus the condenser section was designed to be 0.04m wide and 0.2m tall, giving a cross-sectional area of 0.008m^2. The situation, then, was effectively that of turbulent flow between flat parallel plates. This is physically the simplest configuration, minimising the difficulty involved in modelling the process. Aligning the condenser sections horizontally, with the cold walls vertical, minimised gravitational effects and entrainment problems and allowed a relatively large condenser length to be accommodated comfortably in the laboratory.

5.2.3 Flow velocity

The flow inside industrial condensers is generally turbulent. Hence the investigation of laminar flows was excluded from the study, allowing a lower boundary to be set on the mixture velocity. The boundary between laminar and turbulent flow regimes within a pipe or duct is generally taken to exist at Reynolds number ~ 2300 [14]. The Reynolds number equation is then

$$\mathrm{Re}_{D_h} = \frac{U_m D_h \rho}{\mu} > 2300 \text{ (for stabilised velocity profile turbulent flow).} \tag{5-1}$$

where U_m is the mean mixture velocity, ρ is its density, μ its viscosity and D_h is the hydraulic diameter of the duct given by

$$D_h = \frac{4\times \text{ cross}-\text{sectional area}}{\text{wetted perimeter}} \tag{5-2}$$

and is equal to $0.0\dot{6}$ m for the experimental condenser. Of the range of mixtures given in section 5.2.1, the ratio ρ/μ is lowest for an 80°C saturated mixture. The mean velocity within the condenser when $\mathrm{Re}_{D_h} = 2300$ is then ~ 0.7 m/s. Since the total pressure (of vapour + air) is virtually constant along the length of the condenser, but water vapour is being removed, the mean mixture velocity falls with distance. Therefore to ensure turbulent flow throughout, the minimum mixture velocity at condenser entry was set at 1m/s. The maximum mixture velocity was nominally set at 4m/s. This allowed the effect of velocity and Reynolds number upon droplet formation to be studied over a reasonably large range (4:1), while not increasing the required steam and air flow rates above what was considered practical. The volumetric flow rate at condenser entry then ranged from 0.008 to 0.032m^3/kg. The vast majority of tests were carried out at an intermediate entry velocity of 2m/s (0.016m^3/kg).

5.2.4 Steam flow rate

The largest water vapour mass flow rates were required for the hottest saturated mixtures. At 80°C the specific volume of saturated steam is 3.407 m^3/kg. Hence, to produce a saturated water vapour – air mixture flowing at 2m/s (0.016m^3/kg) requires a water vapour mass flow rate, $\dot{m}_s$, of

$$\dot{m}_s = \frac{V}{v_g} = \frac{0.016}{3.407} \approx 4.7\times10^{-3}\,\text{kg/s}. \tag{5-3}$$

The smallest water vapour mass flow rates were required for producing 40°C, saturated mixtures. At this temperature the specific volume of saturated steam is 19.52 m^3/kg. The mass flow rate, calculated as in equation (5-3) above, is therefore $\approx 8.2\times10^{-4}$ kg/s.

5.2.5 Air flow rate

The lowest temperature mixtures contain the least vapour, and hence the greatest proportion of air. At 40°C the saturated vapour pressure of steam is 0.074 bar. Hence, to produce a 40°C saturated mixture flowing at 2m/s (0.016m^3/kg), the required air flow rate may be calculated by assuming the air to be an ideal gas and using

$$m_a = \frac{p_a V}{R_a T} \tag{5-4}$$

where

$$p_s + p_a \approx 1.013 \tag{5-5}$$

This results in an air mass flow rate of 16.5g/s. However, greater air flow rates were required to produce mixtures of higher velocity. It was intended to perform experiments using mixtures flowing at up to 4m/s, at an intermediate temperature of 60°C, for which p_g=0.1994 bar. These experiments therefore require air mass flow rates of up to 26.8g/s. The smallest air flow rate was required for the smallest mixture flow velocity, i.e. 1m/s (0.008m^3/kg), again at 60°C, and so was 6.7g/s.

5.2.6 Summary

The resulting rig design envelope at condenser entry is presented in Table 5-1.

Bulk mixture temperature	40 - 110 °C
Vapour partial pressure	0.074 - 0.474 bar
Total pressure	~ 1.01325 bar
Mean velocity	1.0 - 4.0 m/s
Volumetric flow rate	0.008 - 0.032 m^3/s
Steam flow rate	0.82 - 4.7 g/s
Air flow rate	6.7 - 26.8 g/s

Table 5-1 Salient conditions for the rig envelope.

5.3 *Mixture Working Section*

5.3.1 Condenser section

The internal dimensions of the condenser section were set at 0.2m high and 0.04m wide, as laid out in section 5.2.2. It was decided that the condenser be made from half metre long sections, a number of which were then bolted together, end to end. This both eased their manufacture and allowed the importance of condenser length upon the exit fog to be studied by simply adding or removing sections during experimentation. The intention was to achieve a constant wall temperature inside the condenser. Hence the obvious choice of material from which to manufacture the condenser sections was copper, due to its high thermal conductivity. It was decided that the easiest way to manufacture the condenser was to machine channels (for the coolant flow) out of the back of a 10mm thick plate. Subsequently it was decided to use aluminium for the condenser side walls, since it is considerably cheaper than copper, is far easier to machine and its thermal conductivity, though less than that of copper, is still reasonably high.

The coolant channels themselves were restricted to a two pass arrangement, and confined to a relatively short plate length (~125mm), to keep the temperature rise on passing through the channel to a minimum, and in an attempt to reduce variations of wall temperature with distance along the condenser. The layout of these channels is pictured in Figure 5-2.

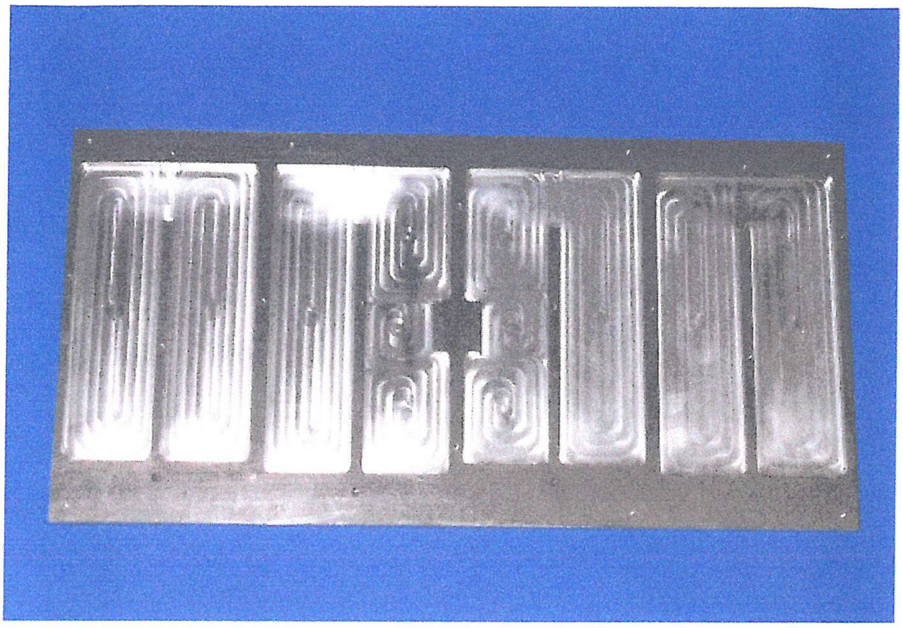

Figure 5-2. Picture of the aluminium condenser side plate, showing the channels cut for coolant flow.

Aluminium backing sheets were then constructed from 14-gauge sheet Aluminium, with which to close off the coolant channels. Holes were cut in the backing sheets at locations corresponding to the bottom of the coolant channels, around which pipe stubs were welded, for the cold water to flow through. These were subsequently bolted to the back of the machined plates and sealed with Silicon rubber. Hence, flat condenser side walls were produced, with coolant channels on the outside and no possibility of any coolant passing through the plates into the duct, and affecting the conditions inside.

Next, collection gutters were machined out of the inside surface of the aluminium plates, and shaped to increase the efficiency of collection of droplets running down the plate surface. Angled holes were then drilled through the side of the plate to enable the condensate collected to be removed and, if necessary, weighed. These gutters are pictured in Figure 5-3. Finally, further holes were drilled through the plates, centred vertically and at 125mm intervals corresponding to the end of the collection gutters, to enable the measurement of the mixture bulk temperature inside the condenser using thermocouples, as described in section 6.5.

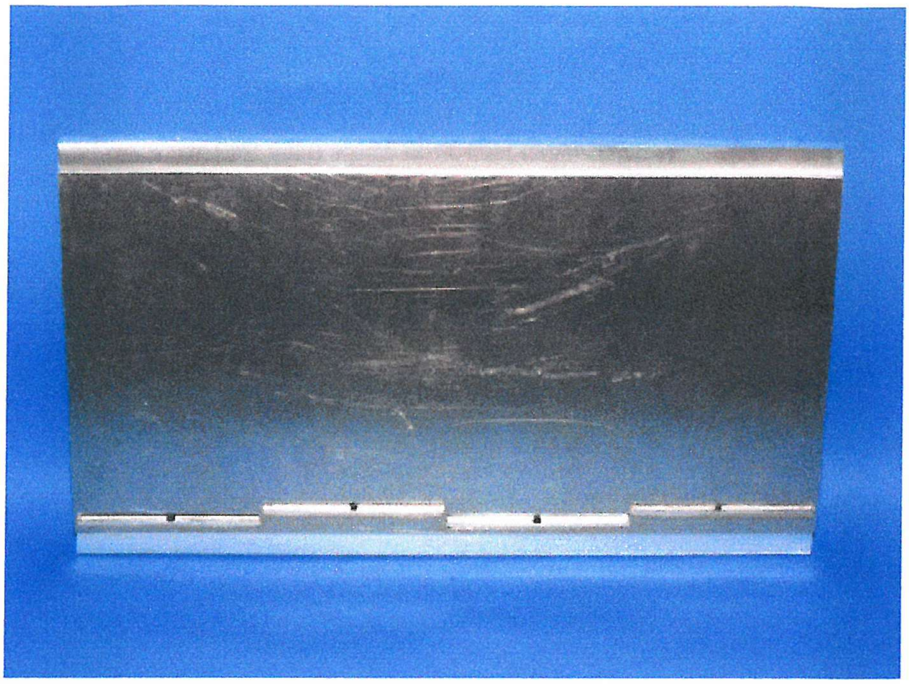

Figure 5-3. Picture showing the condensate collection gutters, cut into the condenser side wall.

In addition to measurements taken in, and upon exit from the condenser, it was envisaged that visual observations would form an important part in understanding the processes involved. It was hoped to obtain visual estimates of the extent of fog formation, along with the axial position of the onset of fog formation, allowing discrimination between film fog and bulk fog formation. Thus, it was resolved to include observation windows in the design of the condenser sections. It was decided that this could be achieved most easily by using uncooled pyrex glass strips, top and bottom, with which to bolt the two side plates together. Consequently, ledges were cut into the inside surface of the plates to accommodate the strips. Vyton was chosen as the accompanying gasket material, working well at high temperatures, and performing equally well with both water vapour and hydrocarbon mixtures. Finally, small pieces of plastic tube were attached to the outside of the condenser section to assist the collection of condensate exiting the condenser, via the collection gutters. A completed condenser section is pictured in Figure 5-4. In all, four such sections were manufactured, each 0.5m in length, to give a maximum condenser length of 2 metres.

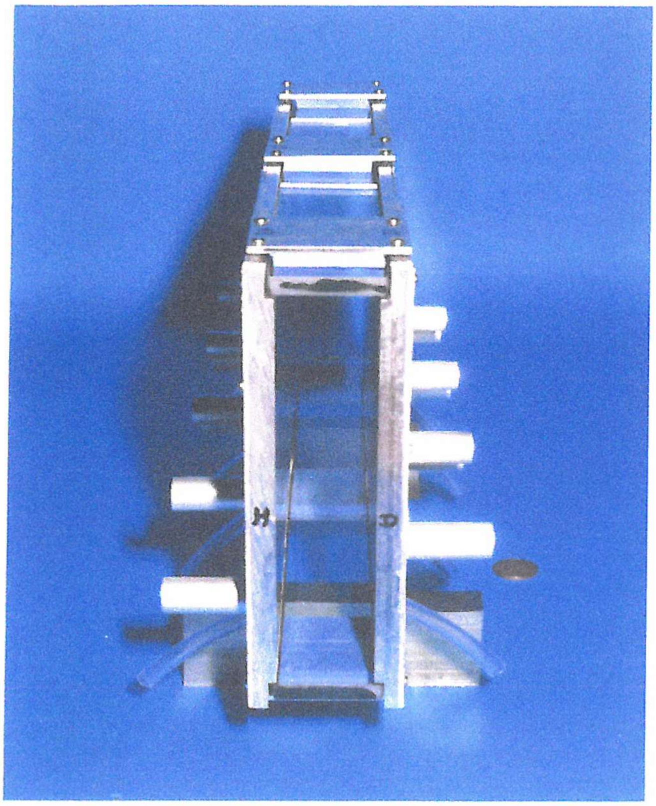

Figure 5-4. End view of a completed condenser section.

5.3.2 Coolant Manifolds

To supply the cold water coolant to the condenser section, a manifold needed to be constructed, whereby water from the ring main, at 3 bar pressure, is carried to each of the condenser channels. Thus the manifold had to incorporate 32 exit tubes / taps. Initially, in an attempt to keep costs to a minimum, attempts were made to use a 102mm (4 inch) steel pipe off-cut. However, it soon became clear that it would be too difficult to position and adequately seal all 32 taps on such a short, curved surface, and so two 2 metre long box sections were bought in, one to supply each side of the condenser. This allowed lock-nuts to be made to tighten the threaded taps against the box section, and allowed for a far more compact arrangement of the plastic tubes carrying the water to the condenser sections. The two manifolds were subsequently laid either side of the condenser sections. The 32 taps, one for each coolant channel, allowed the coolant flow rates to be fully controllable at all points along the condenser section, and hence provided a degree of control over the condenser wall temperature.

5.3.3 Starting section

In order to ensure fully developed turbulent flow in the mixture upon entry to the condenser section, the condenser was preceded by two identical starting sections, one of which is pictured in Figure 5-5.

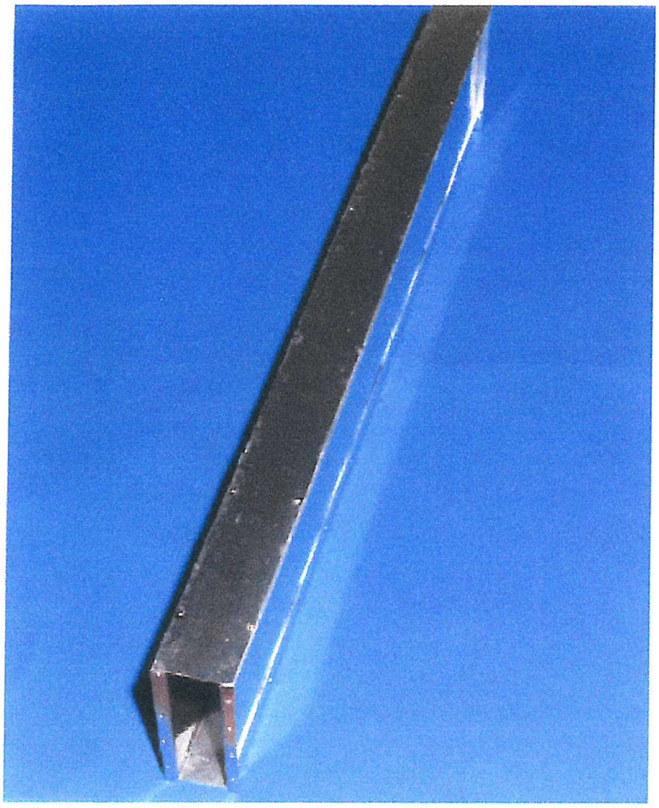

Figure 5-5. Starting section (one metre long).

In general, the turbulent flow of a fluid through a duct may be considered fully developed at a distance of approximately 30 diameters along the length of the duct [3, 52]. The hydraulic diameter of the manufactured condenser section, D_h = (4 × area) ÷ wetted perimeter = 0.066m, so a 1.98m long starting section was required to approach fully developed flow. Consequently two 1 metre long sections were fabricated, and bolted together. The starting sections were simply rectangular ducts, of the same cross-sectional dimensions as the condenser section. Each 1-metre section was fabricated from two pieces of 10-gauge sheet aluminium, which were folded to shape and riveted together. A small drainage hole was cut into the base and simply blocked with a filed-down screw. The drainage hole was added to enable the removal of any condensate forming in the starting sections before they reached the desired rig operating temperature. The sections were then bolted to the first condenser section, and finally insulated.

5.3.4 Entry section

The air and steam flows merged in a 25.4mm (one inch) tee, just upstream of the working section. Thus, in order to carry the resulting mixture from the 25.4mm (one inch) pipe into the working section, an entry section was constructed, and is pictured in Figure 5-6. This was designed to provide a relatively smooth transition into the starting section, and to evenly distribute the mixture across its rectangular cross-section.

Two 50mm long sections were constructed, again by folding pieces of 10-gauge sheet aluminium, with cross-sections equal to that of the starting section. The end of the first section was blanked off, and a hole cut in the top, whereupon a piece of copper pipe was passed down through the hole, until it rested on the section base, and fixed in place with a straight coupling, sealed with PTFE tape. The pipe inside the section had a series of holes of increasing size drilled through its side, in an attempt to obtain a relatively even flow distribution upon exit from the pipe. Placing a fine wire mesh (with a mesh size of 5 x 2.5mm, and ~40% solidity) between the two sections, to encourage micro-mixing, they were then bolted together and sealed with silicon rubber.

Finally, with a second piece of wire mesh, the entry section was bolted to the starting section, and insulated with polystyrene blocks.

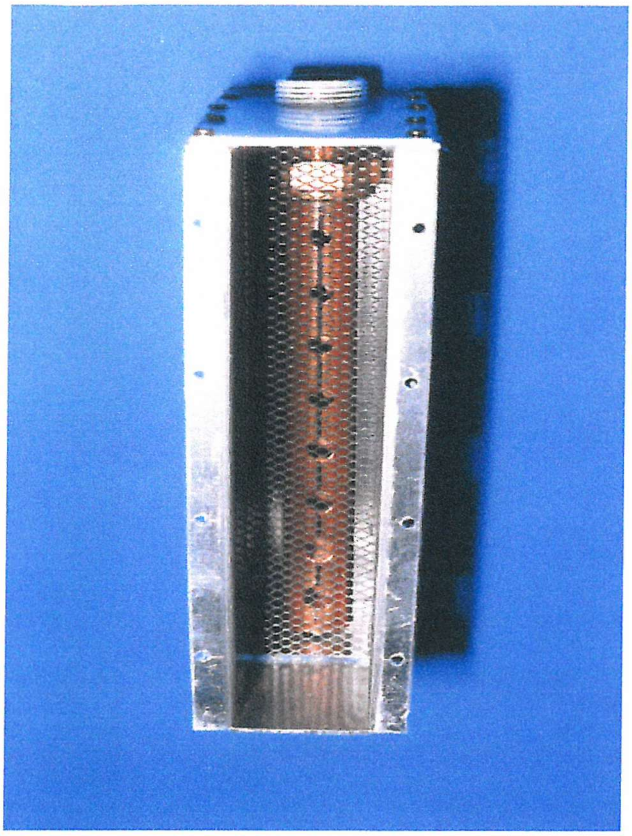

Figure 5-6. Entry section.

5.4 *Steam generation*

A method was required of producing a constant steam flow rate, with which to mix the air, creating a steady stream of moist air for entry into the condenser. The simplest way of achieving this was deemed to be with a constant energy input into a fixed volume of water.

5.4.1 Heater

It was decided to use an immersion heater to boil the water. The maximum steam flow required was calculated to be 4.7g/s. Hence, due to the high latent heat of water, and allowing for heat losses, an immersion heater capable of supplying 18kW was decided upon. Standard immersion heaters, rated at up to 3.6kW are widely available, but are relatively long and bulky, and the need to incorporate five such heaters made their use impractical. Therefore an industrial 3-phase, 18kW immersion heater was purchased. It had nine elements, connected separately in sets of three, such that at maximum power each set provides 6kW. By adding a variable control switch to one phase, with simple independent 'on/off' switches on the other two, it was possible to operate the heater at anywhere from 0 to 18kW, producing a steam flow rate of between 0 and 7g/s.

5.4.2 Steam generating vessel

A cylindrical vessel was designed in which to boil the water. A 1m long piece of 322mm outside diameter pipe was purchased, along with three disks of equal thickness and diameter. Stainless steel, grade 316, was chosen because of its corrosion resistant qualities and its weldability. The dimensions of the pipe were calculated to contain enough water to allow a 40 minute run time at maximum heater power, whilst ensuring that the heating elements remained completely submerged. A hole was cut out of the first disk to accommodate the immersion heater, and it was welded on to one end (the base) of the pipe. Then, three legs were welded to the side of the pipe, near the base, on which to stand the vessel and allow access to the immersion heater once in position. Finally the heater was inserted and bolted into place, with a suitably sized gasket. The central section of the second disk was also removed, a ring of holes drilled and tapped around its edge, and it was welded to the top of the pipe. This allowed the third plate, once the exit pipe was welded to it, to be bolted to the top of the vessel. Constructing the vessel in this way allowed the top plate to be easily removed, providing access to the vessel interior and heater, should, for example, an excessive amount of scale form on the heating elements.

5.4.3 Pressure

In designing the vessel it was important to ensure there was no possibility of a significant pressure build-up inside, once the heater had been activated. In so doing, it was possible to prevent it being classified as a pressure vessel, and escape the ensuing safety regulations and inspections which would have considerably increased the difficulty of manufacture, and time required. It was thus necessary to avoid the use of any valves on the boiler exit pipe allowing any steam generated to flow straight out of the far end of the condenser, to atmosphere. Preliminary calculations of the separation and frictional losses for the system suggested that the pressure needed to force out the steam (and passing air) would be at most 0.2 bar, and hence would cause no concern. This was verified during preliminary experimental runs.

It was also ensured that the boiler exit pipe was sufficiently large to guarantee the flow could not become choked at the flow rates generated.

5.4.4 Additional fittings

A second pipe, with a ball valve, was fitted to the top of the vessel and connected to a water supply with which to refill the boiler after each run. This was also used to empty the vessel by siphoning off the water inside. A pressure gauge was fitted to the top of the vessel to monitor the small pressure rise as steam was first produced, particularly during preliminary test runs. Two holes were then drilled and tapped in the side of the vessel and a pyrex sight glass added. Finally, a control panel was fixed to the side of the vessel, the immersion heater was connected to the 3-phase supply, and the vessel was then insulated with a standard hot water jacket. A picture of the boiler, before the insulation and control panel were attached, is presented in Figure 5-7.

Figure 5-7. Boiler - Stainless steel vessel containing 18kW immersion heater.

5.4.5 Steam heating tape

In order to ensure no liquid water was present in the steam passing through the orifice meter, affecting the flow measurements, a heating tape was wrapped around the pipe between the boiler and the orifice plate. This superheated the steam to an average of 110°C.

5.5 *Air supply*

The air supply was taken from a single feed pipe in the laboratory, (supplied by the main compressor, via a drier) which was capable of supplying cool air in the range of flow rates required, i.e. 1 - 33g/s. The pressure in this pipe cycled over approximately 1 bar, as the compressor cut in and out. Thus, to ensure a steady flow of air through the rig, a pressure regulator was included. The air flow rate was controlled with a pair of gate valves. A length of 25.4mm (one inch) bore steel pipe then carried the air to the tee, where it was mixed with the steam and passed into the main section.

5.5.1 Heating tapes

In order to have a degree of control over the temperature of the mixture entering the condenser, it was decided that a method for heating the air, prior to mixing, was required. Thus a heating tape was wrapped around a 3m length of pipe through which the air flowed prior to mixing. A 1.5kW heating tape was chosen, being sufficiently powerful to heat the maximum 26.8g/s air flow by 55 °C $\left(q = \dot{m}c_p\Delta t\right)$. During standard experimental runs [V = 0.016m^3/s] the air flow rates ranged from 8 to 17g/s and could be heated to an even greater degree.

5.5.2 Variac (for air heating tapes)

In order to control the temperature of the water vapour – air mixtures at condenser entry a variac was added to control the voltage to the heating tapes and hence the power output. A variac which passed 8 amps of current from a standard 240V power supply was chosen. Adjusting the voltage with the variac then allowed any power from 0 to 1.5kW to be selected. Since the steam with which the air was mixed was generally at 110°C, the variac controlled the temperature of the mixture, ensuring it was not supersaturated at condenser entry, and allowing a significant, predetermined degree of superheat to be applied to the mixture as required.

To conclude the set-up of the test rig, the entire length of steel pipe through which heated air or steam flowed, was insulated, to keep heat losses to a minimum.

5.6 *Overview*

A picture of the completed rig, focussing on the main working section is presented in below.

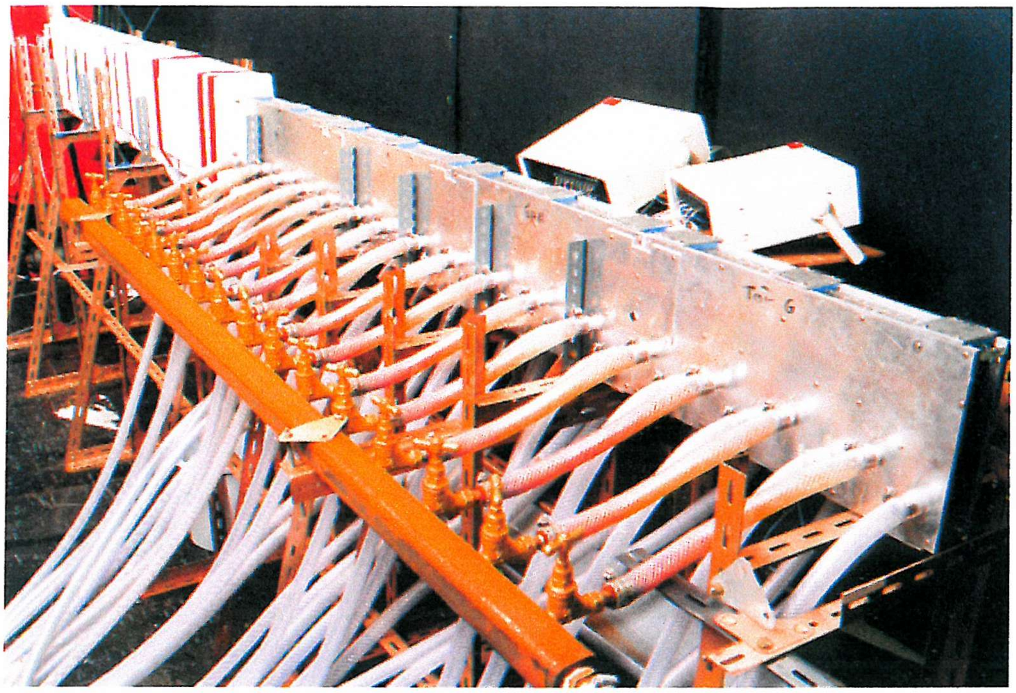

Figure 5-8. The experimental rig.

The construction of this main section was by far the most time consuming part of the rig manufacture, taking far longer than had been envisaged. Though the first designs were submitted in July 1996, it soon ran over into the winter months, whereupon it became significantly more difficult to obtain sufficient workshop time to complete the process, due to the call on their services being at its peak from other areas. Hence the four condenser sections were not finally completed until March 1997, from which point things took shape far more quickly. The starting and entry sections were added in April, and the boiler was in position by May. The associated piping and insulation was added and the air supply connected during June, and although some problems were encountered in the design of the coolant manifolds, as mentioned earlier, they were attached at the beginning of August '97. Finally, preliminary runs were carried out during August and the few sources of leaks in the main section sealed in preparation for the main experimental program.

6. INSTRUMENTATION

6.1 *Introduction*

In this chapter the instrumentation chosen in conjunction with the experimental test rig (see figure 5.1) to study fog formation during the condensation of a water vapour – air mixture is laid out.

The salient conditions for the rig design envelope were presented in the preceding chapter, in table 5.1. These quantities needed to be accurately measured over the entire range of values that were to arise within the rig during experimentation. The desired accuracy of the measurements required was then considered. Finally, measurement devices were chosen based upon these conclusions, in addition to consideration of costs, reliability, and what was readily available in the laboratory and from the industrial sponsors.

Such an approach was important to ensure that the most appropriate instrumentation was chosen, capable of taking the necessary measurements over the design envelope for the rig, to an acceptable accuracy.

6.2 *Orifice Meter*

The range of vapour flow rates expected during experimentation was laid out in table 5.1. Requiring a minimum accuracy of 1% meant it was necessary to have a flow meter capable of measuring steam flow rates of

$$0.8 - 4.7\text{g/s} \quad \pm 0.008\text{g/s} \qquad \text{(i.e. a span range of 6:1).}$$

To measure flow rates through pipes, the instrument with inherently the greatest accuracy is the positive displacement meter [53]. But it is a heavy, delicate and expensive instrument, needing periodical calibration in an expensive meter-calibrating circuit. By comparison, orifice meters are much cheaper, simpler and more flexible devices. So the possibility of using an orifice plate to measure the steam flow rate was considered first, particularly since the budget for the rig was limited.

Orifice meters work as follows. The fluid is forced to flow through a pipe containing a circular orifice. Because of the sudden contraction of the flow area, the fluid accelerates through the orifice, its kinetic energy rises and hence its pressure decreases. A pressure gradient is thus established across the orifice plate. An orifice plate meter is shown schematically in Figure 6-1 below.

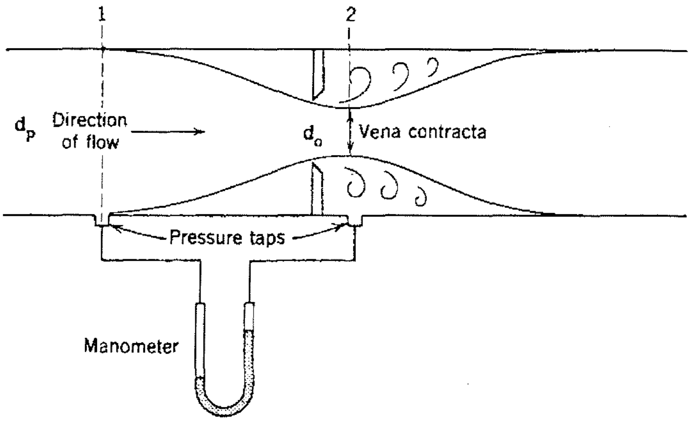

Figure 6-1. An orifice plate meter for measuring flow velocity. [54]

The flow rate is obtained by measuring the pressure difference between the inlet of the meter (point 1), and a point of reduced pressure [42], generally at the vena contracta, downstream of the orifice plate. This pressure difference results in a difference in head of the manometer, positioned as in Figure 6-1, which can then be measured. Assuming the fluid to be incompressible and there to be no loss of energy in passing through the orifice, then the average velocity of the fluid at the vena contracta is given by [54]

$$\bar{u}_2 = C_o \left[\frac{2(P_1 - P_2)}{\rho\left(1 - d_o^4/d_p^4\right)} \right]^{0.5} \tag{6-1}$$

where C_o is the orifice coefficient, accounting for frictional losses etc., P_1 and P_2 are the pressures at points 1 and 2, ρ is the fluid density and d_o and d_p are the diameters of the orifice and pipe respectively. The mass flow rate of the fluid can then be calculated by multiplying the velocity given by equation (6-1) by the density of the fluid and the relevant cross-sectional area. For an incompressible flow the continuity equation reduces to $u_1 A_1 = u_2 A_2 = u_o A_o$, hence the velocity through the orifice

$$u_o = u_2 \frac{A_2}{A_o} = u_2 C_c \tag{6-2}$$

where C_c is the coefficient of contraction. The mass flow rate through the orifice, $u_o A_o \rho$ is then given by [42]

$$\dot{m} = \frac{C_D A_o}{v} \sqrt{\frac{2v\left(P_1 - P_2\right)}{1 - \left(\frac{A_o}{A_p}\right)^2}} \tag{6-3}$$

where the coefficient of discharge, $C_D = C_o C_c$. For a standard orifice meter the discharge coefficient may be assigned a constant value of ~ 0.61 at sufficiently high Reynolds numbers (typically > 10^4). The flow rate is proportional to the square root of the pressure drop.

The orifice meters most serious disadvantage is that most of the pressure drop is not recoverable [42], however this is not of any great significance within the test rig set-up. As differential pressure measurement is, however, basically an inferential method, the accuracy is generally lower than that of other flow measuring devices, e.g. positive displacement meters. A reasonable accuracy can only be obtained when all factors relative to calculation and installation are taken into consideration. Several books have been written on the subject for this reason, e.g. the Shell Flow Meter Engineering Handbook [53]. More intricate equations are presented for the calculation of steam flow rate, taking account of the pipes internal roughness and many correction factors relating to the construction of the orifice meter. A table of the various standard square edged orifice meters available is presented below [53].

Square edged orifice with:	Lower Re_D	Overall approximate error (% full scale value)		Field of application
		Uncalibrated	Calibrated	
flange taps	> 8000	± 1.5	± 0.75	General purpose- non viscous
corner taps	> 5000	± 1.5	± 0.75	Higher pipe roughness
pipe taps	> 14000	± 1.7	± 0.75	Plate between existing flanges, large diameter pressure taps
v. c. taps	> 6000	± 1.4	± 0.75	
radius taps	> 8000	± 1.4	± 0.75	

Table 6-1. Various types of square-edged orifice meters.

To accurately estimate the flow rate through a standard orifice meter using a constant value for the discharge coefficient, there is a minimum Reynolds number (and therefore velocity), with which the fluid must flow. The smallest recommended value occurs for a square edged orifice meter with corner taps, for which the minimum $\mathrm{Re}_D = 5000$. In addition, the normal minimum pipe size in which a standard uncalibrated orifice plate may be fitted is 5.08cm (2inches) in diameter [53]. So for pure steam at 100°C, inserting these values into the equation for the Reynolds number,

$$\mathrm{Re}_D = \frac{U_m D \rho}{\mu} \tag{6-4}$$

implies a minimum velocity through a 2 inch diameter pipe of ≈ 2m/s and hence a mass flow rate of 2.4g/s. Yet, as mentioned in section 5.2.4, the experimental steam flow rate was expected to fall well below this value on occasion.

Thus it was not possible to use a standard, 'off the shelf' orifice meter. Instead, a square-edged orifice meter was designed to fit a 2.54cm (one inch) pipe following the procedure laid out in the Shell Flow Meter Engineering Handbook [53]. The pressure difference across the orifice was to be measured using an inclined alcohol manometer (S.G.=0.784) with a measurement range of 0 – 380 N/m^2. Using equation (6-3) the orifice size needed to produce the necessary pressure differences was estimated. In fact, due to the wide range of steam flow rates it was apparent that two differently sized orifices of approximately 11.0 and 19.0mm diameter were required. Hence two such interchangeable orifice plates were manufactured from stainless steel, which resists corrosion and abrasion. The orifice meter was then calibrated, using each plate in turn, as covered in detail in appendix G.

6.3 *Manometer*

As mentioned in section 6.2 above, the pressure difference across the orifice meter was measured using a manometer. This is basically a U-shaped tube of liquid, attached either side of the orifice, as shown in Figure 6-1. The higher pressure upstream of the orifice causes a column of liquid to rise in the downstream leg of the manometer. The pressure difference across the orifice is then balanced by the pressure produced by the column of liquid (=ρgh). The manometer used during the experiments contained a bulb of liquid in the upstream leg. Therefore the liquid height effectively changed only in the downstream leg, making measurement easier. Because the pressure differences to be measured were quite small a low density alcohol was used in the manometer (of specific gravity = 0.784) and the measurement limb was inclined. A 250mm long scale was marked on the inclined limb, which could be set at an angle of 1:5, 1:10 or 1:20 to the horizontal, meaning a rise of only 1 mm in the liquid level would result in the liquid moving up to 20mm along the scale. Thus the manometer had a range of 0-50mm alcohol (0-380N/m^2) and could be read to 0.05mm (0.38N/m^2).

6.4 *Rotameters*

The range of air flow rates expected during experimentation was also laid out in table 5.1. Seeking a maximum measurement error of 1% required a measurement device capable of measuring air flow rates of

$$6.7 - 26.8 \text{ g/s} \quad \pm 0.06 \text{ g/s}.$$

The most commonly used devices for measuring air flow rates are rotameters. As with an orifice meter, a constriction in the flow causes a drop in pressure, which is used to calculate the flow rate. However, the rotameter is a variable area meter, consisting of a tapered tube containing a freely moving float. When a fluid flows through a rotameter the float rises (increasing the area between the float and the tube wall) until the weight of the float is equal to the upward force resulting from the pressure difference across it. The floats vertical position indicates the rate of flow, which is then read from a scale on the meter. A final adjustment is then made to allow for any difference between the density of the fluid being measured and that in which the rotameter was first calibrated. Rotameters are generally quite accurate and easy to use, though they are moderately expensive, and require that the fluid flow be clean. Since only air flow rates were to be used and rotameters were readily available within the university department and from the sponsors, it was decided that a rotameter be employed within the test rig. In fact, in order to calibrate the orifice meter correctly and to improve the accuracy and measurement range during the main experimental program, two rotameters were installed in parallel. The rotameters chosen operated over the ranges

0.5 – 4.0 g/s ± 0.05 g/s
2.0 – 20.0 g/s ± 0.2 g/s.

Hence by directing the flow through the most appropriate rotameter on any given occasion, or through both simultaneously it was possible to measure air flow rates of 0.5 to 24.0g/s with a reasonable degree of accuracy. Though the measurement of greater air flow rates was not possible, and the measurement accuracy when using the very lowest flow rates was slightly less than that desired, this could soon be rectified by the replacement of either rotameter during testing. In practice, this was not required, and the two rotameters specified were used throughout the experimental program.

6.5 *Thermocouples*

One of the most important properties of the air – water vapour mixture, and the most easily measured is its temperature. It was intended to measure the temperature of the mixture at a number of axial locations within the condenser, to gauge the bulk temperature drop and the rate of heat transfer. The temperature was to be measured at the centre of the condenser, at condenser entry and at 125mm intervals subsequently, coinciding with the junction of the condensate collection gutters, as shown in Figure 6-2, over the page. The temperature was therefore to be measured at 17 locations within the condenser section alone when 4 sections were in place, and a further five locations elsewhere in the rig (refer to Figure 5-1), e.g. for obtaining the temperatures of the steam and air flows prior to mixing.

Starting Section (lagged)

First condenser section, (0.5m long) showing the position of the condensate collection gutters.

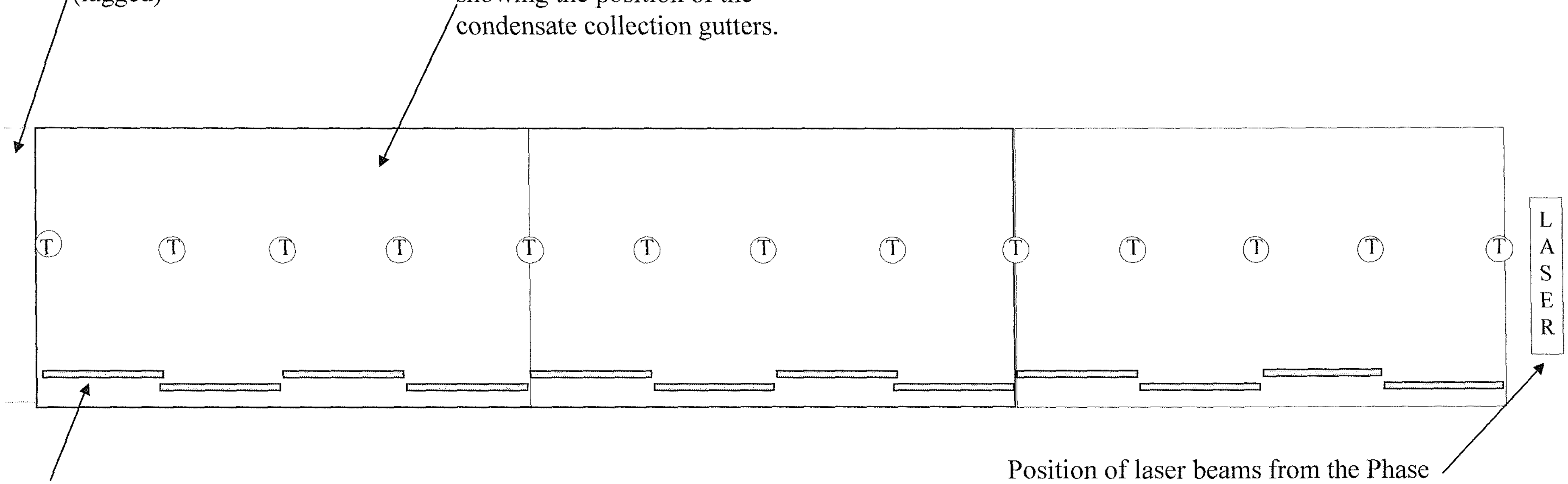

Condensate collection gutter (125 mm long)

Position of laser beams from the Phase Doppler Particle Analyser, allowing measurement of the fog droplet sizes and velocities upon exit from the condenser section.

Ⓣ - Points at which thermocouple temperature measurements were performed (at 125 mm intervals, corresponding to gutter junctions).

Figure 6-2. Diagram showing the measurements performed on the bulk mixture inside the condenser section.

With such a large number of measurements it was decided to use thermocouples, since they are both inexpensive and easy to install. The possibility of any current leakage arising within the thermocouple wires was avoided by coating the exposed wire ends with aroldite. Copper Constantan thermocouples (of ~ 0.1mm diameter wire thickness) were used as they cover the required temperature range (20-110°C). They also provide an adequate response of ~ 39 μV per degree Celsius temperature change when welded, meaning that when connected to a suitable cold junction and digital voltmeter during experimentation it was possible to measure the temperature to an accuracy of at least ± 0.2 °C (i.e. $\leq 1\%$). The thermocouples were passed through small holes drilled in the condenser side plates into the centre of the condenser, at the point of maximum temperature measurement and held in position by using silicon rubber to seal the holes.

6.6 *Droplet sizing*

The main purpose of the experimental program was to study the droplet size distributions of fogs produced during partial condensation. The droplet sizing equipment used was an Aerometrics Phase Doppler Particle Analyser (PDPA), supplied by BP Chemicals. This is a highly sophisticated and expensive instrument which utilises the light scattered by spherical particles to obtain simultaneous size and velocity measurements [55].

The PDPA consists of 5 major components, namely a transmitter, receiver, signal processor, motor control box and computer. The transmitter contains a 10milliwatt, polarised helium-neon laser. The laser beam passes through a radial diffraction grating, rotating at one of three speeds set on the motor control box. The grating partitions the laser beam into two equal intensity light beams, with a fixed frequency difference between them. These beams then enter the output lens, causing them to intersect and form the sample (measurement) volume. Any particles passing through this volume scatter the light, producing a far field interference pattern, which is then collected by the three detectors housed within the receiver, giving measurements of the particles size and velocity. The resulting information passes via the signal processor to the computer, where the data is stored for subsequent analysis.

The principle behind the droplet sizing technique is as follows. Where the two laser beams intersect (the measurement volume), they interfere and a fringe pattern is set up. Particles passing through the measurement volume move through the fringe pattern, scattering the fringes, with refraction being the dominant scattering mechanism for transparent scattering particles in the near forward scattering directions [56]. The smaller the particle, the greater its curvature and hence the greater the distance between the scattered fringes. The receiver, containing three separate detectors is placed at a known location. As the particle moves in the measuring volume, so the fringes move across the detectors, generating temporally fluctuating signals. Since the detectors are a (known) distance apart, there will be a phase shift between the three signals (in fact, only two detectors are necessary to determine this phase shift). Again the smaller the particle, the further apart the scattered fringes, and hence the smaller the phase shift between the signals, i.e. the phase shift is proportional to the diameter of the particle. Hence this phase shift can then be used in conjunction with information about the wavelength of the light, beam intersection angle, particle refractive index and the location of the detectors to determine the particle diameter.

It is impossible to determine the errors of such measurements, but there are several measures which have been incorporated in the design of the PDPA to ensure that the results are as accurate as possible. Firstly the receiver contains three detectors rather than the minimum two. This is in order to provide a redundant measurement, not only as an instrument self check but also to ensure particle sphericity [55]. In addition the third detector extends the sensitivity of the measurement by having detector pairs at different spacings, thus producing different phase shifts for the same particle size. Another likely source of error in measuring droplet size distributions arises from the fact that large particles passing through the measurement volume may obscure smaller particles passing behind. A statistical correction factor has been included in the associated software in an attempt to counter such problems.
Additionally for the measurement of very small particles the resolution of the instrument can be improved by increasing the angle between the incident beams. This is achieved by using a lens with a shorter focal length, allowing the measurement of particles down to 0.5 microns in diameter.

Non-spherical particles and those just clipping the measurement volume, for example, may still cause problems. However, although as previously stated, no error calculations for the droplet sizing technique are possible, the careful choosing of the most appropriate optical set-up for each situation should ensure that the results obtained are as accurate as possible.

6.7 *Summary*

To conclude, below is a table containing the ranges and accuracies of the instrumentation used in conjunction with the test rig.

Instrumentation	Measurement Minimum - Maximum	Measurement error	Maximum error (percentage)
Orifice meter (plate A)	0.3 - 1.3g/s	± 0.02g/s	± 7%
Orifice meter (plate B)	0.7 - 4.8g/s	± 0.05g/s	± 7%
Manometer	20 - 380N/m^2	± 0.38N/m^2	± 2%
Rotameter A	0.5 - 4.0g/s	± 0.05g/s	± 10%
Rotameter B	2.0 - 20.0g/s	± 0.2g/s	± 10%
Thermocouples	20 - 110°C	± 0.2°C	± 1%
PDPA	0.5 - 300 μm	-	-

These were fully adequate for testing the criteria for fog formation.

7. Rig commissioning, operation and modification

7.1 *Introduction*

Having manufactured and assembled the test rig, and incorporated the necessary instrumentation, a number of trial runs were carried out to check that the rig worked properly, and that the full range of conditions the rig had been designed to produce could actually be realised. A few time consuming problems were encountered, but ion generally the rig operated as required.

In this chapter the initial problems, the mixture property calculations performed prior to each experiment, the rig operation and the modifications to the test rig are discussed.

7.2 *Initial problems*

Problems were immediately encountered upon integrating the orifice meter into the steam line. With the manometer tubes attached to the pressure tapings at the top of the 1" steam pipe, some of the steam was forcing its way up the tube, then condensing. The water drops produced were then coalescing to form a blockage in the tube. Movement of the blockage, due to gravity or pressure differences, caused the level of the manometer fluid to fluctuate accordingly, making measurement impossible. The blockage could be removed by shaking the tube, but this proved to no avail as it would soon reform. It was also unsatisfactory because occasionally the blockage was forced further up the tube, increasing the pressure difference between the manometer legs and pushing the manometer fluid above its maximum level, flooding the connecting tubes. As a result the experiment had to be terminated for the excess fluid to be removed. In response to this, steam traps were added to the manometer tubes and the orifice meter and connecting pipe stubs were rotated until the pressure tappings lay near the bottom of the pipe, at approximately 45° to the vertical. This was done to allow any steam condensing in the tubes to drain straight into the steam traps. However, blockages in the tubes between the pressure tapings and the steam traps persisted until these were replaced with shorter, wider tubes, thus solving the problem.

Another problem that arose involved the appearance of condensate in the starting section. Some of this water was evading the collection gutters and draining back from the condenser. Thus a small drainage hole was added between these sections. The remaining water was condensing within the starting section itself, but this problem was subsequently eradicated by pre-heating the test section with hot air before any steam began to flow from the boiler.

With these modifications the rig appeared to be working correctly. A wide range of constant steam and air flow rates was achievable, and fogs of different densities were observed exiting the condenser.

7.3 *Flow rate calculation*

Having overcome the initial problems with the test rig, experimentation could begin. Each experiment was to be performed using a water vapour – air mixture of predetermined bulk condition. The mixture to be studied was chosen by assigning its bulk temperature, relative humidity (or partial vapour pressure) and velocity at condenser entry. The steam and air flow rates required to produce this mixture were then calculated using the following procedure.

7.3.1 Mass flow rates

First, the partial pressure and specific volume of the vapour, p_s and v_s respectively, were calculated from the relative humidity, ϕ, using

$$p_s = \phi p_g \tag{7-1}$$

$$v_s = v_g / \phi \tag{7-2}$$

where p_g and v_g are the saturation values at the temperature of the mixture (obtained from tables). The mass flow rate of water vapour required at condenser entry is then given by

$$\dot{m}_s = \frac{\dot{V}}{v_s} = \frac{uA}{v_s} \tag{7-3}$$

where $\dot{V}$ is the volumetric flow rate [m^3/s] and is therefore equal to the product of the mean mixture velocity and the cross-sectional area of the condenser section. Assuming the air to behave as an ideal gas, the mass flow rate of air at condenser entry is given by

$$\dot{m}_a = \frac{p_a \dot{V}}{R_a T} = \frac{(P - p_s) A u}{R_a T} \tag{7-4}$$

where P is the total pressure of the system $(= p_a + p_s)$. Generally, these values (in addition to other properties and parameters relating to the mixture in question which were required for the theoretical predictions of chapter 4) were calculated using a simple computer program, presented in appendix H.

7.3.2 Corresponding orifice meter and rotameter readings

The vapour and air mass flow rates calculated as in the previous section, were those required at condenser entry. In order to obtain the desired mixture experimentally, the corresponding rotameter and orifice meter (manometer) readings are required. These had to account for the small vapour content of the air used in the experiments. Thus the flow rates were determined using

$$\begin{matrix}\textit{Vapour flow rate}\\ \textit{through orifice}\end{matrix} = \begin{matrix}\textit{Steam flow rate at}\\ \textit{condenser entry}\end{matrix} - \begin{matrix}\textit{Vapour flow rate}\\ \textit{contained in the air}\end{matrix} \qquad \textbf{(7-5)}$$

and

$$\begin{matrix}\textit{Air flow rate}\\ \textit{through rotameter}\end{matrix} = \begin{matrix}\textit{Dry air flow rate at}\\ \textit{condenser entry}\end{matrix} + \begin{matrix}\textit{Vapour flow rate}\\ \textit{contained in the air}\end{matrix} \qquad \textbf{(7-6)}$$

The humidity of the laboratory air supply was measured using a simple wet and dry bulb thermometer. The subsequent calculation of the water vapour content of the air is laid out in Appendix I. This is followed by the calculation of the rotameter and orifice meter (manometer) readings required to attain the correct mass flow rates at condenser entry.

7.4 *Operating Procedure*

Having resolved the initial problems with the test rig, the first experiments were performed. To conduct the experiments as efficiently as possible the various tasks involved in operating the test rig were performed in a fixed, predetermined order. This was also important in order to ensure steady-state conditions, to minimise corrosion and to avoid any water vapour condensation upstream of the condenser, as discussed in section 7.2.

Before starting, softened water was pumped into the boiler until it was approximately 90% full, ensuring there was sufficient water to allow a reasonably long run time while allowing a small space for a vapour buffer which proved helpful in maintaining a constant vapour flow rate. The inclined manometer leg was then adjusted to the angle most appropriate for measuring the pre-calculated pressure drop across the orifice plate.

The experiments were initiated by pre-heating the test section with hot air. The first step was to open the valve on the air feed pipe such that the required air flow reading was observed on the rotameter. The air heating tape was then switched on and the controlling variac adjusted to allow the air temperature to approach that of the mixture to be studied. At the same time two of the boilers three heating elements were switched on, giving 12 kW of power. This ensured the water began to boil relatively quickly but still allowed approximately 30 minutes for the rig to heat up before this happened.

Approximately 20 minutes later, as the temperature in the condenser began to increase notably, the coolant was initiated by opening the gate valve between the ring main and the manifolds. A quick check was performed to ensure that the flow rate through each coolant channel was approximately equal, otherwise the manifold taps were adjusted until this was the case. The heating tape on the pipe between the boiler and orifice meter was then switched on to inhibit condensation in this section, and to guarantee the ensuing steam flow was superheated at the orifice to allow accurate measurement of its flow rate.

At the first sign of steam generation, indicated by movement in the orifice meter manometer fluid, the power to the boiler was adjusted to a value estimated to produce the desired steam flow rate. The variac connected to the air line heating tape was then reduced to a value estimated to produce the required mixture temperature.

After a further 30 minutes, the steam flow rate and mixture temperature would begin to stabilise. At this point it was generally necessary to re-adjust both the power supplied to the boiler via the heating elements and that supplied to the air heating tapes to more closely approach the desired mixture condition. The temperature and pressure of the fluids passing through the orifice meter and rotameters was then noted. This was important to allow any differences between the density of the fluids and those at which the instruments were calibrated to be accounted for (as detailed in appendix I), and further slight changes to be made as necessary.

After another 20 minutes or so the laser was switched on and, finally, after an additional 10 minutes the temperatures and flow rates were usually sufficiently stable to allow measurements to be made. A small air supply was connected to the laser transmitter and receiver lens hoods, to prevent any droplets settling upon the lens surfaces and the intensity of the laser beams was maximised. The beams were then placed at the desired measurement location. A clear signal was sought on the oscilloscope attached to the PDPA, and the beams again adjusted as necessary. A series of droplet size and velocity measurements were then performed, each over a period of 10 to 120 seconds dependent on droplet number concentrations, at a number of different locations. At the same time the temperature measurements of all the thermocouples within the rig were manually recorded.

Throughout the run, attention had to be paid to the level of water remaining in the boiler to ensure it did not run dry, particularly when operating with high steam flow rates. If time permitted a second set of data was then collected using a different mixture temperature (and / or flow rates) by repeating the requisite stages above.

Having collected sufficient experimental data (or been left with insufficient water in the boiler) the rig was then shut down. First the laser was switched off, removed from the measurement area and the lens hood air supply terminated. The boiler heating elements were then switched off as well as the steam line heating tape.

After a further 10 minutes the air supply valves were closed temporarily to allow the ball valve on top of the boiler to be opened and some cold water added to inhibit the release of any more water vapour. This was then closed and the air flow restored permitting hot air to blow through the rig, drying the interior surfaces and thereby reducing corrosion.

After an additional ten minutes the air line heating tape was switched off and the coolant flow stopped. Finally, when the temperature of the air fell sufficiently the air supply was terminated.

7.5 *Temperature control*

The most difficult part of the rig operation was trying to attain the desired mixture temperature at condenser entry. This was because the only way to control the temperature was with the variac connected to the air line heating tape. The required setting for an individual test run was not easily determined since this was affected by the steam flow rate, the air flow rate and the initial air temperature. These variables changed from one run to the next and made it practically impossible to choose the correct variac setting at the first attempt. Thus an initial estimate was made, the temperature noted and the variac setting modified. Often several such iterations were required to produce a mixture temperature sufficiently close to the desired value. This was particularly frustrating because of the slow response time between changing the power to the heating tapes and a new steady mixture temperature being obtained. This process took about 30 minutes so if too many iterations were required in an individual run the boiler would empty before useful results could be obtained.

This problem was countered in later experiments by taking measurements at a range of non-specific temperatures, all at the chosen steam to air mass flow ratio. A greater quantity of experimental data was thereby obtained over an equal time period. The results at the desired temperature could then be estimated by interpolating, or more commonly, the range of results could be compared graphically with those of different component flow rates. This had the added advantage of highlighting any anomalous results, though in general the additional tests helped to indicate the consistency and repeatability of the test results.

7.6 *PDPA replacement*

In June 1998 a problem was encountered with the PDPA system. It soon became apparent that this was a serious malfunction, and that specialist repair was needed, available only by returning the PDPA signal processor to the company that designed the system in the United States.

Since the measurement of droplet sizes constituted the most important part of the experimental program and the funding period for the project was rapidly expiring, the possibility of obtaining an alternative system was explored. The only option was to apply to the EPSRC loan pool, based at the Rutherford Appleton laboratory, for a temporary replacement. However, a minimum four months wait was quoted for a droplet-sizing system.

In the interim period the transportation of the PDPA signal processor for repair was severely delayed. Repeated enquiries regarding its progress eventually lead to the location of the device, which was finally returned in November 1998. However, this was not the end of the saga since during repair the processors internal transformer had been rewired to the standard American setting of 110 volts. The voltage was not returned to its original setting, and hence was immediately overloaded when switched on back in the U.K. The processor was thus sent for repair a second time, returning only in January 1999.

In the mean time the EPSRC loan pool droplet sizing system was also delayed. It was eventually delivered in February 1999, a Dantec Laser Doppler Anemometer (LDA), and is compared briefly to the PDPA in the following section.

These delays considerably hindered the entire project. Without a droplet sizing system it was impossible to quantitatively study fog formation. Thus these problems meant a further extension of the project was required.

In the interim period time was spent modifying the computer program and carrying out a number of tests into the nature of the flow within the condenser, which are presented in chapter 8.

7.7 *Laser Doppler Anemometer*

The new droplet-sizing device on loan from EPSRC, was a laser Doppler Anemometer (LDA), but used the same general principles as the Phase Doppler Particle Analyser (PDPA), described in section 6.6. That is simultaneous droplet size and velocity measurements are obtained from the scattered light produced when a droplet moves through the measurement volume, created by an intersecting pair of laser beams. However, it has several advantages over the PDPA system. Firstly, there are two pairs of perpendicular laser beams, allowing 2-dimensional velocity measurements. Secondly, the laser beams are more powerful than those used in the PDPA system, allowing better detection of the smallest droplets. Thirdly, the laser transmitter and receiver units were housed on a traverse, enabling the measurement region to be moved automatically through a series of pre-programmed 3-dimensional co-ordinates. Lastly, there was no need to adjust the optical set-up during runs, since the laser beam intensities were constant throughout.

While each of these improvements were useful, the most important with regard to this study was the greater beam intensity. The performance of the two systems is compared in Figure 7-1 below, where two droplet size distributions produced under identical conditions are presented.

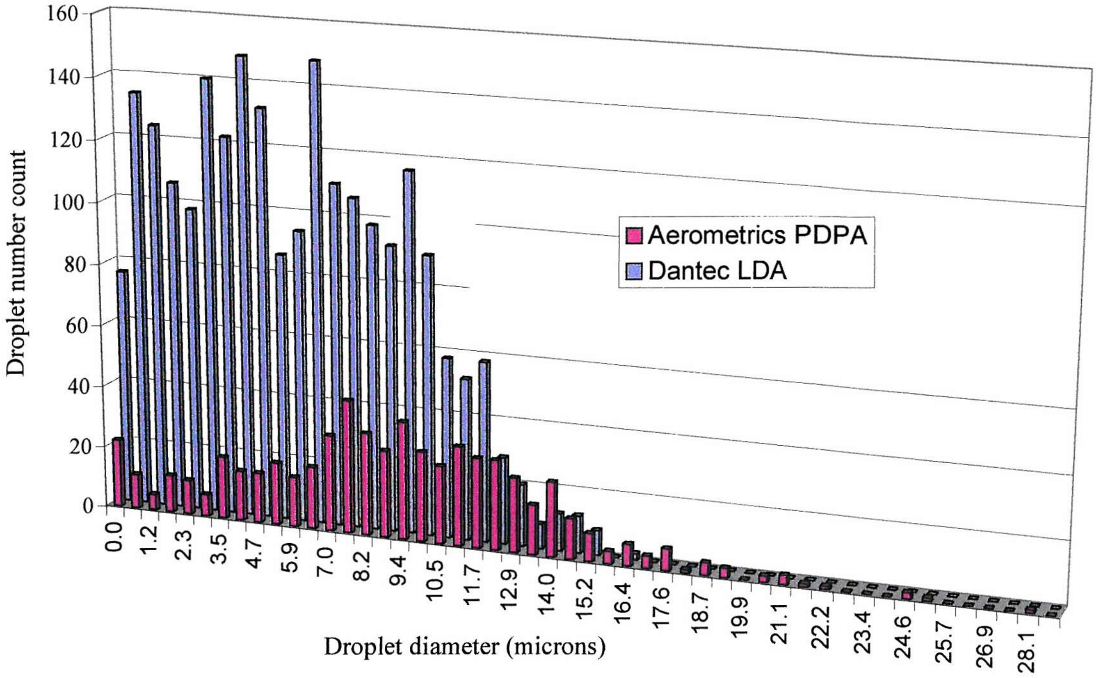

Figure 7-1. Droplet size distributions obtained with the two measurement systems.

While the number of droplets detected near the upper size limit of the distribution (>12μm) is similar, the Dantec LDA system, was able to detect a far greater number of droplets in the smaller size ranges than the PDPA system. This demonstrates the advantages of the greater beam intensities for measuring droplets down to 0.5μm in diameter.

8. Preliminary testing

8.1 *Introduction*

Before proceeding in earnest with the experimental test program for the study of fog formation, it was decided to perform a number of exploratory tests to establish that the rig was functioning as expected. These tests would also provide the necessary data to allow the creation of a simple method for accurately estimating the cross-sectional bulk or mean temperature of the fluid, from the point thermocouple measurements obtained experimentally.

Hence, a study of the flow conditions and heat transfer within the main test section was undertaken, including an examination of the lateral temperature and velocity distributions created during operation, and the axial temperature drop along the condenser. The overall heat transfer coefficient, h, was then determined using

$$h = \frac{q}{A}\frac{\ln[(t_w - t_{b1})/(t_w - t_{b2})]}{t_{b2} - t_{b1}} \tag{8-1}$$

where t_{b1} and t_{b2} are the bulk temperatures of the fluid at cross-sectional locations 1 and 2, t_w is the temperature at the wall. The total heat transferred, q, is calculated using

$$q = \dot{m} c_p (t_{b2} - t_{b1}) \tag{8-2}$$

Since the calculation of the heat transfer coefficient is dependent upon the knowledge of the mass flow rate, $\dot{m}$, to simplify the calculation the majority of the initial temperature measurements were performed during experiments using hot air only. This ensured that the mass flow rate was constant (since there was no condensation of vapour), and that the fluid properties, c_p etc., were easily obtainable, and fairly constant throughout the rig.

8.2 *Lateral velocity profile*

Measurements of point velocity within the rig were obtained using the LDA. This requires the presence of scattering particles and hence velocity measurements could only be carried out in fogging water vapour – air mixtures. By taking a series of measurements across the condenser, from one plate to the other, the lateral velocity profile was obtained. Due to the layout of the LDA transmitter and receiver lenses, it was necessary to perform the measurements outside the condenser section, approximately 5mm downstream of the exit plane.

The velocity profile was expected to be that of fully developed turbulent flow throughout the length of the condenser as a result of the inclusion of the 2m long starting section. Such velocity profiles are usually well represented by the universal velocity distribution (see appendix J). The measured velocity profile at the end of the two metre long condenser is plotted in Figure 8-1 below.

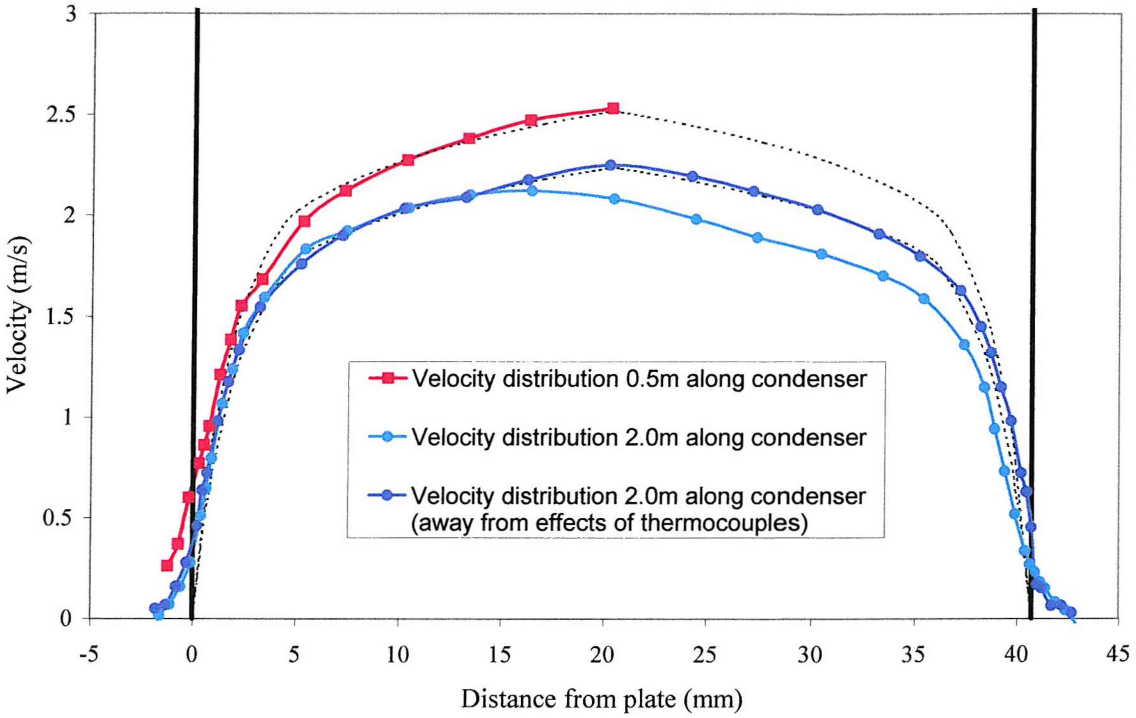

Figure 8-1. Lateral velocity profiles measured horizontally across the condenser, from one cold wall to the other. The dotted lines are those predicted by the universal velocity profile.

Slight discrepancies were expected due to the imperfect nature of the condenser sections, of the connections between them and the connections with the starting section. Additionally, because it was necessary to perform the measurements approximately 5mm outside the condenser. The first measurements at two metres were as expected up to the centre of the condenser, after which they were notably lower. This was due to the measurements being performed in the horizontal plane midway between the base and top of the condenser. This plane was also used for temperature measurement, and hence contained a series of thermocouples protruding out from the right hand condenser wall to the region of maximum temperature. New velocity measurements performed slightly above and below the previously used plane produced the expected results, as did measurements performed using a shortened condenser. The thermocouple wires were clearly responsible for the reduced flow observed in the first measurements. The velocity profiles indicate fully developed turbulent throughout the condenser.

8.3 *Lateral temperature profile*

The first series of lateral temperature measurements was conducted at the end of the 2m long condenser. The measurements were performed using fine wire copper constantan thermocouples. The wires were welded together and coated in Araldite, producing a bead less than 0.5mm in diameter. A simple thermocouple traverse was then constructed, using a wooden frame and a micrometer. The thermocouple wire extended into the direction of flow, and approximately 20 mm into the end of the condenser. The point of measurement could then be moved very slowly and precisely from one wall to the other. An example temperature distribution measured across the centre of the duct (i.e. 100mm above the base of the 200mm tall condenser section) is presented in Figure 8-2 below.

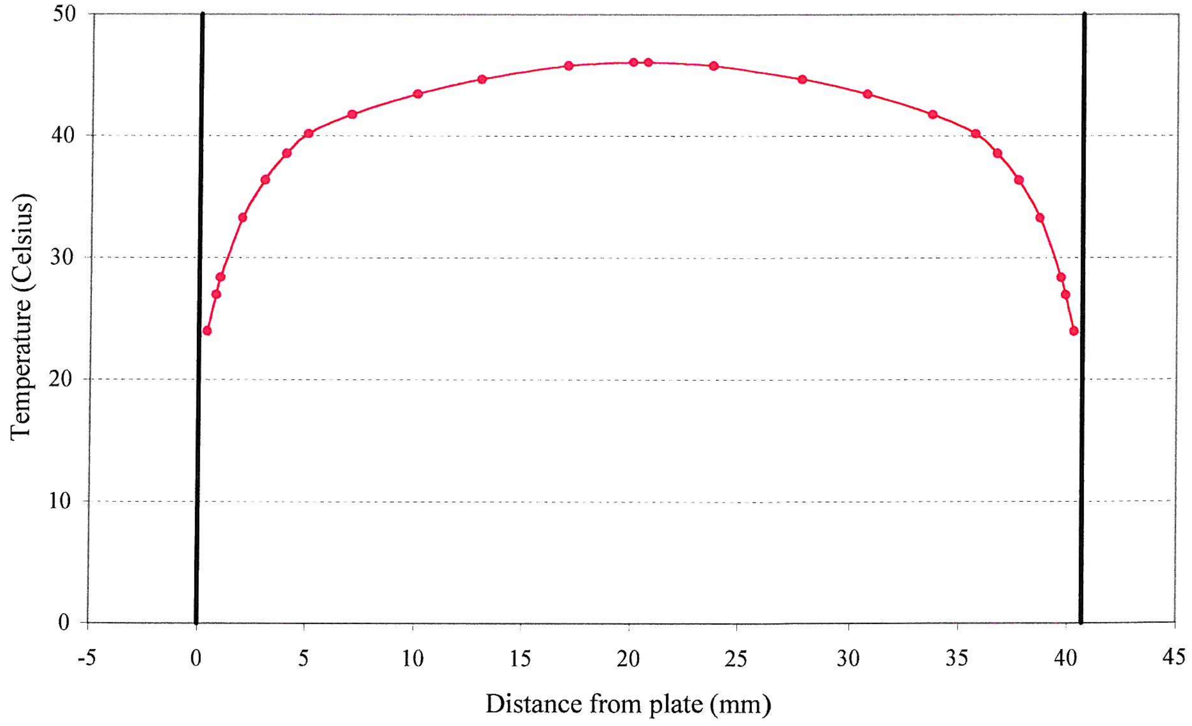

Figure 8-2. Temperature distribution of air at condenser exit.

The temperature distribution illustrated in Figure 8-2 was of the form expected, i.e. symmetrical about the centre of the duct, with the greatest temperature at the centre, falling away towards the cold walls, and with the greatest temperature gradients next to the walls. Having obtained a temperature distribution at the end of the condenser, it was decided to repeat the process further upstream. The only way to perform temperature measurements within the condenser as required was to pass a thermocouple in through a small hole drilled through the side, as had been done for the thermocouples located to measure the axial temperature drop. However, the results were not at all as expected. At first this was attributed to uncertainty in the position of the flexible thermocouple wires. Yet similar results were obtained when the wires were housed inside a hypodermic wire. The main difference between these measurements and those presented in Figure 8-2 above was the direction of the thermocouple. To see if this was affecting the results, the measurements at the end of the condenser were repeated with the thermocouple wires pointing perpendicular to the cold walls. The two results are superimposed in Figure 8-3 below.

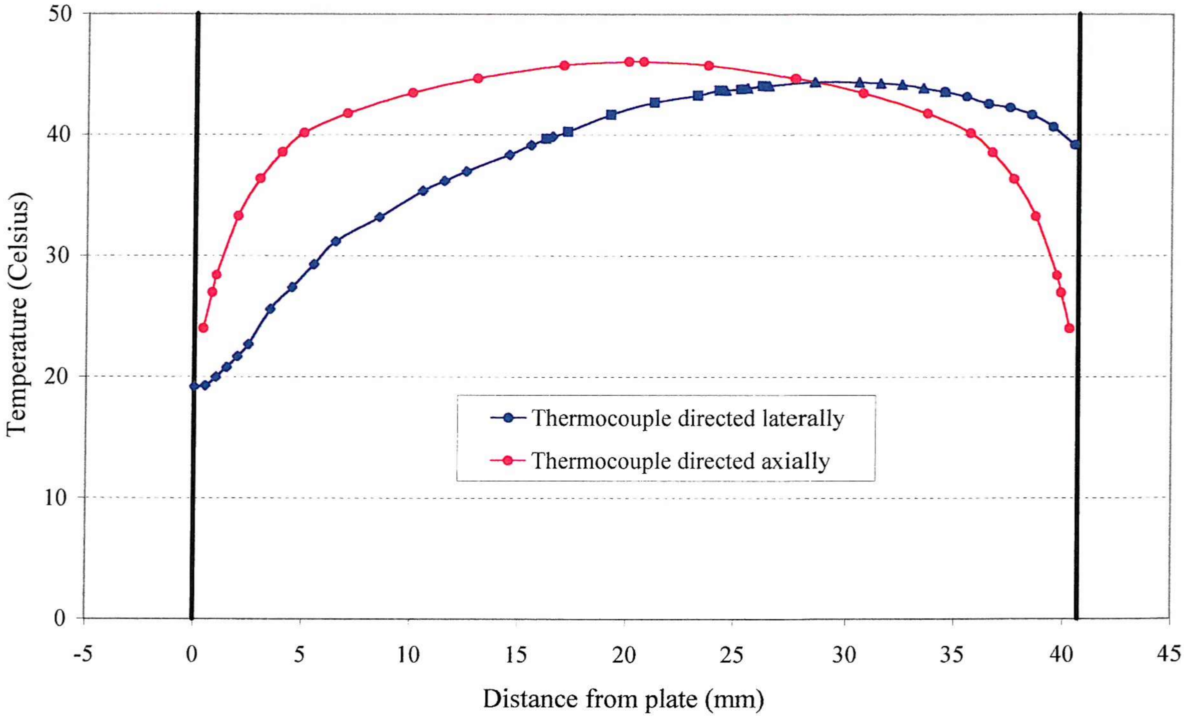

Figure 8-3. Comparison of temperature distributions obtained using thermocouples directed laterally and axially within the condenser.

The measurements obtained with the thermocouple directed laterally are clearly erroneous. This is because of thermal conduction along the length of the wires. In this position the thermocouple is pointing at right angles to the direction of flow, in the direction of the greatest temperature gradients. The thermocouple wires extended to the measurement location from the left hand plate when viewed as in Figure 8-3 above. Thus, conduction of heat away from the measurement tip artificially reduced the temperature measurement until the thermocouple had passed well beyond the centre of the condenser. Thereafter, conduction from the wire in the hottest region of the condenser towards the thermocouple tip resulted in measurements that were too high. A reflection of this distribution was obtained when the thermocouple wire extended from the opposite plate. The temperature measurements obtained using thermocouples pointing directly upstream could be relied upon due to the comparatively small temperature gradients existing in this direction, minimising thermal conduction along the wire.

This was an important discovery that had not been foreseen, and implied that the temperature measurements obtained using thermocouples inserted through the condenser side walls, at 125mm intervals, would all be too low. Since it was not possible to reposition the thermocouples a correction would have to be applied, further complicating the process of bulk temperature estimation from the single point measurements.

To obtain accurate temperature distributions at condenser locations upstream of those presented in Figure 8-2 and Figure 8-3, it was necessary to remove condenser sections. By so doing it was possible to acquire temperature distributions 0.5, 1.0, 1.5 and 2.0m along the condenser. These temperature distributions are plotted in Figure 8-4 over the page.

The dotted lines in Figure 8-4 are the corresponding universal temperature distributions, calculated using the equations presented in appendix J. These are the distributions predicted for fully developed turbulent flow, where the temperature profile is also fully developed. The graphs indicate that the temperature profiles are not fully developed within the first half of the condenser at least. This is to be expected, since though a two metre starting section was included to ensure fully developed turbulent flow at condenser entry, the cooling began in earnest only as the fluid entered the condenser. Only then did the thermal boundary layer begin to develop. The typical development of the temperature profile in pipe flow is illustrated in Figure 8-5, below.

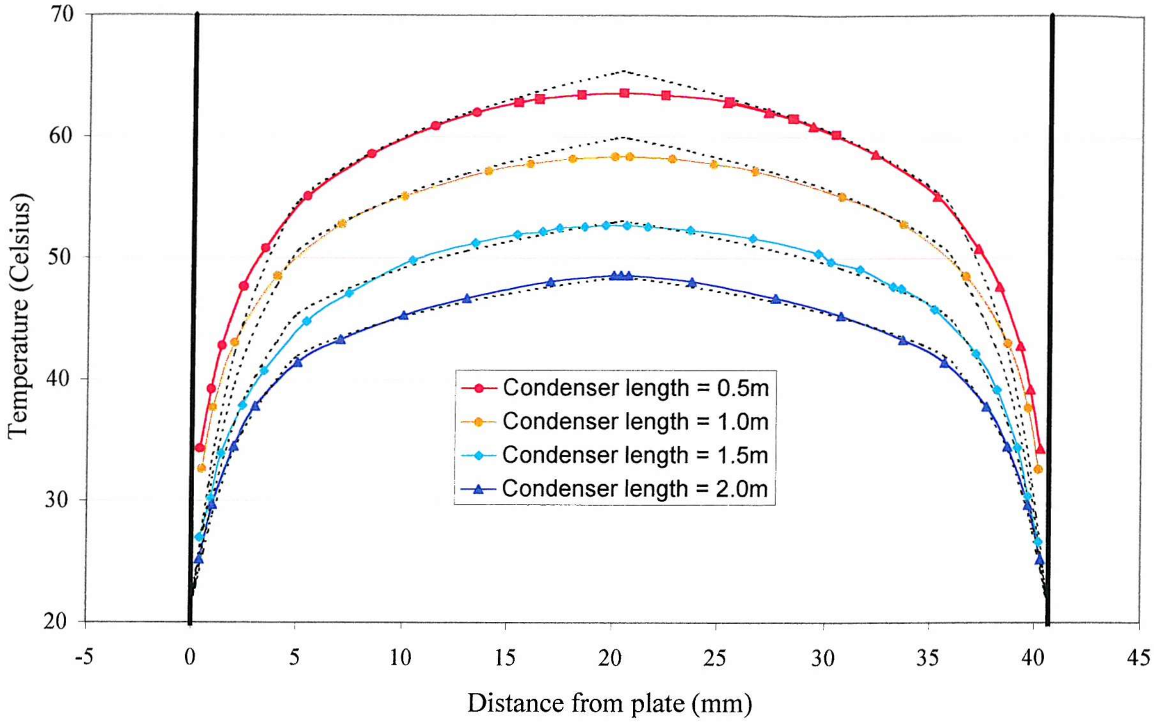

Figure 8-4. Temperature profiles measured between the cold walls at condenser exit and the corresponding universal temperature distributions (dotted lines).

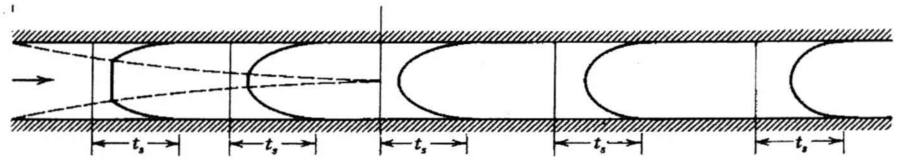

Figure 8-5. Developing and fully developed temperature profiles in pipe flow with constant wall temperature. The arrow indicates the direction of flow and the dotted line represents the thermal boundary layer.

The temperature profiles in Figure 8-4 are not initially perfectly flat at the centre of the duct because some cooling will have occurred in the starting section as it was not perfectly insulated. In addition, the absence of an insulating layer between the end of the starting section and the cold surfaces of the first condenser section will have produced some cooling prior to condenser entry. Otherwise the temperature profiles are as expected.

8.4 *Cross-sectional temperature distribution.*

A two-dimensional picture of the temperature throughout the condenser cross-section, measured at the end of the 2m long condenser is presented in Figure 8-6 below.

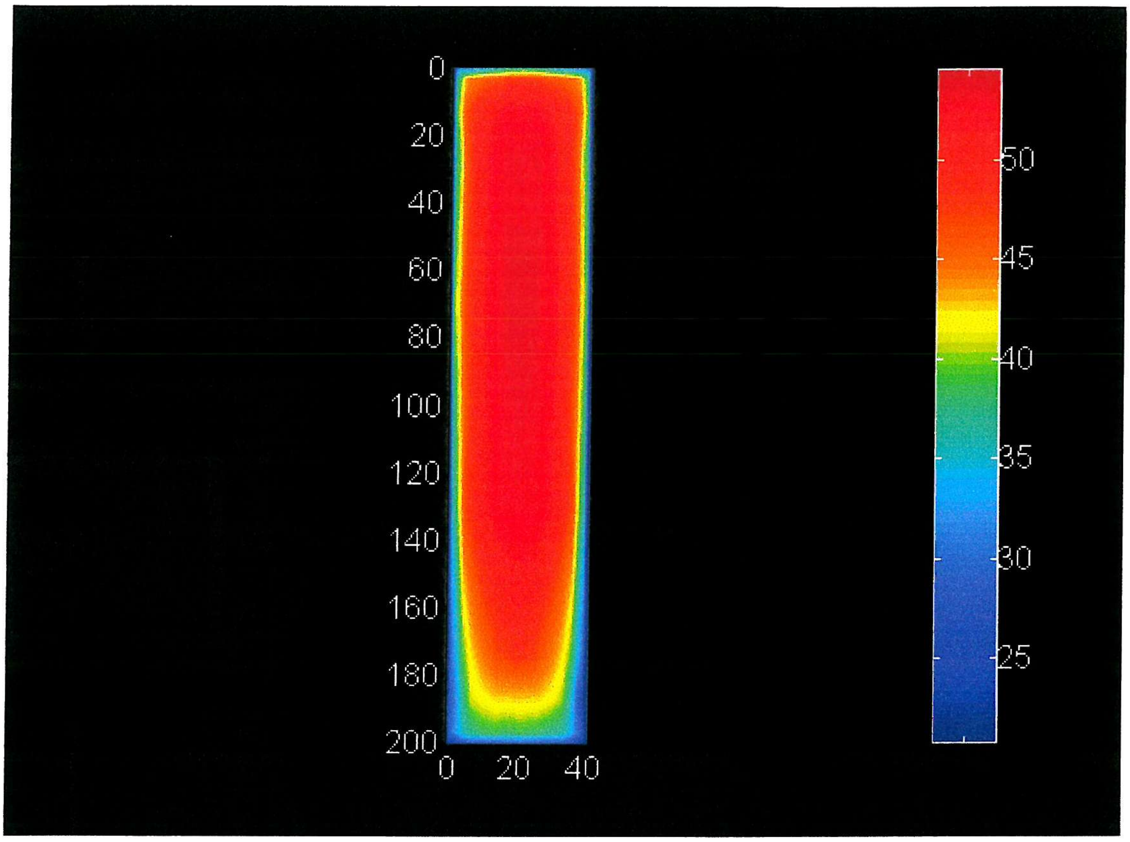

Figure 8-6. Cross-sectional temperature distribution two metres along the condenser

The cold regions at the bottom of the condenser, and near the walls indicate the appearance of a secondary flow driven by density differences within the fluid. This raises the question of whether natural convection effects may be significantly enhancing the rate of heat transfer within the condenser. However, referring to Figure 8-7, taken from the work of Metais and Eckert [57], indicates that this is not the case, since the approximate range of Reynolds numbers is 5000 – 12000 and the product of the Grashoff and Prandtl numbers ranges from

1×10^7 to 4×10^7. Hence the heat transfer is adequately calculated using an empirical correlation for forced convection only.

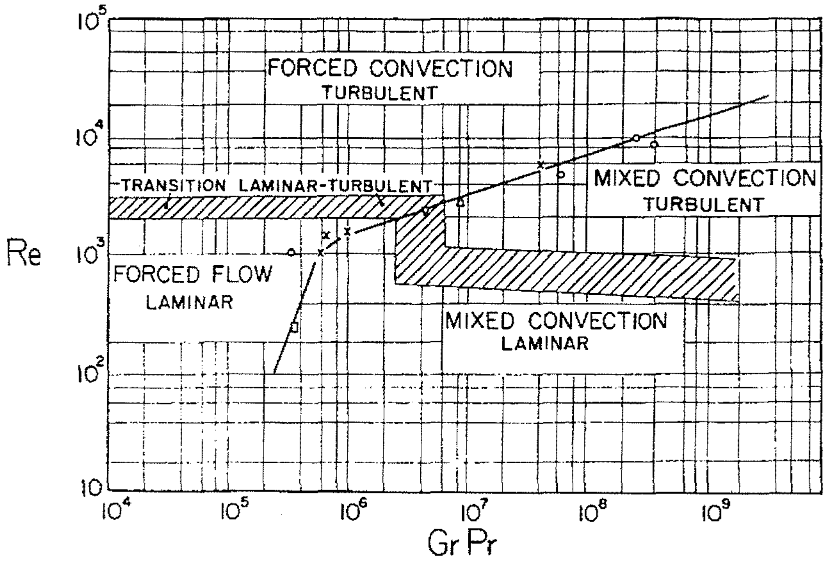

Figure 8-7. Regimes of free, forced and mixed convection for flow through horizontal ducts.

8.5 *Heat transfer coefficient*

The heat transfer coefficient for the 2m long condenser was calculated using equations (8-1) and (8-2) and the experimental temperature measurements plotted in Figure 8-4. The bulk temperatures at the relevant locations were estimated using the methods described in appendix K. This resulted in a condenser heat transfer coefficient of ~ 10 W/m^2 °C. This was in good agreement with the value used to plot the corresponding universal temperature distributions in Figure 8-4.

9. Experimental results, discussion and analysis

9.1 *Introduction*

The experimental results of the present study, obtained using water vapour – air mixtures, are documented in this chapter. The interpretation and discussion of these results is then presented in the following chapter. Initially the visual observations of the experimental program are described, providing an insight into the various stages of fog formation. The effects various parameters, such as initial temperature, vapour pressure, saturation temperature, velocity and condenser length have on the formation of fog are then reported. This focuses in particular on the effects on the droplet size distribution, mean droplet size and droplet concentration.

9.2 *Visual observations*

The experimental rig condenser sections had been designed to allow visual observations of the flow within. This was achieved by incorporating pyrex strips, which ran along the entire condenser length and comprised the base and top of the condenser sections (refer to figure 5-4). However, whenever the experimental conditions were conducive to fog formation, dropwise vapour condensation on the pyrex surfaces made observations impossible. In fact, condensation began on these surfaces only shortly after it did so on the cold walls. Attempts to wipe these surfaces clean proved fruitless, as the drops would immediately reappear. Hence visual observations were generally restricted to those of the fogs exiting the condenser, although when the droplet density was not too great it was also possible to see back into the condenser from the end.

During each experimental run the rig operating procedure was the same (as laid out in section 7.4). As a result the pattern of events observed within the condenser followed a familiar path. At the first sign of steam generation from the boiler, condensation would begin upon the cold condenser walls, closely followed by condensation on the pyrex strips. Over the following 30 minute period the condition of the water vapour – air mixture would slowly approach a steady-state, at which point measurements were taken. In the interim period the steam flow rate would increase, and the temperature would first rise due to the increased steam content of the mixture (the steam being at ~ 110°C), before falling slightly to a steady value due to the reduced heating of the air.

As the steam flow rate increased, so the vapour content and relative humidity of the mixture increased. This resulted in a greater rate of condensation at the walls. As the steam flow rate increased further, a very light fog would begin to appear, exiting the condenser. The visibility of the droplets improved when illuminated from above with a polarised light source. Upon close inspection the droplets were seen to be confined to very thin regions close to the walls (film fog formation), near the bottom of the condenser. As the steam flow rate increased so the droplet containing region rapidly extended up the walls of the condenser, though the flow varied considerably from one moment to the next during this period. Within the condenser the droplets appeared to be rolling along the walls.

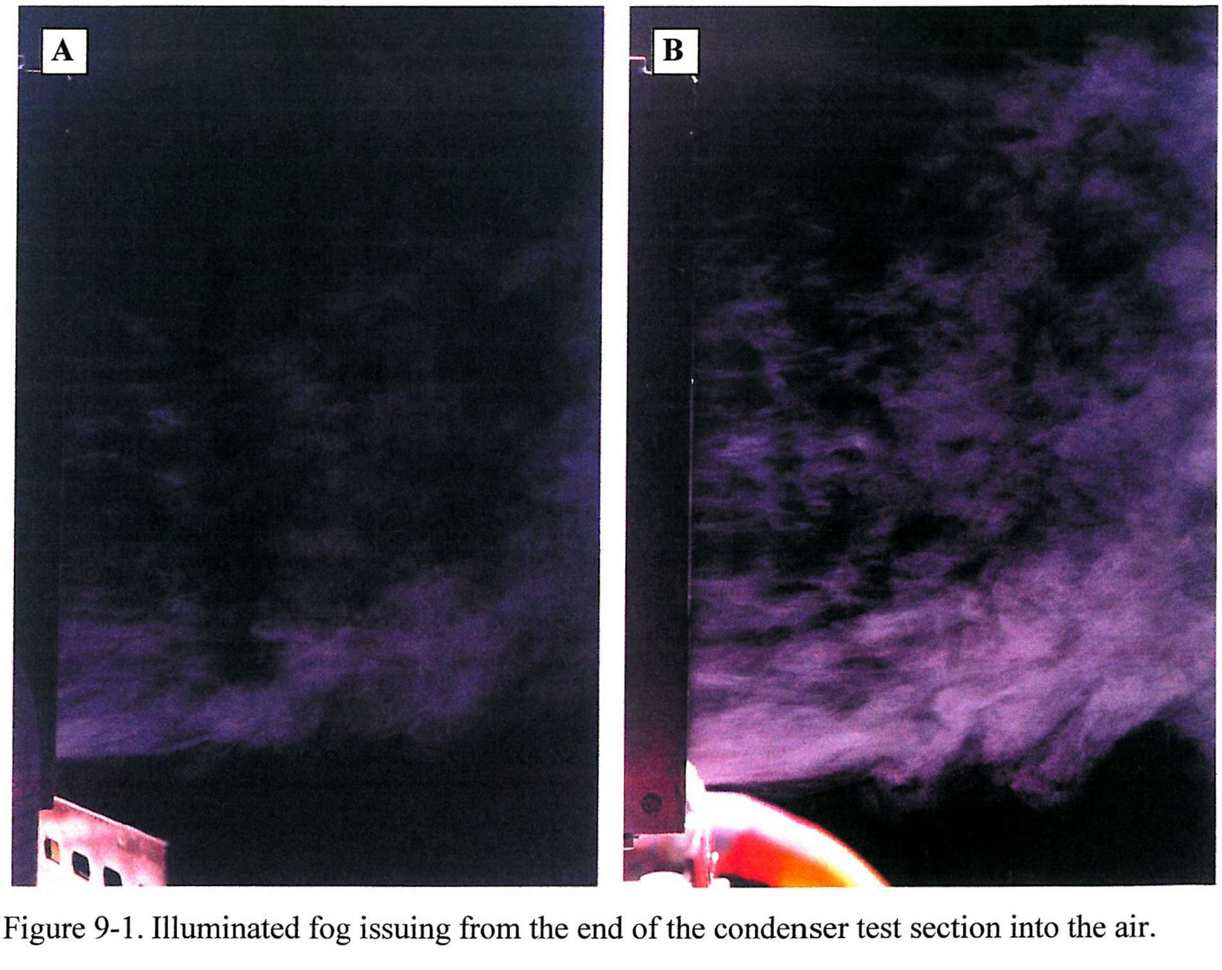

Figure 9-1. Illuminated fog issuing from the end of the condenser test section into the air.

If the final mixture condition was reasonably close to saturation, the droplet containing region would then begin to spread inwards, towards the centre of the condenser, as the steam flow rate increased further. This would be accompanied by a notable increase in the overall fog density, though the fog would remain at its most dense near the bottom of the condenser, as pictured in Figure 9-1.

The light scattered by the droplets in Figure 9-1 made them easier to see. This light scattering was employed by the droplet-sizing systems and was even more clearly visible from the associated lasers. This provided a good indication of the fog densities. Two such examples are pictured in Figure 9-2, where the laser beams are directed across the end of the condenser, as positioned during measurements.

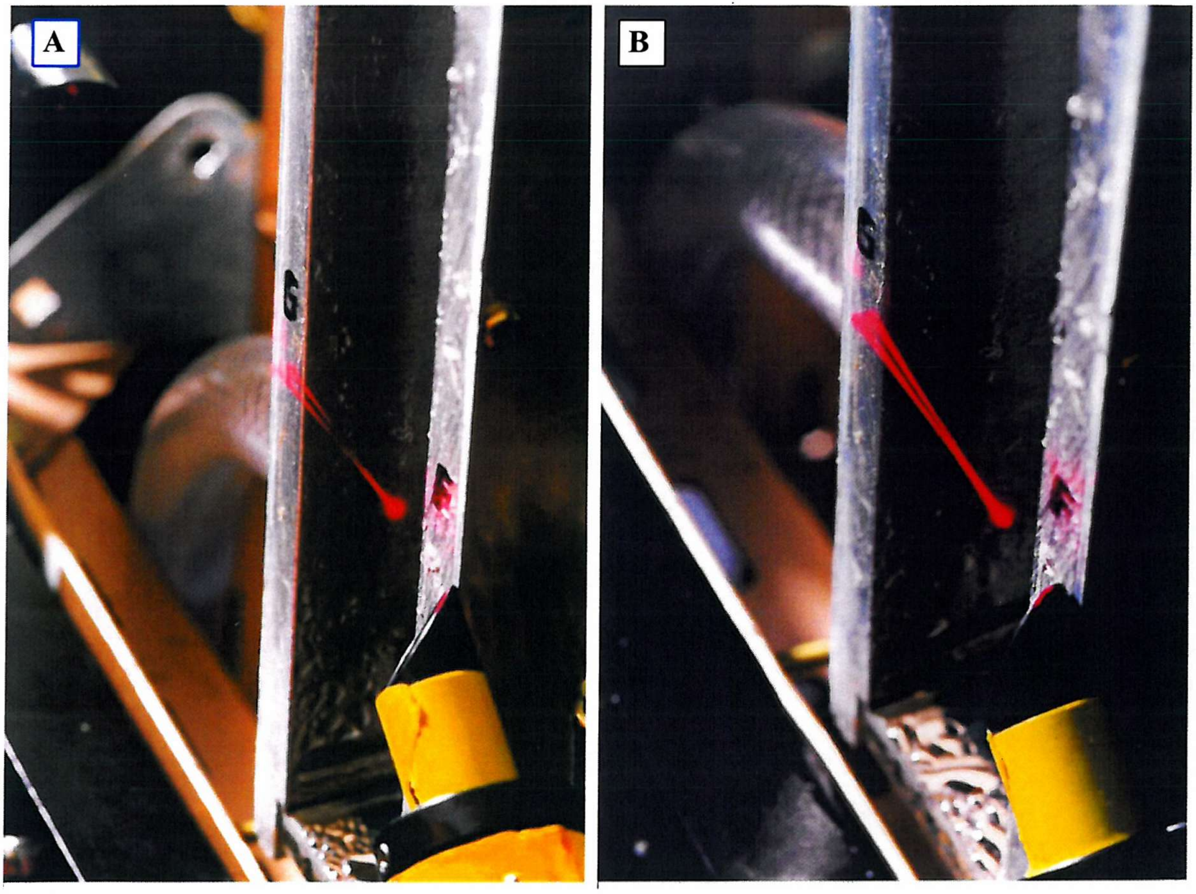

Figure 9-2. Using the PDPA laser beam to highlight the region containing liquid droplets, off which the beam is scattered.

In the first picture, Figure 9-2A the droplet density is clearly greatest near the cold walls and falls off rapidly towards the centre of the condenser, where hardly any droplets are seen. In the second picture, Figure 9-2B obtained using a water vapour-air mixture of high humidity, the beams (and therefore droplets) are clearly visible from one condenser wall to the other. Again the beams are at their brightest in the region near the walls. These pictures support the observations made with the naked eye.

9.1 *Entrainment*

The most important experimental data was collected using the droplet-sizing equipment. Two such devices were used, both of which contained a powerful laser beam source and a receiver lens for collecting the light scattered by the droplets. This receiver had to be placed at an angle of 30° to the incident beams, hence it was necessary to locate the equipment slightly downstream of the condenser exit plane. In general the measurement plane was situated 10mm downstream of the end of the condenser, this being as close as possible to the condenser while preventing the laser beams reflecting off the metallic condenser walls. The most frequently used measurement location is pictured in Figure 9-3.

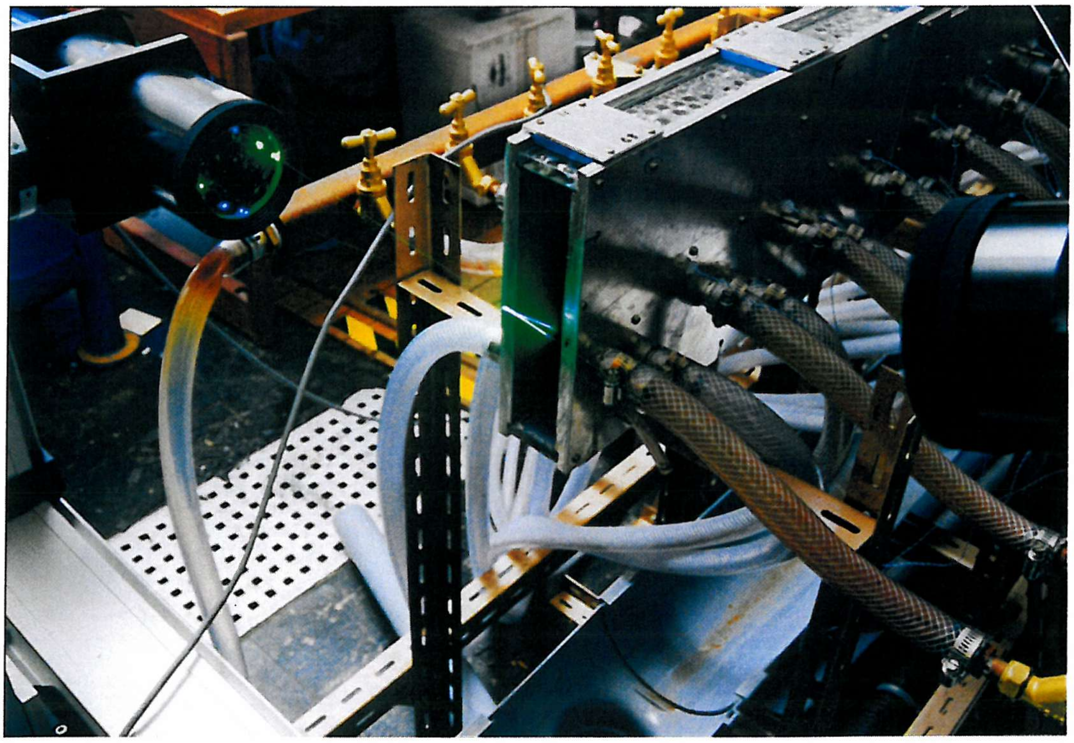

Figure 9-3. Droplet-sizing using the LDA.

Because measurements had to be performed outside the condenser it was necessary to account for any resulting changes in the mixture and suspended droplets. The flow of mixture from the end of the condenser was effectively the issuing of a turbulent jet into a stagnant body of gas, and as such was expected to lead to some entrainment of the surrounding air. Hence a series of six experiments were performed to investigate any changes in the measurements obtained at different downstream locations. The results are plotted in figures 9-4, 9-5 and 9-7 below.

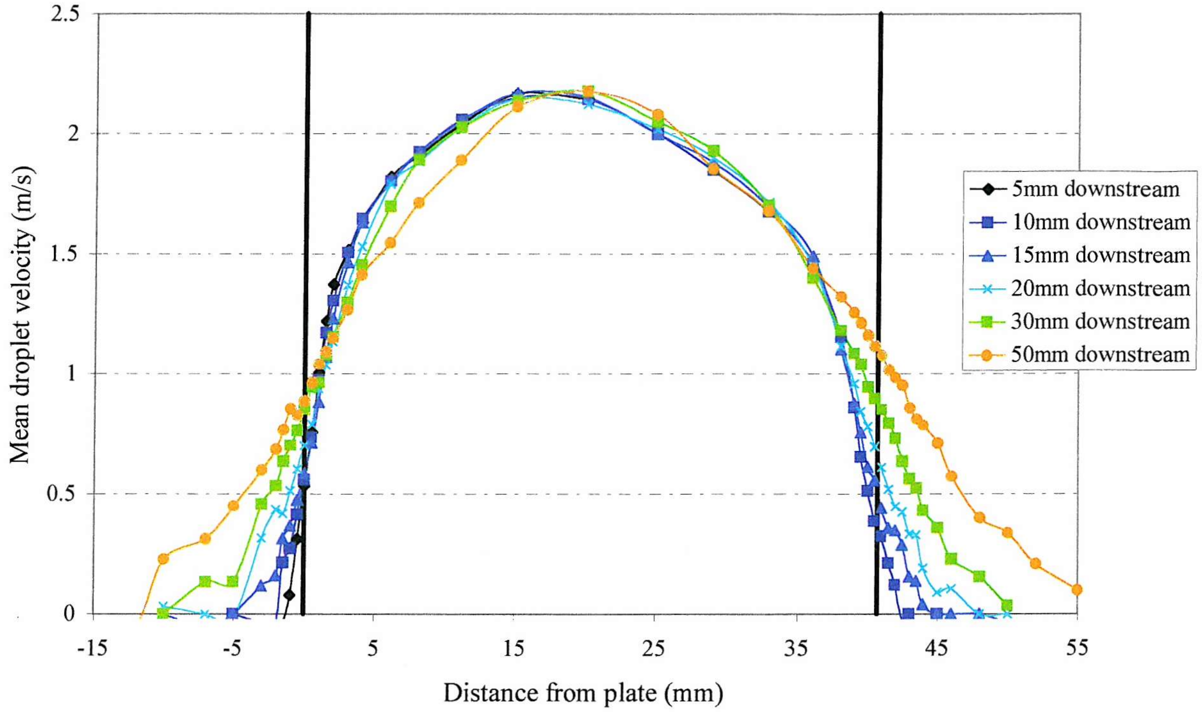

Figure 9-4. Lateral velocity profiles obtained downstream of the condenser exit plane.

In Figure 9-4 the changes in the lateral velocity profile of the mixture with distance from the end of the condenser are displayed. [Note that the dark vertical lines correspond to the location of the condenser walls.] The velocity profile immediately extends out past the condenser walls as some of the surrounding air is effectively dragged along with the mixture. This also affects the mixture within the central 0.04m of the jet, corresponding to the region originally within the condenser walls, and is more clearly demonstrated in Figure 9-5, where the downstream measurement location was extended.

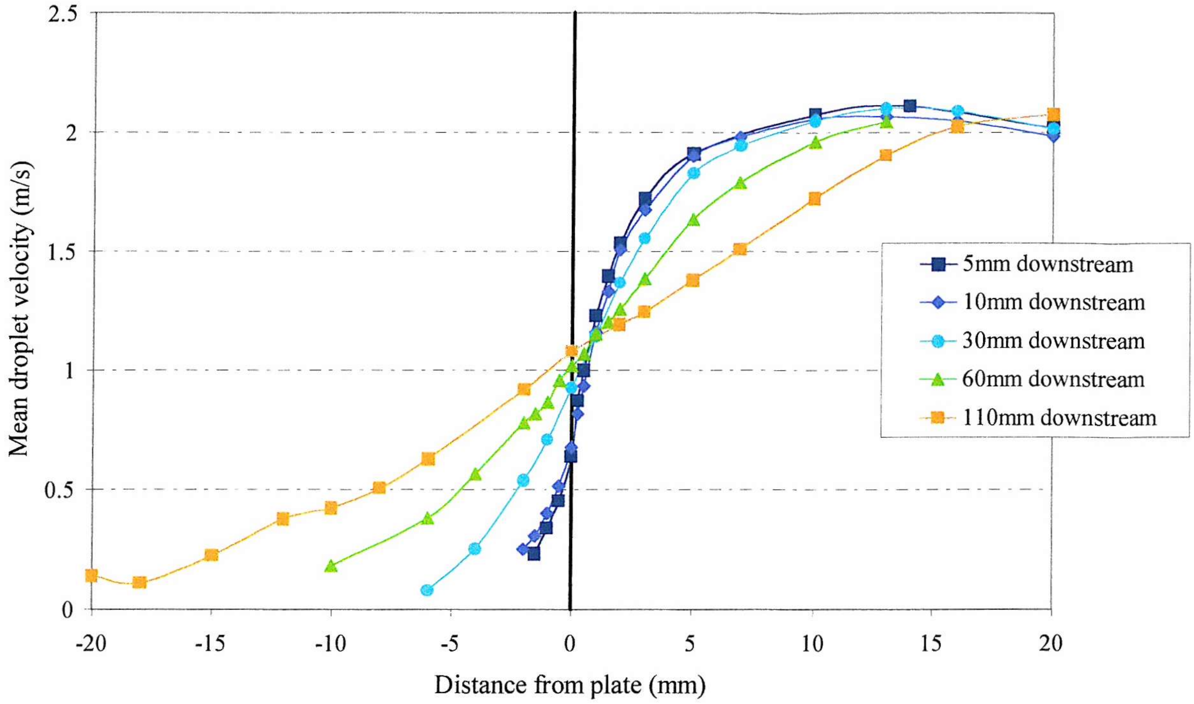

Figure 9-5. Lateral velocity profiles extending further downstream of the condenser exit plane, in the region of the condenser wall.

Thus the increase in the velocity outside the plane of the condenser walls is accompanied by a decrease in velocity on the other side, as would be expected, and is a result of the turbulent mixing which occurs. The region affected clearly increases with distance from the condenser. The region of entrainment actually extends linearly away from the condenser walls, the further downstream, the wider the entrainment region becomes, as illustrated in Figure 9-6.

The consequences of the turbulent mixing upon the mean droplet diameters measured downstream of the condenser are presented in Figure 9-7. The droplet containing region extends out beyond the plane of the condenser walls, due to the eddy motion within the fluid. However, there is also a decrease in the mean size of the droplets within the entrainment region. So either the droplets in this region are partially evaporating, or new droplets are forming which are smaller than those exiting the condenser. The answer was found by studying the changes to a droplet size distribution that was initially devoid of small droplets.

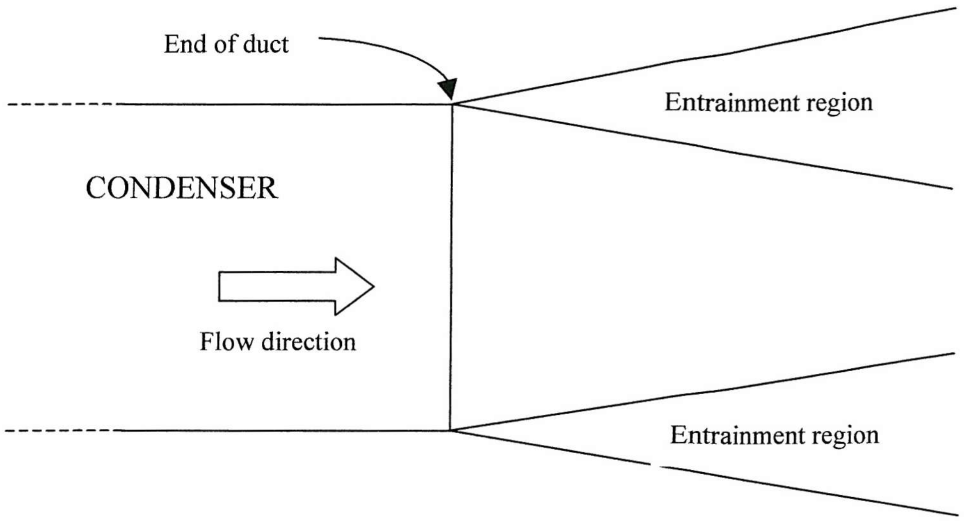

Figure 9-6. Plan view of the region of entrainment.

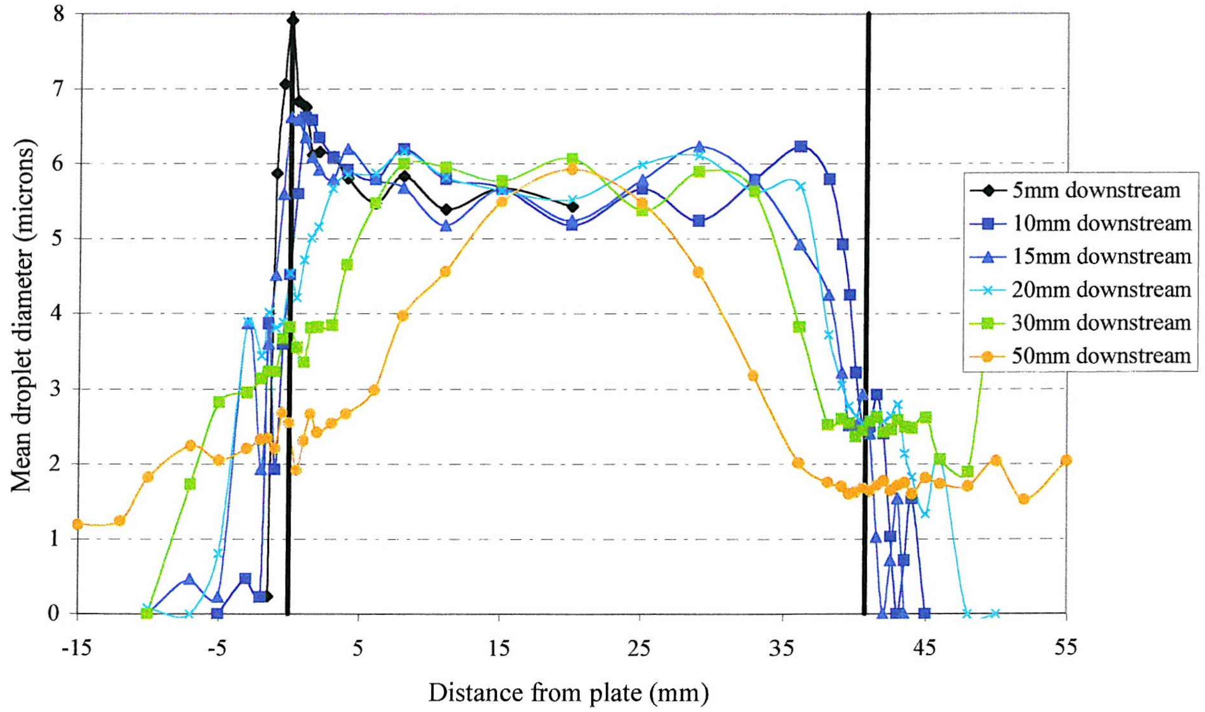

Figure 9-7. Mean droplet size measurements obtained with the LDA at a number of locations downstream of the condenser.

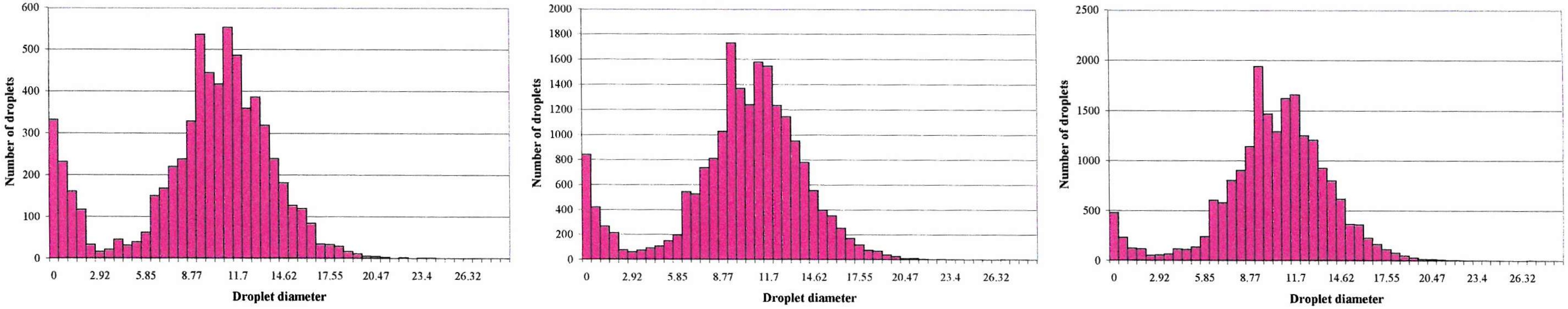

Droplet size distribution: 0.5mm outside the duct

in line with the cold wall

1.0mm from the cold wall

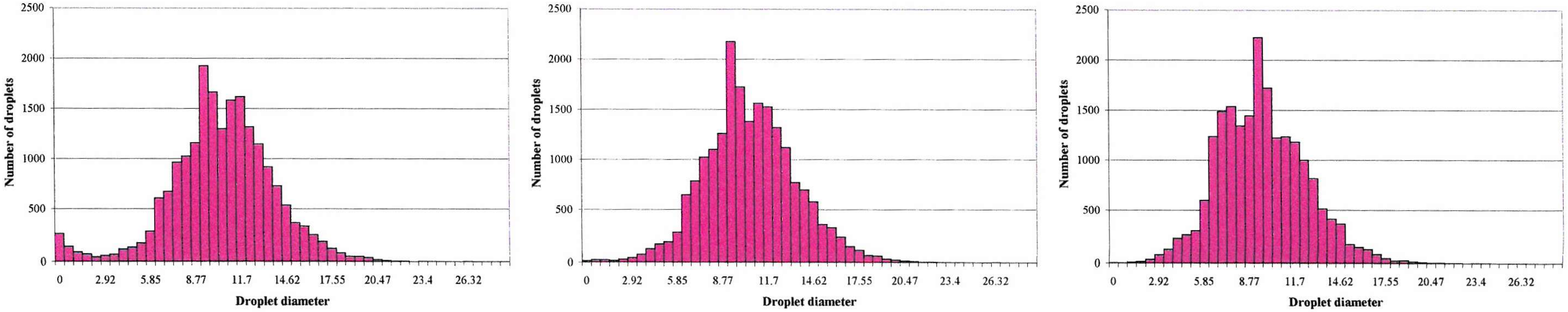

1.5mm from the cold wall

3mm from the cold wall

and 16mm from the cold wall

Figure 9-8. Droplet size distributions obtained at various lateral positions, all 10mm downstream of the condenser exit plane. Mixture conditions: Initial steam to air flow rate of 0.153, mean velocity of approximately 3m/s, and bulk temperature ~ 56.5°C (i.e. supersaturated since the saturation temperature is 60°C at this steam to air flow rate).

The droplet size distributions presented in Figure 9-8 clearly show that within the region of entrainment, where the saturated mixture within the duct merges with the cool air from outside, a number of new, very small, droplets are formed. These are almost solely responsible for the observed decrease in the mean droplet size, since there appears to be very little change in the spectra of the larger drops. The results presented in Figure 9-8 were collected when the ambient air temperature was approximately 22°C, and the moisture content was high as a result of the build up of water vapour in the laboratory during the test. Hence, mixture of the two streams resulted in a supersaturated mixture of intermediate temperature, from which vapour immediately condensed. This gave rise to the appearance of small droplets, accompanied by a very slight increase in the size of the large drops already present. It is probable that the new droplets that form in the region of entrainment are nucleating upon dry soluble nuclei that were initially outside the condenser. This is because droplets have already formed upon the nuclei with the smallest critical supersaturation levels that were inside the condenser. Indeed, in the example presented in Figure 9-8 the saturation temperature was 60°C and the actual bulk temperature was ~ 56.5°C, resulting in an initial supersaturation of the mixture of approximately 18%. This was the maximum supersaturation, $S_{\max}$, inside the test rig during this experiment, as immediate copious fog formation acts to reduce the supersaturation, leading to experimentally measured droplet number concentrations of ~ 40,000 per cubic centimetre. The air outside the condenser therefore contained a very large number of nuclei with critical supersaturations below those of any remaining dry nuclei exiting the condenser, and these nuclei are the most susceptible to droplet formation. If the supersaturation produced by the mixing was sufficiently great however, i.e. greater than the maximum supersaturation reached inside the test rig, $S_{\max}$, new droplet formation may also have occurred on nuclei that were inside the condenser.

If this were the case, it may be expected that the total number of new droplets forming would be fairly significant. In line with the condenser wall, the ratio of the new mixture formed from the air outside the condenser to that from inside may be assumed to be approximately 50:50. It is also assumed that the supersaturation spectra for the two bodies of gas, i.e. the graphs of number of activated nuclei against supersaturation (as in figure 2-8 on p.27), are of approximately the same form (at condenser exit, t_b ~45°C, and > 90% of the mixture by mass is air). Hence it may be expected that in line with the condenser wall the number of new droplets formed would have to be greater than the number already present to indicate droplet formation upon previously dry nuclei from within the condenser. Referring to the three droplet size distributions obtained nearest the wall in Figure 9-8, it is clear that this is not the case. The number of new droplets ($\leq$ 3μm in diameter) is very much smaller than the number ($\geq$ 3μm) exiting the condenser. Hence it is inferred that the new droplet formation in the region of entrainment takes place solely on nuclei previously resident in the air outside the condenser.

In summary, since the majority of LDA measurements were taken 10mm downstream of the condenser exit plane, entrainment of the surrounding air is likely to have affected only those results obtained near the wall. Results obtained $\geq$ 3mm from the wall are unlikely to have been affected, see Figure 9-8. Hence when comparing droplet size distributions obtained under different experimental conditions, measurements 5mm from the wall are generally used to exclude any entrainment effects from the results.

9.4 *Effect of temperature*

The importance of the bulk mixture temperature at the condenser entry upon fog formation was studied using mixtures of a fixed steam to air mass flow rate. The bulk temperature was adjusted by varying the rate of heat flow to the air prior to mixing. This allowed experiments to be conducted at a number of temperatures giving rise to both wet and superheated mixtures at a set mass flow ratio of steam to air. By repeating this set of experiments at a number of different ratios it was intended that the results could also be used to study the importance of the mixtures saturation temperature, in addition to substantiating the data from the initial test set. The flow ratios chosen for study were those corresponding to saturated steam-air mixtures flowing through the test rig with an initial velocity of 2m/s and bulk temperatures at condenser entry of 50, 60, 70 and 80°C. This range was essentially the largest it was possible to produce and accurately measure with the test rig facility. The entire set of mixtures studied during the investigation into bulk temperature effects is presented graphically in Figure 9-9.

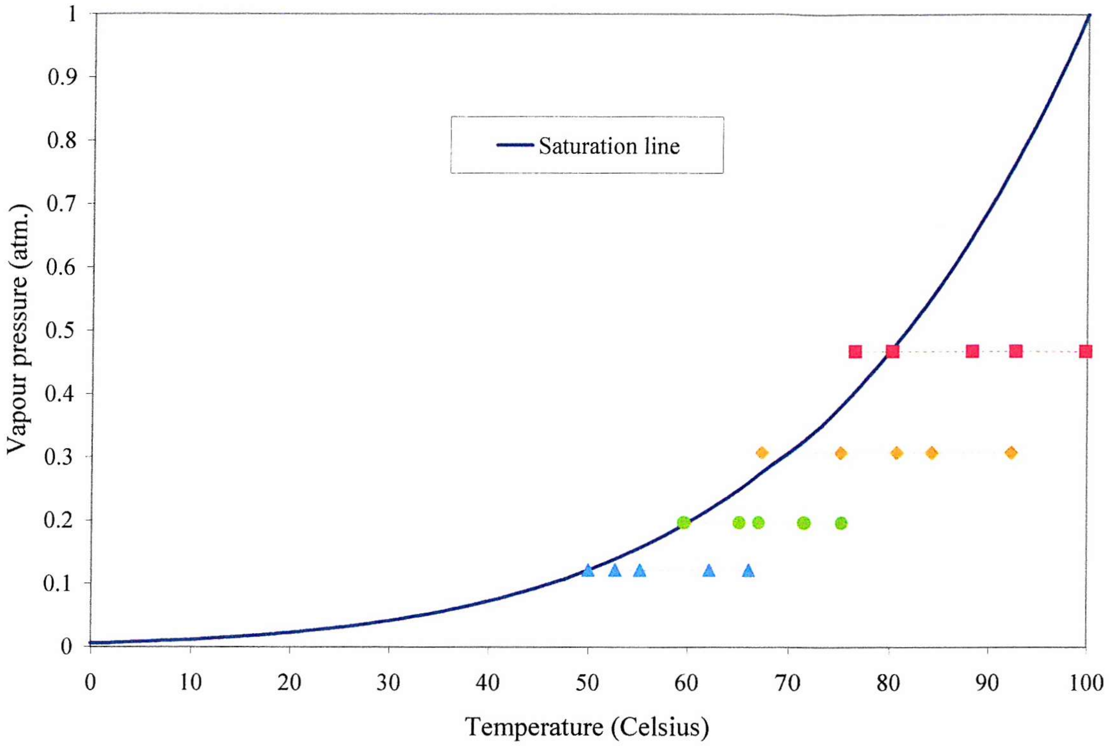

Figure 9-9. Condition of mixtures used to study bulk temperature effects.

The results of the four different tests were in good agreement, hence initially only one set, that of the mixtures formed using a steam to air mass flow ratio of 0.552 will be presented in detail here. The bulk saturation temperature for these mixtures was 80°C, and the condition of the five mixtures studied at condenser entry is marked by the red squares in Figure 9-9. Note that droplet formation will have occurred within the one mixture that lies in the supersaturated region of the graph as soon as the air and steam mixed, well upstream of the condenser.

The droplet size distributions measured when conducting experiments with the five different mixtures are presented in Figure 9-10, and the corresponding volume size distributions are presented in Figure 9-11. In each case the measurements were made 10mm downstream of the condenser exit plane, and 5mm in from the wall, in order to escape any effects due to entrainment. The droplets were measured over a 120 second time interval, during which time the flow rates were constant and the thermocouple temperature measurements fluctuated slightly due to the turbulent nature of the flow.

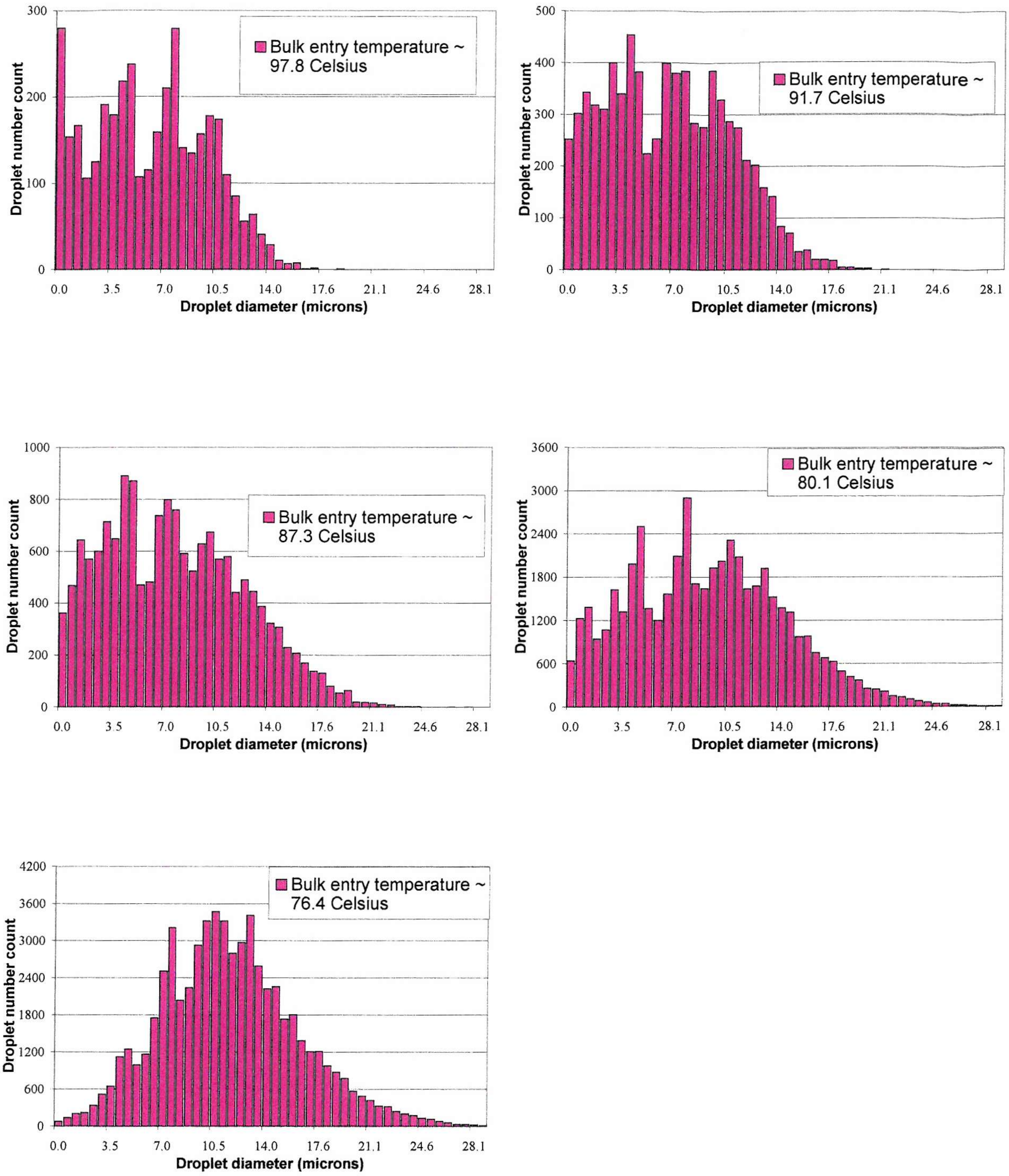

Figure 9-10. Volume size distributions obtained using mixtures produced with an initial steam to air mass flow ratio of 0.552 (saturation temperature = 80^{o}C) and bulk temperatures as indicated in the charts.

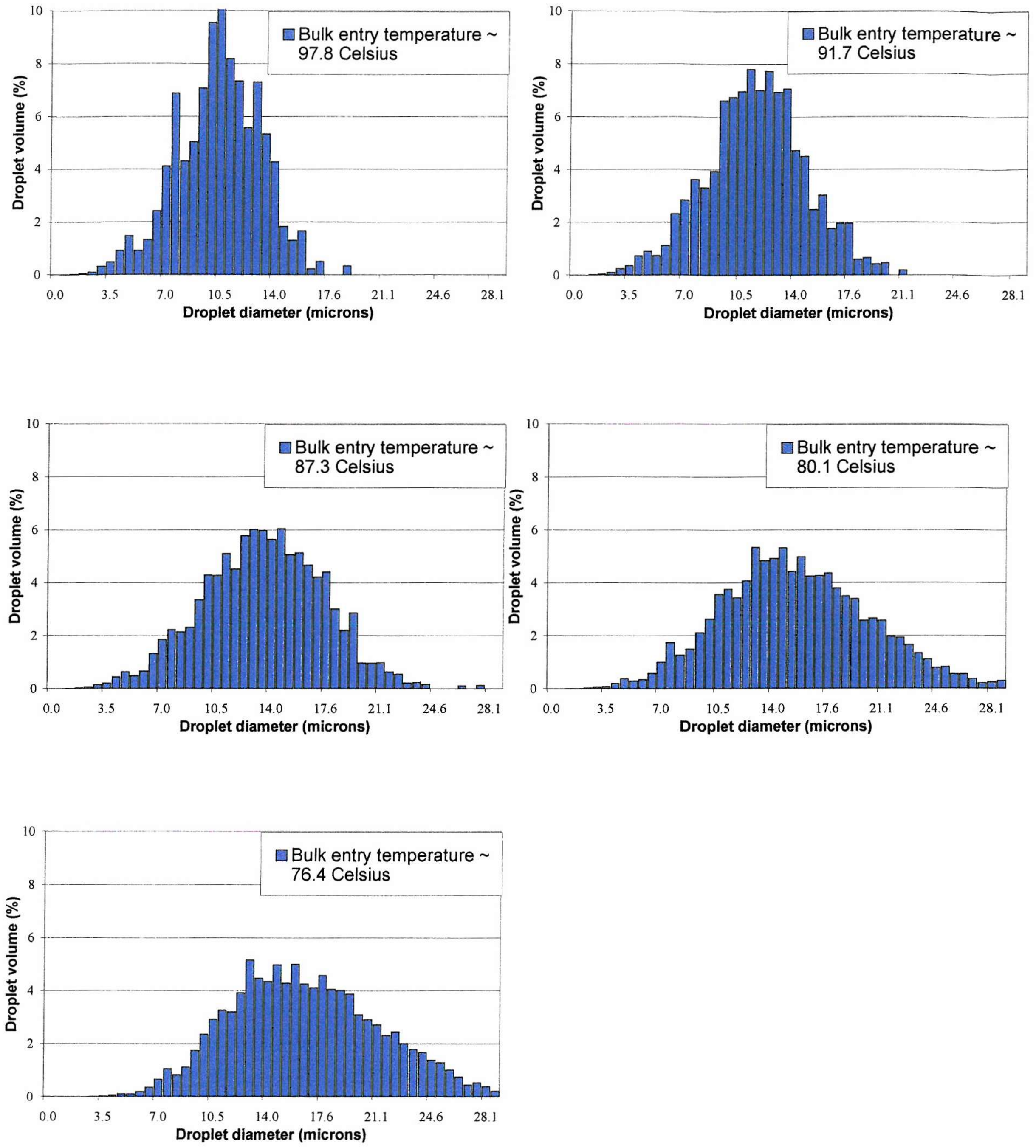

Figure 9-11. Volume size distributions obtained using mixtures produced with an initial steam to air mass flow ratio of 0.552 (saturation temperature = 80°C) and bulk temperatures as indicated in the charts.

As the bulk entry temperature of the mixture falls, the total number of droplets increases, as indicated by the scales on the droplet size distribution graphs, Figure 9-10. At the same time the droplet size distribution extends to greater droplet sizes. The number of droplets measured in the smallest size ranges also increases. However, the percentage of droplets in the smallest size ranges consistently decreases with the initial bulk temperature. In the one case where droplets are expected to already exist at condenser entry (bulk temperature = 76.4°C), the number of the smallest droplets is extremely small.

The percentage of very small droplets as a proportion of the total fog volume (or mass), is far smaller, as demonstrated by the accompanying volume size distributions of Figure 9-11. Because of the cubed relationship between droplet diameter and volume, the smallest droplets almost fail to register on the volume size distribution, even at the greatest bulk temperatures. The shift in the distributions towards larger droplet sizes is even more marked. The vast majority of the total mass of fog exists in the form of droplets greater than 7 microns in diameter in all cases.

The droplet size and volume distributions produced during experimentation with mixtures of saturation temperature 80°C, presented in Figure 9-10 and Figure 9-11 respectively, demonstrate clearly the effect of increasing initial temperature (and decreasing relative humidity). The smallest droplets are of the greatest concern due to the difficulty associated with their recovery from the gas – vapour stream (section 1.3). As noted above, the number of the smallest droplets as a proportion of the total droplet count increases with temperature. Though the total droplet count decreases with temperature, the greatest initial bulk temperature considered, 99.8°C, still resulted in a considerable number of droplets. Therefore, though in previous results the mass of the smallest droplets has been negligible, there remains the possibility of the total mass of droplets below 1μm in diameter becoming significant at higher temperatures. Hence it is instructive to present the distributions obtained using mixtures with saturation temperatures at condenser entry of 50°C also. The number and corresponding volume size distributions are presented for the four highest bulk temperature mixtures studied in Figure 9-12.

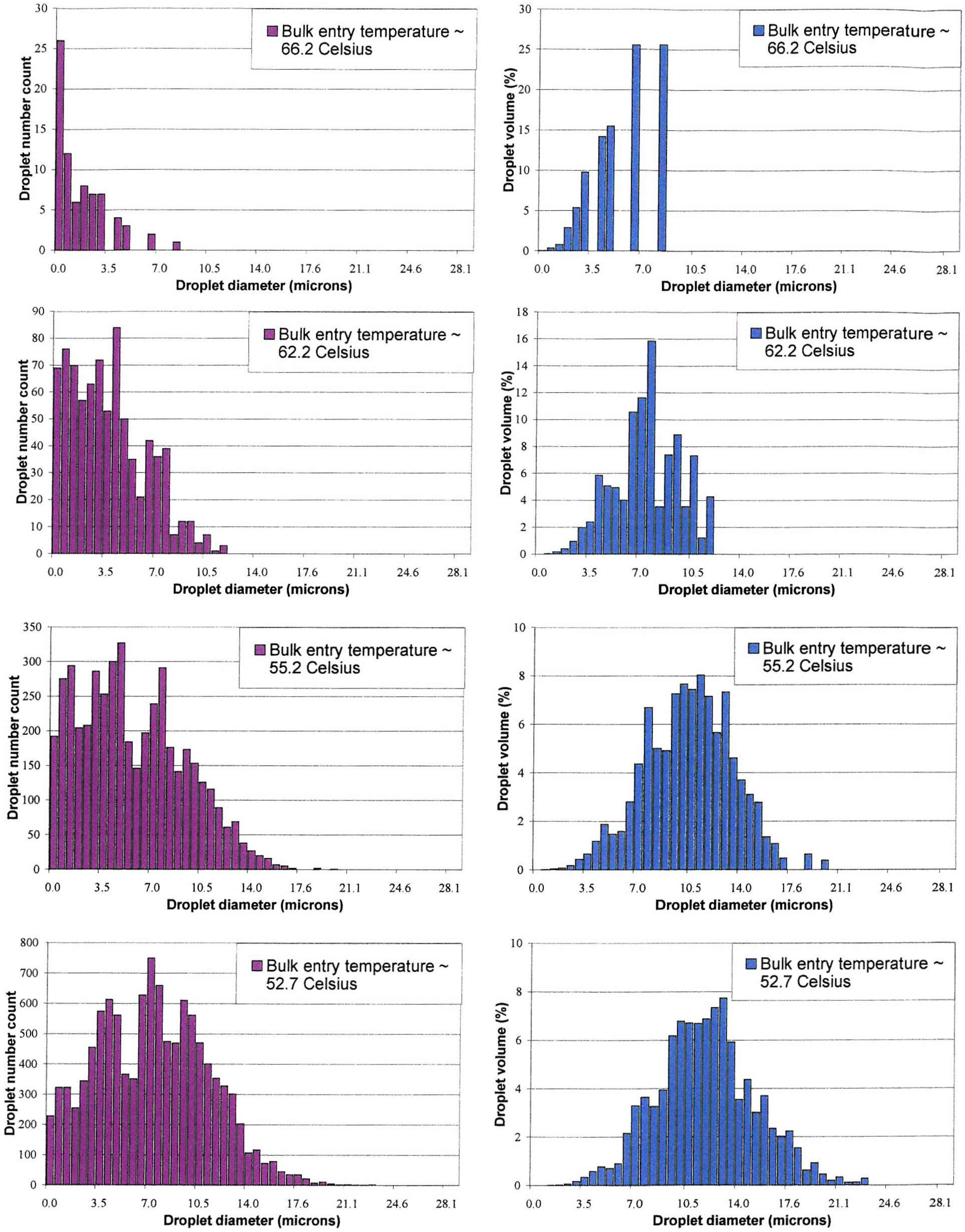

Figure 9-11. Number and volume size distributions obtained using mixtures produced with an initial steam to air mass flow ratio of 0.0866 (saturation temperature = 50°C).

The general form of the results presented in Figure 9-12 is in good agreement with those presented for the mixtures with saturation temperature 80°C, in the two previous figures. The highest temperature results presented, i.e. 66.2°C do indicate that when the bulk mixture is sufficiently superheated at condenser entry, the majority of droplets exiting the condenser are $< 1\,\mu\text{m}$ in diameter. However, their small size ensures that the mass (or volume) of these droplets is still only a very small fraction of the total droplet mass. The total number of droplets detected, indicated on the scale of the number distributions, is also important. Only 76 droplets were detected in a 120 second interval, equating to 15 droplets per cubic centimetre, or 2.5×10^{-7} m^3 of fog for every cubic metre of gas-phase mixture. This is less than 0.03% by mass, and it should be recalled (refer back to the volume distribution of Figure 9-12) that very little of this mass resides within droplets $< 1\,\mu\text{m}$ in diameter.

It is clear that at higher temperatures the number of droplets would have been even smaller, while at lower temperatures the fraction of submicron droplets falls rapidly. Hence it may be concluded that the total mass of submicron droplets forming within the test rig from mixtures with saturation temperature 50°C, entering the condenser at any temperature, would have been negligible. The droplet size and volume distributions obtained using mixtures with initial saturation temperature of 80°C (and indeed 60 and 70°C) indicate this is true for water vapour - air mixtures with a wide range of bulk vapour pressures. However, these conclusions are only valid under the experimental conditions observed. In fact, they are also only valid at one location within the condenser, approximately 5mm from the cold wall, where the droplet distributions in Figure 9-10, Figure 9-11 and Figure 9-12 were measured.

9.4.1 Changes in average droplet measurements with distance from the wall

Droplet size distributions at a number of distances from the condenser walls were presented for an initially supersaturated mixture in Figure 9-8. In the case studied, the droplet size distributions measured 5mm from the condenser wall were indicative of those across the entire condenser cross-section, outside the region of entrainment. To assess if this is true in general, during each experimental run the droplets were measured at a series of points between the condenser walls. This produced a vast amount of data, thus to simplify matters and to identify areas for further study, average measurement values were plotted against lateral position. Returning to the mixtures of saturation temperature 80°C, the average droplet size and the droplet number concentration measured at each location, for each mixture, are plotted in Figure 9-13.

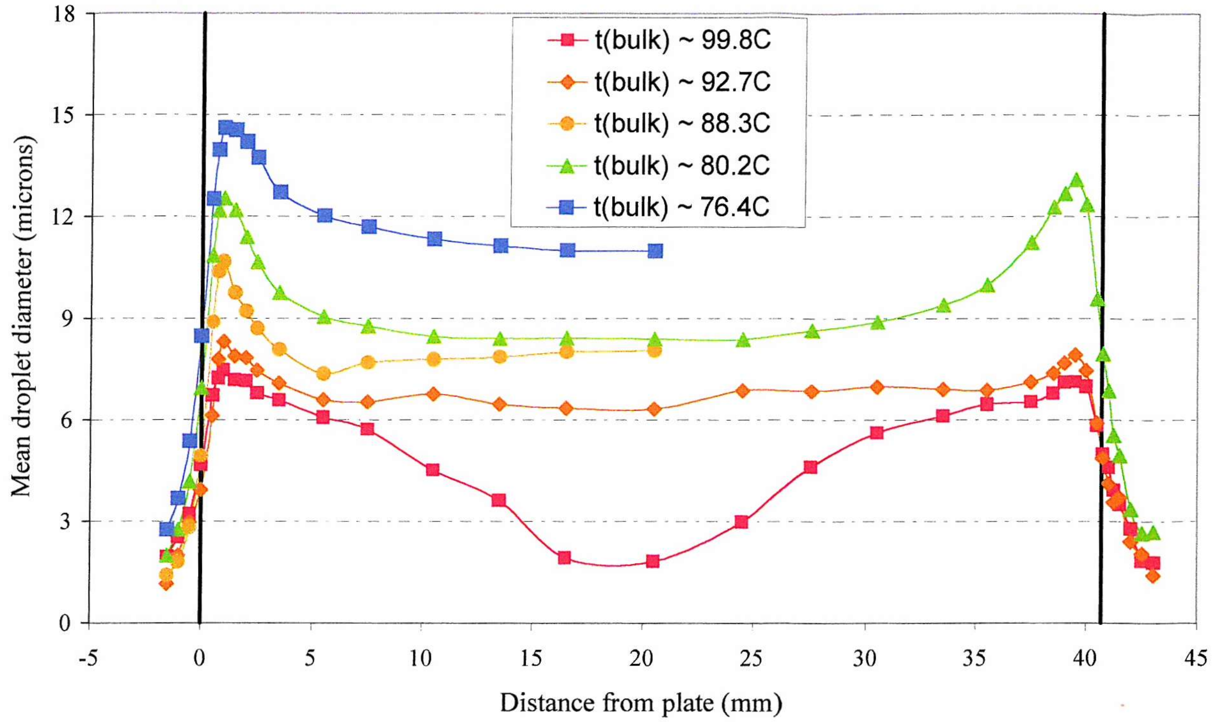

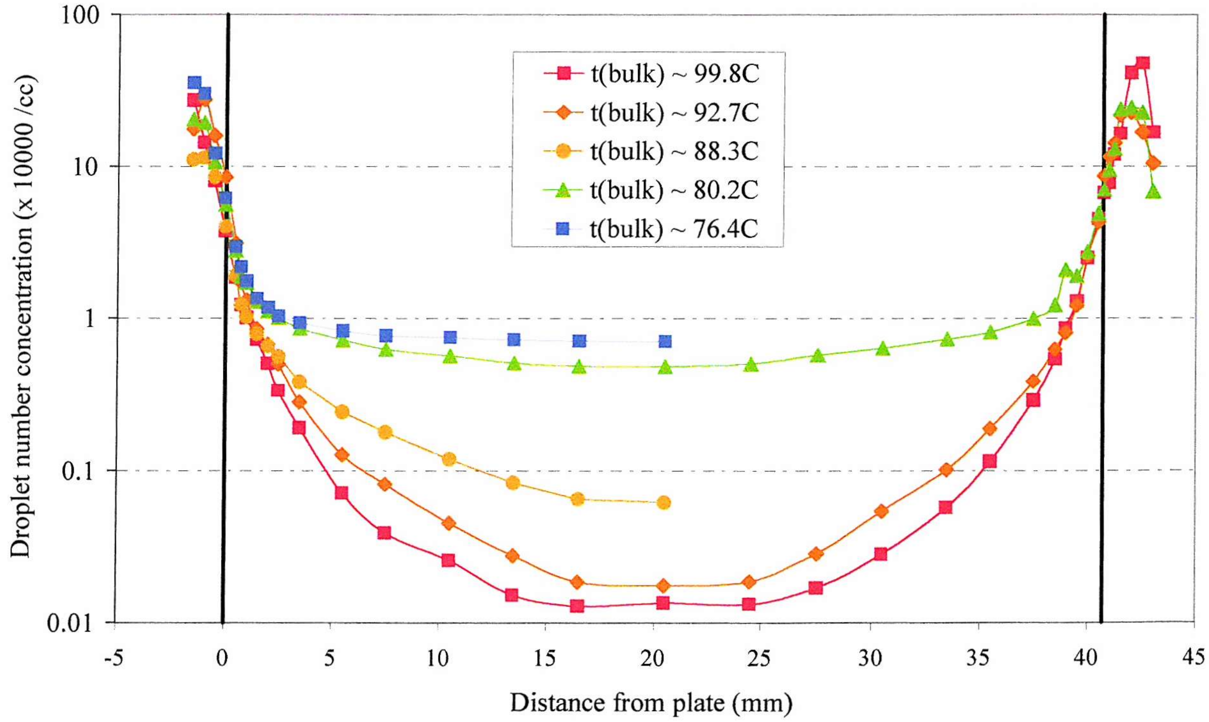

Figure 9-13. Mean droplet size and number concentration data obtained at numerous lateral locations using water vapour – air mixtures produced with an initial steam to air mass flow ratio of 0.552 (saturation temperature = 80°C) and bulk temperatures as indicated in the charts.

This demonstrates that not only do the droplet sizes and number concentrations measured 5mm in from the duct wall increase as the initial mixture temperature is reduced, but this is also true right across the condenser. It follows that the fog flow rates should also increase as the bulk temperature decreases, and this is shown to be the case in Figure 9-14. Again, the results obtained using mixtures of all four water vapour to air mass flow rates demonstrated the same behaviour as that illustrated in Figure 9-13 and Figure 9-14.

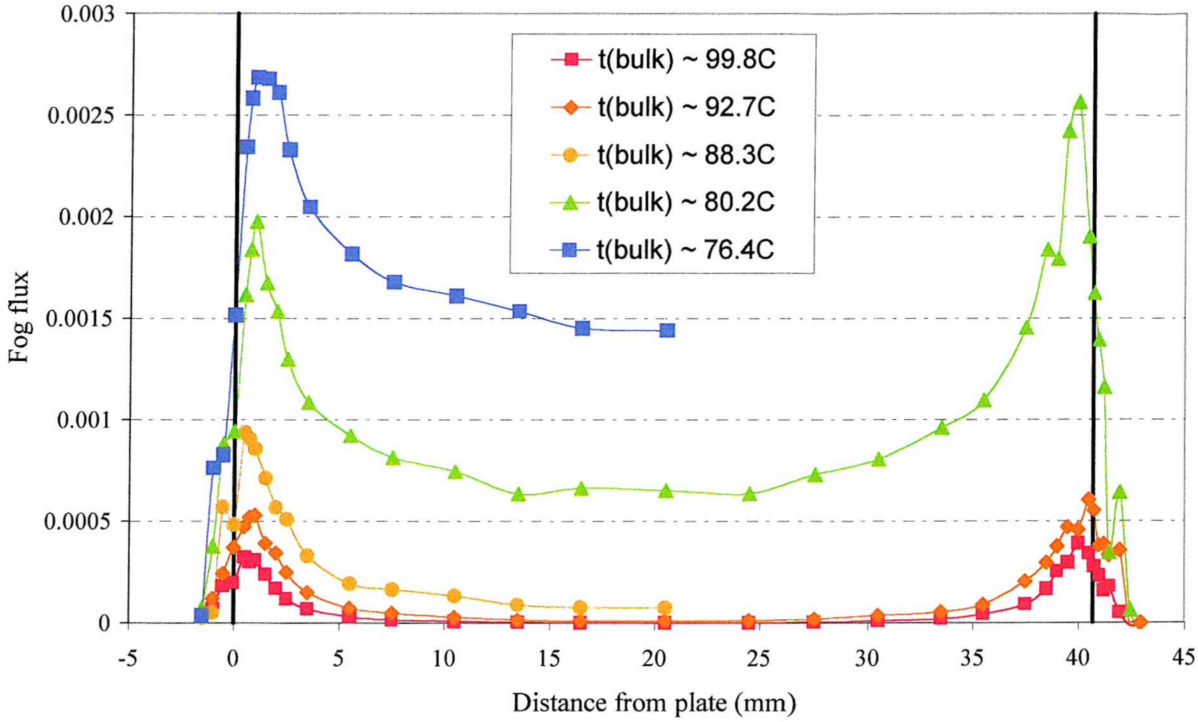

Figure 9-14. Fog fluxes measured during experiments with mixtures produced with an initial steam to air mass flow ratio of 0.552 (saturation temperature = 80°C) and bulk temperatures as indicated in the charts.

The measured fog fluxes of Figure 9-14 concur with the visual observations of the fog described in section 9.2. In the highest temperature mixtures studied the fog appeared to be confined to a relatively thin region near the condenser walls. When the bulk mixture condenser entry temperature is reduced, the fog becomes denser and the region containing fog spreads. As the temperature is reduced further, the fog spreads throughout the condenser and the density of the fog continues to increase. Ignoring entrainment effects, the fog flux remains at its greatest near the cold walls, despite the fact that the velocity of the mixture increases with distance from the wall.

Fog formation is driven by supersaturation of the gas – vapour mixture. The number of stable droplets formed is primarily determined by the maximum supersaturation, $S_{\max}\left[=\left(p_v/p_g\right)_{\max}\right]$. The rate of droplet growth is governed by the difference in vapour pressure between the droplet surface and the surrounding mixture, $p_{v,a}-p_{v,\infty}$, (equation 2-35). Both of these quantities increase as the cold wall is approached due to the form of the radial temperature and vapour pressure profiles. These profiles were discussed for bulk superheated mixtures in sections 3.4 and 3.5. The mean droplet sizes and concentrations are therefore expected to decrease with distance from the wall. The one exception is the droplet number concentration of mixtures that are supersaturated on formation. If the initial supersaturation is greater than the maximum produced inside the condenser, this will determine the droplet number concentration and if there is adequate mixing, the droplet concentrations would be expected to be constant with distance from the condenser wall. Referring to Figure 9-13, while the variation of droplet concentration with distance from the wall is much less pronounced in the supersaturated mixture (76.4°C initial bulk temperature, S~18%), the droplet concentration still increases towards the wall. This increase is probably due to droplets being carried towards the wall with the Stefan flow, and may also be caused by thermophoresis [60].

9.4.2 Changes in the droplet size distribution with distance from the wall

From the results presented in figures 9-13 and 9-14, it appears that the droplet size distributions obtained 5mm from the condenser wall and presented in Figure 9-10 and Figure 9-12, may only accurately reflect the droplet sizes at all points between the walls when the mixture was wet at condenser entry. Therefore, the droplet number and volume distributions were examined for a number of mixtures that were superheated at condenser entry. The distributions obtained at a number of locations, defined by their distance from the cold wall, were plotted as line graphs and superimposed to aid comparison of the results. The results for a mixture of saturation temperature 80°C and bulk temperature at condenser entry of ~ 88.3°C are illustrated in Figure 9-15 below.

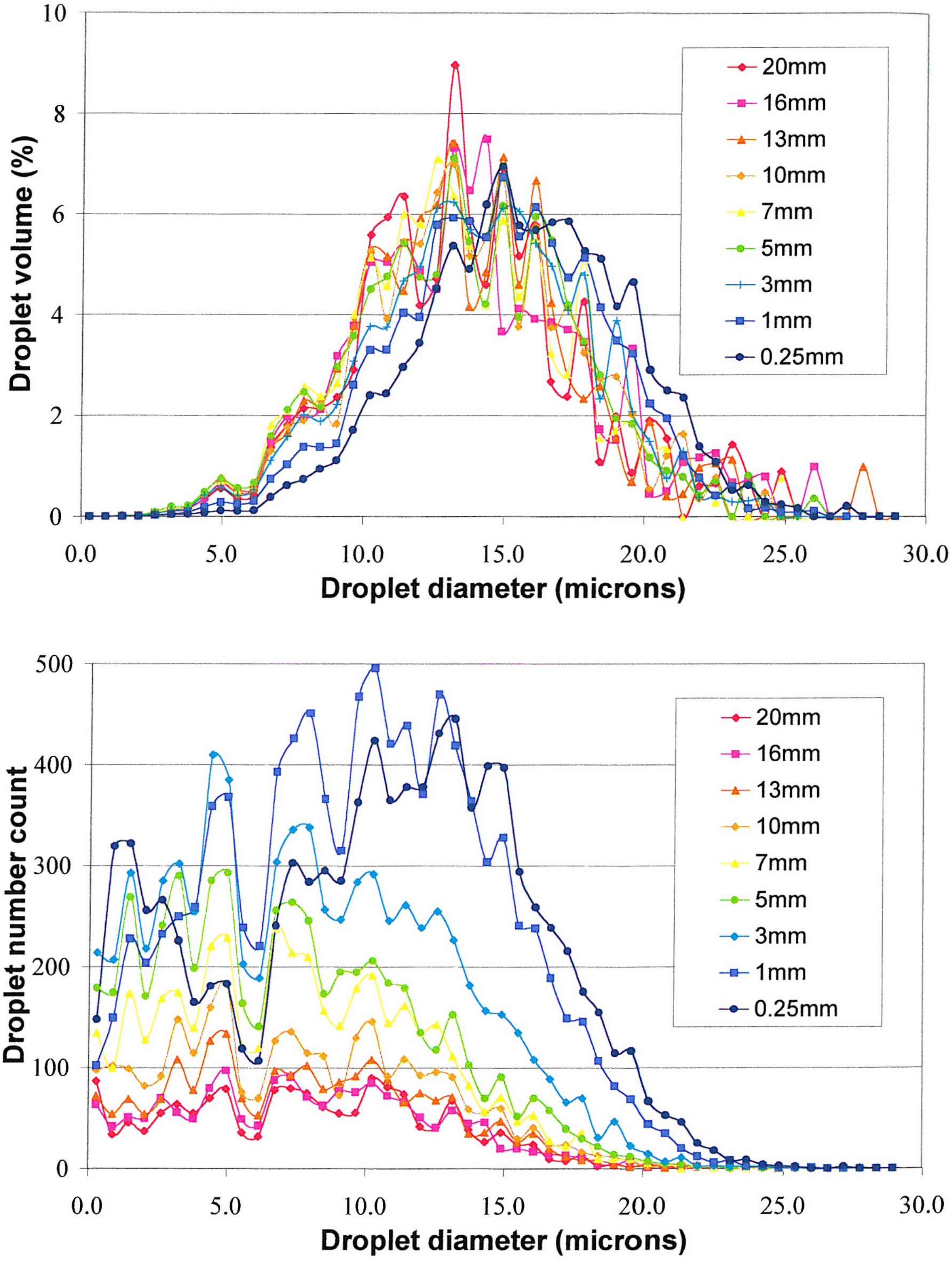

Figure 9-15. Droplet number and volume distributions measured at a number of distances from the condenser wall during experiments with a mixture of bulk entry temperature 88.3°C and saturation temperature 80°C.

A decrease in the number of droplets with distance from the cold wall is clearly evident, as is a slight shift towards droplets of smaller size. However, the form of the volume distribution is remarkably consistent. From this it is clear that under the conditions studied, the form of the distributions measured 5mm from the wall are still indicative of those at all points between the condenser walls and the total mass of submicron droplets is insignificant.

At a fixed location the mean droplet size falls with bulk entry temperature. For the hottest mixture studied in the series of experiments on mixtures with saturation temperature 80°C, the mean droplet diameter fell considerably towards the centre of the condenser, from approximately 7μm to less than 3μm (Figure 9-13). The size and volume distributions obtained from the relevant experiment (t_b=99.8°C) are plotted in Figure 9-16 below.

Even at such a high initial temperature, corresponding to a bulk mixture humidity of less than 50% entering the condenser, the peak droplet numbers are not greatly diminished (compare with those of Figure 9-15. However, the vast majority of the droplets now appear to be located within a few millimetres of the condenser wall. This is symptomatic of film fog formation and implies that the bulk mixture may still be superheated at condenser exit.

Another very significant difference between the droplet number distribution of the 99.8°C and the 88.3°C mixtures occurs at very small drop sizes. At the higher temperature the number of droplets greater than 2μm in diameter falls rapidly with distance from the condenser wall. The number of droplets less than 2μm in diameter measured in a fixed time interval was almost constant throughout the central ¾ of the condenser. Though the concentration of these droplets falls slightly with distance from the wall due to the velocity profile, it remains in the region of 150 droplets per cubic centimetre. These are therefore being formed well away from the condenser walls. Yet they have grown little. One explanation for this is that the mixture in this region may have reached saturation near the end of the condenser whereupon droplet nucleation and activation began, with little time for droplet growth. (The few larger drops found near the centre of the condenser probably became activated and began to grow nearer the wall and were subsequently transported towards the centre by the turbulent eddies within the fluid.)

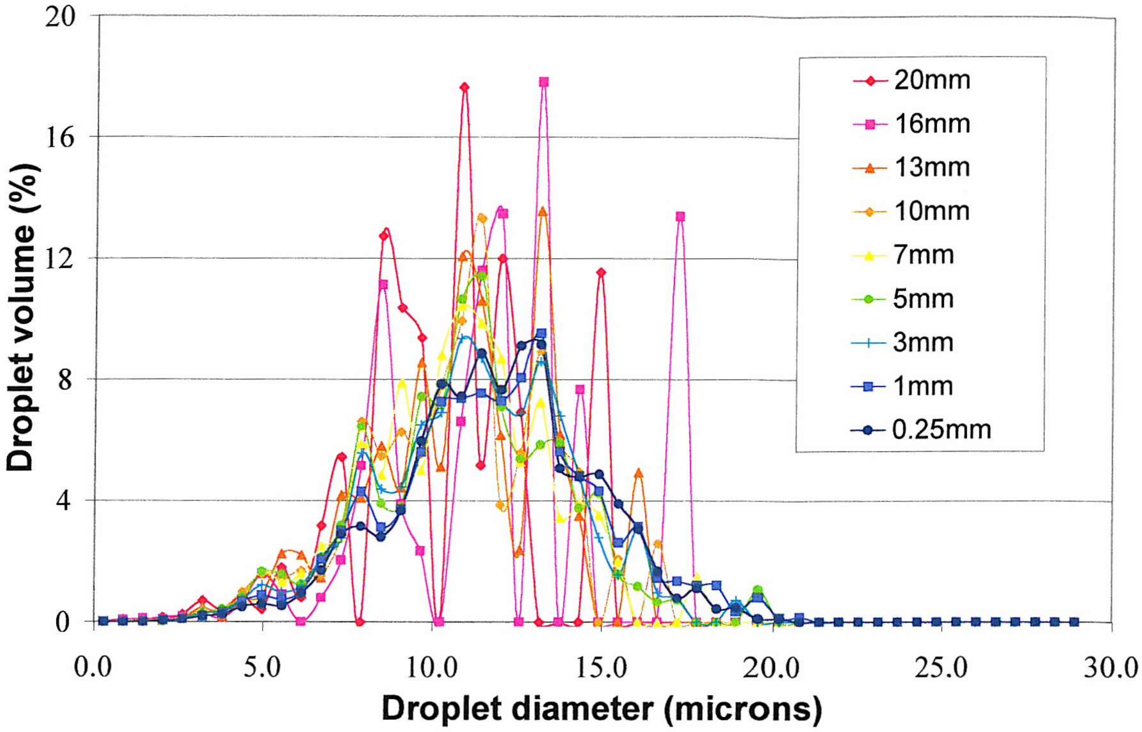

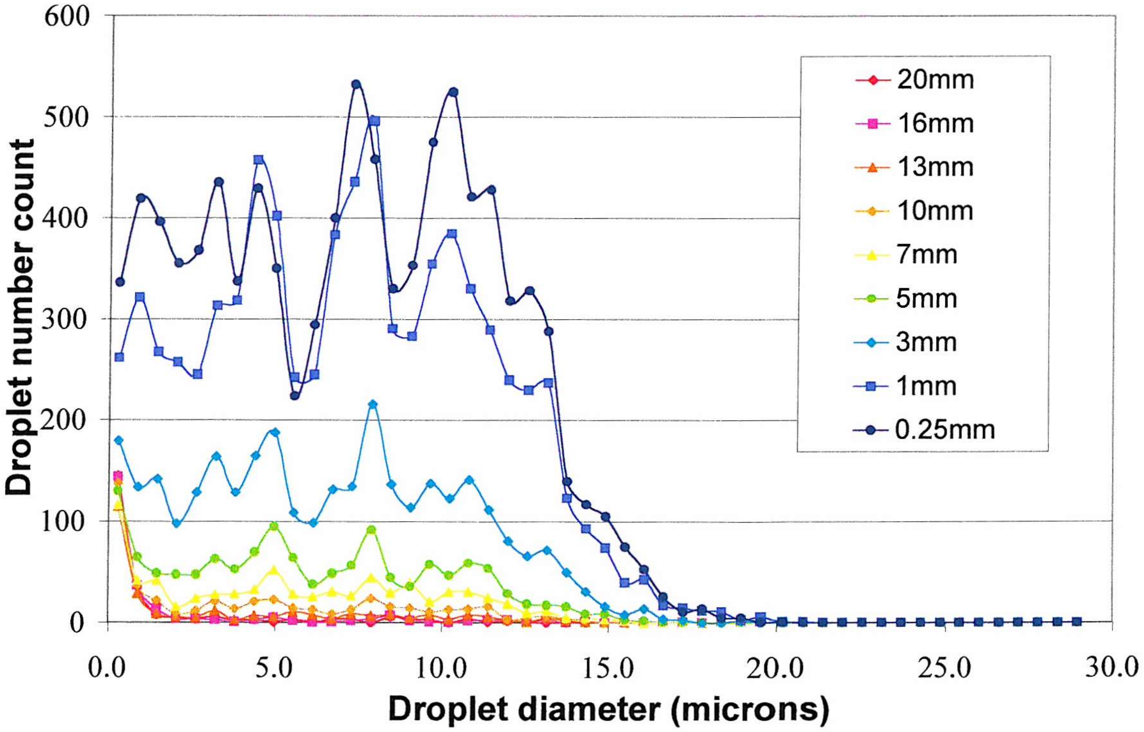

Figure 9-16. Droplet number and volume distributions measured at a number of distances from the condenser wall during experiments with a mixture of bulk entry temperature 99.8°C and saturation temperature 80°C.

There is also the possibility that the mixture in the centre of the duct remained superheated. The small droplets detected there would then exist in the form of 'haze' droplets upon the largest nuclei in the mixture (as described in section 2-5). The number of these nuclei may well be greater than in normal atmospheric air due to the boiling of de-ionised tap water used to produce the water vapour. To determine which explanation is correct it is necessary to return to the theoretical predictions of the condition of the mixture as it flows through the condenser.

9.4.3 Comparison of experimental results with theoretical predictions

The experimental observations and results presented thus far provide a useful insight into the formation of fog within a condenser of fixed dimensions as the relative humidity of the gas-vapour mixture increases. These results are represented effectively in Figure 9-17, where experimentally measured droplet size distributions are presented alongside theoretical predictions of the bulk temperature and vapour pressure as the mixture flows through the condenser. These were obtained by setting the initial condition of the mixture in the computational procedure equal to that measured during the experiments (ignoring the possibility of fog formation when the mixture becomes supersaturated). The predicted condition of the three mixtures with saturation temperature at condenser entry of 80°C was first presented in Figure 4-4, on page 61. The results obtained with the 66.2°C mixture of saturation temperature 50°C have been included to illustrate the onset of fog formation within a condenser.

The first thing to note is that the calculations for the first three mixtures all predict that the mixture remains superheated (and hence fog free) throughout the condenser. This is clearly not the case and the discrepancy is due primarily to the neglection of 'film fog' from the simple model of fog formation used for the predictions.

Fog formation begins with the formation of a small number of droplets close to the condenser walls, near the end of the condenser. As the average humidity at condenser entry increases slightly, so the formation of droplets near the walls begins further upstream within the condenser. Droplet formation and growth proceeds near the wall as the mixture flows through the condenser.

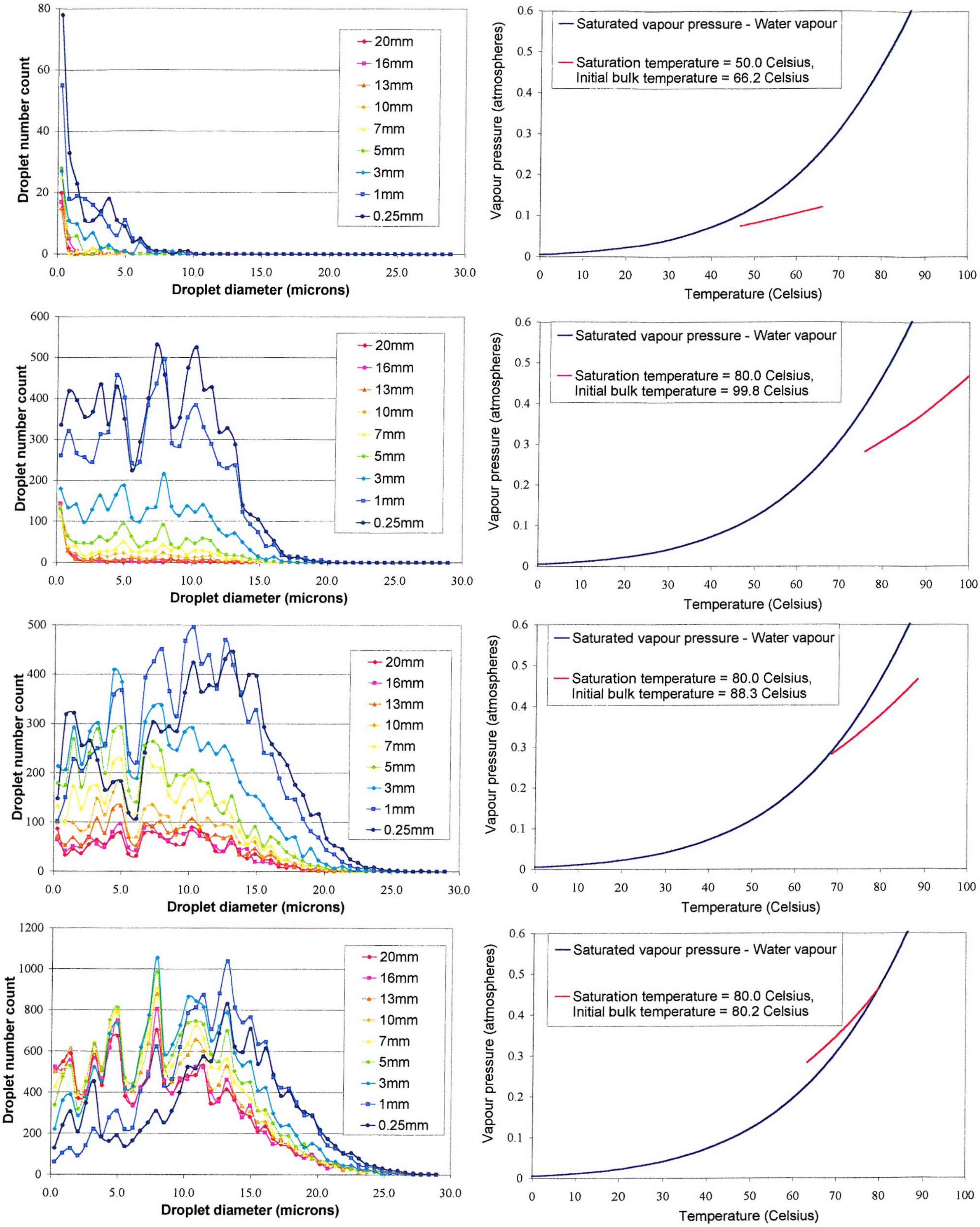

Figure 9-17. Droplet size distributions obtained at a number of distances from the condenser wall (marked) and the accompanying computer predictions of the condition of the bulk mixture as it passes through the condenser.

This describes the situation arising within the 2m long condenser during experiments upon a 66.2°C mixture with saturation temperature 50°C. Under these conditions no droplets were visible with the naked eye. Only when a laser beam was directed across the end of the condenser was it possible to see some droplets were present near the wall, scattering the laser light as they passed. The resulting droplet spectrum, the first presented in Figure 9-17, demonstrates that in fact, a small number of submicron droplets are present at all locations between the condenser walls. These droplets formed upon the largest soluble nuclei within the mixture. They exist in the form of 'haze' droplets in the superheated mixture, as described in section 2-5, and hence do not grow as rapidly as they would if activated in a supersaturated environment. [Note that despite the majority of the droplets being < 2μm in diameter in such a highly superheated mixture, these droplets still comprise only a very small fraction of the corresponding volume distribution. The total volume (or mass) of droplets is also very small.]

As the initial relative humidity of the mixture increases, so the supersaturation near the wall increases and the supersaturated region extends further from the wall. This leads to a much greater number of droplets and a greater rate of droplet growth, resulting in the presence of larger droplets in the second graph of droplet size distributions in Figure 9-17. The theoretical predictions show that the bulk mixture is still significantly superheated at condenser exit. This supports the argument presented in the preceding section that the larger droplets (> 2μm) found away from the wall actually became activated and grew near the wall before being transported towards the centre of the duct by the turbulent eddies present within the fluid. The increased number of small droplets detected away from the wall must still exist in the form of haze droplets.

Further reduction of the initial relative humidity of the mixture eventually leads to the bulk mixture becoming saturated at the end of the condenser. However, even when the bulk mixture is saturated a central superheated core will remain (since the mixture is supersaturated near the wall). The corresponding droplet size spectrum, the third in Figure 9-17 shows that though the number of droplets still falls with distance from the wall, the decrease is much less marked than in the previous case. The region of supersaturation, droplet activation and growth has spread out from the wall. Previously all droplets > 2μm in diameter originated within a few millimetres of the wall, where the turbulent eddies were damped by the proximity of the wall (the laminar sublayer and buffer zone calculated using the Universal velocity distribution typically extend to a distance of 2.5mm from the condenser wall). Now the supersaturated region is much larger, there are more droplets and they are growing further from the wall, in regions where turbulence is more pronounced. Hence there is a greater movement of droplets perpendicular to the wall and an increased number of larger drops near the centre of the condenser. The droplet numbers plateau near the centre of the condenser (i.e. there is less difference between the droplet size spectra at 16 and 20mm from the wall) as a result of droplet transfer from the regions of increased saturation on either side.

The final pair of graphs in Figure 9-17 relate to a mixture that is very nearly saturated at condenser entry (bulk temperature ~ 80.2°C, saturation temperature ~ 80°C). The theoretical calculations consequently predict a highly supersaturated mixture at condenser exit, or alternatively, a significant quantity of fog. The experimentally obtained droplet size distributions reveal that the total number of droplets detected now changes much less with distance from the condenser wall. The total quantity of fog is very much greater than in the previous cases owing both to a much greater number of droplets, particularly in the central three quarters of the condenser, and also to the greater droplet sizes throughout the condenser.

9.4.4 Supersaturation as a function of time within a condenser

In previous sections the condition of the bulk mixture has been assessed theoretically either by setting a condition of no fog formation or by using the saturation condition and excluding supersaturation. In reality supersaturation and fog formation occur simultaneously. The level of supersaturation affects the rate of fog formation and vice versa. Information regarding the true variation of supersaturation with time and the relative degrees of supersaturation from one radial location to another during the experiments can be obtained from the droplet size distributions. The deductions presented in this and the subsequent section are based upon the following assumptions:

I. The rate of droplet growth is greater the smaller the droplet size and the greater the difference between the vapour pressure at the droplet surface and that of the surrounding mixture (in accordance with equation 2-35).

II. The rate of condensation of liquid mass upon a drop is approximately proportional to the radius of the drop and the difference between the vapour pressure at the droplet surface and that of the surrounding mixture (equation 2-33).

III. The final droplet concentration is primarily governed by the maximum supersaturation, as discussed in section 2.11.

IV. The number of nuclei activated, N, at a given supersaturation, S, increases monotonically with increasing supersaturation inside the condenser. In fact for atmospheric water vapour in air, it was noted that N $\sim$ $S^{1/2}$ over the range of supersaturations from ~ 0.1 - 2% in section 2.6.

Now returning to the computational predictions of bulk fog formation rates presented in chapter 4, the rate of fog formation was generally predicted to be greatest immediately after the onset of fog formation, after which it fell steadily to zero (e.g. Figure 4-5, page 62). This was the case for all mixtures that reached bulk saturation at temperatures less than 80°C. These predictions were arrived at by assuming that all 'excess' vapour condensed as a fog, thereby excluding the possibility of supersaturation.

In reality the mixture does become supersaturated, leading to the activation of a number of nuclei. The resulting droplets grow rapidly in the supersaturated mixture and in so doing remove some of the 'excess' vapour, which tends to reduce the supersaturation, while further cooling acts to increase the degree of supersaturation further. The balance between these two processes is critical in determining both the way the supersaturation of the bulk mixture varies with time inside a condenser and the resulting droplet size distribution.

Following the initial onset of supersaturation, a number of nuclei are activated and the resulting droplets begin to grow. A short time after the onset of fog formation, Δt, the supersaturation is S(Δt) and the number of nuclei activated n(Δt). The droplets formed are still fairly small, though they will be growing quite quickly (assumption I). After a further short period of time, again Δt, the supersaturation will have increased to S(2Δt), the number of activated nuclei will have increased to n(2Δt) and the droplets activated initially will have grown further. Now the rate of condensation upon the droplets activated in the first Δt seconds will be greater during the period from Δt to 2Δt than it was during the equivalent time interval from 0 to Δt because the droplets are larger and the surrounding supersaturation has increased (assumption II). The rate of condensation in the form of fog will also have increased due to the formation of additional droplet as the maximum supersaturation has increased (assumption III). Thus the rate of removal of vapour by fog formation increases with time as the supersaturation increases.

The computational predictions imply that the quantity of 'excess' vapour (condensing immediately as fog) increases monotonically, yet the rate of increase falls with time, eventually approaching zero. Hence, once the mixture becomes saturated the processes acting to increase the supersaturation become less effective with time, while the processes of droplet formation and growth that act to reduce the supersaturation become increasingly significant. Therefore, following the onset of fog formation inside a partial condenser, the supersaturation is expected to rise at a decreasing rate. A graph of bulk supersaturation against time will initially be of the form represented in Figure 9-18. Since the number of nuclei activated increases steadily as the supersaturation increases, in fact N $\sim S^{1/2}$ (assumption IV), the rate of droplet formation also decreases with time.

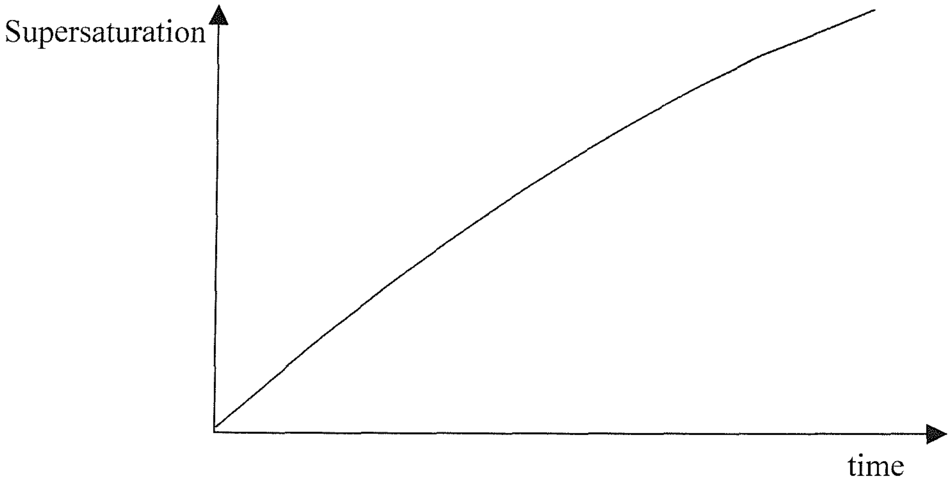

Figure 9-18. Supersaturation as a function of time during the initial phase of fog formation.

Now if the condenser is sufficiently long, the temperature of the mixture eventually approaches that of the coolant, at which point the driving force that lead to supersaturation of the mixture no longer exists. However, provided the mixture remains supersaturated the activated droplets continue to grow, depleting the supersaturation. As the supersaturation falls it may drop below the equilibrium supersaturation associated with the smallest droplets, as discussed in section 2-5, and they will slowly begin to evaporate. Thus the larger droplets, having lower equilibrium supersaturations (as indicated in Figure 2-6, page 23), will continue to grow at the expense of the smallest ones. The supersaturation will finally fall to a small, constant value. In a sufficiently long condenser the variation of supersaturation with time is expected to be of the form presented in Figure 9-19.

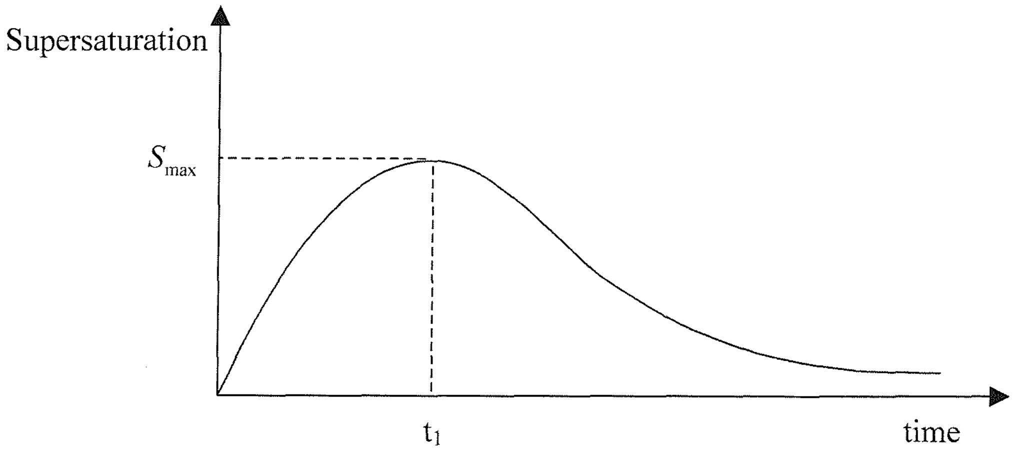

Figure 9-19. Supersaturation as a function of time in a partial condenser when the exit temperature of the mixture approaches that of the coolant.

This is in agreement with the graphs of supersaturation as a function of time presented by Frank et al. [34]. These were produced using a model of droplet formation and growth for an atmospheric fog, in which the changes in the level of supersaturation took place over a period of hours rather than seconds. The form of Figure 9-19 is very significant for the prediction of the resulting droplet size distribution. The fact that the supersaturation reaches a maximum level, S_{max}, at time t_1, suggests that thereafter no new droplets are formed. Hence the number of small droplets (> 0.1µm and < 1.0µm) will decrease as the majority of droplets continue to grow and the smallest ones revert to haze droplets, < 0.1µm in diameter. However, it should be noted that if the condenser is relatively short, the time spent by the mixture inside the condenser may be less than t_1 and consequently droplet formation will continue throughout the condenser.

9.4.5 Variation of supersaturation with time at different radial locations

The supersaturation inside a condenser varies both axially and radially from one point to another. The previous section dealt with the axial variation, that is, the variation with time as the mixture flows through the condenser, ignoring the radial differences. The radial variation of supersaturation may be evaluated via the relevant temperature and vapour pressure profiles, as discussed in section 3.5. Such a procedure shows that the supersaturation is generally lower the greater the distance from the wall. It follows that in a mixture that is saturated or superheated on entry to a condenser, supersaturation is achieved further along the condenser (if at all) the greater the distance from the wall.

The droplet size distributions obtained during experiments upon mixtures of saturation temperature 80°C are plotted alongside estimations of the supersaturation as a function of time at a number of distances from the wall in Figure 9-20. The droplet size distributions obtained with the three superheated mixtures all contain a large number of very small droplets, indicating that droplet activation is occurring at the end of the condenser. This implies that the supersaturation is still increasing with time, reaching new maximum values. Note that the estimated supersaturation curves are time averaged, since the flow is turbulent.

In the first two cases the number of submicron droplets at the end of the condenser is greatest near the wall. The droplet size distributions were obtained over equal time periods, yet the mixture velocity and hence volume flow rate, increase with distance from the wall. Therefore the difference in the number of submicron droplets detected per unit volume of mixture near the wall and near the centre of the condenser is even greater than is apparent from the graphs. Hence the droplet activation rate and the rate of supersaturation increase is greatest near the wall. In the third case however, the mixture is much nearer saturation at condenser entry. The droplet activation rate per unit volume of mixture is then greater at the centre of the condenser than near the wall, despite the velocity at the centre of the condenser being ~ 2.4 times that 1mm from the wall. [Note that any removal of the submicron droplets as a result of coalescence is likely to be more effective near the centre of the condenser, where the velocity and turbulence are greater.] The number of submicron droplets 1mm from the wall is also lower than in the previous two cases, suggesting that the rate of supersaturation increase with time at the point of measurement is less great.

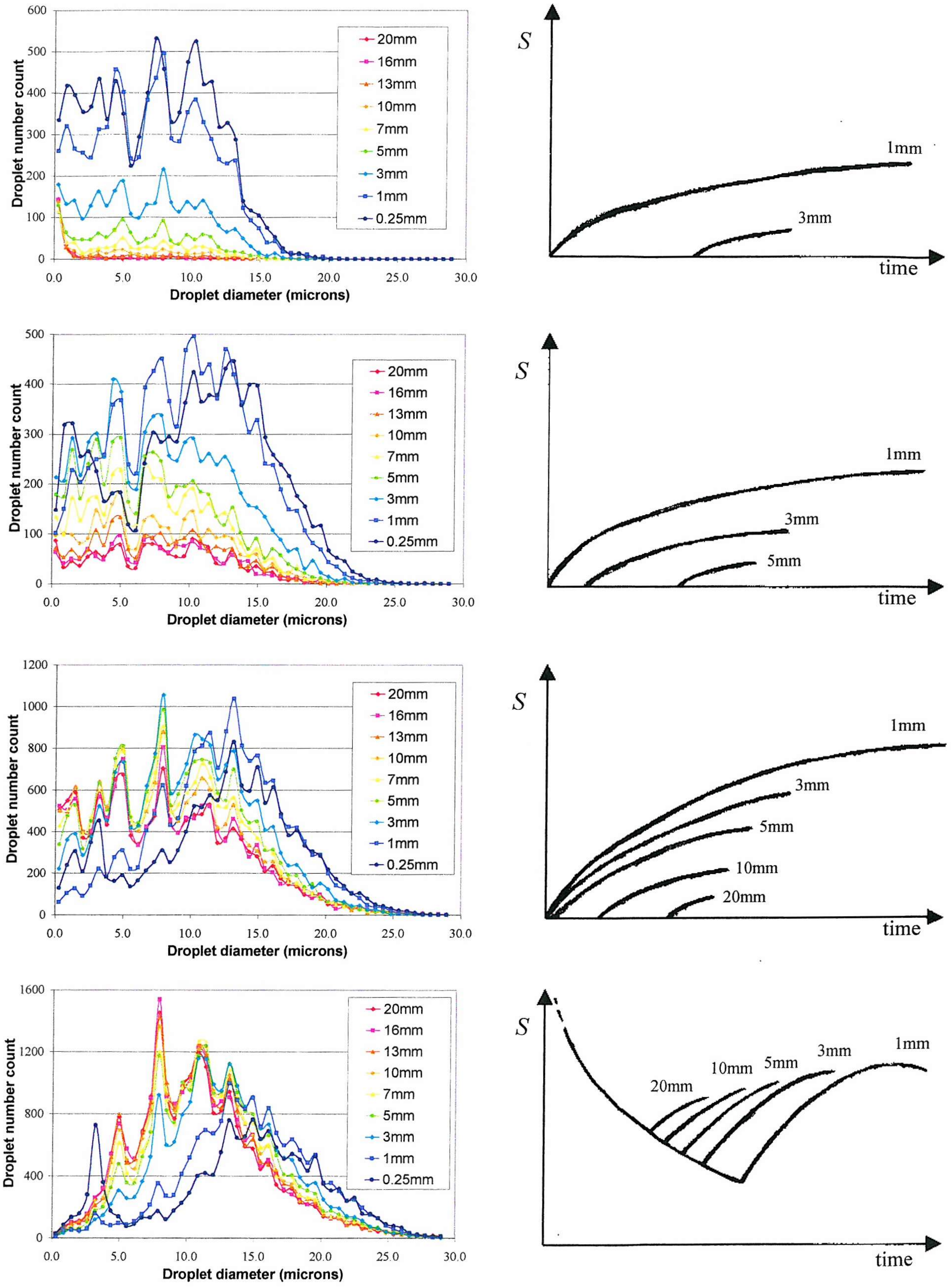

Figure 9-20. Droplet size distributions and corresponding estimations of the supersaturation at a number of distances from the condenser wall.

It appears therefore, from the form of the droplet size distributions and the number of submicron droplets, that under the conditions studied the experimental condenser was insufficiently long (or the cross-sectional area too great) for the supersaturation to peak and begin to fall. The only droplet spectra with very few submicron droplets are those obtained with a wet mixture at condenser entry. This situation is quite different from the previous three cases because an initial supersaturation of ~ 18% was established as soon as the steam and air flows merged. Activation then resulted in a very large number of small droplets that began to grow, depleting the supersaturation and thereby terminating new droplet formation. Droplet growth continued to reduce the supersaturation until the mixture reached the condenser and it began to rise again. However, the lack of submicron droplets reveals that the supersaturations remained below the levels obtained on mixing. The peak at ~ 3μm in the droplet size distribution 0.25 mm from the wall is attributed to the entrainment of air outside the condenser.

9.5 *Effect of saturation temperature*

The mean droplet diameters measured 5mm from the condenser wall during the experiments discussed in section 9.4 are plotted against the initial bulk mixture temperature in Figure 9-21. Experimental results marked by points of the same colour were obtained using mixtures produced using equal water vapour and air flow rates and so have the same saturation temperature. The lines have been added to indicate the trends in the data.

As the mixture temperature at condenser entry falls, so the mean diameter increases and it does so at an increasing rate. The variation of mean diameter with temperature is fairly consistent between the four data sets, the main difference appearing to be a shift of ~10°C between the results (owing to the saturation temperatures being 50, 60, 70 and 80°C). The mean diameter of the droplets formed when the bulk temperature equals the saturation temperature of the mixture at entry to the condenser (the mixture is saturated) is approximately 10μm in each case. However, as the temperature of the mixture increases above that of the saturation temperature, the mean droplet diameter falls less rapidly the greater the saturation temperature. This is partly because an increase in temperature of say 1°C results in a smaller percentage increase in the temperature difference between the bulk mixture and the interface, the driving force for heat transfer, the greater the saturation temperature.

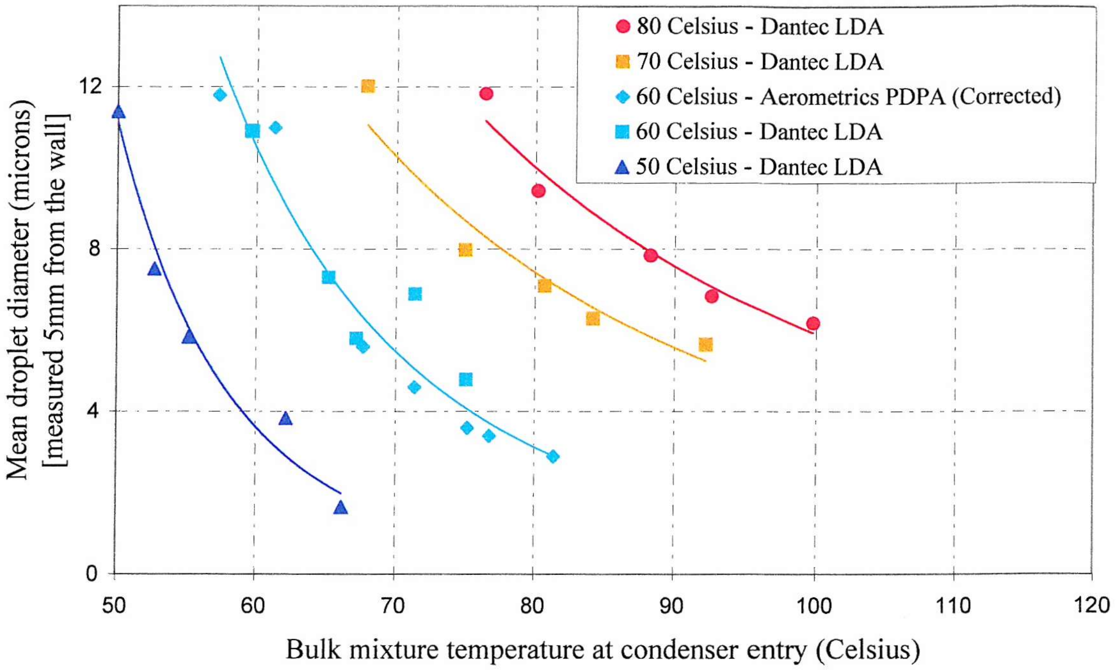

Figure 9-21. Mean droplet diameter measurements 5mm from the condenser wall obtained during experiments on mixtures of different saturation temperatures and bulk condenser entry temperatures.

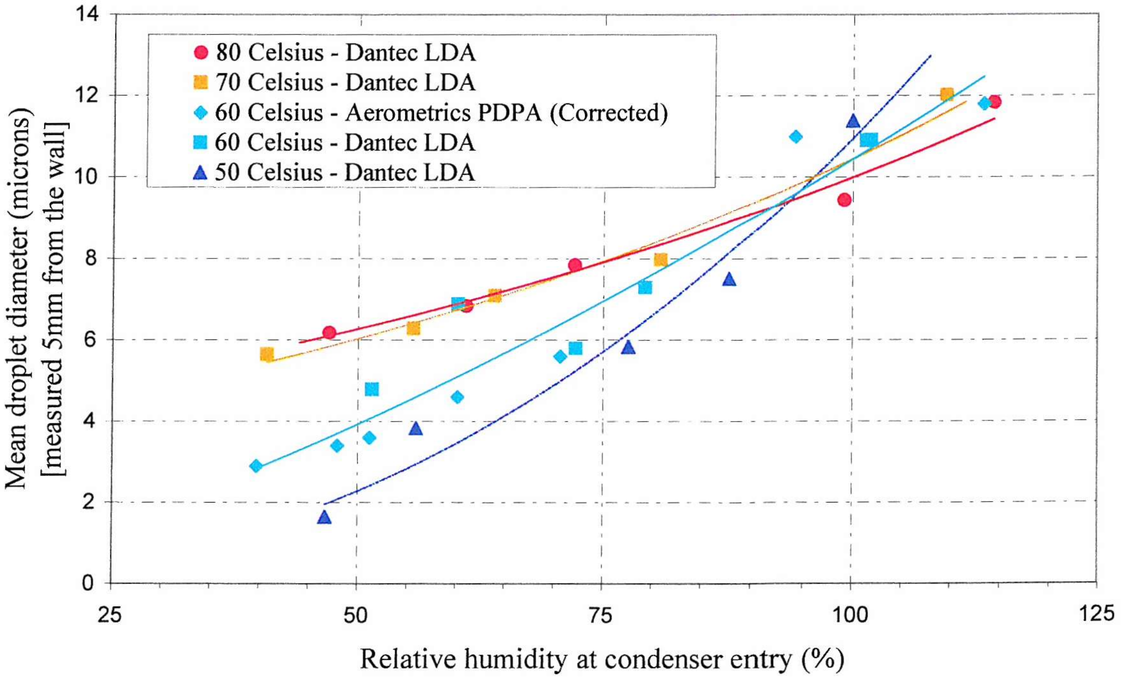

Figure 9-22. Mean droplet diameter measurements plotted against the bulk mixture relative humidity at condenser entry.

Due to the form of the saturation function the relative humidity of the mixture falls most greatly for a fixed temperature increase the greater the saturation temperature of the mixture. Plotting the mean droplet diameter against the initial relative humidity of the mixture, as in Figure 9-22, allows a more direct comparison of the results at the four different saturation temperatures.

The mean droplet diameters are approximately equal when the relative humidity is ~ 95%. As the humidity decreases below 95% the mean droplet diameter is smaller the lower the initial saturation temperature. When the relative humidity reaches 50% the mean droplet size is almost three times greater for a mixture with an initial saturation temperature of 70°C than one of 50°C (equating to a ratio of nearly 27 between the mean droplet masses). A similar result is obtained if the mean droplet diameter is plotted against the ratio of initial bulk temperature to saturation temperature. The reason may be found by comparing the bulk mixture conditions in relation to the saturation function on a graph of vapour pressure against temperature, as in Figure 9-23.

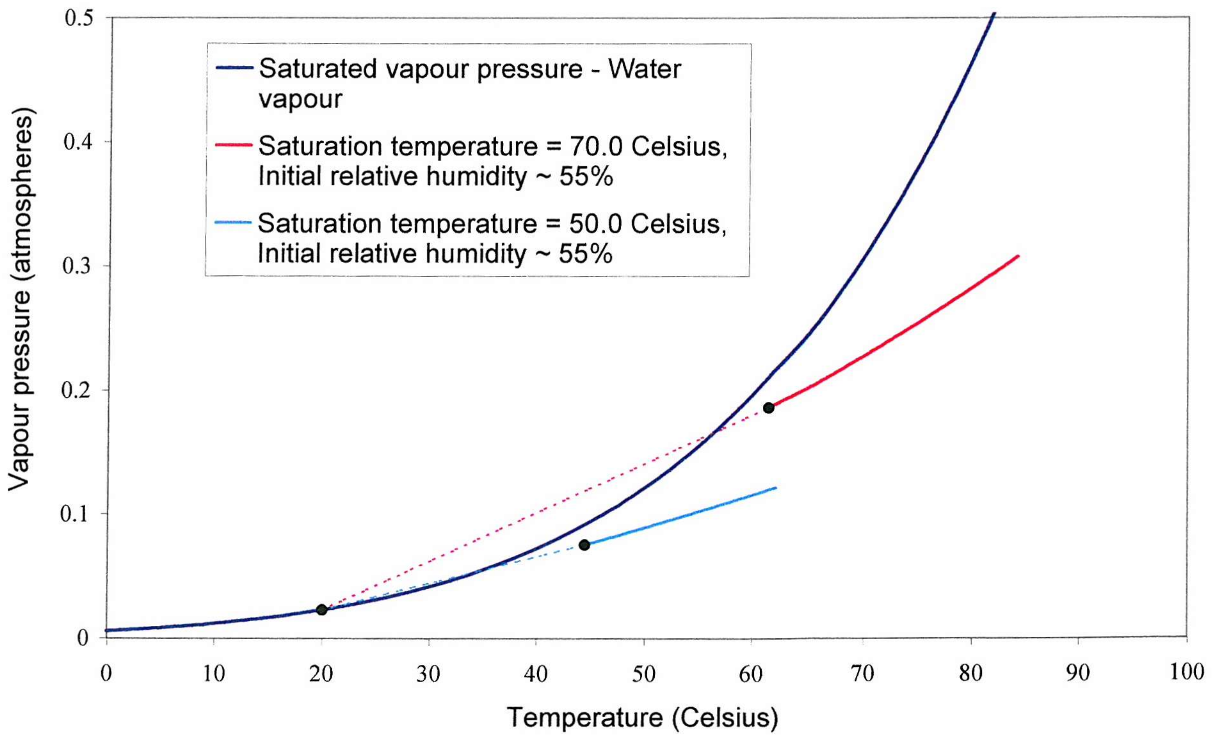

Figure 9-23. Computational predictions of the variation in bulk temperature and vapour pressure of two mixtures with equal relative humidities at condenser entry.

The predicted condition of the bulk mixtures are represented by the solid lines in Figure 9-23, and the condition at the end of the 2m long condenser is marked by a black dot. These were obtained using the numerical methods described in chapter 4. The bulk condition of the two mixtures approach saturation, yet both remain superheated. The reason for the large discrepancies between the droplet sizes is clear when the lateral variation of mixture condition is considered. For a water vapour – air mixture this is closely approximated by a straight line between the bulk mixture condition and that at the mixture-condensate interface, as illustrated at the end of the condenser by the dotted lines in Figure 9-23. These lines indicate that film fog formation will occur in both mixtures, though a much greater degree of supersaturation occurs (and the region of fog formation extends further from the wall) in the mixture of greatest initial saturation temperature, due to the curvature of the saturation function.

The graph of droplet number concentration against relative humidity for the same set of experiments (ignoring the measurements obtained with the Aerometrics PDPA using a weaker laser) is presented in Figure 9-24.

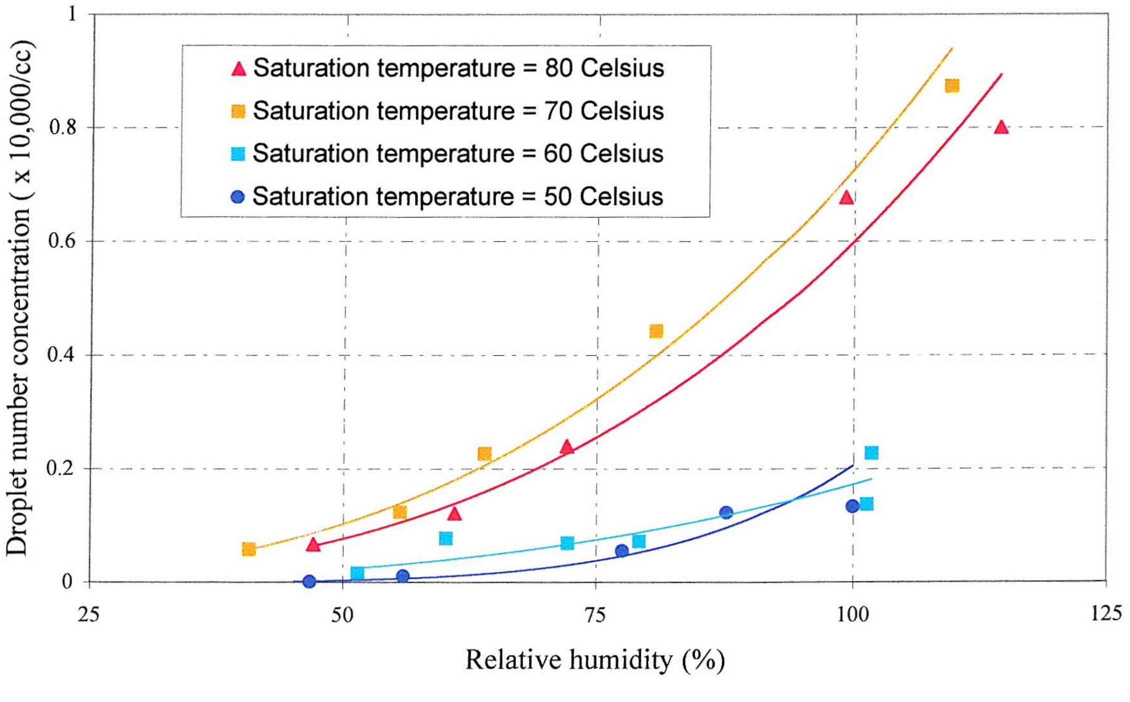

Figure 9-24. Droplet number concentration measurements plotted against the bulk mixture relative humidity at condenser entry.

There is an increase in the droplet number concentration with increasing relative humidity of the initial mixture that appears approximately exponential in nature. This is true of all four experimental data sets, though there is a greater variation in the results obtained at saturation temperature 60°C. These results were collected during experiments spanning a period of 6 months, whereas the other data sets were obtained within two weeks of one another. This fact is significant due of the periodical contact between the LDA transmitter and the end of the condenser, following which it was necessary to re-align the receiver lens. This alignment process affected the measurement location and the strength of the signal collected at the receiver and hence the droplet number concentrations detected. However, despite the clear trends within each data set there is no obvious relationship between the results obtained using mixtures of different saturation temperature. Though an increase in droplet number concentration with saturation temperature is likely, possibly falling again as the saturation temperature approaches 80°C (in potential agreement with the theoretical predictions of section 4.4.2) there is insufficient data to arrive at any firm conclusions.

9.6 *Effect of velocity*

The importance of the mean velocity of the mixture passing through the condenser was studied next. It was initially intended to perform a series of experiments with mixtures of a fixed steam to air flow rate and range of temperatures, flowing through the condenser with one of three velocities. However, in order to obtain the desired mean velocity at condenser entry, it was necessary to achieve the requisite bulk mixture temperature. Too high a temperature at given steam and air flow rates would result in too high a velocity and vice versa. The difficulty associated with obtaining a specific bulk temperature at condenser entry was discussed in section 7.5. Hence, to obtain a wide range of results in a restricted period of time it was decided to hold the mass flow rates constant (not simply the ration of steam to air mass flow rates). Thus, the velocities quoted are only truly accurate when the bulk mixture entry temperature was 60°C. At higher temperatures the velocity increases accordingly. However, the ratio of velocity between the series is constant when the bulk temperatures are equal. To keep the number of new experiments required to a minimum, a previously used steam – air ratio was employed. This was chosen to be 0.153, i.e. that of a 60°C saturated mixture, to allow the widest range of velocities to be used, while ensuring turbulent flow.

Two experimental data sets were then collected, at the practical extremities of velocity. Under the conditions stated, these corresponded to mean flow velocities of 1.36 and 3.42m/s (and Reynolds numbers of approximately 4,700 and 12,000 respectively). To allow a direct comparison of the data at all three velocities, the average values obtained at a single location, again 5mm from the cold wall, are superimposed in Figure 9-25.

Referring to Figure 9-25, the mean droplet diameter decreases as the initial mixture temperature increases (and the initial relative humidity falls), in agreement with the results presented in section 9.5. This is true for the results obtained at all three velocities.
The effect of velocity upon the droplet size is also clearly evident. The lower the velocity, the greater the mean droplet diameter. The reason for this may be found by considering the theoretical predictions of chapter 4, presented in Figure 4-7, on page 65, and the equation for the rate of droplet growth presented in section 2.8.1, $(dr/dt)_{CR} = D(p_{v,a} - p_{v,\infty})/\rho_L R_v Tr$. For droplets of equal size, the rate of droplet growth is therefore approximately proportional to the ratio $(p_{v,a} - p_{v,\infty})/T$, that is, the partial vapour pressure difference between the droplet surface and the surrounding mixture divided by the temperature, in Kelvin. From Figure 4-7, the ratio of mass transfer to heat transfer (or vapour pressure drop to temperature drop) decreases as the velocity decreases. Thus the magnitude of the ratio $(p_{v,a} - p_{v,\infty})/T$ increases for droplets of equal size (constant $p_{v,a}$) as the velocity decreases.

In addition to the rate of droplet growth increasing as the velocity of the mixture falls, the residence time of the mixture inside the condenser also increases. Thus, not only do the droplets grow faster the lower the velocity of the mixture, the growth of the droplets persists for longer, resulting in greater mean droplet sizes. The effect on the droplet size distribution is illustrated in Figure 9-26, where measurements obtained with mixtures of different velocity, but approximately equal condenser entry temperatures are superimposed. The percentage of the total number of droplets that are below 5μm in diameter (and 1μm) falls significantly as the velocity decreases and this coincides with an increase in the percentage of droplets greater than 10μm in diameter. This is as expected. A constant droplet activation rate would lead to a steadily falling percentage of small droplets as condensational droplet growth of these droplets produces an increasing number of larger drops. The rate of supersaturation increase

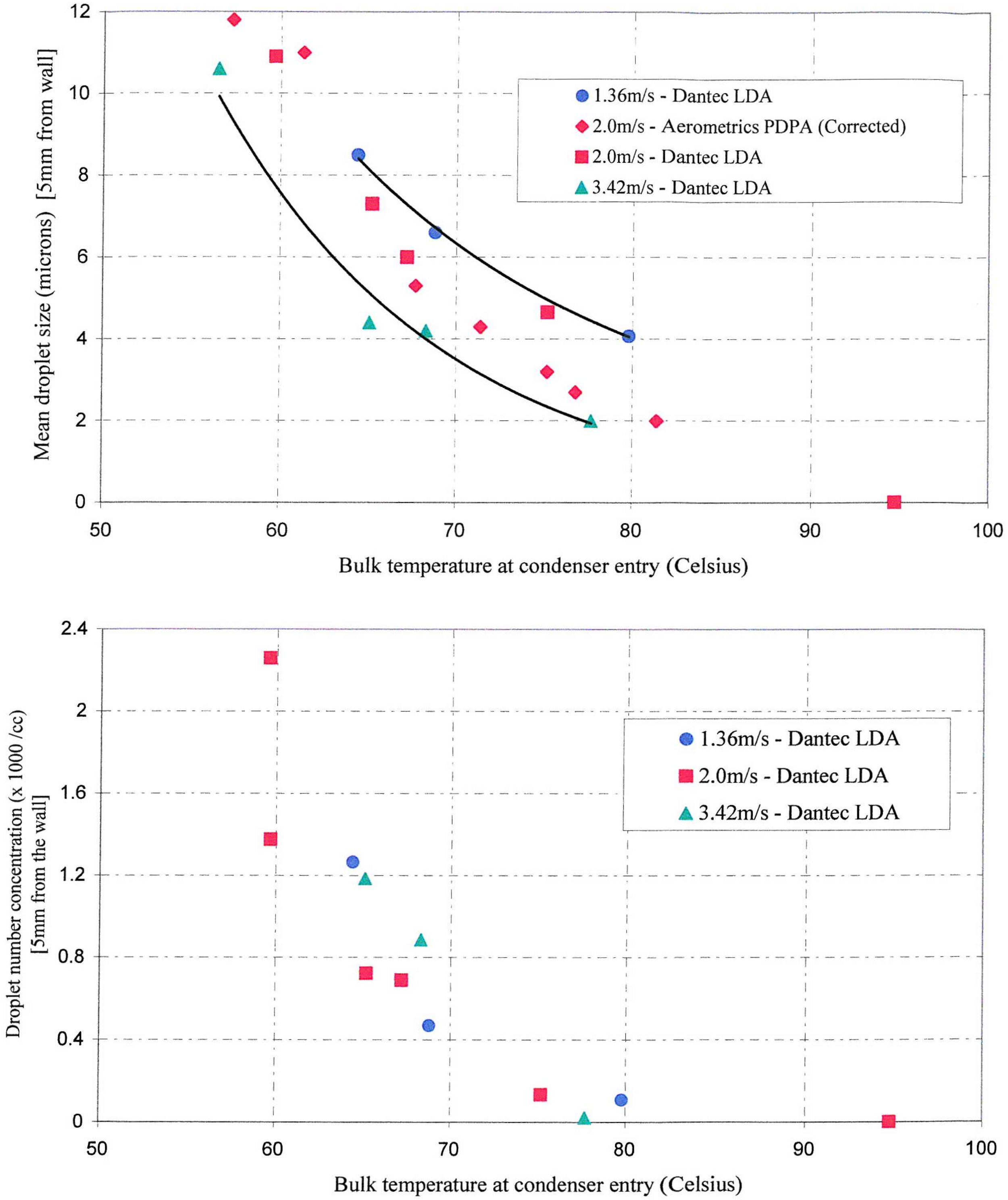

Figure 9-25. Superimposed mean droplet size and concentration data obtained at all three velocities, 1.36, 2.0 and 3.42 m/s. The ratio of steam to air flow rate was constant at 0.153 throughout these experiments [equivalent to that of a 60°C, saturated mixture].

and hence the droplet activation rate actually decreases with time, hence the percentage of small droplets falls fairly quickly. The lower the velocity, the greater the residence time in the condenser and the smaller the percentage of small droplets in the size spectrum. The percentage of large droplets increases as a direct consequence of the increasing growth rates and residence times as the velocity falls.

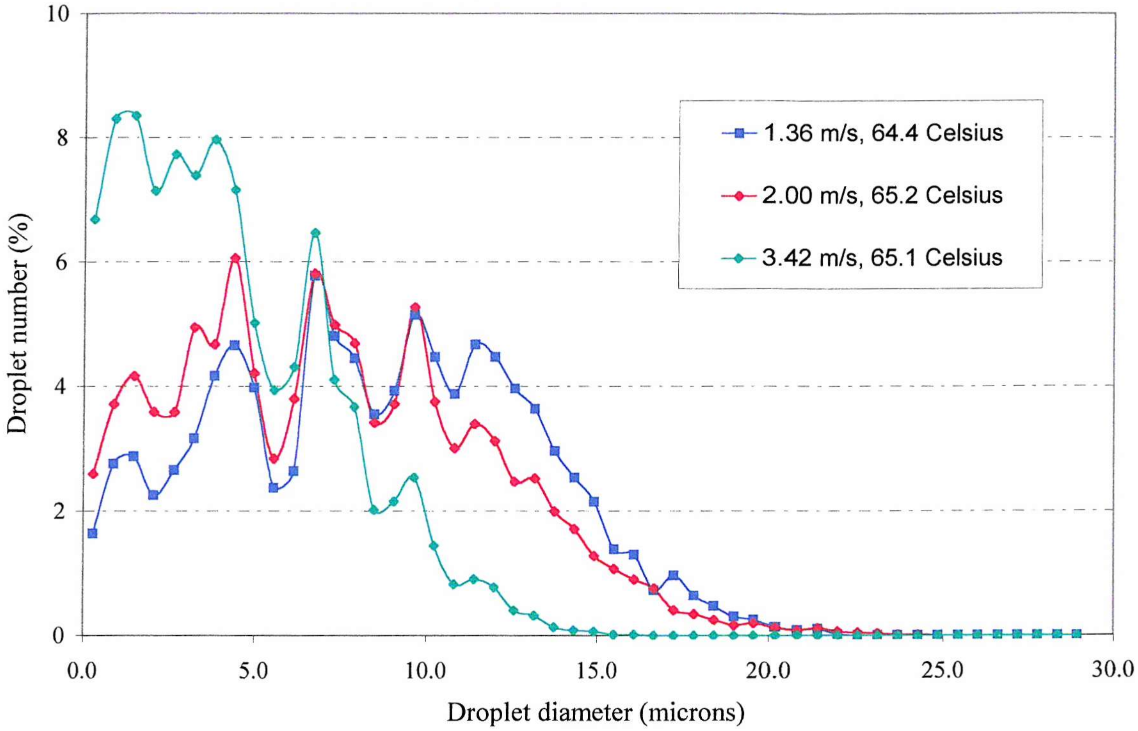

Figure 9-26. Experimentally measured droplet size distributions obtained with mixtures of different velocity but approximately equal bulk temperature at condenser entry.

The size of the largest droplets present rises from ~ 15μm to ~ 22μm as the velocity falls from 3.42 to 2.0 m/s, yet changes little between the mixtures flowing at 2.0 and 1.36 m/s. This is probably because though the condensational growth of the droplets increases as the mixture velocity falls, the rate of droplet coalescence is lower since the mixture is less turbulent. The rate of droplet growth is approximately proportional to the inverse of the droplet diameter (equation 2-35, page 30). It dominates any droplet growth by coalescence at relatively small droplet sizes (<10μm). However, at droplet diameters of 20μm, near the upper end of the range of droplet sizes presented in Figure 9-26, the rate of condensational droplet growth will have slowed significantly and droplet coalescence becomes increasingly important.

The effect of mixture velocity on the droplet number concentration is far more difficult to discern. Though the droplet concentrations, presented in Figure 9-25, generally increase with falling bulk temperature at condenser entry, there are no obvious trends in the data as the velocity changes. It was anticipated that the droplet number concentrations would increase as the mixture velocity was reduced, in accordance with the increased supersaturations predicted theoretically in Figure 4-7. However, the results presented in Figure 9-25 are inconclusive. It is possible this is due to slight discrepancies in the alignment of the LDA transmitter and receiver between the experiments. Alternatively, the measurement time periods of 40 seconds may have been too short to obtain accurate average droplet number concentrations, owing to the turbulent nature of the flow and the large variations in the droplet concentration with distance from the wall.

9.7 *Effect of coolant flow rate*

The rate of coolant flow within a condenser affects the rate of transfer of heat away from the condenser walls. It also alters the residence time of the coolant within the condenser and subsequently the final coolant temperature, the average coolant temperature and the mixture – condensate interface temperature. Increasing the coolant flow rate therefore leads to a greater temperature difference between the bulk mixture and the interface and a greater bulk temperature drop with distance along the condenser.

It was decided to conduct the experiments upon the effect of coolant flow rate using wet mixtures initially. Previous such experiments revealed an absence of droplets $\leq 2\mu m$ in diameter in the mixture exiting the condenser outside the region of entrainment (Figure 9-8, page 120). This suggests no new droplet formation within the condenser, all condensation occurring at the cold walls or on droplets already present at condenser entry. It was therefore interesting to investigate the effect of coolant flow rate on the droplet sizes and concentrations of the fog. Three sets of experiments were performed, as detailed below.

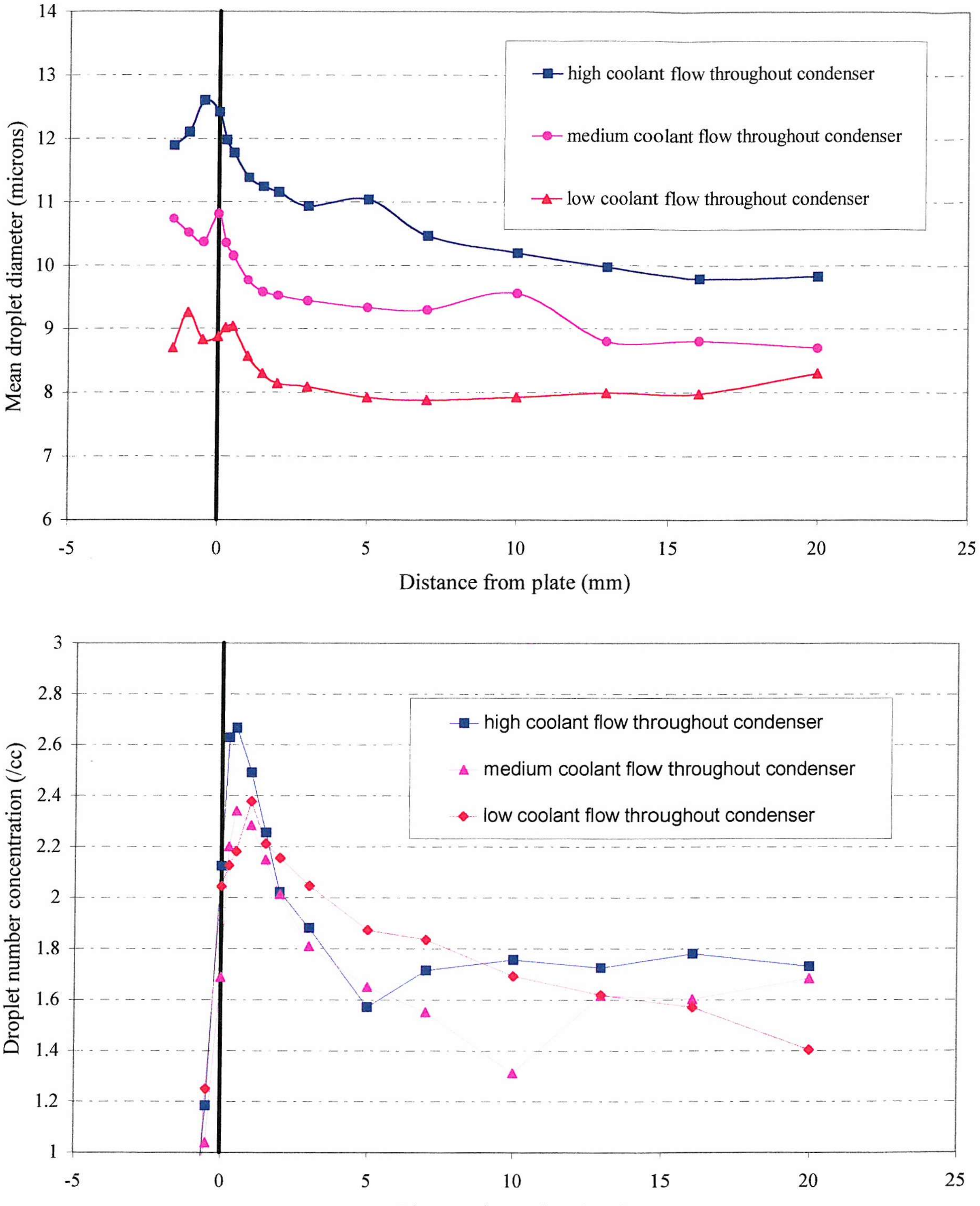

Figure 9-27. Mean droplet diameter and concentration measurements obtained during experiments on a wet mixture using different coolant flow rates.

9.7.1 Increase in overall coolant flow (using a wet mixture)

The first set of experiments was conducted by adjusting the overall coolant flow rates. Once a steady-state had been achieved inside the condenser, the inlet valve to the coolant manifolds was adjusted, the temperatures allowed to stabilise and measurements taken. This process was then repeated at a number of different coolant flow rates, ensuring the steam to air flow rates and condenser entry temperature remained constant.

Figure 9-27 shows the results obtained during tests with an initially supersaturated mixture of steam to air mass flow ratio = 0.153 and flow rates chosen to produce a mean mixture velocity of 2m/s when the bulk mixture temperature equals 60°C, the saturation temperature of the mixture. The actual bulk temperature at condenser entry was ~ 56.0°C, ensuring an instant supersaturation of more than 20% on mixing and a wet mixture at condenser entry. The associated axial temperature drops are presented in Figure 9-28.

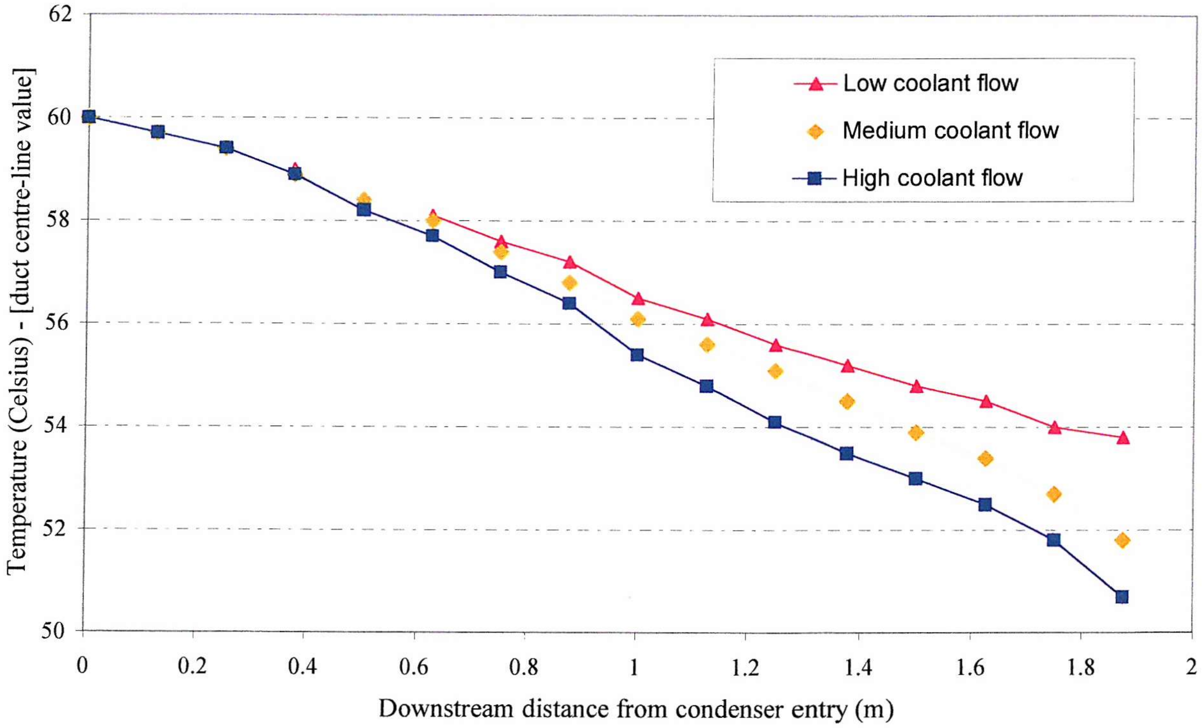

Figure 9-28. Centre-line temperatures measured within the condenser during experiments upon a wet mixture using different coolant flow rates.

Three different coolant flow rates were employed, high, medium and low, resulting in thermocouple temperature measurements adjacent to the wall of 22.4, 29.0 and 36.7°C respectively. Measurement of the temperature of the fluid at different axial locations within the condenser, presented in Figure 9-28, confirmed that the temperature drop increased as the coolant flow rate increased. Referring back to Figure 9-27, it is clear that the mean droplet diameter also increased as the coolant flow rate increased. This is as expected since the reduced wall temperatures, combined with the curvature of the saturation function, produce a much greater increase in the temperature difference between the bulk mixture and the interface than in the corresponding vapour pressures. For example, for a mixture that is saturated and has a bulk temperature, t_b, of 60°C, a reduction in the interface temperature, t_i, from 36.7 to 22.4°C produces a 61% increase in the temperature difference, $(t_b - t_i)$, but only a 25% increase in the corresponding vapour pressure difference, $(p - p_i)$. These temperature and vapour pressure (concentration) differences are the driving forces for heat and mass transfer respectively. The heat transfer rate in the absence of fog formation is given by $q = hA(t_b - t_i)(C_o / e^{C_o} - 1)$, and the mass transfer rate is given by $N_A = k_g^* P \ln(P - p_i / P - p)$. In general, over the range of pertinent values of P, p and p_i, the percentage change in the group $\ln(P - p_i / P - p)$ is approximately equal to that in $(p - p_i)$. In the example above it increases by 23% compared with a 25% increase in $(p - p_i)$. The rate of heat transfer increases to a greater degree than the rate of mass transfer. Hence, when the coolant flow rate is increased, the increase in the bulk temperature drop within the condenser is much greater than the increase in the bulk vapour pressure drop. As a result, greater supersaturations are produced, resulting in greater droplet growth rates, the greater the coolant flow rate.

Droplet size distributions obtained at a single point for all three coolant flow rates are presented in Figure 9-29. These measurements were performed at the usual location, that is 10mm downstream of the condenser exit plane and 5mm in from the plane of the condenser wall. In each case there is an absence of any small droplets, implying no new droplet formation within the condenser. All the droplets present at the end of the condenser formed when the air and steam flows merged, where the resulting mixture supersaturation was over 20%. Droplet formation and growth immediately depleted the supersaturation and despite the subsequent increases occurring within the condenser, the supersaturation remained below the previous maximum level at all points within the condenser.

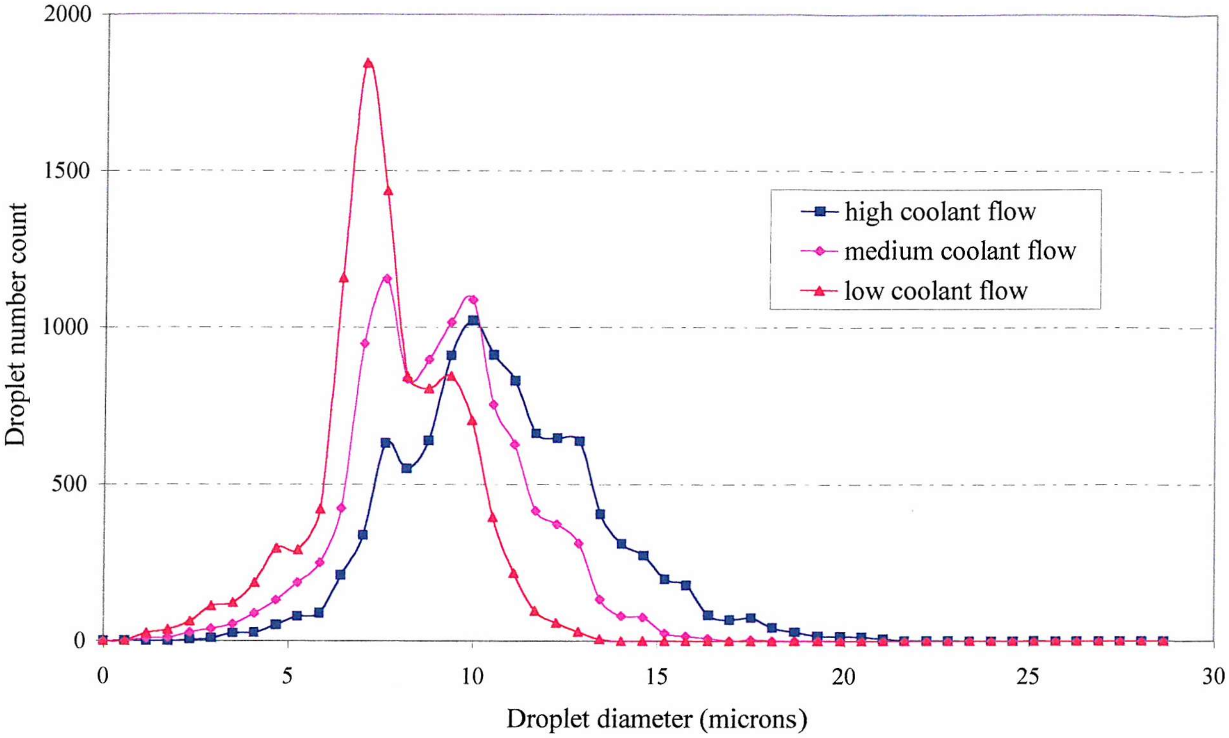

Figure 9-29. Droplet size distributions obtained at condenser entry during experiments with different coolant flow rates.

It was therefore expected that the change in coolant flow rate would have little effect on the droplet number concentrations. However, this is not readily apparent from the measurements presented in the second graph in Figure 9-27, though it is possible this is due to large variations in droplet number concentrations with time. Therefore a number of additional experiments were performed.

9.7.2 Axial variations in coolant flow (using a wet mixture)

The additional experiments were conducted by adjusting the coolant flow rates through the individual channels, using the manifold taps. Thus, beginning with a low coolant flow in the condenser, the flow was increased to two channels at a time, starting near the condenser exit, and moving back along the condenser until a high flow rate was achieved throughout. The results are presented in Figure 9-30.

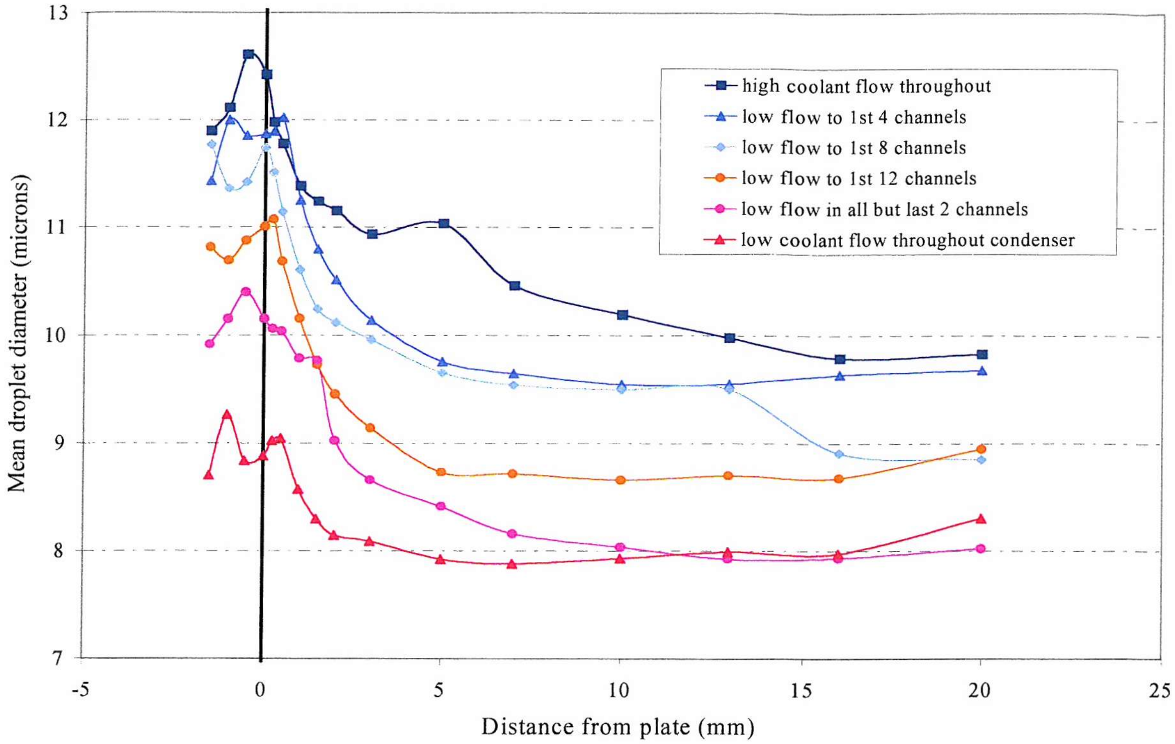

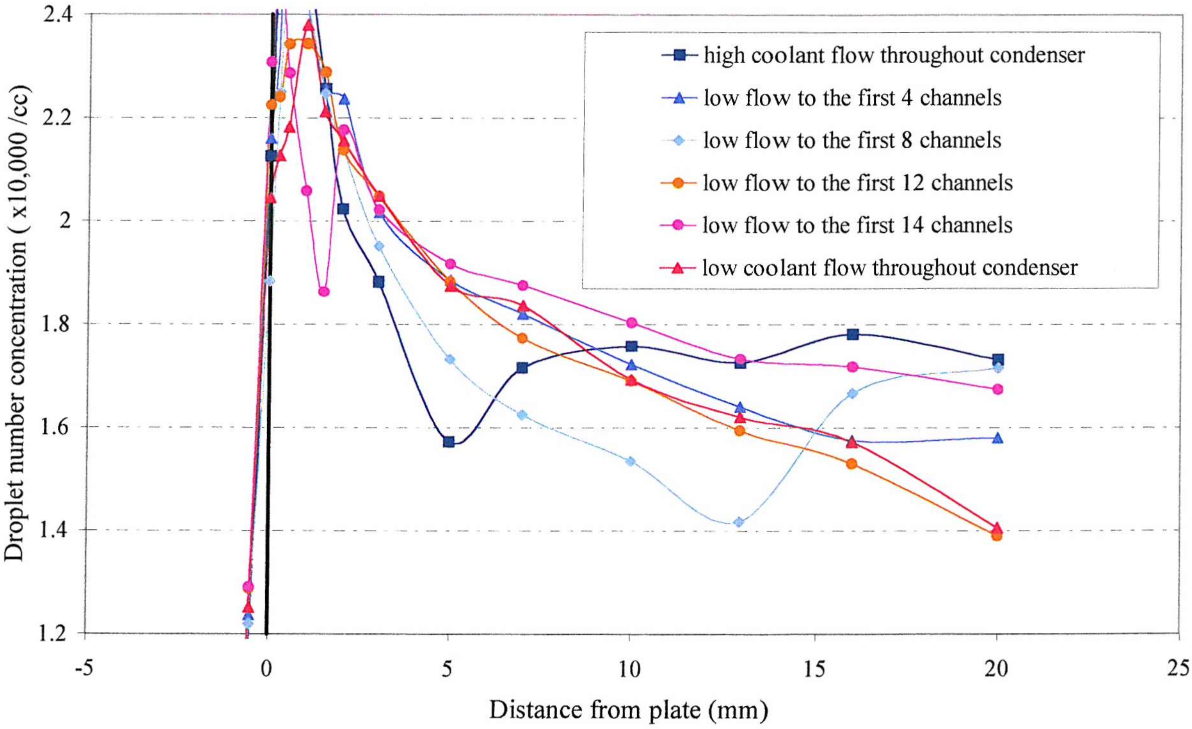

Figure 9-30. Mean droplet diameter and concentration measurements obtained during experiments on a wet mixture using different coolant flow rates through the individual condenser plate coolant channels.

As in the previous tests, the mean droplet diameter increases with coolant flow, while no trend is visible in the droplet concentration data. The increased number of droplet concentration measurements confirms the assumption that the mean droplet concentration at a point within the condenser is not affected by the coolant flow rate when the supersaturations within the condenser remain below that produced previously.

9.7.3 Increase in overall coolant flow (using superheated mixtures)

To conclude the investigations into the effects of coolant flow rate upon fog formation it was necessary to check the effect on superheated mixtures. The analysis presented in section 9.7.1 demonstrated that the supersaturation increases with coolant flow rate. Therefore, if the mixture is not supersaturated before entering the condenser, the droplet concentrations should increase with condenser flow rate, in addition to the mean droplet sizes. Several experiments were conducted, all of which produced increasing mean droplet diameters and droplet concentrations with increasing coolant flow rates.

9.8 *Effect of condenser length*

The final set of experiments conducted focussed on the length of the condenser. All experiments performed to this point had taken place with all four half-metre condenser sections in place. Thus before the test rig was decommissioned, these sections were removed one at a time to allow experiments with a condenser of length 0, 0.5, 1, and 1.5 metres. The results are presented in Figure 9-31.

The measurements conducted in the absence of any condenser sections confirmed that the number of droplets entering the condenser was negligible when operating with mixtures of relative humidity below 90%. Such mixtures were not completely droplet free however, since they contained a small number of haze droplets, the vast majority of which were less than 1μm in diameter. These droplets were invisible to the naked eye.

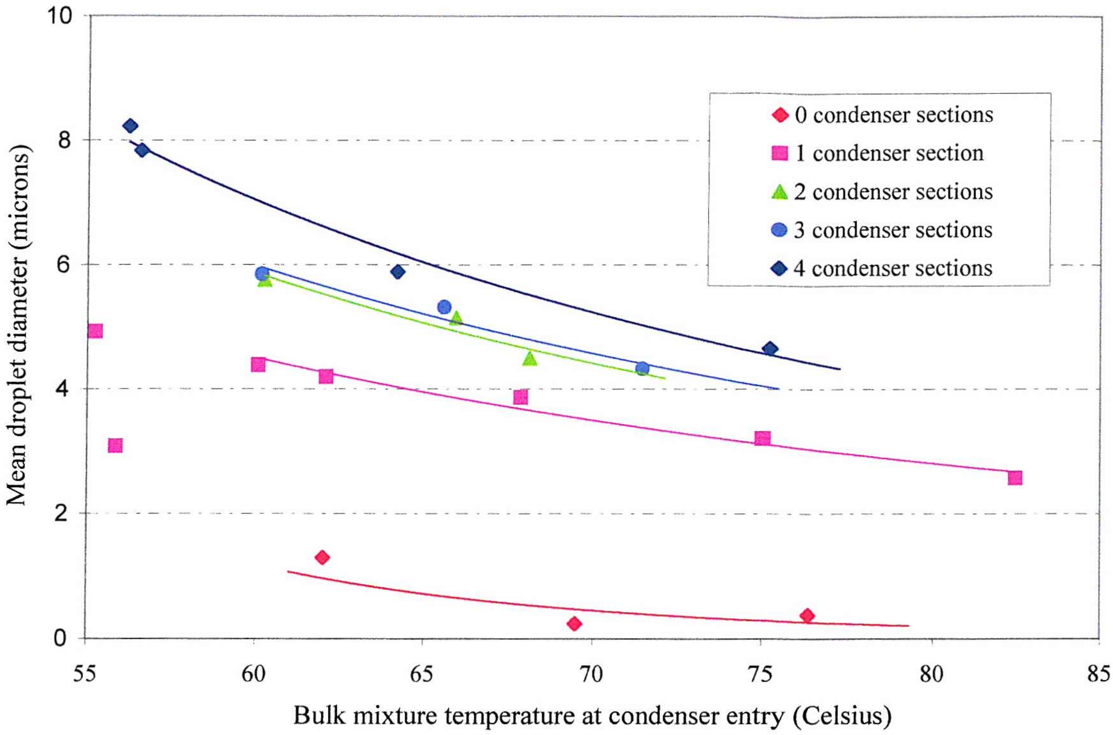

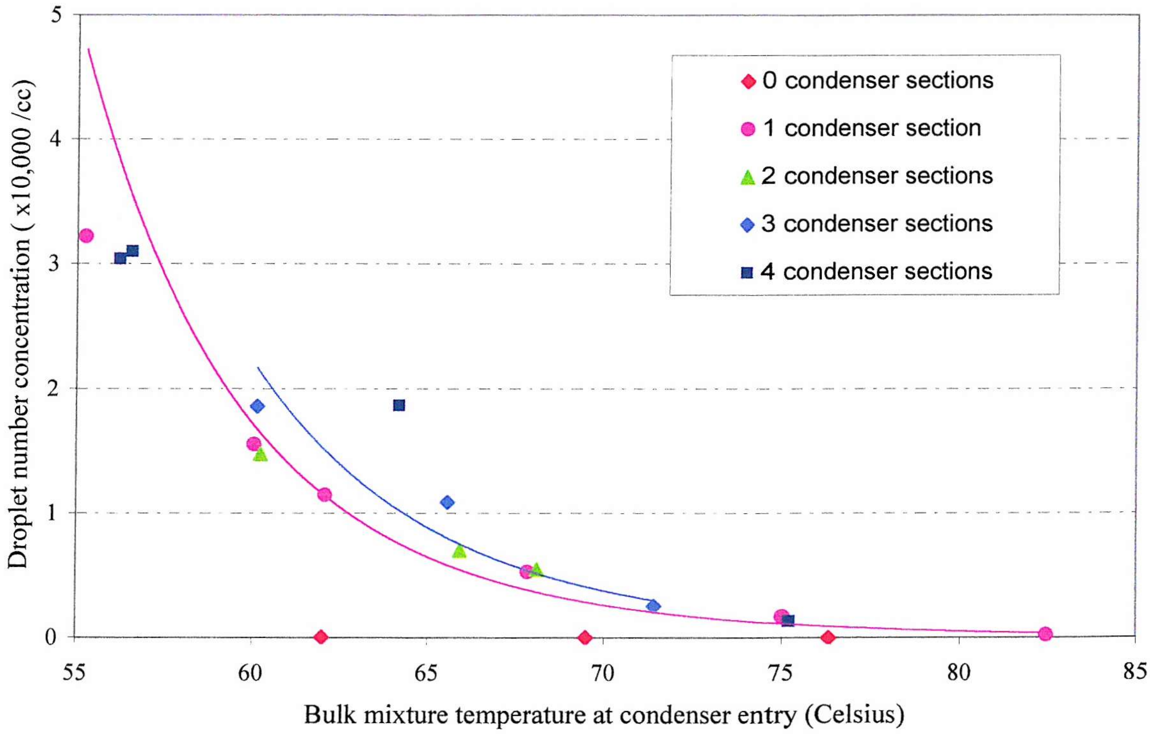

Figure 9-31. Mean droplet sizes and concentrations measured 5mm from the condenser wall during experiments with different condenser lengths on mixtures of steam to air mass flow ratio = 0.153 at condenser entry.

The mean droplet diameter increases with the number of condenser sections, or the condenser length. The greatest increase in mean droplet diameter occurs over the first 0.5 metres of the condenser, i.e. with the addition of a single condenser section. In a little over 0.25 seconds, the time it takes for the mixture to flow through the first section, the mean droplet diameter increases by over 3μm for a wide range of bulk mixture entry temperatures. This is greater than the mean droplet diameter increase in the following 3 sections or 1.5 metres. This is because the droplet growth rate at constant supersaturation is approximately proportional to the inverse of droplet radius (equation 2-35). Thus the droplets grow fastest when they are small and the first condenser section contains only small droplets. In the subsequent condenser sections droplet activation continues to produce small, fast growing droplets (provided the mixture was not wet at condenser entry), but these droplets exist alongside other larger drops activated in previous sections, which are slower growing.

The droplet number concentration graph, also presented in Figure 9-31, possesses the approximately exponential increase in droplet number concentration with decreasing bulk temperature observed in the results of previous experiments, for all condenser lengths. It is also possible to discern an increase in the droplet concentrations between the results obtained with one condenser section and those obtained with three (marked). However, there is no such clear distinction between the results obtained with the other condenser lengths. This is thought to be due to a combination of a lack of sufficient data and the general volatility of the droplet concentration measurements, as highlighted in section 9.7.

Example droplet size distributions measured using condenser lengths of 0.5 and 1.0 metres during experiments on mixtures of almost identical condition are presented in Figure 9-32. The increase in the mean size of the droplets and the size of the largest drops increases as the condenser length is doubled from 0.5 to 1m. The mixtures are both very nearly saturated at condenser entry and droplet activation and growth occurs rapidly. After only ~ 0.25 seconds and 0.5 metres of condenser there are as many droplets of 6 - 7μm in diameter as there are from 0.5 - 1.5μm. The droplet volume distribution shows how little mass resides upon droplets < 2μm in diameter.

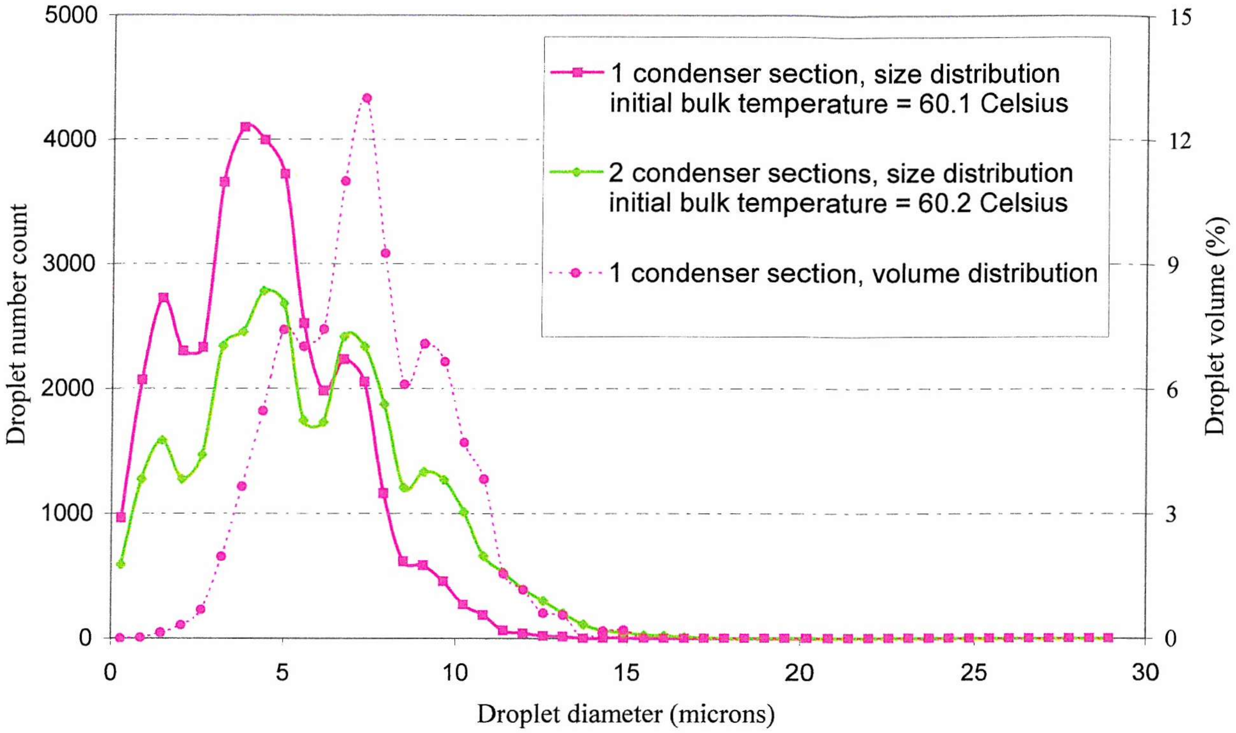

Figure 9-32. Droplet size distributions resulting from the cooling and partial condensation of two mixtures of almost identical condition in condensers of 0.5m and 1.0m.

When the mixture is superheated by ~ 8°C, equating to an initial relative humidity of only ~ 70%, the results, presented in Figure 9-33 change only slightly. The number of droplets detected has fallen and there are fewer droplets above 10µm but the peak in the distribution is still around 3.8µm. Once again, very little of the droplet mass exists in the form of droplets < 2µm in diameter even when a condenser section of only 0.5m length is used. This demonstrates just how rapidly the droplets grow during the initial stages of fog formation.

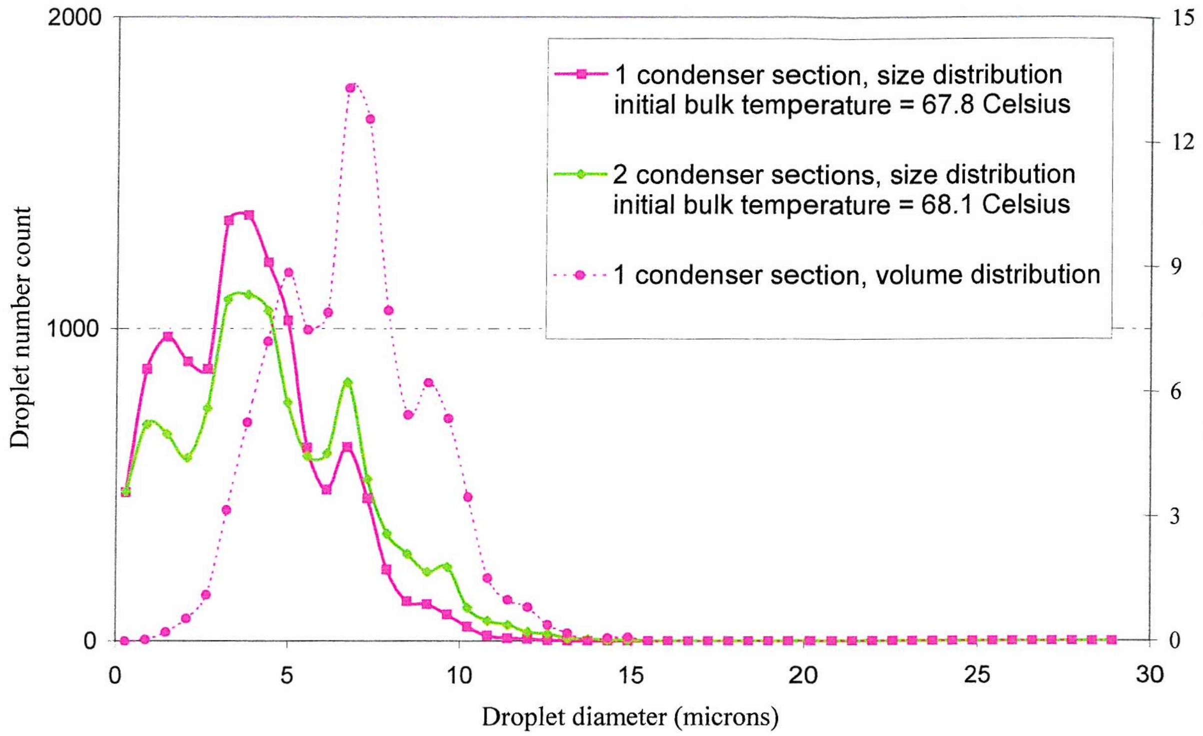

Figure 9-33. Droplet size distributions resulting from the cooling and partial condensation of two superheated mixtures of almost identical condition in condensers of 0.5m and 1.0m.

10. Further Work

The process of fog formation within industrial separators and condensers is far from straightforward. While it is possible to predict whether fog formation is likely to occur within a given condenser, a wide range of factors influence the rate of fog formation. Predicting the size distribution of the resulting droplets and the droplet number concentration is even more complicated, and this probably accounts for the present absence of any detailed work on the subject from the literature.

Not only do relatively small changes in the composition and temperature of the mixture lead to large differences in the number of droplets formed, but the droplet numbers and sizes often vary significantly across the cross-section due to the nature of the flow. A complete description of fog formation would require instantaneous knowledge of the local pressures and temperatures throughout the condenser. The turbulent nature of the flow makes this impossible, so simple models are required, based upon the bulk mixture properties, with which to estimate the supersaturations that lead to fog formation. Currently no such model exists and the development of a model would require a knowledge of the critical variables.

The present study has provided a useful insight into the variables of greatest significance to the droplet size and concentration of droplets formed during partial condensation. While the experimental results were confined to a relatively narrow range of temperatures, pressures etc. compared to those incorporated throughout the chemical process industry, the behaviour exhibited allows tentative predictions to be made for a much wider range of conditions. However, in order to ensure the predictions are accurate an extended experimental investigation would be required. Based on the results presented in this thesis, it is recommended that any future work in this area focus upon the influence of the following:

- Increased vapour pressures
- Increased condenser length
- Different total pressures
- Different gas – vapour mixtures

10.1 *Increased vapour pressures*

The partial vapour pressure in the mixtures studied ranged from approximately 0.04 bar to 0.4 bar. Since the total pressure within the condenser was approximately 1.013 bar (the condenser was open to atmosphere to allow access for droplet size measurement), this meant that maximum vapour mole fraction at condenser entry was ~ 0.47, and the vapour mass fraction ~ 0.35. The vapour flow rate could not be increased because to do so would have required more than 18kW of power, more than the boiler heating elements could supply. Also, it was not possible to increase the vapour mole fraction of the mixture by simply reducing the air flow because the resulting decrease in flow velocity would have lead to a transition to laminar flow.

The experiments and theoretical predictions both showed an increase in the fog flow rate with initial vapour pressure (and temperature). However, theoretical calculations performed when the vapour content of the mixture approached 50% began to show a reversal of the process. This may be attributable to the increased inaccuracy of equations requiring the vapour mole fraction at the interface, such as that for the molar flux of vapour towards the condenser surface. This is because the partial vapour pressure at the interface could only be estimated by assuming ideal gas behaviour. The errors then increase as the proportion of the non-ideal water vapour in the mixture becomes comparable to that of the air. However it is far from certain that this is the only cause of the change in the theoretical relationship between saturation temperature and fog formation rate. Since it was not possible to carry out experiments at sufficiently high saturation pressures to draw any firm conclusions it would be useful perform further investigations.

10.2 *Increased condenser length*

The length of the experimental condenser used during this investigation was restricted to 2m in order to accommodate it within the laboratory. The condenser had a relatively large hydraulic diameter of 6.66 x 10^{-2} m, hence the maximum value of the differential condenser area (total condenser surface area / cross-sectional area) was 120. While this was sufficient to allow the formation and growth of droplets to a reasonably large size it was insufficiently long for the bulk mixture temperature to closely approach the coolant temperature. It was predicted in chapter 4 that in a long condenser the fog formation rate would slow considerably and the supersaturation would begin to fall. It would be very interesting to check whether the number of small droplets inside the condenser falls significantly under such conditions as expected, when this is first noticeable and whether it is possible to detect the evaporation of any droplets as the saturation falls.

Note that in order to perform such experiments it would be more practical to use a condenser of reduced hydraulic diameter than it would be to accommodate a condenser of increased length. This has the added advantages of requiring smaller vapour flow rates and allowing mixtures of greater vapour content to be accommodated more easily.

10.3 *Different total pressures*

The experimental test rig was designed to be open to atmosphere in order to avoid the stringent regulations surrounding the manufacture and operation of pressure vessels and to allow measurement of the droplets as they left the condenser section. As a result the total pressure inside the condenser section was approximately 1.013 bar throughout the experimental program. Had the total pressure inside the condenser been increased yet the partial vapour pressure remained fixed, the proportion of inert gas would have risen. This would be expected to further impede the diffusion of vapour molecules towards the condenser surface, reducing the rate of mass transfer and increasing the rate of fog formation. It would be interesting to confirm this with a number of experiments at both increased and reduced total pressures.

If the total pressure inside a condenser is increased at constant temperature, but the ratio of partial vapour pressure to total pressure held constant, the relative humidity of the mixture would rise and the rate of fog formation and the size of the resulting droplets would be expected to increase.

10.4 *Different gas – vapour mixtures*

For reasons of simplicity, cost and primarily safety the vapour used throughout this experimental program was water vapour. However in the majority of fog formation related problems that occur within the chemical process industry, hydrocarbon vapours are involved. The greatest difference between hydrocarbon and water vapour mixtures is the size of the molecules. The hydrocarbons relevant to chemical plant operation usually comprise long chain molecules or aromatics (incorporating a benzene ring). The size of the vapour molecules adversely effects the rate of diffusion towards the cold walls and reduces the rate of wall condensation. Hence, the ration of heat to mass transfer is greater for hydrocarbon mixtures and fog formation is generally more likely and when it does occur will be more profuse. The computational predictions based upon a benzene – nitrogen mixture, presented in section 4.4.4, support the deductions presented above. However direct comparisons are impossible due to the differences in the saturation functions of the two vapours. The saturated vapour pressure at any given temperature is greater for benzene than for water vapour. The coolant temperature used inside industrial condensers is unlikely to vary too greatly from that of cold water (0 – 20°C), thus greater vapour pressures (and mole fractions) are necessary for fog formation in hydrocarbon mixtures.

Additional differences in droplet formation rates and sizes between mixtures of different constituents may arise owing to different critical saturation of the nuclei. The level of supersaturation required for droplet activation upon nuclei of a given size and composition may be markedly different when the condensing vapour is a hydrocarbon as opposed to water vapour. Indeed while soluble nuclei are much more conducive to droplet formation and comprise the vast majority of nuclei activated at low supersaturations, those nuclei that are soluble in water vapour may be insoluble in the relevant hydrocarbon and vice versa. Thus the supersaturation spectrum, that is, the graph of the number of activated nuclei against the supersaturation, may be of a different form than is the case for water vapour. This is therefore another factor that must be considered. It is very difficult to account for the supersaturation spectrum of the nuclei in a given situation, since this will vary from one plant to another and from one moment to the next. However such changes are likely to have relatively minor effects upon the droplet size distribution. In comparison it is unclear to what extent the condensation of different vapours will alter the supersaturation spectrum and the droplet size distributions and another reason why further experimental tests with hydrocarbons are desirable.

However, changes in the supersaturation spectrum may not have too significant an effect due to the abundance of potential nuclei. Mixtures of high vapour mole fraction and saturated mixtures will still result in greater fog formation rates from hydrocarbons. This, combined with the smaller latent heat released upon condensation mean it is probable that the droplets formed from hydrocarbon based vapour – gas mixtures will be larger than those formed from water vapour under similar conditions.

10.5 *Application to industry*

This final section addresses the application of this work to industry, specifically to the formation of fogs inside chemical plant separators and condensers. Such condensers come in many different forms and operate with a variety of different substances over a wide range of temperatures, total pressures, vapour pressures etc. The purpose of the majority of these condensers is to recover the maximum percentage of vapour from a gas – vapour mixture in the minimum amount of time. As a result, they employ high mixture flow rates and present large areas of cooled surfaces for condensation.

As discussed in the previous section, the vapours concerned are usually of a long chain or aromatic hydrocarbon and the conditions are such that fog formation will be common. The experimental program undertaken as a part of this study used a water vapour – air mixture. The results of the experiments consistently demonstrated the insignificance of the submicron droplets in respect to the total mass of droplets. This in itself offers reassurance for the process engineer. It suggests that the presence of a large number of submicron droplets in the volume size distribution of a fog exiting a condenser is more likely to be attributable to other sources, e.g. the mixing of saturated vapour streams at different temperature. However, as discussed previously in this chapter, the results of the experimental study are far from complete. A large number of further experiments would be required to confidently predict the exact form of the droplet size distributions formed inside all industrial condensers.

A reasonable estimate of the chances of a significant number of submicron droplets being produced inside a condenser may be obtained by plotting the relevant points on a graph of temperature against vapour pressure. Plotting the condition of the bulk mixture at condenser entry and the appropriate temperature of the condenser surface (assumed to be saturated) on the graph and drawing a straight line between the two (the line should be slightly concave for most hydrocarbons), this will not differ too greatly from the path of the bulk mixture condition as it flows through the condenser. If the temperature of the mixture at condenser entry is known this indicates how far along this line the mixture will be at condenser exit (otherwise this can be estimated via the rate of heat transfer). Comparison of this line with the saturation curve for the vapour then implies little fog if the line is constantly well below the saturation curve and profuse fog if it intersects it. The conditions most likely to produce difficulties with regard very small droplets appear to be highly superheated mixtures that approach saturation slowly near the end of the condenser.

11. Concluding Comments

The purpose of the research was to investigate the phenomena of fog formation from gas – vapour mixtures during partial condensation, paying particular attention to the number of submicron droplets formed. Fog formation was studied in terms of the onset of supersaturation and droplet activation, the significance of the condition of the mixture at condenser entry, and the effect of additional variables relating to the condenser. Combining visual observations with theoretical predictions and data collected during experiments upon water vapour – air mixtures in a partial condenser, a number of key points were established.

I. Fog formation occurred readily during the partial condensation of wet, saturated and superheated water vapour – air mixtures, over a wide range of conditions.

The fog formation took place by heterogeneous nucleation upon the foreign particles in the gaseous mixture. Due to the rapid temperature drop in the mixture within the condenser much larger supersaturations were produced than in atmospheric air. This lead to the activation and rapid growth of a large number of the nucleated droplets. After a period of only one second a clear distinction could be drawn between the activated droplets and the much smaller 'haze' droplets. Despite their greater numbers, the total mass of the liquid existing in the form of haze droplets is insignificant compared to that in the much larger, activated droplets.

II. Fog formation from a dry mixture began close to the condenser walls where, due to the form of the temperature and vapour pressure gradients extending from the cold condenser surface, the relative humidity / supersaturation of the mixture was greatest. Thereafter the region of supersaturation and fog formation extended from the cold wall into the bulk mixture until, when the humidity at the centre of the condenser had increased sufficiently, droplet activation occurred at all points in the condenser cross-section.

III. Throughout the process of fog formation the supersaturations within the condenser remained at their greatest close to the condenser walls. In addition, despite the turbulent nature of the flow the mean velocity increased with distance from the wall.

Hence droplets activated nearer the wall remained in the condenser for longer, on average, than those activated further away. These two points resulted in the greatest concentration of droplets and the greatest droplet sizes being located close to the condenser walls.

IV. The droplet concentration and mean droplet diameter of the fog formed increased as the bulk mixture temperature at condenser entry fell. Consequently the mass of the submicron droplets as a fraction of the total droplet mass decreased with decreasing bulk entry temperature. As the bulk entry temperature falls, so the initial relative humidity (or supersaturation) of the mixture increases. This increases the subsequent supersaturation within the condenser, and hence the resulting droplet concentrations and mean droplet sizes.

V. The results discussed in IV. above indicate that the relative humidity of a mixture is of more importance in determining the characteristics of the resulting fog than the temperature. Yet the mean droplet diameter of the fogs produced from mixtures of equal relative humidity at condenser entry was greater the higher the saturation temperature of the bulk mixture. However the theoretical predictions suggest this may only be true for a restricted range of saturation temperatures (that is, when the vapour mole fraction of the mixture is less than 50%)

VI. The mean droplet diameter decreased and the mass fraction of submicron droplets increased when the velocity of the mixture through the condenser increased. This was due to the reduced residence time of the mixture within the condenser and to a decrease in the ratio of heat to mass transfer to the condenser walls.

VII. The mean droplet diameter increased and the mass fraction of submicron droplets decreased when the flow rate of coolant through the condenser was increased. The increased coolant flow reduced the mean temperature of the condenser walls. This resulted in a greater increase in the rate of heat transfer than in the rate of mass transfer, producing greater supersaturations and greater droplet sizes.

VIII. Increasing the length of the condenser also lead to an increase in the mean droplet diameter and a reduction in the mass fraction of the submicron droplets in the fog at condenser exit. This was as a result of increasing supersaturations with distance along the condenser and the consequent increased times for droplet growth. The greatest droplet diameter increases were obtained within the first part of the condenser.

The points raised above were presented largely in terms of their effects upon the overall rate of fog formation in the condenser and upon the form of the droplet size distribution. A number of additional points, of particular significance to the numbers and mass fractions of the submicron droplets were noted during the investigations. These are summarised in the following three paragraphs.

IX. In wet mixtures, that is those that were supersaturated and contained a large number of droplets before entering the condenser, there was a complete absence of droplets of diameter between 0.1 and 2μm. The previous supersaturation of the mixture where the steam and air flows met resulted in droplet activation of all nuclei with critical supersaturations below the value reached within the mixture. The subsequent growth of the droplets depleted the supersaturation level and the levels inside the condenser did not reach that achieved on mixing. Hence there was no further activation within the condenser and, except for an insignificant increase in the size of the haze droplets, all condensation within the mixture occurred on the droplets activated upstream of the condenser. Thus the lack of small droplets during experiments on wet mixtures is explained by the absence of new droplet activations within the condenser accompanied by the condensational growth of those droplets already present to larger sizes.

X. In general, for superheated mixtures at condenser entry the total number of droplets below 1μm in diameter increased as the rate of fog formation increased. However, the number of submicron droplets as a proportion of the total number of drops falls. The comparable mass fraction is always smaller still, and was invariably much less than 1% of the total droplet mass. The only time this ratio rose above 1% was when the mixture was highly superheated at condenser entry, in which instances the total mass of fog formed was so small as to be inconsequential.

XI. The only occasions on which a large proportion of the droplets formed had diameters less than 1 μm, the supersaturations giving rise to droplet activation were short lived, curtailing droplet growth. The supersaturations were produced when two fluids of different temperature and humidity mixed. This occurred intermittently at two locations within the test rig, as the saturated mixture exiting the condenser mixed with the cool air outside and, if using sufficiently high steam to air mass flow rates, when the steam and air flows merged. The resulting droplet size distributions were masked by the pre-existence of larger droplets in the first case and by the subsequent growth of the small droplets in the condenser in the second case.

Hence, in dealing with fog formation problems relating to partial condensation, attentions should be paid to the possibility of sudden supersaturations that may occur in or around the condenser for reasons other than the simple cooling of the mixture faster than the vapour is condensed out.

Without any additional sources of supersaturation it appears unlikely than submicron droplets will form a significant fraction of the total droplet mass. This is because the supersaturations produced inside partial condensers are maintained, by the continued cooling, for a sufficiently long period of time to ensure that the majority of activated droplets grow to much larger sizes.

A Predicting the onset of fog formation

Inside partial condensers, gas-vapour mixtures flow over cold surfaces, and large radial temperature and vapour pressure gradients are established. Any fog formation, due to localised supersaturation, first appears in the region adjacent to the cold surface, at the condensate – mixture interface (section 3.4). Fog formation becomes possible when the saturation and actual partial vapour pressure (or temperature) profiles are tangent at the interface. This 'tangency condition' was first used by Johnstone, Kelley and McKinley [12] to study fog formation.

A.1 *Johnstone et al.'s predictions (The tangency condition)*

Johnstone et al. [12] derived the following equation to predict the conditions for which these profiles are first tangent

$$\frac{(p_v - p_s)}{(t_v - t_s)} = \left[\frac{(C\mu/k)^{1/3}}{(\mu/\rho D)^{1/3}}\right]\left(\frac{a}{1-e^{-a}}\right)\left(\frac{\lambda p_s}{RT_s^{\,2}}\right) \qquad \textbf{(A-1)}$$

where

$$a = \frac{(C\mu/k)^{2/3}}{(\mu/\rho D)^{2/3}} \ln\frac{P - p_s}{P - p_v} \ . \qquad \textbf{(A-2)}$$

p_v, t_v and p_s, t_s are the partial vapour pressure and temperature in the bulk mixture and at the interface respectively. All other letters have their usual meanings, as laid out in the nomenclature. The tangency condition defines the boundary between fogging and non-fogging conditions. Equation A-1 can therefore be used to predict the critical bulk conditions necessary for fog formation at a specified interface temperature (or vice versa). So using a simple algorithm (section A.4) it is possible to calculate and hence plot the range of critical conditions for fog formation at a given interface temperature, as in Figure A-1, below.

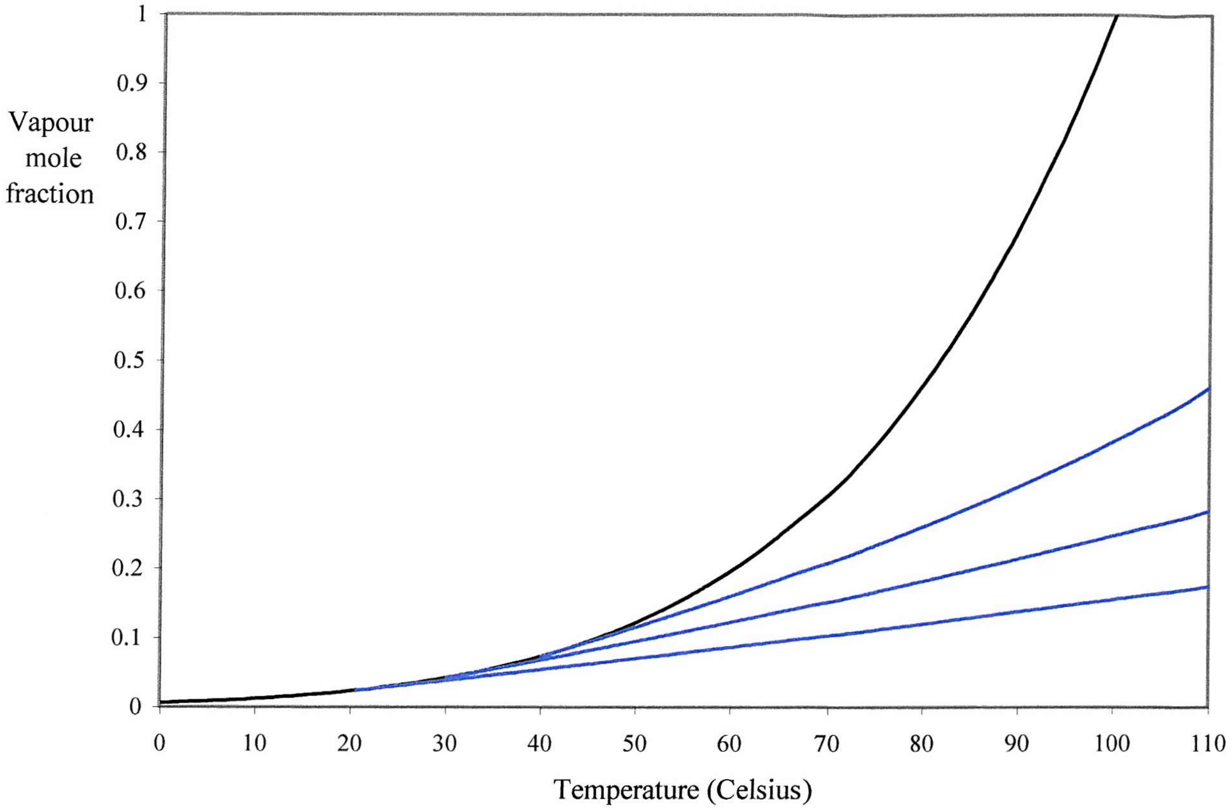

Figure A-1. Determination of the critical conditions for fog formation using the equations derived by Johnstone et al. (equation A-1), at interface temperatures of 20°C, 30°C, and 40°C.

Bulk conditions of the mixture lying above these lines at the specified interface temperatures will, according to Johnstone et al., result in fog formation. However as Brouwers demonstrates [47], the condition employed by Johnstone et al. is erroneous, and an improved equation is derived.

A.2 *Brouwers' predictions*

According to Brouwers the relation between vapour mole fraction and temperature perpendicular to the interface is often non-linear, and in the water vapour and air case is a convex curve. So by removing an (unjustified) simplifying assumption incorporated by Johnstone et al, Brouwers suggests the following equations are more accurate

$$\left.\frac{dG^+}{dt}\right|_{t=t_i} = \frac{Le\ c_p^+}{c_{p,v}^+}\left(\frac{c_i^+ - 1}{t_b - t_i}\right) \times \left(\exp\left\{\frac{c_{p,v}^+\,\delta_t}{c_p^+\,Le\,\delta_c}\ln\left(\frac{1-c_b^+}{1-c_i^+}\right)\right\} - 1\right) \rangle \left.\frac{dF^+}{dt}\right|_{t=t_i} \tag{A-3}$$

and

$$\left.\frac{dF^+}{dt}\right|_{t=t_a} = \left.\frac{dG^+}{dt}\right|_{t=t_a} = \frac{\delta_t}{\delta_c}\,\frac{\theta_c^+}{\theta_t^+}\,\frac{c_b^+ - c_a^+}{t_b - t_a} \tag{A-4}$$

where the thermal (Ackerman) correction factor is introduced as

$$\theta_t^+ = \frac{\dfrac{c_{p,v}^+\,\delta_t}{Le\ c_p^+\,\delta_c}\ln\left(\dfrac{1-c_b^+}{1-c_a^+}\right)}{\exp\left\{\dfrac{c_{p,v}^+\,\delta_t}{Le\ c_p^+\,\delta_c}\ln\left(\dfrac{1-c_b^+}{1-c_a^+}\right)\right\} - 1} \qquad (\equiv a) \tag{A-5}$$

and the diffusional mass transfer correction factor as

$$\theta_c^+ = \frac{\ln\left(1 - \dfrac{c_b^+ - c_a^+}{1-c_a^+}\right)}{-\dfrac{c_b^+ - c_a^+}{1-c_a^+}} \tag{A-6}$$

So using Brouwers' condition above and another simple algorithm (section A.5), a similar graph to Figure A-1 can be obtained of the critical conditions for fog formation at specified interface temperatures.

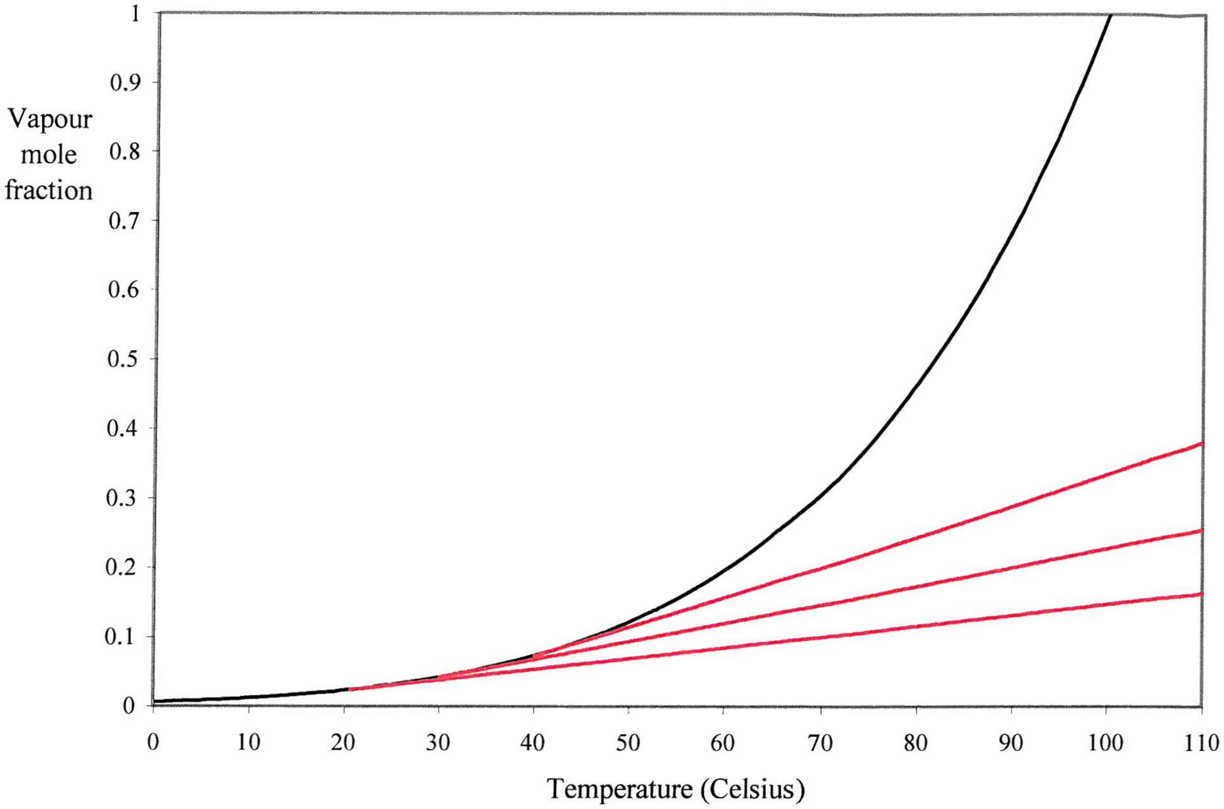

Figure A-2. Determination of the critical conditions for fog formation using the equation derived by Brouwers (equation A-3), also at interface temperatures 20°C, 30°C and 40°C.

A.3 *Summary*

The predictions of equations (A-1) and (A-3) can be compared more easily if Figure A-1 and Figure A-2 are superimposed onto one another, as shown over the page in Figure A-3.

From this it becomes apparent that Brouwers' condition is the more likely to predict fog formation, although at low interface and bulk temperatures the difference is slight. Both predict fog formation for a wide range of mixtures, for example at temperatures of 100°C or below, and an interface temperature of 20°C, a vapour mole fraction of 0.4 (vapour mass fraction ~ 0.3) will cause fogging. The results presented were obtained from theoretical studies into the critical conditions for fog formation in gas - vapour flows.

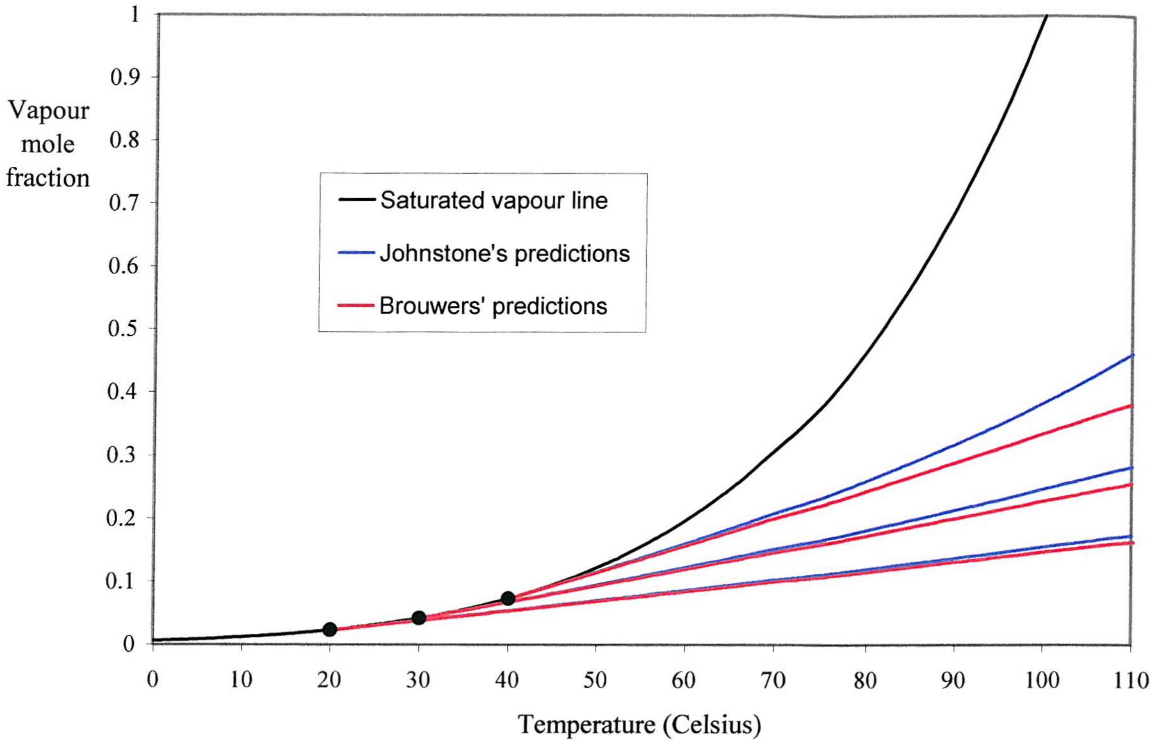

Figure A-3. The determination of the critical conditions for fog formation using both Johnstone et al.'s equation (A-1), and Brouwers' improved equation (A-4), again at the selected interface temperatures 20°C, 30°C, and 40°C.

The graphs drawn are specific to water vapour - air mixtures. Experimental results obtained by Johnstone et al. [12] using mixtures of nitrogen with sulphur, n-butyl alcohol and water vapour agreed reasonably well with Brouwers' equation. These experiments were confined to laminar flows, and point condensing conditions (i.e. a short condensing surface). Indeed, the predictions are only applicable at a single axial position. However, if the bulk mixture condition and interface temperature are known throughout the condenser, the equations can be applied at any axial location. The position of the onset of fog formation can then be accurately determined. The results apply equally well to turbulent mixtures. Equations A-3 and A-4 have been applied fruitfully in linearized form by Toor, Koch, and Hayashi et al. [16] to determine fog formation and assess the boundary of the superheated and saturated regions in flowing mixtures of dilute wall condensing water vapour [47]. Hence the results presented of equations A-3 and A-4 can be confidently used to predict whether a fog will form in gas-vapour mixtures.

A.4 *Computer program used to generate the results presented in Figure A-1.*

```
‘ PROGRAM FOR CALCULATING THE CRITICAL CONDITIONS FOR FOG FORMATION,
‘ USING EQUATION (9) FROM JOHNSTONE ET AL.(1950) [?], {EQUATION (A-1) HERE} THE
‘ RESULTS OF WHICH WERE PRESENTED GRAPHICALLY IN FIGURE A-1, FOR A WATER
‘ VAPOUR – AIR MIXTURE.

‘ First, open a text file to write the program results to
OPEN “A:\QBFOG.TXT” FOR APPEND AS #1

A = 40!                     ‘Define the interface temperature (Celsius), A
B = 0.072856                ‘Define the saturation vapour mole fraction, B (at temperature A)
C = 0.073                   ‘Define the initial vapour mole fraction to be considered, C
D = 43.359724#              ‘Define the relative latent heat of evaporation, D
                            ‘ (at temperature A)
E = A + 273.15              ‘Define the interface temperature (Kelvin), E

F = (120.27326# * D * B) / (E * E)      ‘Set the approximation to dF/dt, as used by Johnstone et al.

‘ Using equation (A-1), now calculate the critical bulk temperature for fog formation at increments of
‘ 0.001 in bulk vapour mole fraction, starting slightly above the interface vapour mole fraction.

DO
G = (1! – B) / (1! – C)
H = LOG(G)
J = 1.1414514# * H                  ‘1.1414514 =  1 / the third root of the Lewis number squared
K = 1! – EXP(-J)
L = J / K
M = 1.0683873# * L * F              ‘1.0683873 =  1 / the third root of the Lewis number
N = (C – B) / M
X = N + A                           ‘X is the critical bulk temperature
Y = C                               ‘Y is the critical bulk vapour mole fraction

f1$ = “#####.#####”
PRINT #1, USING f1$; Y; X           ‘Print these numbers to file so that suitable graphs may be
plotted

C = C + 0.001                           ‘Increment the vapour mole fraction
LOOP UNTIL ((Y > 0.9) OR (X > 140!))    ‘Repeat the calculation until the vapour mole fraction
                                        ‘is greater than 0.9, or the bulk temperature is greater
                                        ‘than 140 Celsius.
CLOSE #1                                ‘Close the text file.
STOP
END
```

A.5 *Computer program used to generate the results presented in Figure A-2.*

```
‘ PROGRAM FOR CALCULATING THE CRITICAL CONDITIONS FOR FOG FORMATION,
‘ USING BROUWERS’ EQUATIONS, {EQUATIONS (A-3) to (A-6) HERE} THE RESULTS OF
‘ WHICH WERE PRESENTED GRAPHICALLY IN FIGURE A-2, FOR A WATER VAPOUR –
‘ AIR MIXTURE.

‘ First, open a text file to write the program results to
OPEN “A:\QBFOG.TXT” FOR APPEND AS #1

A = 40!                     ‘Define the interface temperature (Celsius), A
B = 0.072856                ‘Define the saturation vapour mole fraction, B (at temperature A)
C = 0.073                   ‘Define the initial vapour mole fraction (vmf) to be considered, C
D = 0.0038825#              ‘Define  d(vmf) / d(interface temperature) :  dF/dt, D

E = A + 273.15              ‘Define the interface temperature (Kelvin), E

F = (120.27326# * D * B) / (E * E)      ‘Set the approximation to dF/dt, as used by Johnstone et al.

‘ Using Brouwers’ equations (A-3) to (A-6), now calculate the critical bulk temperature for fog
‘ formation at increments of 0.001 in bulk vapour mole fraction, starting slightly above the interface
‘ vapour mole fraction.

DO
E = ((1! – C) / (1! – B))
F = LOG(E)
G = 1.33713 * F             ‘1.33713 =  c(p)/c(p,v) x third root of the Lewis number squared
H = EXP(G) – 1!
J = G / H
K = ((C – B) / (1! – B))
L = LOG(1! – K) / -K
M = (((L / J) * 0.9359902#  * (C – B)) / D)     ‘0.9359902 = Third root of the Lewis number

X = M + A                                       ‘X is the critical bulk temperature
Y = C                                           ‘Y is the critical bulk vapour mole fraction

F1$ = “#####.#####”
PRINT #1, USING f1$; Y; X                       ‘Print these values to a file so that suitable graphs
                                                ‘may be plotted
C = C + 0.001                                   ‘Increment the initial vapour mole fraction value
LOOP UNTIL ((Y > 0.9) OR (X > 140!))            ‘Repeat the calculation at the new vapour mole
                                                ‘fraction until this value is greater than 0.9, or the
                                                ‘bulk temperature is greater than 140 Celsius.

CLOSE #1
STOP
END
```

B. Mass transfer

B.1 *Introduction*

In this appendix the basics of mass transfer theory are introduced. Starting from first principles, the basic equations of mass transfer and ordinary diffusion are presented, and discussed in relation to surface condensation of the vapour component of a gas-vapour mixture. In this case an additional flow, known as the Stefan flow, arises which exactly counterbalances the diffusion of inert gas away from the surface (section 3.3).

The models most commonly used to study mass transfer problems are then reviewed and assessed. The film model is subsequently applied to the equations of motion, energy and continuity across a thin film, accounting for the effect of the Stefan flow (resulting in a predicted augmentation of the rates of mass, heat and momentum transfer in the case of condensation). The results are compared to solutions obtained by neglecting this additional flow leading to the derivation of correction factors, which are commonly used to account for the Stefan flow. These correction factors provide a simple and effective way of calculating heat and mass transfer rates associated with the partial condensation of a gas-vapour mixture from standard empirical formulae.

B.2 *Mass transfer*

Mass transfer "refers to the motion of molecules or fluid elements caused by some form of potential or 'driving force'" [44]. The condensation of a vapour onto a cold surface from an inert gas / vapour mixture is an example of mass transfer. Vapour next to the cold surface cools and condenses onto it. Thus the vapour concentration adjacent to the surface falls. A concentration gradient is set up and more vapour is transported towards the cold surface, where it again condenses to a liquid. Hence mass transfer takes place within the vapour phase, in the direction of the phase boundary. In this case mass is also transferred between phases. Within the vapour phase, this transport takes place by molecular diffusion, eddy diffusion or both.

Molecular diffusion may occur as a result of concentration, temperature, or pressure gradients, or because a directed external electrical or other potential field is applied to a mixture.
The diffusion of a vapour in a binary system of a vapour and an inert gas occurs because of a concentration gradient of vapour [58]. This type of molecular diffusion is known as *ordinary diffusion*, since it is the diffusion which is observed in most situations of technical importance [44]. It results from the thermal motion of the molecules, which move at high speeds over short distances before colliding.

B.3 *Rate equations for molecular diffusion*

The fundamental equation of mass transport is Fick's law, (or Fick's first law of diffusion), which describes the movement of one species, say A, through a binary mixture of A and B because of the concentration gradient of A. [So in the case to be considered, A ≡ vapour, and B ≡ inert gas.] Note that in it's most general form, Fick's law describes the diffusion of one species in a multi-component system. Here it is confined to binary mixtures only.

Fick's law, neglecting temperature gradients, pressure gradients and external forces (which are usually minor), is expressed by the simple differential equation

$$J_A = -D_{AB}\frac{\partial c_A}{\partial x}. \tag{B-1}$$

It defines the diffusion coefficient, D_{AB}, for species A in a mixture of A and B, as the ratio of the unidirectional molar flux density, J_A , to the negative gradient of the molar concentration in the direction of diffusion [44]. It is negative because species A diffuses in the direction of decreasing concentration of A. To complete the definition of D_{AB}, it is specified that the flux density, J_A , must be referred to a plane across which there is no net volume transport. This plane may move with respect to the fixed apparatus, even though the medium in which diffusion occurs is completely stagnant.

The molar flux of A relative to the apparatus, N_A , is far more useful, and may be obtained from equation (B.1) as follows. Diffusion in the y-direction only shall be considered here, as is the case in wall condensation of a vapour where the bulk flow is parallel to the walls (i.e. in the x-direction).

The velocity of the plane of no net volume transport is given by [44],

$$\overline{U}_y = \sum_j N_j \overline{V}_j \quad , \qquad \textbf{(B-2)}$$

which for a binary mixture of A and B becomes

$$\overline{U}_y = N_A \overline{V}_A + N_B \overline{V}_B \quad , \qquad \textbf{(B-3)}$$

where $\overline{U}_y$, N_A, and N_B are defined with reference to the fixed apparatus. $\overline{V}_A$ and $\overline{V}_B$ are the partial molal volumes of A and B respectively. Then from the definitions of N and J,

$$N_A = \overline{U}_y c_A + J_A \quad , \qquad \textbf{(B-4)}$$

so

$$N_A - c_A\left(N_A \overline{V}_A + N_B \overline{V}_B\right) = J_A = -D_{AB}\frac{dc_A}{dy} \quad , \qquad \textbf{(B-5)}$$

or

$$N_A = -D_{AB}\frac{dc_A}{dy} + c_A(N_A \overline{V}_A + N_B \overline{V}_B) \quad . \qquad \textbf{(B-6)}$$

The first term on the right hand side is the flux due to the diffusion of vapour, A. The second term is the additional flux resulting from the movement of the plane of no net volume transport. This flow is known as 'Stefan flow' and results in the movement of both vapour and gas towards the wall. The flow is such that the associated flow of gas, B, exactly counterbalances the diffusion of gas away from the wall. Hence there is a net flow of vapour only towards the condensing surface. Note that in the absence of condensation, the total flux of A would be that occurring due to diffusion only, hence

$$N_A = -D_{AB}\frac{dc_A}{dy} \qquad \textbf{(B-7)}$$

Returning to the pertinent case of vapour condensation, when large mass transfer rates are considered, the Stefan flow (perpendicular to the direction of bulk fluid flow) may have a significant effect on the heat transfer rate. In order to account for this effect, a detailed study within the immediate region of the phase boundary, or interface, is needed. Being difficult to observe experimentally, it is necessary to develop a model of the process.

B.4 *Models*

There are three such models which are widely used. These are the (stagnant) film model, the penetration model, and the turbulent boundary layer model. The important aspects of each model shall be considered, followed by their applicability to the study of wall condensation from an inert gas - vapour mixture.

B.4.1 The film model

This is physically the most simple description of the effect of the mass transfer. As Sherwood et al. [44] point out, "the most important relevant fact pertaining to mass transfer to or from a turbulent stream is that the resistance to transfer is confined largely to a thin region adjacent to the interface." Further, within this 'film' there is no eddy motion [58].

During the condensation of water from a water vapour - air mixture, the problem of interest here, this interface defines the boundary between the liquid and gaseous phases. When fluid flows over such a phase boundary, its local velocity approaches zero at the surface. Furthermore, the only flow normal to the surface is generally that corresponding to the mass-transfer flux. The fluid in immediate contact with the fixed surface can properly be said to be stagnant.

The fact that resistances to mass transfer (and heat transfer) are confined largely to a region close to the phase boundary, suggests the idea of a thin film adjacent to the surface, over which the fluid flow is turbulent. Since this thin layer is stagnant, the transport must be due to molecular diffusion only. So, in summary, "the picture then is that of a thin stagnant film through which transport is solely by molecular diffusion, and which is of such a thickness y_o as to explain the experimentally observed magnitude of the mass-transfer resistance" [44]. With this picture it is logical to treat mass transfer at a phase boundary by the use of the equations for molecular diffusion (equation B-6). Hence equations for the steady-state diffusion of only one of the two species in a binary mixture of ideal gases may be obtained by integrating equation B-6, which may first be reduced to

$$N_A(1-Y_A) = -D_{AB}\frac{dc_A}{dy} = -\frac{D_{AB}P}{RT}\frac{dY_A}{dy} \tag{B-8}$$

with $V_A = V_B = RT/P$, $c_A = PY_A/RT$, $N_B = 0$, and the volume fraction c_AV_A equal to the mole fraction Y_A. Then integrating across the film of thickness y_o,

Then integrating across the film of thickness y_o,

$$\int_0^{y_o} N_A dy = \int_{Y_{A1}}^{Y_{A2}} \frac{D_{AB}P}{RT}\frac{1}{1-Y_A}dY_A \tag{B-9}$$

gives

$$N_A = \frac{D_{AB}P}{RTy_o}\ln\left(\frac{1-Y_{A2}}{1-Y_{A1}}\right) \qquad \left[\equiv \frac{D_{AB}P}{RTy_o}\left(\frac{c_{A1}-c_{A2}}{c_{BM}}\right)\right] \tag{B-10}$$

a form of the well known Stephan equation [48]. The situation is illustrated in figure B.1. The concentrations c_{A1} and c_{A2} relate to those of water vapour in air at the interface (phase boundary), and in the bulk mixture respectively.

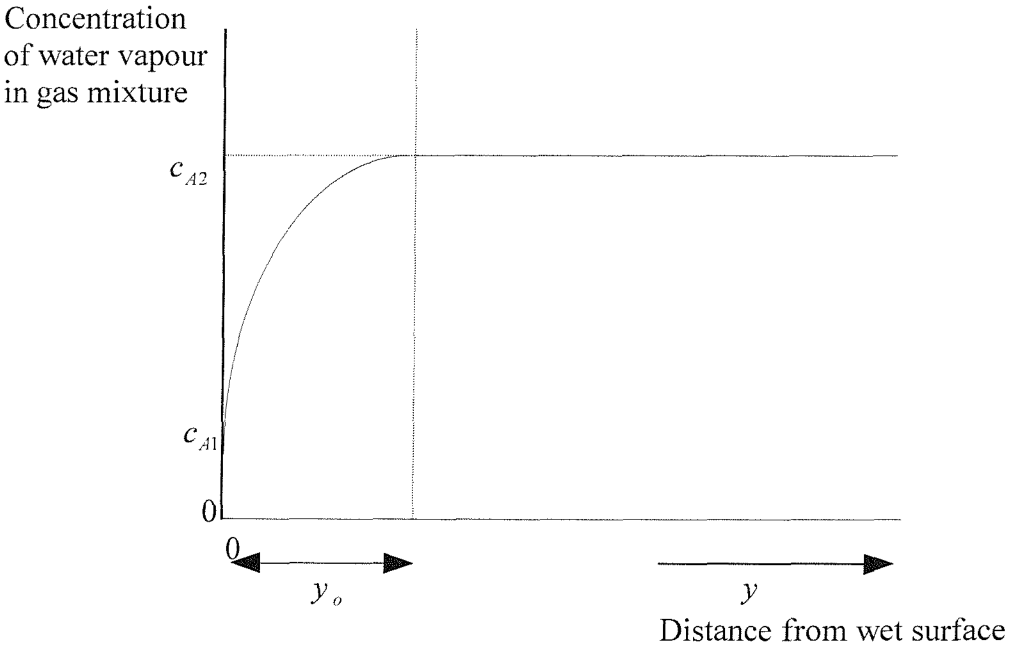

Figure B-1. Film model for mass transfer at a phase boundary, e.g. the condensation of water vapour from a water vapour - air mixture onto a cold surface.

For comparison, consider now a case in which the Stefan flow may be neglected. The total vapour flux is then given by equation B-7. Integrating across the film of thickness y_o,

$$\int_0^{y_o} N_A dy = \int_{c_{A1}}^{c_{A2}} - D_{AB} dc_A \tag{B-11}$$

i.e.

$$N_A y_o = -D_{AB}\left[c_{A2} - c_{A1}\right] = \frac{-D_{AB}P}{RT}\left[Y_{A2} - Y_{A1}\right] \tag{B-12}$$

Thus, the total molar flux is given by

$$N_A = \frac{-D_{AB}P}{RTy_o}\left[Y_{A2} - Y_{A1}\right] \tag{B-13}$$

B.4.2 Penetration Theory

The penetration theory was propounded in 1935 by Higbie, who was investigating whether or not a resistance to transfer existed at the interface when a pure gas was absorbed in a liquid [42]. The theory pictures a small fluid element, of uniform (solute) concentration, c_o, being brought to the interface by the turbulent eddies within the fluid. Hence, fluid with an initial composition corresponding to that of the bulk fluid remote from the interface, is suddenly exposed to the second phase (liquid). It is assumed that equilibrium is immediately attained by the surface layers, and that a process of unsteady state molecular diffusion then occurs. The fluid element is in contact with the phase boundary for a definite interval of time, γ, after which it is re-mixed with the bulk. The concentration at the boundary remains constant at c_{A1}. The diffusion then proceeds as a transient process, the rate decreasing with time. Throughout, the existence of velocity gradients within the fluid is ignored and the fluid at all depths is assumed to be moving at the same rate as the interface [42].

Then since, neglecting convective flux,

$$N_A = -D_{AB}\frac{\partial c}{\partial y}, \tag{B-14}$$

the average mass transfer rate over the time , γ , is given by

$$N_A = 2(c_{A1} - c_o)\sqrt{\frac{D_{AB}}{\pi\gamma}} \quad , \tag{B-15}$$

from which the time-average mass transfer coefficient is obtained as

$$k_c = \frac{N_A}{(c_{A1} - c_o)} = 2\sqrt{\frac{D_{AB}}{\pi\gamma}} \, . \tag{B-16}$$

No precise value can be assigned to γ in any industrial equipment, but its value will clearly decrease as the degree of agitation of the fluid is increased. [42]

B.4.3 The boundary layer model

This model pertains to transport between a fixed surface (wall) and a turbulent stream of fluid. There is no slip at the wall and turbulence is damped out in the fluid immediately in contact with it. In this limit transport is by molecular diffusion only, since there is no mixing or eddy diffusion normal to the wall. Eddy diffusion is rapid in the turbulent stream at large distances from the wall, where the contribution of molecular diffusion is relatively insignificant [44]. It is proposed that both molecular and eddy diffusion play a role in the intermediate region, and that at any distance y from the wall the rate of mass transfer can be expressed by

$$N_A = -\left(D_{AB} + E_D\right)\frac{\partial c}{\partial y} \tag{B-17}$$

Again, assuming simply that the flux is proportional to the concentration gradient normal to the wall, the convection term in the equation for molecular diffusion, $c_A N_A \overline{V}_A$, being neglected. As opposed to the film and penetration models however, the total diffusion coefficient has been used, which is the sum of the diffusion coefficient, D_{AB} , and the eddy diffusion coefficient for mass transfer, E_D. Hence, it is assumed that molecular and eddy diffusion take place in parallel. Sherwood notes that this last point has been questioned, though it seems not unreasonable [44]. The region of importance is so thin that even in the case of turbulent flow in a round pipe the flux N_A can be taken to be essentially independent of y. If E_D can be expressed as a function of y, the equation can be integrated to relate c to y and the steady state flux. The utility of this model evidently depends on a knowledge of E_D as a function of y.

B.4.4 Model summary

As Coulson et al. [42] point out, the penetration theory has been developed for conditions of equimolar counterdiffusion only; the equations are too complex to solve explicitly for transfer through a stationary carrier gas. The boundary-layer model is similarly complex, and there appear to have been no direct measurements of the relation between E_D and y, utilised in this model [44].

The film model, on the other hand, though accepted to be a gross oversimplification of the actual conditions near a phase boundary, (e.g. a sharp boundary at y_o is implied, though no such boundary actually exists) and no basis is suggested for the prediction of y_o, has proved remarkably useful [17]. Further, Brouwers also points out that satisfactory agreement has been found in the past between the predictions of the film model, the boundary-layer model, and experimental results. The film model has proved particularly effective in predicting the effect of large mass transfer rates on heat transfer (as is the case in the partial condensation of a gas mixture).

Hence the film model is to be used here, and applied to channel flow to obtain the correction factors for the additional velocity (due to diffusion) on heat, mass and momentum transfer. Though the correction factors supplied by the film model are based on a simple physical model, they are widely used in engineering applications. This is due to the fact that the physical accuracy of the correction factors is generally sufficiently high for engineering end purposes, and they are easily applicable [17].

B.5 *The film equations and their solutions*

The effect of the Stefan flow upon the overall rate of mass transfer predicted using the film model can be obtained by comparing equations B-10 and B-13. The additional mass flux is often accounted for by the inclusion of a correction factor in the basic equation [17]. The Stefan flow also augments the rates of heat and momentum transfer during condensation.

In this section the equations describing heat, mass and momentum transfer, for a binary gas mixture, are to be derived and solved analytically using the film model described in section B.4.1. Following the derivations presented by Brouwers and Chesters [17], the equations are to be derived in terms of mass fluxes $\dot{m}$, as opposed to molar fluxes N_A etc., used in previous sections, and by many authors e.g. Sherwood et al. [44], and Bird et al. [59]. The solutions obtained by each method may be shown to be equivalent. These solutions are then used in the next section to derive the film model correction factors.

B.5.1 Mass transfer

Consider a film containing a vapour and a non-condensable gas, as depicted in Figure B-2 below, through which there is a transfer of heat, mass and momentum in the y-direction, with flow parallel to the wall in the x-direction.

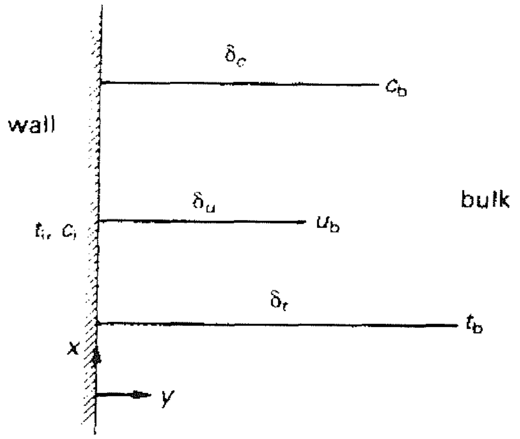

Figure B-2. The film. [17]

At the wall (or interface, e.g. denoting the surface of a falling liquid film, $y = 0$) the vapour mass fraction is c_i and the temperature t_i. At a distance δ_c the bulk vapour mass fraction c_b, is attained, at a distance δ_t the bulk temperature, t_b, and at a distance δ_u the bulk velocity relative to the wall, u_b. In the analysis to be presented, the physical properties in the film are assumed to be constant and the mixture to behave as an ideal, incompressible Newtonian gas. The full Fickian diffusion equation, without source terms, reads

$$\rho\left(\frac{\partial c}{\partial \gamma}+u\frac{\partial c}{\partial x}+v\frac{\partial c}{\partial y}\right)=\rho D_{AB}\left(\frac{\partial^2 c}{\partial x^2}+\frac{\partial^2 c}{\partial y^2}\right). \tag{B-18}$$

Confining the study to steady-state diffusion, $\partial c/\partial \gamma = 0$, and the variation of c (and t and u) in the x-direction can be neglected in comparison to changes in the y-direction (across the film), hence equation B-18 reduces to

$$\rho v\frac{dc}{dy}=\rho D_{AB}\frac{d^2 c}{dy^2}\ . \tag{B-19}$$

In this equation the convective velocity, v, caused by the diffusion of vapour through the mixture, towards the surface, is given by equation (B-8) written in terms of mass fractions, i.e.

$$v=-\frac{D_{AB}}{1-c}\frac{dc}{dy}\ . \tag{B-20}$$

When this velocity is substituted into equation (B-19), an ordinary differential equation (O.D.E.) of c in y is obtained. The boundary conditions on c are given by

$$c(y=0)=c_i \tag{B-21}$$

and $$c(y=\delta_c)=c_b\ . \tag{B-22}$$

Hence by solving the resulting O.D.E. and applying the above boundary conditions (B-21) and (B-22), the following distribution of the vapour fraction in the film as a function of y is obtained

$$c(y)=1-(1-c_i)\exp\left\{\frac{y}{\delta_c}\ln\left(\frac{1-c_b}{1-c_i}\right)\right\}. \tag{B-23}$$

B.5.2 Heat transfer

In order to investigate the effect of the induced velocity on heat transfer, (caused by the diffusion, or mass transfer, towards the interface), attention is now focused on the energy equation of the film. Neglecting variations of t in the x-direction, neglecting viscous dissipation, heat sources or radiation, the equation becomes

$$\rho c_{p,v} v \frac{dt}{dy} = k \frac{d^2 t}{dy^2} \qquad \textbf{(B-24)}$$

with the boundary conditions

$$t(y=0) = t_i \qquad \textbf{(B-25)}$$

and $t(y=\delta_t) = t_b$. **(B-26)**

Substitution of equations (B-20) and (B-23) into equation (B-24), solution of the resulting equation, and application of the above boundary conditions (B-25) and (B-26) leads to the following temperature profile in the film

$$t(y) = (t_b - t_i)\left[\frac{\exp\left\{\frac{y}{Le_v\,\delta_c}\ln\left(\frac{1-c_b}{1-c_i}\right)\right\}-1}{\exp\left\{\frac{\delta_t}{Le_v\,\delta_c}\ln\left(\frac{1-c_b}{1-c_i}\right)\right\}-1}\right] + t_i \qquad \textbf{(B-27)}$$

where $Le_v \left(\equiv Le\, c_p / c_{p,v}\right)$ is the modified Lewis number.

B.5.3 Momentum transfer

To examine the influence of the induced velocity on the wall shear stress, the momentum equation is investigated. Again, neglecting gradients of properties in the x-direction, as well as volume forces, this becomes

$$\rho v \frac{du}{dy} = \eta \frac{d^2 u}{dy^2} \qquad \textbf{(B-28)}$$

with the appropriate boundary conditions on u at the wall and bulk,

$$u(y=0)=0 \tag{B-29}$$

$$u(y=\delta_u)=u_b \ . \tag{B-30}$$

Substituting equations (B-20) and (B-23) into equation (B-28), solving the resulting equation and applying the boundary conditions (B-29) and (B-30), above, results in an equation of the same form as that for the temperature profile,

$$u(y) \ = \ u_b\left[\frac{\exp\left\{\dfrac{y}{Sc\delta_c}\ln\left(\dfrac{1-c_b}{1-c_i}\right)\right\}-1}{\exp\left\{\dfrac{\delta_u}{Sc\delta_c}\ln\left(\dfrac{1-c_b}{1-c_i}\right)\right\}-1}\right] \ , \tag{B-31}$$

where the Schmidt number , $Sc\ (=\eta/\rho D_{AB})$, has been introduced.

In this section the vapour concentration, temperature, and velocity profiles in the film have been deduced, following the derivations presented by Brouwers and Chesters [17], and are expressed in equations (B-23), (B-27) and (B-31) respectively. These are now to be used to derive the correction factors mentioned earlier.

B.6 *Correction factors for the effect of the induced velocity.*

Now the classical film model correction factors for mass, heat and momentum transfer are to be established by comparing the transfer rates in the binary film with and without the induced velocity, employing the profiles deduced in the previous section.

B.6.1 Mass transfer

The mass transfer from the fluid to the wall is governed by Fick's law, which from equation (B-20) accounting for the induced velocity is written

$$\dot{m} \equiv \ -\rho v(y=0) \ = \ \frac{\rho D_{AB}}{1-c}\left.\frac{dc}{dy}\right|_{y=0} \ . \tag{B-32}$$

Without accounting for the induced velocity, the mass transfer is simply described by

$$\dot{m} = g_m \frac{c_b - c_i}{1 - c_i} \tag{B-33}$$

since without the induced velocity, the profile of c (and t and u) as a function of y is a straight line (the limiting cases of equations (B-23), (B-27), and (B-31) for small c). The mass transfer coefficient g_m appearing in equation (B-33) is given by

$$g_m = \frac{\rho D_{AB}}{\delta_c} \tag{B-34}$$

To derive the diffusional transport of mass from the mixture to the wall, equations (B-32) and (B-34) are applied to equation (B-23), giving

$$\dot{m} = -g_m \ln\left(\frac{1 - c_b}{1 - c_i}\right) . \tag{B-35}$$

The film model correction factor is now introduced by comparing the expression for the transfer rate with induced velocity and that without, i.e. equations (B-35) and (B-33). Hence the classical film model correction factor is derived:

$$\Theta_c = \frac{-\phi_c}{e^{-\phi_c} - 1} \tag{B-36}$$

with the diffusional dimensionless mass flux

$$\phi_c = \frac{\dot{m}}{g_m} \quad , \tag{B-37}$$

where $\dot{m}$ follows from equation (B-35).

B.6.2 Heat transfer

The heat transfer from the fluid to the wall is described by Fourier's law as

$$q = k \left. \frac{dt}{dy} \right|_{y=0} \tag{B-38}$$

where q is the heat flux at the wall. For a negligible induced velocity the heat transferred through the film is simply given by

$$q = h_g \left(t_b - t_i \right) \quad , \tag{B-39}$$

with the heat transfer coefficient, h_g, defined as

$$h_g = \frac{k}{\delta_c} \ . \tag{B-40}$$

The heat transfer from the fluid to the wall, when accounting for an induced velocity due to mass transfer, is obtained by combining equations (B-27), (B-35), (B-38) and (B-40), resulting in

$$q = h_g \left(t_b - t_i \right) \left[\frac{-\dfrac{\dot{m} c_{p,v}}{h_g}}{\exp\left(-\dfrac{\dot{m} c_{p,v}}{h_g} \right) - 1} \right] \ . \tag{B-41}$$

On comparison of equation (B-41) with equation (B-39) the following film model correction factor is derived:

$$\Theta_t = \frac{-\phi_t}{e^{-\phi_t} - 1} \tag{B-42}$$

with as thermal dimensionless mass flux

$$\phi_t = \frac{\dot{m} c_{p,v}}{h_g} \ . \tag{B-43}$$

The thermal correction factor (B-42) is commonly referred to as the Ackermann correction factor.

Bird et al. [59], and Sherwood et al. [44] present equivalent equations for the heat transfer and Ackermann correction factor in terms of the molar flux, namely

$$q_H = h \left(t_1 - t_2 \right) \frac{C_o}{1 - \exp\left(- C_o \right)} \tag{B-44}$$

and

$$C_o = \left(N_A C_{pA} + N_B C_{pB} \right) / h \tag{B-45}$$

where q_H and C_o are directed away from the surface. (Hence for condensation, q_H, equation (B-41), and C_o are both negative). Note that in the case of condensation from an inert gas - vapour mixture, there is no flux of inert gas towards the surface, i.e. $N_B = 0$.

B.6.3 Momentum transfer

The shear stress exerted by the fluid on the wall is governed by Newton's law

$$\tau = \eta \left.\frac{du}{dy}\right|_{y=0} \quad . \tag{B-46}$$

Without mass transfer the shear stress is described by

$$\tau = \tfrac{1}{2}\rho f u_b^2 \tag{B-47}$$

with the friction coefficient defined as

$$f = \frac{2\eta}{\rho u_b \delta_u} \tag{B-48}$$

since $\left.\frac{du}{dy}\right|_{y=0}$ across the film without mass transfer $= \frac{u_b - 0}{\delta_u}$.

The interfacial shear stress exerted by the fluid on the wall, when mass transfer is occurring, may be determined by combining equations (B-31), (B-35), (B-46) and (B-48) to give

$$\tau = \tfrac{1}{2}\rho f u_b^2 \left[\frac{-\frac{2\dot{m}}{\rho f u_b}}{\exp\left(-\frac{2\dot{m}}{\rho f u_b}\right) - 1} \right] \quad . \tag{B-49}$$

Hence, on comparison of equation (B-49) with equation (B-47), the film model correction factor for momentum transfer is obtained

$$\Theta_u = \frac{-\phi_u}{e^{-\phi_u} - 1} \tag{B-50}$$

with, as frictional dimensionless mass flux

$$\phi_u = \frac{2\dot{m}}{\rho f u_b} \quad . \qquad \textbf{(B-51)}$$

For small mass transfer rates, $\dot{m} \approx 0$, or $(c_b - c_i)/(1 - c_i) \approx 0$ from equation (B-33), the correction factors tend asymptotically to unity. In other words, the induced velocity plays no role of importance and consequently, uncorrected heat transfer, mass transfer and momentum transfer predictions will suffice.

For large mass transfer rates, as in the example of wall condensation, the effect of the induced velocity can not be ignored, and the correction factors (B-36), (B-42) and (B-50) must be applied.

B.7 *Concluding remarks*

Starting from the basic equations of diffusion, mass transfer in a vapour - inert gas mixture has been studied. The models commonly used for mass transfer have been reviewed , and their ease of use and applicability to problems of condensation from binary gas mixtures discussed. Subsequently, the film model was identified as being the most appropriate for calculating the effect of high mass transfer rates, associated with surface condensation.

The film model was then applied to the energy, mass and momentum transfer, accounting for the diffusion induced velocity, or Stefan flow, and the correction factors for this effect were derived. These correction factors allow the accurate prediction of heat and mass transfer rates inside partial condensers, from the simple empirical relations laid out in standard heat transfer texts.

C DERIVATION OF THE EQUATIONS GOVERNING BULK FOG FORMATION

C.1 *Introduction*

In this section a detailed study is to be performed on the steady-state partial condensation of an inert gas – vapour mixture. The work will focus on the properties of the bulk mixture as it passes through a partial condenser of the form employed in the experimental program. That is, a condenser comprising a central conduit through which the mixture flows, around which there is a sufficiently large external flow of coolant for the condenser conditions to approximate to those of constant wall temperature. A differential section of such a partial condenser is illustrated in Figure C-1 below.

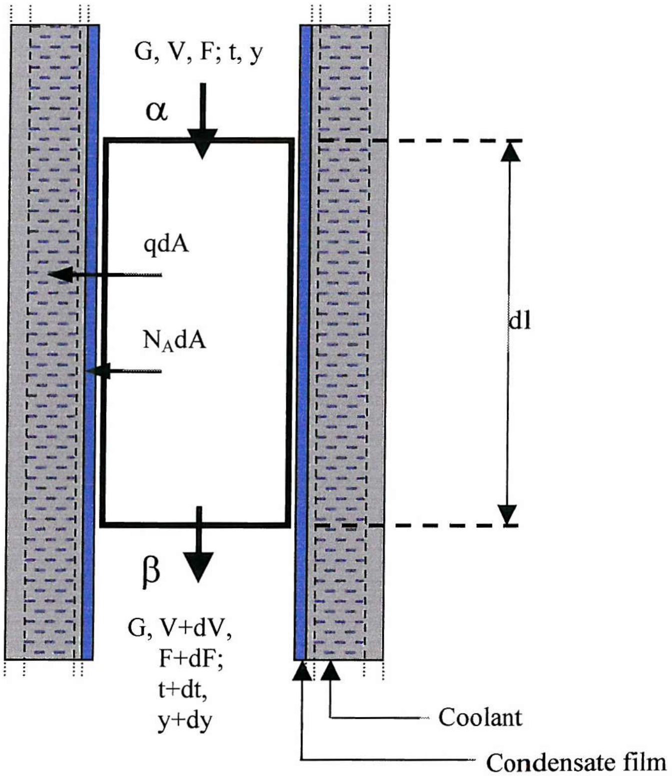

Figure C-1. Differential section of a partial condenser (plan view).

G, V and F are the molar mass velocities of inert gas (B), condensable vapour (A) and fog respectively, while t is the bulk mixture temperature and y is the axial position in the condenser. After flowing through a differential section of condenser of length dl these properties all attain new values, except the inert gas flow rate, G, which is constant throughout the condenser.

Material and energy balances are to be carried out on the above section using the changes in these properties and incorporating terms for the heat and mass transfer rates, qdA and $N_A dA$, resulting from the cooling and partial condensation of the mixture. This will allow a series of differential equations, describing the condition of the flow, to be derived. The method used is based upon that presented in condensed form by Sherwood et al. [44]. However, in expanding the quoted derivation, errors are noted in Sherwood's equations. The correction of these equations here allows them to be incorporated with confidence into a method of predicting the rates of fog formation inside partial condensers, in section 4 of this thesis.

C.2 *Material and energy balances inside a condenser*

Consider the enthalpy flow rate entering the differential condenser section in Figure C-1, at point α, relative to pure liquid and inert gas at temperature t_o. The additional enthalpy of the inert gas, B, is proportional to its temperature above the reference temperature t_o, and is equal to

$$GC_{pB}\left(t-t_o\right). \tag{C-1}$$

Compared to pure liquid A, the enthalpy of the fog is given similarly by

$$FC_{pL}\left(t-t_o\right) \tag{C-2}$$

while that of the vapour contains an additional term pertaining to the evaporation of the liquid at temperature t_o, i.e.

$$V\left[\lambda_o + C_{pA}\left(t-t_o\right)\right] \tag{C-3}$$

The total enthalpy flow rate of the mixture entering the section, relative to pure liquid and inert gas at temperature t_o is therefore equal to

$$GC_{pB}\left(t-t_o\right) + V\left[\lambda_o + C_{pA}\left(t-t_o\right)\right] + FC_{pL}\left(t-t_o\right) \tag{C-4}$$

Now consider the enthalpy of the mixture exiting the differential condenser section of length dl, equating to a surface area per unit of tube cross-section dA, at point β in Figure C-1. The temperature, vapour and fog flow rates change to new values $t+dt$, $V+dV$, and F+dF respectively, while the flow rate of inert gas, G, remains constant. The new enthalpy flow rate is therefore

$$GC_{pB}\left((t+dt)-t_o\right) \;+\; (V+dV)\left[\lambda_o + C_{pA}\left((t+dt)-t_o\right)\right] \;+\; (F+dF)C_{pL}\left((t+dt)-t_o\right) \qquad \textbf{(C-5)}$$

So subtracting equation (C-4) from equation (C-5), the change in enthalpy flow rate across the differential section is

$$GC_{pB}dt \;+\; VC_{pA}dt \;+\; FC_{pL}dt + \; dV\left[\lambda_o + C_{pA}\left((t+dt)-t_o\right)\right] \;+\; dF\left[C_{pL}\left((t+dt)-t_o\right)\right] \qquad \textbf{(C-6)}$$

The secondary terms $dVdt$ and $dFdt$ will be sufficiently small to be neglected, so the differential enthalpy flow then approximates to

$$GC_{pB}dt \;+\; VC_{pA}dt \;+\; FC_{pL}dt + \; dV\left[\lambda_o + C_{pA}(t-t_o)\right] \;+\; dF\left[C_{pL}(t-t_o)\right]. \qquad \textbf{(C-7)}$$

Now the first three terms of this equation may be written

$$GC_{pB}dt \;+\; VC_{pA}dt \;+\; FC_{pL}dt \;=\; G+V+F\left(\frac{GC_{pB}dt + VC_{pA}dt + FC_{pL}dt}{G+V+F}\right) \qquad \textbf{(C-8)}$$

where, by definition, the total molar mass velocity is

$$G+V+F = M \qquad \textbf{(C-9)}$$

and

$$\left(\frac{GC_{pB} + VC_{pA} + FC_{pL}}{G+V+F}\right) = C_{p,av} \qquad \textbf{(C-10)}$$

i.e. the mole-weighted average of C_{pB}, C_{pA} and C_{pL}. Therefore the change of enthalpy flow rate, relative to pure liquid and inert gas at temperature t_o, given by equation (C-7) may be simplified to

$$MC_{p,av}dt \;+\; \left[\lambda_o + C_{pA}(t-t_o)\right]dV \;+\; C_{pL}(t-t_o)dF. \qquad \textbf{(C-11)}$$

An energy balance may then be established by equating the change in enthalpy of the mixture across the differential section to the enthalpy lost due to sensible heat transfer, $q\ dA$, and the latent heat released by the condensation of vapour at the interface, at temperature t_i. The rate of condensation must be equal to the sum of the change of vapour and fog flow rates, i.e.

$dV + dF$. The enthalpy lost from the differential section in this way, again relative to a pure liquid and inert gas at temperature t_o may therefore be expressed as

$$(dV + dF)C_{pL}(t - t_o) + (dV + dF)\lambda + (dV + dF)C_{pA}(t_i - t) + qdA \tag{C-12}$$

So, equating the enthalpies of equations (C-11) and (C-12) gives

$$\begin{aligned} MC_{p,av}dt + \left[\lambda_o + C_{pA}(t - t_o)\right]dV + C_{pL}(t - t_o)dF &= \\ (dV + dF)C_{pL}(t - t_o) + (dV + dF)\lambda + (dV + dF)C_{pA}(t_i - t) + qdA & \end{aligned} \tag{C-13}$$

Expanding the first two terms on the right hand side of the equation and subtracting the $C_{pL}(t - t_o)dF$ terms gives

$$\begin{aligned} MC_{p,av}dt + \left[\lambda_o + C_{pA}(t - t_o)\right]dV &= \\ C_{pL}(t - t_o)dV + \lambda dV + \lambda dF - (dV + dF)C_{pA}(t - t_i) + qdA & \end{aligned} \tag{C-14}$$

and since

$$\lambda = \lambda_o + (C_{pA} - C_{pL})(t - t_o) \tag{C-15}$$

$$\begin{aligned} MC_{p,av}dt + \left[\lambda_o + C_{pA}(t - t_o)\right]dV = {} & C_{pL}(t - t_o)dV + \left[\lambda_o + C_{pA}(t - t_o)\right]dV \\ & - C_{pL}(t - t_o)dV + \lambda dF - (dV + dF)C_{pA}(t - t_i) + qdA \end{aligned} \tag{C-16}$$

Finally, removing similar terms the steady-state energy balance for a system enclosing the vapour space of differential volume reduces to

$$MC_{p,av}dt - \lambda dF + C_{pA}(t - t_i)(dV + dF) + qdA = 0. \tag{C-17}$$

in agreement with the equation presented by Sherwood et al. (their errors appear in subsequent equations, as highlighted in section C.6). The material balance stems simply from the fact that the rate of change of vapour and fog flow must be equal to the rate of vapour condensation, that is

$$-N_A dA = dV + dF \tag{C-18}$$

C.3 *Relation between vapour partial pressure and vapour flow rate*

Dalton's Law states that the total pressure of a mixture of gases is equal to the sum of the partial pressures of the individual gases at the temperature and volume of the mixture[14], i.e.

$$P = \sum p_i \big|_{V,T} \tag{C-19}$$

where P is the total pressure of the mixture, and p_i is the partial pressure of the i'th component. The ideal gas law states that

$$p_i V = n_i R_i T \tag{C-20}$$

so

$$\frac{p_1}{n_1 R_1} = \frac{p_2}{n_2 R_2} = \dots \tag{C-21}$$

where

$$n_i R_i = x_i \tag{C-22}$$

the mole fraction of mixture component i. Therefore in an inert gas – vapour mixture

$$\frac{p_v}{x_v} = \frac{p_g}{x_g} = \frac{P - p_v}{x_g} \tag{C-23}$$

Now if the inert gas and vapour molar flow rates are represented by G and V respectively, as in the previous section, then the gas mole fraction is given by $G/(G+V)$, and the vapour mole fraction by $V/G+V$. Therefore, inserting these values into equation (C-23), and using p to denote the partial pressure of the vapour gives

$$\frac{p(G+V)}{V} = \frac{(P-p)(G+V)}{G} \tag{C-24}$$

i.e.

$$\frac{V}{G} = \frac{p}{P-p}. \tag{C-25}$$

The differential of V with respect to p is then given by

$$\frac{dV}{dp} = \frac{G}{P-p} + \frac{Gp}{(P-p)^2} = \frac{G(P-p)}{(P-p)^2} + \frac{Gp}{(P-p)^2} \tag{C-26}$$

so

$$\frac{dV}{dp} = \frac{GP}{(P-p)^2}. \qquad \textbf{(C-27)}$$

It should be noted however that the above equation is only an approximation, and stems from the ideal gas law. The behaviour of the vapour component is likely to deviate from ideal gas behaviour, and so introduces a possible source of errors. The magnitude of these errors increases the larger the vapour component of the mixture, and the less 'ideal' the vapour, i.e. the larger its molecules etc.

C.4 *Condensation from a superheated mixture*

When the gas – vapour mixture is superheated no fog is carried in the gas stream, and no bulk fog is created, so $dF = 0$. The material balance, equation (C-18), then reduces to

$$-N_A dA = dV. \qquad \textbf{(C-28)}$$

Hence the rate of change of vapour flow with condenser surface area per unit cross-section, A, is simply

$$\frac{dV}{dA} = -N_A = -k_g^* P \ln \frac{1-Y_i}{1-Y} \qquad \textbf{(C-29)}$$

where Y_i and Y are the vapour mole fractions at the condensate – mixture interface and in the bulk mixture respectively. The corresponding relation for the vapour partial pressure may be determined from equations (C-27) and (C-29) such that

$$\frac{dp}{dA} = \frac{dp}{dV}\frac{dV}{dA} = -\frac{(P-p)^2}{GP} k_g^* P \ln\left(\frac{1-Y_i}{1-Y}\right) \qquad \textbf{(C-30)}$$

When no fog is being formed the energy balance, equation (17), reduces to

$$MC_{p,av} dt + C_{pA}(t-t_i)dV + q\,dA = 0. \qquad \textbf{(C-31)}$$

Substituting for dV in equation (C-31) using equation (C-28) and then dividing through by dA gives

$$MC_{p,av}\frac{dt}{dA} - C_{pA}(t-t_i)N_A + q = 0. \qquad \textbf{(C-32)}$$

Now the total heat transfer rate, q, towards the interface is given by Sherwood et al. [44] as

$$q = h(t - t_i)\frac{C_o}{1 - e^{-C_o}} \tag{C-33}$$

and since

$$C_o = N_A C_{pA}/h \tag{C-34}$$

for a mixture in which only component A is diffusing, equation (C-32) may be written

$$MC_{p,av}\frac{dt}{dA} = -h(t - t_i)C_o + h(t - t_i)\frac{C_o}{1 - e^{-C_o}} \tag{C-35}$$

or

$$MC_{p,av}\frac{dt}{dA} = h(t - t_i)\left[\frac{C_o}{\left(1 - e^{-C_o}\right)} - C_o\right] \tag{C-36}$$

which, using the fact that

$$\frac{1}{\left(1 - e^{-C_o}\right)} - 1 \equiv \frac{1}{\left(e^{C_o} - 1\right)} \tag{C-37}$$

becomes

$$\frac{dt}{dA} = -\left(\frac{h}{MC_{p,av}}\right)(t - t_i)\frac{C_o}{\left(e^{C_o} - 1\right)} \tag{C-38}$$

giving the rate of change of bulk temperature of the mixture within the condenser with the surface area per unit of tube cross-section dA.

C.5 *Condensation from a saturated mixture*

If a superheated mixture is cooled sufficiently, the mixture may become saturated. Further cooling will then result in fog formation, giving rise to a change in the flow rate of fog, $dF \neq 0$. The rate of fog formation will be such that the mixture remains saturated at the new bulk mixture temperature. The partial vapour pressure will thus always equal the saturation pressure of the vapour. Thus, the changes in bulk partial pressure and temperature are related by the widely used [44, 60, 61] Clausius-Clapeyron equation

$$\frac{dp}{dt} = \frac{\lambda p}{RT^2} \tag{C-39}$$

Returning to the steady-state energy balance equation, (C-17),

$$MC_{p,av}dt \;-\; \lambda dF \;+\; C_{pA}(t-t_i)(dV+dF) + \; qdA \;=\; 0$$

and expanding using equation (C-33) for the heat transfer rate, and the material balance, equation (C-18), gives

$$MC_{p,av}dt \;-\; \lambda(-N_A dA - dV) - \; C_{pA}(t-t_i)N_A dA \;+\; h(t-t_i)\frac{C_o}{1-e^{-C_o}}dA \;=\; 0 \qquad \textbf{(C-40)}$$

or, using equation (C-34)

$$MC_{p,av}dt \;+\; \lambda N_A dA \;+\; \lambda dV - \; N_A C_{pA}(t-t_i)dA\left[1-\frac{1}{1-e^{-C_o}}\right] \;=\; 0 \qquad \textbf{(C-41)}$$

which, using equation (C-37) and dividing through by dV gives

$$MC_{p,av}\frac{dt}{dV} \;+\; \lambda N_A\frac{dA}{dV} \;+\; \lambda \;+\; N_A C_{pA}(t-t_i)\frac{1}{e^{C_o}-1}\frac{dA}{dV} \;=\; 0 \qquad \textbf{(C-42)}$$

Now, since the first differential appearing may be written

$$\frac{dt}{dV} = \frac{dt}{dp}\frac{dp}{dV} \qquad \textbf{(C-43)}$$

equation (C-42) may be expanded using equations (C-27) and (C-39) into an equation containing only one, repeated differential

$$MC_{p,av}\frac{RT^2}{\lambda p}\frac{(P-p)^2}{GP} \;+\; \lambda N_A\frac{dA}{dV} \;+\; \lambda \;+\; N_A C_{pA}(t-t_i)\frac{1}{e^{C_o}-1}\frac{dA}{dV} \;=\; 0 \qquad \textbf{(C-44)}$$

Thus collecting like terms gives

$$\frac{dA}{dV}\left[\lambda N_A + \frac{N_A C_{pA}(t-t_i)}{e^{C_o}-1}\right] \;=\; -\,\lambda \;-\; MC_{p,av}\frac{RT^2}{\lambda p}\frac{(P-p)^2}{GP} \qquad \textbf{(C-45)}$$

and finally, the rate of change of vapour flow rate in a fog forming mixture

$$\frac{dV}{dA} \;=\; -N_A\left(\frac{\lambda \;+\; \dfrac{C_{pA}(t-t_i)}{e^{C_o}-1}}{\lambda \;+\; MC_{p,av}\dfrac{RT^2}{\lambda p}\dfrac{(P-p)^2}{GP}}\right) \qquad \textbf{(C-46)}$$

The other differential equations for vapour pressure, temperature and fog flow rate may then be obtained from the vapour flow rate as follows. Using equation (C-27), that is

$$\frac{dV}{dp} = \frac{GP}{(P-p)^2} \tag{C-47}$$

the rate of change of partial vapour pressure with distance along the condenser may be obtained from the vapour flow rate (C-46), since

$$\frac{dp}{dA} = \frac{dp}{dV}\frac{dV}{dA} = \frac{-(P-p)^2}{GP}N_A\left(\frac{\lambda + \dfrac{C_{pA}(t-t_i)}{e^{C_o}-1}}{\lambda + MC_{p,av}\dfrac{RT^2}{\lambda p}\dfrac{(P-p)^2}{GP}}\right) \tag{C-48}$$

or

$$\frac{dp}{dA} = -N_A\left(\frac{\lambda + \dfrac{C_{pA}(t-t_i)}{e^{C_o}-1}}{\dfrac{\lambda GP}{(P-p)^2} + MC_{p,av}\left(\dfrac{RT^2}{\lambda p}\right)}\right) \tag{C-49}$$

The temperature, being related to the vapour pressure according to the Clausius-Clapeyron equation, (C-39), can then be obtained using

$$\frac{dt}{dA} = \frac{dt}{dp}\frac{dp}{dA} = -\frac{RT^2N_A}{\lambda p}\left(\frac{\lambda + \dfrac{C_{pA}(t-t_i)}{e^{C_o}-1}}{\dfrac{\lambda GP}{(P-p)^2} + MC_{p,av}\left(\dfrac{RT^2}{\lambda p}\right)}\right) \tag{C-50}$$

i.e.

$$\frac{dt}{dA} = -N_A\left(\frac{\lambda + \dfrac{C_{pA}(t-t_i)}{e^{C_o}-1}}{\dfrac{\lambda^2 p}{RT^2}\dfrac{GP}{(P-p)^2} + MC_{p,av}}\right) \tag{C-51}$$

Finally, the change in fog flow rate with condenser area may be obtained from the material balance, equation (C-18), and the derived vapour flow equation, (C-46)

$$\frac{dF}{dA} = -N_A - \frac{dV}{dA}$$

$$= -N_A\left(1 - \frac{\lambda + \dfrac{C_{pA}(t-t_i)}{e^{C_o}-1}}{\lambda + MC_{p,av}\dfrac{RT^2}{\lambda p}\dfrac{(P-p)^2}{GP}}\right) \tag{C-52}$$

Therefore

$$\frac{dF}{dA} = N_A\left[\frac{\dfrac{C_{pA}(t-t_i)}{e^{C_o}-1} - MC_{p,av}\dfrac{RT^2}{\lambda p}\dfrac{(P-p)^2}{GP}}{\lambda + MC_{p,av}\dfrac{RT^2}{\lambda p}\dfrac{(P-p)^2}{GP}}\right] \tag{C-53}$$

C.6 *Sherwood's equations*

The above derivation follows the work presented by Sherwood et al. [44]. Their equations for superheated mixtures are in agreement with those derived in section C.4. However there are several discrepancies in the equations relating to saturated mixtures, in which bulk fog formation becomes a possibility. The equations presented by Sherwood are

$$\frac{dp}{dt} = \frac{\lambda p}{RT^2} \tag{C-54}$$

$$\frac{dV}{dA} = -N_A\frac{\lambda + C_{pV}\left[(t-t_i)/\left(e^{C_o}-1\right)\right]}{\lambda + C_{pV}\left(RT^2/\lambda\right)\left[(P-p)/p\right]} \tag{C-55}$$

$$\frac{dp}{dA} = \frac{P-p}{M}\frac{dV}{dA} = -N_A\frac{\lambda + C_{pV}\left[(t-t_i)/\left(e^{C_o}-1\right)\right]}{\lambda + C_{p,av}\left(RT^2/\lambda\right)\left[(P-p)/p\right]} \tag{C-56}$$

$$\frac{dF}{dA} = N_A\frac{C_{pA}\left[(t-t_i)/\left(e^{C_o}-1\right)\right] - C_{p,av}\left(RT^2/\lambda\right)\left[(P-p)/p\right]}{\lambda + C_{p,av}\left(RT^2/\lambda\right)\left[(P-p)/p\right]} \tag{C-57}$$

From equation (C-56) it is clear that an alternative to equation (C-27) has been used for dp/dV, that is

$$\frac{dp}{dV} = \frac{P-p}{M} \tag{C-58}$$

However, allowing for this acceptable alteration, (C-55) then becomes

$$\frac{dV}{dA} = -N_A\left(\frac{\lambda + \dfrac{C_{pV}(t-t_i)}{e^{C_o}-1}}{\lambda + MC_{pV}\dfrac{RT^2}{\lambda p}\dfrac{(P-p)^2}{GP}}\right) \tag{C-59}$$

Comparison with equation (C-46), assuming the subscript V refers to the vapour phase such that $C_{pV} \equiv C_{pA}$, shows the two equations to be the same but for the appearance of C_{pV} in the denominator as opposed to $C_{p,av}$. This could easily be attributable to a printing error but the following equation, (C-56), is clearly erroneous since multiplying (C-55) by the factor $P-p/M$ affects only one half of its denominator. However, allowing for the use of equation (C-58), the fog flow rate of equation (C-57) stemming from the vapour flow rate equation, (C-55), is identical to that derived here, (C-52). Hence it becomes clear that several errors appear in Sherwood's equations, though it is impossible to identify the source of these errors due to the lack of information presented. The equations derived in section C.5 are the correct form of these equations.

C.7 *Summary*

So, to summarise, the set of differential equations describing the cooling and partial condensation of a superheated inert gas – vapour mixture are

$$\frac{dt}{dA} = -\left(\frac{h}{MC_{p,av}}\right)(t-t_i)\frac{C_o}{\left(e^{C_o}-1\right)} \tag{C-60}$$

$$\frac{dp}{dA} = -\frac{(P-p)^2}{GP}k_g^* P \ln\frac{1-Y_i}{1-Y} \tag{C-61}$$

$$\frac{dV}{dA} = -k_g^* P \ln\frac{1-Y_i}{1-Y} \tag{C-62}$$

$$\frac{dF}{dA} = 0 \tag{C-63}$$

In a saturated mixture within which bulk fog formation may be taking place the corresponding equations are

$$\frac{dt}{dA} = -N_A \left(\frac{\lambda + \dfrac{C_{pA}(t-t_i)}{e^{C_o}-1}}{\dfrac{\lambda^2 p}{RT^2}\dfrac{GP}{(P-p)^2} + MC_{p,av}} \right) \tag{C-64}$$

$$\frac{dp}{dA} = -N_A \left(\frac{\lambda + \dfrac{C_{pA}(t-t_i)}{e^{C_o}-1}}{\dfrac{\lambda GP}{(P-p)^2} + MC_{p,av}\left(\dfrac{RT^2}{\lambda p}\right)} \right) \tag{C-65}$$

$$\frac{dV}{dA} = -N_A \left(\frac{\lambda + \dfrac{C_{pA}(t-t_i)}{e^{C_o}-1}}{\lambda + MC_{p,av}\dfrac{RT^2}{\lambda p}\dfrac{(P-p)^2}{GP}} \right) \tag{C-66}$$

$$\frac{dF}{dA} = N_A \left[\frac{\dfrac{C_{pA}(t-t_i)}{e^{C_o}-1} - MC_{p,av}\dfrac{RT^2}{\lambda p}\dfrac{(P-p)^2}{GP}}{\lambda + MC_{p,av}\dfrac{RT^2}{\lambda p}\dfrac{(P-p)^2}{GP}} \right] \tag{C-67}$$

The solution of these equations, detailed in section 4, will allow prediction of the scale of any bulk fog formation which may occur during the cooling and partial condensation of a gas – vapour mixture of known initial composition.

D Choice of solution method for the rate equations

The two possible systems of equations (3-12) to (3-15) and (3-16) to (3-19), both comprise a series of four first order ordinary differential equations. If the values of the dependent variables t, p, F and V are known, or are specified, at condenser entry, then they become initial value problems of the form

$$\begin{aligned} \mathbf{y}' &= \mathbf{f}(A,\mathbf{y}) \\ \mathbf{y}(a) &= \mathbf{y}_o \end{aligned} \qquad \textbf{(D-1)}$$

where $\mathbf{y}$, $\mathbf{f}$ and $\mathbf{y}_0$ are 4 dimensional vectors, e.g.

$$\mathbf{y} = \begin{bmatrix} y_1 \\ y_2 \\ y_3 \\ y_4 \end{bmatrix} = \begin{bmatrix} t \\ p \\ F \\ V \end{bmatrix}. \qquad \textbf{(D-2)}$$

Such problems cannot be solved exactly, and so a numerical method must be used to find solutions.

D.1 *Runge-Kutta Method*

The most widely used numerical method for the solution of initial value problems of the form of equation D-1, involves the application of a Runge-Kutta formula. This is a step-by-step method, generating a series of points $A_1, A_2, \ldots.$, at which the solution of the differential equation is approximated. The basic idea behind the class of Runge-Kutta methods is to use a linear combination of values of $\mathbf{f}(A,\mathbf{y})$, to approximate $\mathbf{y}(A)$, which match up as well as possible with the Taylor series for $\mathbf{y}(\mathbf{A})$ [51].

Fourth order formulas are commonly used because they require only four evaluations of $\mathbf{f}$, whilst the results produced are quite accurate. Hence a Runge-Kutta algorithm of order four was employed in the computational program for the solution of the rate equations (3-12) to (3-15) and (3-16) to (3-19). The relevant Runge-Kutta algorithm is laid out below.

D.2 *Runge-Kutta algorithm of order p=4 for systems of first order equations*

To obtain an approximate solution of order p=4 to the initial value problem D-1 on $[a,b]$, using n steps of step size $h=(b-a)/n$, generate the sequences

$$\begin{aligned} \mathbf{y}_{i+1} &= \mathbf{y}_i + \frac{h}{6}(\mathbf{k}_1 + 2\mathbf{k}_2 + 2\mathbf{k}_3 + \mathbf{k}_4), \\ A_{i+1} &= A_o + (i+1)h, \qquad i = 0,1,2,\ldots.,n-1 \end{aligned} \tag{D-3}$$

where

$$\begin{aligned} \mathbf{k}_1 &= \mathbf{f}(A_i,\ \mathbf{y}_i), \\ \mathbf{k}_2 &= \mathbf{f}\left(A_i + \frac{h}{2},\ \mathbf{y}_i + \frac{h}{2}\mathbf{k}_1\right), \\ \mathbf{k}_3 &= \mathbf{f}\left(A_i + \frac{h}{2},\ \mathbf{y}_i + \frac{h}{2}\mathbf{k}_2\right), \\ \mathbf{k}_4 &= \mathbf{f}(A_i + h,\ \mathbf{y}_i + h\mathbf{k}_3), \end{aligned} \tag{D-4}$$

and $A_o = a$, $\mathbf{y}_0 = \mathbf{y}(a)$. At $A = A_i$, $\mathbf{y}_i$ is an approximation to $\mathbf{y}(A_i)$, the exact value of $\mathbf{y}$ at the point A_i.

E Theoretical Predictions

First order ordinary equations of the type derived in section 3.8 may be solved numerically using a Runge-Kutta method (described in appendix D). General routines for the computational solution of such problems, written in Fortran, are available from the NAG Fortran Library (Numerical Algorithms Group) [62]. Such a routine has been taken and adapted for the specific set of equations pertaining to the problem in question, as laid out in (3-12) to (3-15), or (3-16) to (3-19).

First the state of the mixture entering the condenser must be specified. This is done by stating the initial bulk molar velocities of vapour, V_o, non-condensable gas, G_o and fog, F_o, the bulk temperature, t_o and vapour partial pressure, p_o. Then values must be obtain for the numerous constants and parameters appearing in the rate equations. Those of the bulk mixture properties, specific heat, c_p, viscosity, μ etc. may be acquired from tabulated data. These values will obviously vary as the temperature and composition of the mixture changes along the length of the condenser. Hence, at the start of the program the tabulated data is read from data files to allow subsequent interpolation of the data at the relevant temperature.

Also appearing in the rate equations are the temperature and vapour partial pressure at the condensate – mixture interface, and parameters relating to the heat and mass transfer rates, i.e. the heat transfer coefficient, h, via the Ackermann correction factor $C_o\left(= N_A C_{pA}/h\right)$, and the molar flux of vapour towards the condensing surface, N_A. The calculation of these values is also dependent upon the knowledge of conditions at the interface, i.e. the temperature and vapour mole fraction – see equations (3-7) and (3-5). However, the conditions at the interface are unknown and very difficult to measure experimentally.

E.1 Evaluation of the interface conditions

The actual temperature at the interface will lie somewhere between that of the coolant and the bulk gas – vapour mixture, see Figure E.1. It's value may be obtained using a method such as that described by Collier et al. [41] involving the calculation of the gas and coolant side heat transfer coefficients. The method then utilises the fact that the heat transfer from the bulk gas – vapour mixture at temperature t_b to the condensate / mixture interface at temperature t_i, must equal that from the interface to the coolant at temperature t_w, to find the interface temperature.

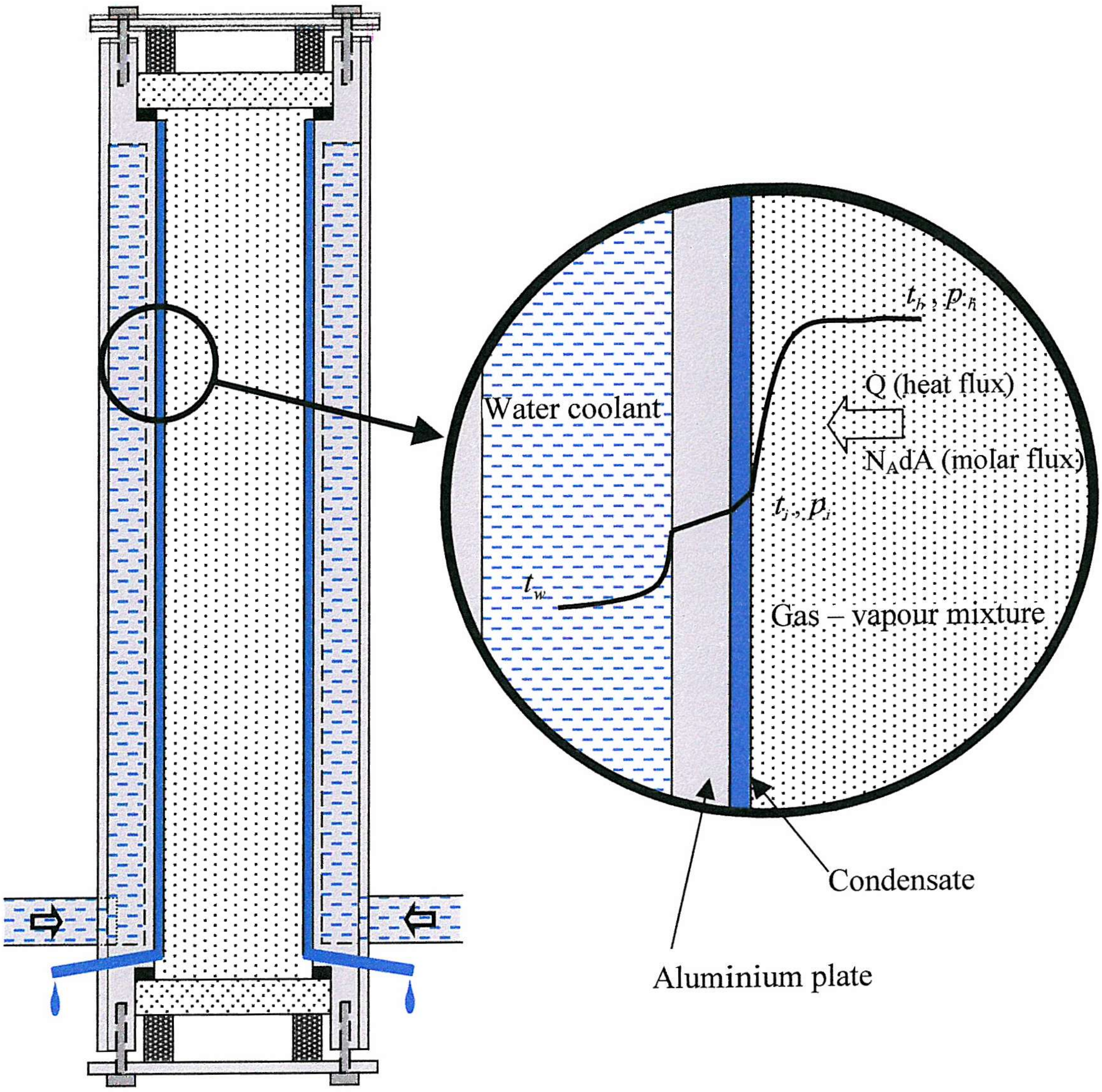

Figure E.1 Differential section of experimental condenser section showing the temperature profiles from the coolant to the gas-vapour mixture.

The interface is usually assumed to be at saturation condition for the vapour [refs], since condensation is occurring there. A knowledge of the interface temperature is therefore sufficient to specify the latent heat of vapourisation, the vapour pressure and the vapour mole fraction at the interface.

E.1.1 Coolant side heat transfer rate

The heat flux from the mixture-condensate interface to the water coolant is

$$\frac{Q_c}{A} = q_c = U\left(t_i - t_w\right) \qquad \textbf{(E-1)}$$

where U represents the overall heat transfer coefficient, comprising the thermal resistances of the condensate layer, the aluminium plate, and a fluid film on the coolant side, see Figure E.1. Hence

$$q_c = \left(\frac{1}{\frac{1}{h_w} + \frac{\Delta x_{al}}{k_{al}} + \frac{\Delta x_c}{k_c}}\right)\left(t_i - t_w\right) \qquad \textbf{(E-2)}$$

where Δx_{al} and Δx_c are the aluminium plate and condensate layer thickness' respectively, with thermal conductivities k_{al} and k_c which may be obtained from tables. The coolant water heat transfer coefficient, h_w, is calculated using

$$h = \frac{Nu_{Dh} k}{D_h} \,, \qquad \textbf{(E-3)}$$

where the Nusselt number is calculated using the empirical relation for 'short' tubes [3], which includes both the thermal and hydrodynamic starting length, i.e.,

$$Nu_{Dh} = 1.86\left[\left(\frac{D}{L}\right)\mathrm{Re}_{Dh}\,\mathrm{Pr}\right]^{\frac{1}{3}}\left(\frac{\mu}{\mu_s}\right)^{0.14} . \qquad \textbf{(E-4)}$$

E.1.2 Gas side heat transfer rate

The transfer of heat from the bulk mixture to the interface, Q_g, is made up of two components; firstly, the sensible heat transferred through the diffusion layer to the interface, Q_s, and secondly, the latent heat released due to condensation of the vapour reaching the interface, Q_l, [41]. This model of heat transfer in the vapour phase was first expressed by Colburn and Hougen [64], and written in terms of heat fluxes gives

$$q_g = q_s + q_l = q_s + \lambda_{Ai} N_A \tag{E-5}$$

which, inserting equations (3-7) and (3-5), becomes

$$q_g = h_g (t_b - t_i) \frac{C_o}{1 - e^{-C_o}} + k_g^* \lambda_{Ai} P \ln \frac{1 - Y_i}{1 - Y} . \tag{E-6}$$

Therefore, to evaluate the gas-side heat transfer rate, the heat and mass transfer coefficients, h_g and k_g^*, must be determined.

Heat transfer coefficient:

The vapour-gas mixture in the condenser flows parallel to the interface, hence the heat transfer coefficient, h_g, may be evaluated from a standard correlation appropriate to the flow regime and geometry. Since this study is confined to forced convection condensation from turbulent mixtures flowing within a duct, the equation [3]

$$Nu_{Dh} = \frac{(f/8) \mathrm{Re}_{Dh} \mathrm{Pr}}{1.07 + 12.7 \sqrt{f/8} \left(\mathrm{Pr}^{2/3} - 1 \right)} \qquad \begin{bmatrix} 0.5 < \mathrm{Pr} < 200 \\ 10^4 < \mathrm{Re}_{Dh} < 5 \times 10^6 \\ \textit{properties at } t_b \end{bmatrix} \tag{E-7}$$

suggested by Petukhov is used to obtain the Nusselt number. The friction factor, f, is obtained from the widely used Moody diagram. The heat transfer coefficient may then be deduced using

$$h_g = \frac{Nu\, k}{D_h} . \tag{E-8}$$

Mass transfer coefficient:

Having obtained the heat transfer coefficient, a mass transfer coefficient, K_g, may be evaluated using an analogy between heat and mass transfer. The Chilton-Colburn analogy [65],defining a 'heat transfer factor'

$$j_{heat} = \frac{h_g}{c_p G} \mathrm{Pr}^{2/3} = j_{mass} = \frac{K_g p_{BM} M_{av}}{G} Sc^{2/3} , \tag{E-9}$$

where p_{BM} is the log mean partial pressure of non-condensable gas at the interface and in the bulk mixture, i.e.,

$$p_{BM} = \frac{p_{Bb} - p_{Bi}}{\ln(p_{Bb}/p_{Bi})} \tag{E-10}$$

has been shown to agree with a range of experimental data [65, 66], and has been widely used [64, 67, 68], to predict mass transfer rates. Re-writing equation (E-9) in terms of the mass transfer coefficient gives

$$K_g = \frac{h_g}{c_p p_{BM} M_{av}} \left(\frac{\mathrm{Pr}}{Sc} \right)^{2/3} . \tag{E-11}$$

This mass transfer coefficient, K_g, differs from that used in previous chapters (k_g^*), so, in terms of k_g^*, the Chilton-Colburn analogy of heat and mass transfer may be written

$$k_g^* = \frac{h_g}{c_p M_{av} P} \left(\frac{\mathrm{Pr}}{Sc} \right)^{2/3} . \tag{E-12}$$

E.1.3 Interface temperature solution

The simplest method to arrive at the correct interface temperature is to start with a 'low' value, $t_i(j=0)$ only just above the coolant temperature (assumed constant at 15°C), and calculate the rates of heat transfer. The gas-side heat transfer (E-2) will then be greater than that on the coolant side (E-6) due to the fact that $(t_b - t_i) \rangle\rangle (t_i - t_w)$. The temperature is increased incrementally using a small step-size (e.g. 0.1°C), until a temperature $t_i(N)$ is reached for which the coolant-side heat transfer, q_c, is first greater than the gas-side heat transfer q_g. The most appropriate value of the temperature at the interface is then the value $t_i(N)$, or $t_i(N-1)$ for which $\left|q_c - q_g\right|$ is the least.

E.2 *Solution generation*

Now that the temperature at the interface has been adequately evaluated, the other mixture properties necessary for the solution of the rate equations may be obtained by interpolation from saturation data tables. All the relevant parameters have thus been obtained and the Runge-Kutta routine may then be executed to solve the rate equations and predict the bulk mixture properties at a point a small distance along the condenser.

Solutions are then generated by repeating this whole process, at the new bulk values of t_1, p_1, F_1, and V_1, and so on, to the end of the condenser.

F Computer Program

The computer program used to predict the mixture conditions inside the condenser and the extent of any fog formation is presented below. The program is valid for saturated mixtures, and the example below is that of an 80°C saturated water vapour – air mixture entering a 2m long condenser section with a mean velocity of 2m/s. A very similar program was used for superheated mixtures, and mixtures of benzene and nitrogen.

```
*
*     This program is to solve the set of differential equations
*     describing the cooling and partial condensation of a saturated
*     gas-vapour mixture, passing through a condenser in which fog
*     formation may occur.
*
*     A runge-kutta algorithm of order p=4, obtained from the NAG fortran
*     library is to be employed and modified to solve the appropriate set
*     of four first order non-linear ordinary differential equations.
*     Hence, the variation of pressure, temperature and heat and mass
*     transfer rates with distance along the condenser are to be
*     obtained.
*     In addition, this will allow predictions of fog and vapour flow
*     rates at any point along the length of a partial condenser.
*
*
*
*     .. Parameters ..
      INTEGER          NOUT, NEQ, LENWRK, METHOD
      PARAMETER          (NOUT=6,NEQ=4,LENWRK=32*NEQ,METHOD=1)
      real*8           ZERO, ONE, TWO
      PARAMETER          (ZERO=0.0d0,ONE=1.0d0,TWO=2.0d0)
*     .. Local Scalars ..
      real*8           HNEXT, HSTART, TEND, TGOT, TINC, TOL, TSTART,
     +                 TWANT, WASTE
      INTEGER          I, IFAIL, J, L, NPTS, STPCST, STPSOK, TOTF
      LOGICAL          ERRASS
*     .. Local Arrays ..
      real*8           THRES(NEQ), WORK(LENWRK), YGOT(NEQ), YMAX(NEQ),
     +                     YPGOT(NEQ), YSTART(NEQ)
*     .. External Subroutines ..
      EXTERNAL         D02PCF, D02PVF, D02PYF, F
*     .. Executable Statements ..
      WRITE (NOUT,*) 'Program Results (coolant temp.=15 Celsius)'
*
*
*     Set initial conditions and input for subroutine D02PVF
*
      TSTART = 0.0d0        ! cumulative condenser surface area per unit of
                            ! tube cross-section at entry
      YSTART(1) = 80.0d0    ! bulk temperature at condenser entry [Celsius]
      YSTART(2) = 0.4677d0  ! vapour pressure at condenser entry [atm.]
```

```
      YSTART(3) = 0.0d0      ! fog flow rate [moles/m^2 s]
      YSTART(4) = 32.46d0    ! vapour flow rate on entry [moles/m^2 s]
      TEND = 120.0d0         ! cumulative condenser surface area per unit of
                             ! tube cross-section at exit
      DO 20 L = 1, NEQ
         THRES(L) = 1.0d-8
   20 CONTINUE
      ERRASS = .FALSE.
      HSTART = ZERO
*
*     Set control for output
*
      NPTS = 32                    ! number of iterations along condenser
      TINC = (TEND-TSTART)/NPTS    ! Increment of iterations
*
      DO 60 I = 1, 2
         IF (I.EQ.1) TOL = 1.0d-3
         IF (I.EQ.2) TOL = 1.0d-4
         IFAIL = 0
         CALL D02PVF(NEQ,TSTART,YSTART,TEND,TOL,THRES,METHOD,
     +               'Usual Task',ERRASS,HSTART,WORK,LENWRK,IFAIL)
*
         WRITE (NOUT,'(/A,D8.1)') 'Calculation with TOL = ', TOL
         WRITE (NOUT,'(/A/)') '    dA          t        p          F
     +    V'
         WRITE (NOUT,'(1X,F7.3,4(3X,F7.4))') TSTART, (YSTART(L),L=1,NEQ)
         DO 40 J = NPTS - 1, 0, -1
            TWANT = TEND - J*TINC
            IFAIL = 1
            CALL D02PCF(F,TWANT,TGOT,YGOT,YPGOT,YMAX,WORK,IFAIL)
*
            WRITE (NOUT,'(1X,F7.3,4(3X,F7.4))') TGOT, (YGOT(L),L=1,NEQ)
   40    CONTINUE
*
         IFAIL = 0
         CALL D02PYF(TOTF,STPCST,WASTE,STPSOK,HNEXT,IFAIL)
         WRITE (NOUT,'(/A,I6)')
     +     ' Cost of the integration in evaluation of F is', TOTF
*
   60 CONTINUE
*
      STOP
      END
*
**************************************************************************
*
      SUBROUTINE F(T,Y,YP)
*     Subroutine specifying the equations to be solved, and the
*     numerous parameters contained therein.
*
*     .. Scalar Arguments ..
      REAL*8           T
*     .. Array Arguments ..
      REAL*8             Y(*), YP(*), Z, PIA, CPA, CPB, X1, X2,
     +                 TK, R, CPL, CPAV, TIF, H, FOG, cpwl, muwl(800),
     +                 tc, pg, ywv, ya, w, muwv(800), mua(800), cpwv,
     +                 kwv, ka, A, MWV, MA, RWV, RA, P, pwv, dh, k,
     +                 PR(800), SC(800), RE(800), NU(800), mfa, mfwv,
```

```
     +                cp, mu(800), hg(800), G, mg, cpair, u, dxc, mf,
     +                ms, D, V, M, ti(800), pi(800), lht(800), kc,
     +                dxal, hw, Uc, HTc(800), tw, YA1(800), YA2,
     +                Le(800), ff, x, kwl, mug(800), kgas, Mmm(800),
     +                KG(800), Pat, rho(800), kal, TILO,
     +                HTg(800), NA(800), CO(800), TIHI
      REAL*8          TEC, PRESINT, LAMINT, CPWVKGINT, CPAIRKGINT,
     +                KWVAPINT, KAIRINT, VISCWVINT, VISCAIRINT,
     +                CPLKGINT, KWLIQINT, VISCWLINT, Vwv, Va
      REAL*8          TECPRES(100), PRES(100), TECLAM(100), LAM(100),
     +                TECCPWVKG(100), CPWVKG(100), TECCPAIRKG(100),
     +                CPAIRKG(100), TECKWVAP(100), KWVAP(100),
     +                TECKAIR(100), KAIR(100), TECVISCWV(100),
     +                VISCWV(100), TECVISCAIR(100), VISCAIR(100),
     +                TECCPLKG(100), CPLKG(100), TECKWLIQ(100),
     +                KWLIQ(100), TECVISCWL(100), VISCWL(100)
*
      INTEGER         NPRES, NLAM, NCPWVKG, NCPAIRKG, NKWVAP, NKAIR,
     +                NVISCWV, NVISCAIR, NCPLKG, NKWLIQ, NVISCWL, J, Q
*     .. Intrinsic functions ..
      INTRINSIC       LOG, EXP, LOG10
      IMPLICIT        NONE
*
*
*     First, read in tabulated values of all the parameters to be
*     used during subsequent calculations.
*
      CHARACTER*80 INFILE       ! Input file
*
      INFILE = '../Tables/pres.dat'
*         table of saturation pressure [bar], against temperature.
      CALL READTAB(NPRES,TECPRES,PRES,INFILE)
*         read data from INFILE
*
*     Now repeat, to read in values of latent heat, viscosity etc.
*
      INFILE = '../Tables/lam.dat'     ! latent heat of vaporisation [J/kg]
      CALL READTAB(NLAM,TECLAM,LAM,INFILE)
*
      INFILE = '../Tables/viscwv.dat'  ! viscosity of vapour [kg/m s]
      CALL READTAB(NVISCWV,TECVISCWV,VISCWV,INFILE)
      INFILE = '../Tables/viscair.dat' ! viscosity of inert gas [kg/m s]
      CALL READTAB(NVISCAIR,TECVISCAIR,VISCAIR,INFILE)
      INFILE = '../Tables/viscwl.dat'  ! viscosity of liquid [kg/m s]
      CALL READTAB(NVISCWL,TECVISCWL,VISCWL,INFILE)
*
      INFILE = '../Tables/cpwv.dat'   ! specific heat of vapour [J/kg degC]
      CALL READTAB(NCPWVKG,TECCPWVKG,CPWVKG,INFILE)
      INFILE = '../Tables/cpair.dat'  ! specific heat of inert [J/kg degC]
      CALL READTAB(NCPAIRKG,TECCPAIRKG,CPAIRKG,INFILE)
      INFILE = '../Tables/cpl.dat'    ! specific heat of liquid [J/kg degC]
      CALL READTAB(NCPLKG,TECCPLKG,CPLKG,INFILE)
*
      INFILE = '../Tables/kwv.dat'    ! thermal conductivity of vapour
                                      ! [J/m s degC]
      CALL READTAB(NKWVAP,TECKWVAP,KWVAP,INFILE)
      INFILE = '../Tables/kair.dat'   ! thermal conductivity of inert gas
                                      ! [J/m s degC]
```

```
      CALL READTAB(NKAIR,TECKAIR,KAIR,INFILE)
      INFILE = '../Tables/kwl.dat'    ! thermal conductivity of liquid
                                      ! [J/m s degC]
      CALL READTAB(NKWLIQ,TECKWLIQ,KWLIQ,INFILE)
*
*    Input value of bulk temperature, saturation pressure, vapour
*    flow rate, and relative humidity for each case!
*
      tc = Y(1)                    ! bulk temperature [Celsius]
      TK = 273.15d0 + tc           ! bulk temperature [Kelvin]
      FOG = Y(3)                   ! molar velocity of fog [moles/m^2 s]
      V = Y(4)                     ! molar velocity of vapour [moles/m^2 s]
      G = 36.74d0                  ! molar velocity of inert gas [moles/m^2 s]
      M = G + V + FOG              ! molar velocity of mixture [moles/m^2 s]
      TEC = tc
      CALL INT(TEC,NPRES,TECPRES,PRES,PRESINT)
      pg = PRESINT * 1.0d5         ! saturated vapour pressure [N/m^2]
      P = 1.01325d5                ! total pressure [N/m^2]
      Pat = P/1.01325d5            ! total pressure [atm.]
      w = 1.0d0                    ! relative humidity (100%)
      pwv = w*pg                   ! vapour partial pressure [N/m^2]
      MWV = 18.015d-3              ! molar mass of vapour [kg/mole]
      MA = 28.96d-3                ! molar mass of inert gas [kg/mole]
      R = 8.3143d0                 ! Universal gas constant [J/mole degK]
      RWV = R/MWV                  ! gas constant of vapour [J/kg K]
      RA = R/MA                    ! gas constant of inert gas [J/kg K]
      Vwv = 12.7d0                 ! diffusion volume of vapour [m^3/mole]
      Va = 20.1d0                  ! diffusion volume of inert gas [m^3/mole]
*
*  - - - - - - - - - - - - - - - - - - - - - - - - - - - - - - - - - - - -
*
      A = 0.008d0                  ! c-s area of duct [m^2]
      dh = 0.06666d0               ! hydraulic diameter of duct [m]
      tw = 15.0d0                  ! coolant temperature [Celsius]
      mfa = G*A                    ! molar flow rate of inert gas [moles/s]
      mfwv = V*A                   ! molar flow rate of vapour [moles/s]
      ywv = mfwv/(mfa+mfwv)        ! vapour mole fraction
      ya = 1.0d0-ywv               ! inert gas mole fraction
      mg = G*MA*A                  ! inert gas flow rate [kg/s]
      ms = V*MWV*A                 ! vapour flow rate [kg/s]
      mf = FOG*MWV*A               ! fog flow rate [kg/s]
      x = (mg+ms)/(mg+ms+mf)       ! mass quality of gas/vapour
*
      D = 1.0d-4*((0.001d0*(TK**1.75d0))/(Pat*(((Vwv**0.333d0)+
     +    (Va**0.333d0))**2.0d0)))*
     +    (((1.0d0/(1.0d3*MWV))+(1.0d0/(1.0d3*MA)))**0.5d0)
*         diffusion coefficient [m^2/s]
*
*    The velocity of the mixture through the duct is obtained via
*    Dalton's law, treating the inert component as an ideal gas.
*
      u = (mg*RA*TK)/((P-pwv)*A)      ! mixture velocity [m/s]
*
*  -------------------------------------------------------------------------
*
*    Now it is necessary to determine the interface temperature,
*    ti (and hence pi), by equating the gas and coolant side heat
*    transfer rates.
```

```
*     Hence, starting with a low value for the interface temperature
*     (to ensure gas side heat transfer > coolant side) calculate the
*     heat transfer rates. Then repeat, increasing ti by 0.1degC each
*     time until the Coolant side heat transfer rate > that of the gas
*     side.
*
      DO 1 J = 150,800,1
         ti(J) = J/10.0d0           ! initially set ti = 15 degC.
         TEC = J/10.0d0
         CALL INT(TEC,NPRES,TECPRES,PRES,PRESINT)
         CALL INT(TEC,NLAM,TECLAM,LAM,LAMINT)
*
*        Hence, from tables
         pi(J) = PRESINT*1.0d5      ! vapour pressure at interface [N/m^2]
         lht(J) = LAMINT*MWV        ! latent heat of vapourisation [J/mole]
*
*     Then estimate the overall heat transfer on the coolant side,
*     through the condensate layer, aluminium plate, and (water)
*     coolant boundary layer.
*
         CALL INT(TEC,NKWLIQ,TECKWLIQ,KWLIQ,KWLIQINT)
         kc = KWLIQINT    ! thermal conductivity of condensate[J/m s degC]
         dxc = 5.0d-4     ! estimated film thickness [m]
         kal = 2.0d2      ! thermal conductivity of aluminium [J/m s degC]
         dxal = 3.0d-3    ! aluminium plate thickness [m]
         hw = 550.0d0     ! coolant heat transfer coefficient [J/m^2 s degC]
*
         Uc = 1.0d0/((dxc/kc)+(dxal/kal)+(1.0d0/hw))
*            overall coolant side heat transfer coefficient [J/m^2 s degC]
*
*        And the coolant side heat transfer, HTc [J/m^2 s] is therefore
         HTc(J) = Uc*(ti(J)-tw)
*
* - - - - - - - - - - - - - - - - - - - - - - - - - - - - - - - - - - - -
*
*     Now in order to calculate the gas side heat transfer, the
*     appropriate heat and mass transfer coefficients must first
*     be determined.
*
*     The gas side heat transfer coefficient is determined using the
*     correlation suggested by Petukhov for turbulent heat transfer within
*     a pipe. But first need to calculate the parameters appearing
*     in these equations.
*
*     The gas and vapour viscosities are obtained by interpolating
*     from tables at the average of the bulk and interface
*     temperatures
*
         TEC = (tc + ti(J))/2.0d0
         CALL INT(TEC,NVISCWV,TECVISCWV,VISCWV,VISCWVINT)
         muwv(J) = VISCWVINT          ! vapour viscosity [kg/ms]
         CALL INT(TEC,NVISCWL,TECVISCWL,VISCWL,VISCWLINT)
         muwl(J) = VISCWLINT          ! liquid viscosity [kg/ms]
         CALL INT(TEC,NVISCAIR,TECVISCAIR,VISCAIR,VISCAIRINT)
         mua(J) = VISCAIRINT          ! inert gas viscosity [kg/ms]
*
*     Then the specific heats and thermal conductivities of the gas,
*     vapour and liquid are determined, again by interpolating from
```

```
*     tables, but at the bulk mixture temperature.
*
         TEC = tc
         CALL INT(TEC,NCPWVKG,TECCPWVKG,CPWVKG,CPWVKGINT)
         cpwv = CPWVKGINT      ! vapour heat capacity [J/kg degC]
         CALL INT(TEC,NCPAIRKG,TECCPAIRKG,CPAIRKG,CPAIRKGINT)
         cpair = CPAIRKGINT    ! inert gas heat capacity [J/kg degC]
         CALL INT(TEC,NCPLKG,TECCPLKG,CPLKG,CPLKGINT)
         cpwl = CPLKGINT       ! liquid heat capacity [J/kg degC]
         CALL INT(TEC,NKWVAP,TECKWVAP,KWVAP,KWVAPINT)
         kwv = KWVAPINT        ! vapour thermal conductivity [J/m s Kelvin]
         CALL INT(TEC,NKWLIQ,TECKWLIQ,KWLIQ,KWLIQINT)
         kwl = KWLIQINT        ! liquid thermal conductivity [J/m s Kelvin]
         CALL INT(TEC,NKAIR,TECKAIR,KAIR,KAIRINT)
         ka = KAIRINT          ! inert gas thermal conductivity[J/m s
Kelvin]
*
*     Now using these values, the average mixture values of viscosity,
*     thermal conductivity, and specific heat are calculated.
*
         mug(J) = ((ywv*muwv(J)*(MWV**0.5d0))+(ya*mua(J)*
     +   (MA**0.5d0)))/((ywv*(MWV**0.5d0))+(ya*(MA**0.5d0)))
*                 gas-phase viscosity [kg/ms]
         mu(J) = 1.0d0/((x/mug(J))+((1.0d0-x)/muwl(J)))
*                 mean 2-phase viscosity [kg/ms]
*
         kgas = ((ywv*kwv*(MWV**3.333d-1))+(ya*ka*(MA**3.333d-1)))/
     +   ((ywv*(MWV**3.333d-1))+(ya*(MA**3.333d-1)))
*                 gas-phase thermal conductivity [J/m s Kelvin]
         k = 1.0d0/((x/kgas)+((1.0d0-x)/kwl))
*                 mean 2-phase thermal conductivity [J/m s Kelvin]
*
         cp = ((ms*cpwv)+(mg*cpair)+(mf*cpwl))/(ms+mg+mf)
*             mass-weighted average specific heat [J/kg degC]
*
*     This allows the flow Reynolds, Prandtl and Schmidt numbers
*     to be determined, and hence the Nusselt number of the flow,
*     and the gas-side sensible heat transfer coefficient.
*
         rho(J) = (ms+mg+mf)/(u*A)
*           density of mixture [kg/cubic meter]
*
         RE(J) = (u*rho(J)*dh)/(mu(J))
*           Reynolds number
         PR(J) = (cp*mu(J))/(k)
*           Prandtl number
         SC(J) = (mu(J))/(rho(J)*D)
*           Schmidt number
*
*     The fanning friction factor, ff, is then estimated using
         ff = 1.0d0/(4.0d0*(((1.82d0*(LOG10(RE(J))))-1.64d0)**2.0d0))
*
*     And the Nusselt Number [Petukov 1970]
         NU(J) = ((ff/2.0d0)*RE(J)*PR(J))/(1.07d0+(12.7d0*((ff/2.0d0)
     +   **0.5d0)*((PR(J)**(2.0d0/3.0d0))-1.0d0)))
*
*     Allowing the heat transfer coefficient, hg(J) [J/m^2 s degC], to
*     be determined using
```

```
         hg(J) = (NU(J)*k)/dh
*
*  - - - - - - - - - - - - - - - - - - - - - - - - - - - - - - - - - - -
*
*     The Chilton-Colburn analogy for heat and mass transfer may then be
*     used to estimate the mass transfer coefficient, KG(J), from the
*     heat transfer coefficient, hg(J), determined above.
*
         Mmm(J) = ((V*MWV)+(G*MA)+(FOG*MWV))/(V+G+FOG)
*          mean molecular mass [kg/ mole]
*
         Le(J) = SC(J)/PR(J)
*          Lewis number
*
         KG(J) = (hg(J)/(Mmm(J)*cp*Pat))*((1.0d0/Le(J))**(2.0d0/3.0d0))
*          mass transfer coefficient  [moles/ m^2 s atm.]
*
*  - - - - - - - - - - - - - - - - - - - - - - - - - - - - - - - - - - -
*
*     Now the gas side heat transfer is to be evaluated.
*     First the molar flux of vapour to the condensing surface, NA, and
*     the Ackermann correction factor for mass transfer, CO, are
*     calculated
*
         YA1(J) = pi(J)/P        ! vapour mole fraction at interface
         YA2 = pg/P              ! vapour mole fraction in bulk
*
         NA(J) = KG(J) * Pat * LOG((1.0d0-YA1(J))/(1.0d0-YA2))
*          Molar flux of vapour towards cold surface [moles/m^2 s]
*
         CO(J) = (NA(J)*(cpwv*MWV))/hg(J)
*          Ackermann correction for mass transfer [dimensionless]
*
*     And finally, the gas side heat transfer, HTg [J/m^2 s], is
*     given by the sum of the sensible heat transferred and the latent
*     heat released due to vapour condensation at the interface
*
         HTg(J) = (hg(J)*(tc-ti(J))*(CO(J)/(1.0d0-EXP(-CO(J)))))
     +    + (lht(J)*NA(J))
*
*     If this gas side heat transfer agrees with the coolant side heat
*     flux calculated earlier, then the correct interface temperature
*     has just been passed. If not, the true value of the interface
*     temperature is greater than the value selected, and is determined
*     by an iterative procedure.
*
         IF (HTc(J).GT.HTg(J)) THEN
            TIHI = J
            TILO = J-1
            GOTO 2
         ENDIF
    1 CONTINUE
*
*     Finally, to decide whether this interface temperature or the
*     previous one is nearer the true interface temperature value, the
*     temperature for which the gas and coolant side heat transfers
*     are closest is calculated, and used in the subsequent equations
*
```

```
    2 IF (ABS(HTg(TIHI) - HTc(TIHI)).LT.ABS(HTg(TIHI-0.1d0)
     +   - HTc(TIHI-0.1d0))) THEN
         Q = TIHI
            ELSE
         Q = TILO
      ENDIF
*
*  -----------------------------------------------------------------------
*
*     Having evaluated the interface temperature, the set of differential
*     equations may now be specified, with the parameters used therein
*
      TEC = tc                   ! bulk temperature [Celsius]
      CALL INT(TEC,NLAM,TECLAM,LAM,LAMINT)
      Z = LAMINT*MWV             ! latent heat of vapourisation [J/mole]
      PIA = pi(Q)/1.01325d5      ! interface vapour pressure [atm.]
      CPA = cpwv*MWV             ! specific heat of vapour [J/mole degC]
      CPB = cpair*MA             ! specific heat of inert gas [J/mole degC]
      CPL = cpwl*MWV             ! specific heat of liquid [J/mole degC]
      TIF = ti(Q)                ! interface temperature [Celsius]
      H = hg(Q)                  ! Heat transfer coefficient [J/m^2 s degC]
*
      CPAV = ((Y(4)*CPA)+(G*CPB)+(Y(3)*CPL))/(Y(4)+G+Y(3))
*          The mole weighted average of CPA, CPB, and CPL [J/mole degC]
      R = 8.3143d0               ! Universal gas constant [J/mole degK]
*
      X1 = (Y(1)-TIF)/(EXP(CO(Q))-1.0d0)
      X2 = ((R*(TK**2.0d0))/Z)*((Pat-Y(2))/Y(2))
*
*
*     Finally, the four differential equations for temperature,
*     pressure, fog flow and vapour flow are
*
      YP(1) = ((R*(TK**2.0d0))/(Z*Y(2)))*
     +       (((Pat-Y(2))**2.0d0)/(G*Pat))*
     +       -NA(Q)*((Z+(CPA*X1))/(Z+((M*CPAV*R*(TK**2.0d0)*
     +      ((Pat-Y(2))**2.0d0))/(Z*Y(2)*G*Pat))))
*             [rate of change of bulk temperature]
*
      YP(2) = (((Pat-Y(2))**2.0d0)/(G*Pat))*
     +       -NA(Q)*((Z+(CPA*X1))/(Z+((M*CPAV*R*(TK**2.0d0)*
     +      ((Pat-Y(2))**2.0d0))/(Z*Y(2)*G*Pat))))
*             [rate of change of bulk vapour pressure]
*
      YP(3) = -NA(Q) - (-NA(Q)*((Z+(CPA*X1))/(Z+((M*CPAV*R*
     +   (TK**2.0d0)*((Pat-Y(2))**2.0d0))/(Z*Y(2)*G*Pat)))))
*             [rate of change of fog flow]
*
      YP(4) = -NA(Q)*((Z+(CPA*X1))/(Z+((M*CPAV*R*(TK**2.0d0)*
     +         ((Pat-Y(2))**2.0d0))/(Z*Y(2)*G*Pat))))
*             [rate of change of vapour flow]
*
      RETURN
      END
*
*
***************************************************************************
*
```

```
*
      SUBROUTINE READTAB(NPRES,TECPRES,PRES,INFILE)
*     Subroutine designed to read in tabulated data for the numerous
*     parameters and gas and vapour properties used in the calculations.
*
      REAL*8 TECPRES(100), PRES(100)
*
      INTEGER NPRES, I
*
      CHARACTER*80 INFILE
*
      OPEN (UNIT=25, FILE=INFILE)
*
      READ (25,*) NPRES
*
      DO 20 I=1,NPRES
         READ(25,*) TECPRES(I), PRES(I)
 20   CONTINUE
*
      CLOSE (UNIT=25)
*
      RETURN
      END
*
*
***************************************************************************
*
      SUBROUTINE INT(TEC,NPRES,TECPRES,PRES,PRESINT)
*     Subroutine which linearly interpolates between points in the data
*     tables, to obtain approximate value at the desired temperature.
*
      REAL*8 TEC, PRESINT
      REAL*8 TECPRES(100), PRES(100)
*
      INTEGER NPRES, I
*
      DO 20 I = 1,NPRES
         IF ((TEC.GE.TECPRES(I)).AND.(TEC.LT.TECPRES(I+1))) THEN
            NLO = I
            GOTO 21
         ENDIF
 20   CONTINUE
*
 21   PRESINT = PRES(NLO) + (PRES(NLO+1)-PRES(NLO))*
     +      (TEC-TECPRES(NLO))/(TECPRES(NLO+1)-TECPRES(NLO))
*
      RETURN
      END
*
***************************************************************************
```

G Orifice meter calibration

Having manufactured an orifice meter with two interchangeable plates (11.0mm and 19.0mm in diameter) it was necessary to calibrate it. For simplicity it was decided to do so against a pair of standard rotameters, using the pressurised laboratory air supply.

G.1 *Set-up*

A pressure regulator was attached to the air supply, followed by a pair of gate valves and rotameters (in parallel), a straight length of pipe, and finally the orifice meter, complete with pressure tapings and an adequate length of straight pipe either side of the orifice. The rotameters covered different mass flow rates and were each calibrated at 15°C, 1bar. An inclined alcohol manometer was attached to the orifice meter pressure tapings in order to accurately measure any pressure drop across it.

G.2 *Effect of fluid density changes during calibration.*

During the orifice meter calibration the temperature and pressure in the air line naturally deviated from the 15°C, 1bar at which the rotameters were themselves calibrated so it was necessary to account for the effects of such variations. The rotameter may be considered as an orifice meter with a variable area aperture, and so the formula for calculating the flow rate through a rotameter is very similar to that for an orifice meter, and is given by

$$G = C_D A_2 \sqrt{\frac{2\rho(-\Delta P)}{1-\left(A_2/A_1\right)^2}} \tag{G-1}$$

where $-\Delta P$ is the pressure difference over the float, and is given by

$$-\Delta P = \frac{V_f\left(\rho_f - \rho\right)g}{A_f} \quad . \tag{G-2}$$

When using a rotameter to measure air flow, the density of the float (usually aluminium, brass or steel) is very much greater than that of the fluid, i.e. $\rho_f \rangle\rangle \rho$, and the pressure difference over the float, ΔP, is effectively independent of small changes in fluid density. Thus, from equation (G-1), the flow rate measured by a rotameter is proportional to the square of the density of the fluid, $G \propto \sqrt{\rho}$.

The flow rate calculated to be passing through an orifice plate is also proportional to the square of the density of the fluid. Therefore, when a rotameter is placed in series with an orifice plate in order to calibrate it, any variations in fluid density will affect both instruments equally. Hence there was no need to account for pressure or temperature changes in the fluid during the calibration of the orifice meter.

G.3 *Calibration procedure.*

The instrumentation was configured as detailed in section G.1. The first set of tests was carried out using the 19.0mm diameter orifice plate. By opening and carefully adjusting one of the gate valves a pre-determined mass flow rate of air was established through the orifice meter, as registered on the rotameter. The rotameter reading and corresponding height of liquid in the inclined manometer leg were recorded. Then, the air mass flow rate was adjusted, and new measurements taken. Finally the 19.0mm plate was replaced by the 11.0mm diameter orifice plate, and the process repeated.

Initial inconsistencies in the results due to air bubbles within the manometer, the manometer tube failing to lie precisely parallel with the measurement scale, and old, inaccurate rotameters conspired to make this a more time consuming task than was initially envisaged. However, once these problems had been rectified, and reliable rotameters obtained, the runs were completed quite quickly.

G.4 *Calibration results*

The ensuing results for the 11.0mm and 19.0mm orifice plates are presented in Figure G-1 below.

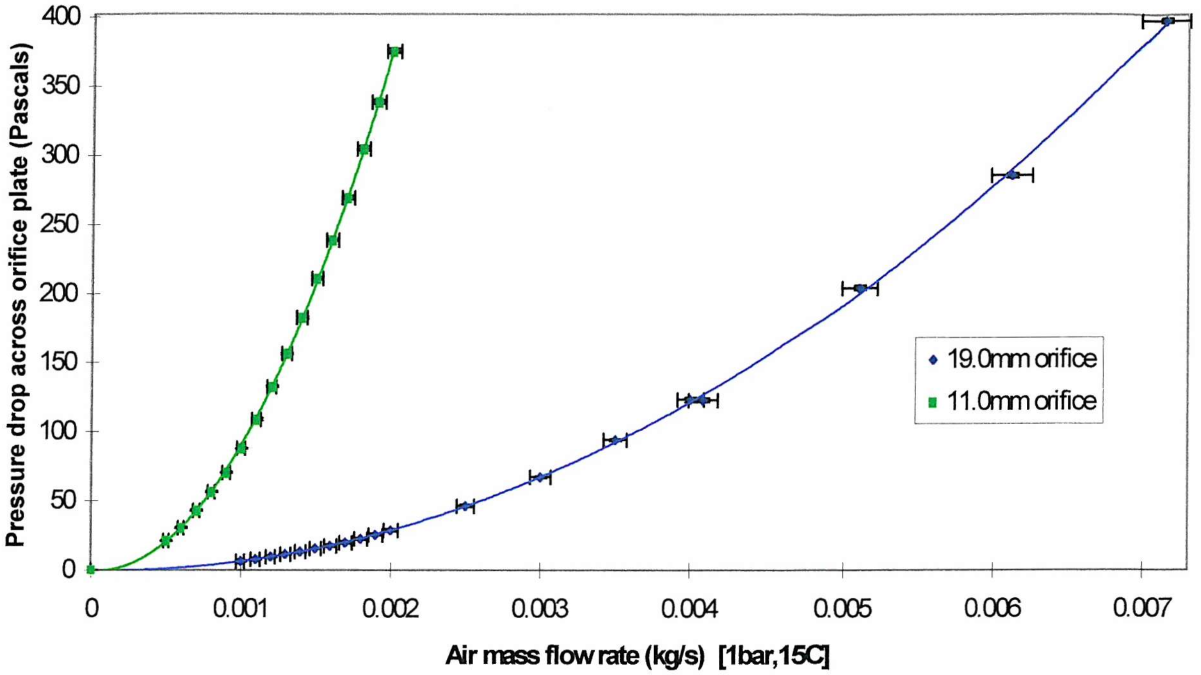

Figure G-1. Pressure drop measurements across orifice meter.

The measured pressure drop across the orifice plate was proportional to the square of the mass flow rate passing through it, i.e. $\delta P \propto G^2$, in agreement with the equation for flow through an orifice [42], i.e.

$$G = \frac{C_D A_o}{v} \sqrt{\frac{2v(P_1 - P_2)}{1 - \left(\frac{A_o}{A_1}\right)^2}} \quad . \qquad \textbf{(G-3)}$$

The implementation of equation (G-3) was not as simple as it first appeared, since the discharge coefficient, C_D, is not a simple function and depends on the value of the Reynolds number at the orifice and the precise form of the meter. However, in general this variation with Reynolds number is as depicted in Figure G-2, below.

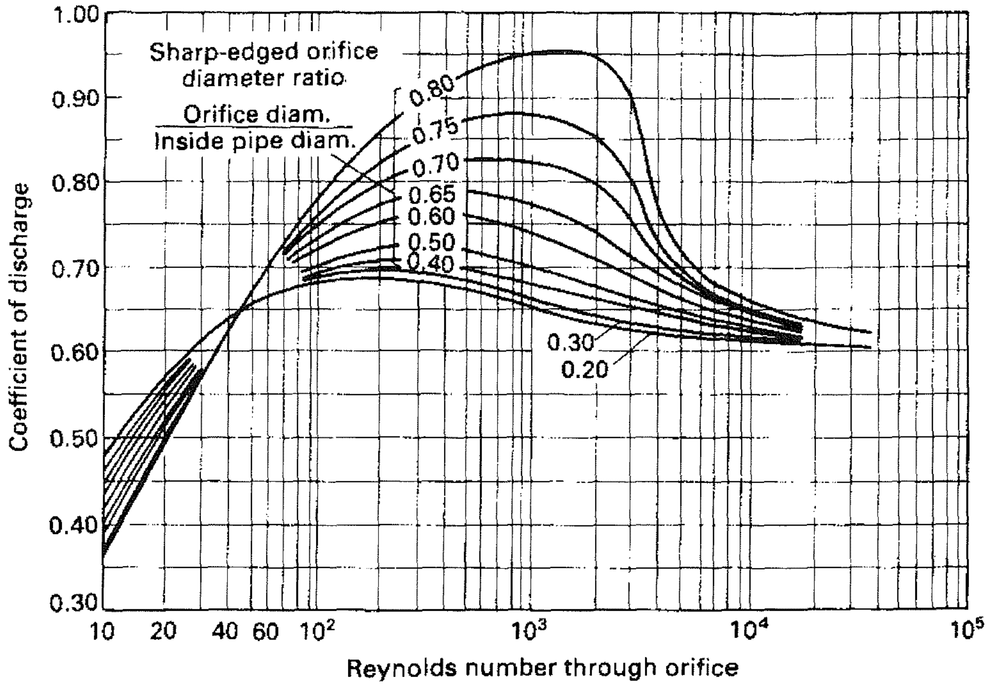

Figure G-2. Approximate form of the discharge coefficient for sharp-edged orifice Meters [42]

The measurements of Figure G-2 were then used in conjunction with equation (G-3) to determine the actual variation in discharge coefficient with Reynolds number obtained during calibration. By far the largest error in the calculation of the discharge coefficient arose due to the uncertainty in the diameter of the pipe in which the orifice meter was placed (a standard 1" galvanised steel pipe). A 4% error in this value leads to an error in excess of 16% for C_D. Hence, the group $C_D\sqrt{1/\left(1-\left(A_o/A_p\right)^2\right)}$ was used in preference to C_D. These values are plotted against the Reynolds number at the orifice, calculated using

$$\mathrm{Re} = \frac{\bar{U}D_o}{\mu v} = \frac{GD_o}{A_o\mu}, \qquad \textbf{(G-4)}$$

in Figure G-3 below. Ignoring the parameter $\sqrt{1/\left(1-\left(A_o/A_p\right)^2\right)}$, it can be seen that the experimentally determined variation of discharge coefficient with Reynolds number for the manufactured orifice plates is of the form depicted in Figure G-2.

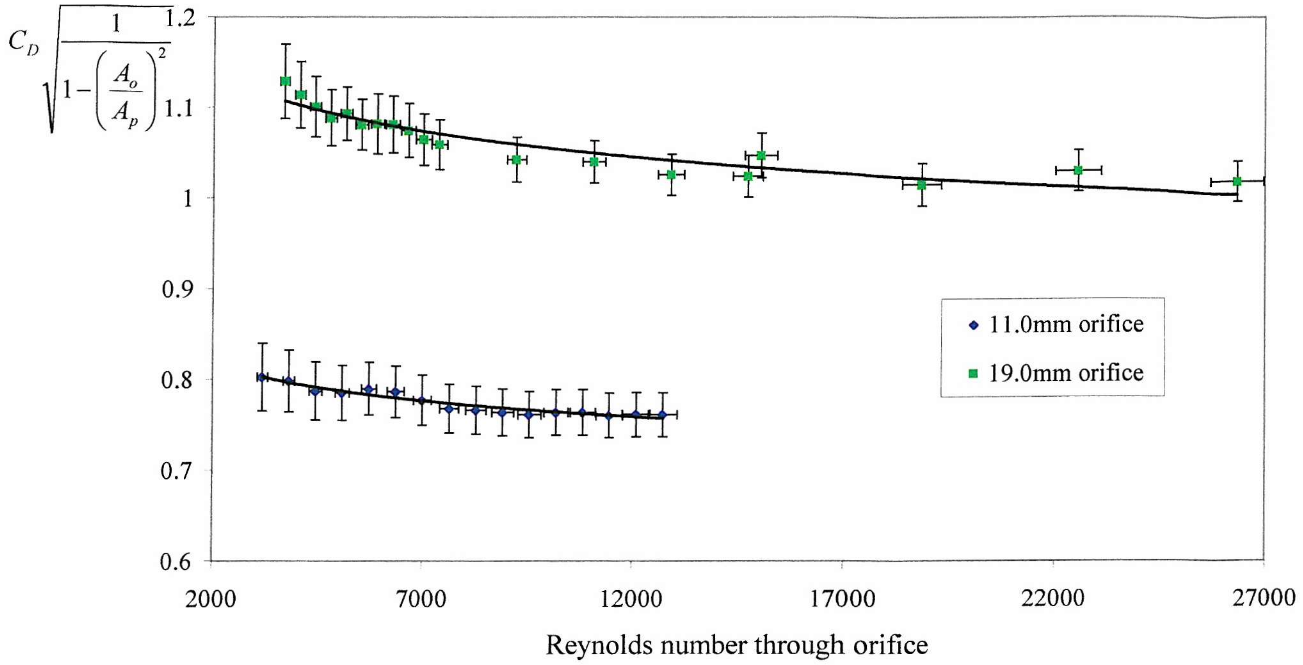

Figure G-3. Experimental measurements illustrating the variation of discharge coefficient with Reynolds number for the two orifice plates.

G.5 *Calculation of steam flow rates*

Having calibrated the orifice meter with air, as described above, it was then placed between the boiler and the mixing section to enable the steam flow rate to be measured. In order to produce the desired conditions within the main test section, for any specified steam flow rate, the corresponding pressure difference across the meter had to be determined. This allowed the desired steam flow rate to be obtained during experimentation by adjusting the power to the heating elements within the boiler until the appropriate reading was obtained on the manometer. Rearranging equation (G-3) gives

$$\frac{G}{\left(C_D\sqrt{\frac{1}{1-\left(A_o/A_p\right)^2}}\right)\sqrt{\rho}\sqrt{\Delta P}} = \sqrt{2}\,A_o = \text{constant} \qquad \textbf{(G-5)}$$

when using a single orifice plate. So, to calculate the pressure drop across the plate that must be obtained when using steam, from the results for air, the equation becomes

$$\sqrt{\Delta P_s} = \frac{G_s\left(C_{Da}\sqrt{\dfrac{1}{1-\left(A_o/A_p\right)^2}}\right)\sqrt{\rho_a}}{G_a\left(C_{Ds}\sqrt{\dfrac{1}{1-\left(A_o/A_p\right)^2}}\right)\sqrt{\rho_s}}\sqrt{\Delta P_a} \qquad \textbf{(G-6)}$$

where G_s is the desired steam flow rate, ρ_s is the density of steam at the measured temperature and pressure, obtained from steam tables, ρ_a is the density of air at 15°C 1 bar (at which the orifice plate was calibrated), and G_a and ΔP_a are any flow rate and pressure drop obtained during a typical run during calibration with air. The quantities in brackets are obtained from Figure G-3, using the appropriate orifice Reynolds numbers determined from G_s and G_a using equation (G-4).

H Mass flow rate calculation

Below is the simple computer program used to calculate the experimental air and water vapour mass flow rates at condenser entry to produce a mixture of given condition and velocity. The program was also used to specify the entry molar flow rates for the computer program used to predict the changing mixture properties within the condenser and the rate of fog formation.

```
*
*     PROGRAM INCORPORATING THE IDEAL GAS LAW TO CALCULATE THE AIR
*     AND VAPOUR FLOW RATES OF A MIXTURE OF KNOWN CONDITION FLOWING
*     THROUGH A PARTIAL CONDENSER WITH A SPECIFIED MEAN VELOCITY.
*
      real*8          tc, pg, mfa, mfwv, T, A, MWV, MA, RWV, RA, P,
     +                pwv, u, vg, vs, phi, V, G, X, Y
*
*    Input value of bulk temperature, saturation pressure,
*    relative humidity and specific volume of water vapour for
*    each case.
*
        tc = 95.0d0
*           temperature [Celsius]
        pg = 0.8455d5
*           partial vapour pressure at saturation (tc) [N/m^2]
        phi = 1.0d0
*           relative humidity
        vg = 1.9819d0
*           specific volume of water vapour [cubic metres/kg]
        u = 2.0d0
*           desired mean mixture velocity [m/s]
*  ----------------------------------------------------------------------
*
        T = 273.15d0 + tc      ! Temperature [Kelvin]
        P = 1.01325d5          ! Total pressure [N/m^2]
        A = 0.008d0            ! c-s area of duct  [m^2]
        MWV = 18.015d-3        ! molar mass of vapour [kg/mole]
        MA = 28.96d-3          ! molar mass of inert gas [kg/mole]
        RWV = 8.3144d0/MWV     ! gas constant of vapour [J/kg K]
        RA = 8.3144d0/MA       ! gas constant of inert gas [J/kg K]
*
*  - - - - - - - - - - - - - - - - - - - - - - - - - - - - - - - - - - -
*
        pwv = phi*pg      ! actual partial pressure of the vapour
        vs = vg/phi       ! actual specific volume of the vapour
*
        mfwv = (u*A)/vs         ! velocity of mixture on entry
*
        mfa = ((P-pwv)*A*u)/(RA*T)
*         mass flow rate of air [kg/s], from ideal gas law.
*
        rho = (mfwv/(u*A))+(mfa/(u*A))
```

```
*           density of mixture [kg/cubic meter]
*
*        And the corresponding molar velocities of vapour and inert
*        gas through a duct of cross-sectional area A, are
*
         V = mfwv/(MWV*A)    ! molar velocity of vapour [moles/m^2 s]
         G = mfa/(MA*A)      ! molar velocity of inert gas [moles/m^2 s]
*
         X = V/G
         Y = (pg/(P-pg))
*
*        The results are then written to file
*
         OPEN(UNIT=16, FILE='massflow.f', STATUS='UNKNOWN')
         WRITE (16,10)
         WRITE (16,20) tc, rho, phi, mfwv, u, mfa
         WRITE (16,30)
         WRITE (16,40)
         WRITE (16,50) V, G, X, Y
   10    FORMAT(3x,'t=[Celsius]',3x,'rho=[kg/m^3]',4x,'phi=',6x,
     +   'mfwv=[kg/s]',3x,'u=[m/s]',5x,'mfa=[kg/s]')
   20    FORMAT(6f13.6)
   30    FORMAT('')
   40    FORMAT(5x,'V[moles/m^2 s]',3x,'G[moles/m^2 s]',6x,'V/G',
     +   10x,'p/(P-p)')
   50    FORMAT(4f16.6)
      CLOSE(UNIT=16, STATUS='KEEP')
      STOP
      END
```

I Calculating air and vapour flow rates

Having chosen the mixture conditions required for a given experimental run (that is, mean temperature, T, relative saturation, ϕ, and mean channel velocity, u) it was then necessary to calculate the required water vapour and air mass flow rates at condenser entry. The associated saturation pressure and specific volume of the vapour in the mixture were then obtained from steam tables [15]. These values were used in conjunction with the relevant parameters for steam - air mixtures, e.g. gas constant, R_a, and those of the condensing section, e.g. cross-sectional area, A, to calculate the required vapour mass flow rate

$$\dot{m}_s = \frac{uA}{v_s} = \frac{uA\phi}{v_g} , \qquad \text{(I-1)}$$

and, using the ideal gas law, the air mass flow rate

$$\dot{m}_a = \frac{(P - p_s)Au}{R_a T} = \frac{(P - \phi p_g)Au}{R_a T} . \qquad \text{(I-2)}$$

These flow rates were those required at entry to the condenser. However, it was important to account for the water vapour present in the laboratory air supply, to ensure that the measured steam and air flow rates produced the desired mixture condition. Thus the required measurement value of the steam mass flow rate through the orifice meter was calculated using

$$\begin{matrix} \textit{Steam flow rate} \\ \textit{through orifice} \end{matrix} = \begin{matrix} \textit{Vapour flow rate} \\ \textit{from equation}\ (1) \end{matrix} - \begin{matrix} \textit{Vapour flow rate} \\ \textit{contained in the air} \end{matrix} \qquad \text{(I-3)}$$

and that for the air mass flow rate through the rotameter is given by

$$\begin{matrix} \textit{Air flow rate} \\ \textit{through rotameter} \end{matrix} = \begin{matrix} \textit{Dry air flow rate} \\ \textit{from equation}\ (2) \end{matrix} + \begin{matrix} \textit{Vapour flow rate} \\ \textit{contained in the air} \end{matrix} \qquad \text{(I-4)}$$

I.1 *Rotameter measurement*

To calculate the rotameter reading needed to ensure the correct air flow rate at the condenser, the humidity of the air supply had to be determined. The partial pressure of water vapour in the laboratory air supply was obtained with a standard wet and dry bulb thermometer, using the equation [69]

$$p_s = p_g - [0.00066(1 + 0.00115t_{wb})P(t_{db} - t_{wb})] \ , \tag{I-5}$$

allowing the mass ratio of water vapour to dry air, or the specific humidity of the air to be calculated from

$$\frac{m_s}{m_a} = \omega = \frac{R_a p_s}{R_s p_a} \approx 0.622\frac{p_s}{P - p_s} \ . \tag{I-6}$$

The mass flow rates of water vapour and air through the rotameter, $\dot{m}_s(rot)$ and $\dot{m}_a(rot)$ respectively could then be deduced from the measurement value of the rotameter $\dot{m}_{a+s}(rot)$ using the equations

$$\dot{m}_a(rot) = \frac{\dot{m}_{a+s}(rot)}{(1+\omega)} \tag{I-7}$$

and

$$\dot{m}_s(rot) = \dot{m}_{a+s}(rot) - \dot{m}_a \ . \tag{I-8}$$

Testing the laboratory air supply, and performing the necessary calculations using equations (I-5) to (I-8) above, showed that the air had a low specific humidity of approximately 0.00148. The associated vapour flow rates therefore comprised only a small fraction of the overall vapour flow rate. The small variations in the specific humidity of the air between runs were ignored, and a fixed value of $\omega = 0.00148$ used throughout.

Finally, since the rotameters used to measure the air mass flow rate were calibrated at 1 bar, 15°C, and the equation for the flow rate through a rotameter [42]

$$G = C_D A_2 \sqrt{\frac{2gV_f(\rho_f - \rho)\rho}{A_f\left[1 - (A_2/A_1)^2\right]}} \quad , \qquad \textbf{(I-9)}$$

contains a density term, it was necessary to compensate for any deviation in air density from that of air at 15°C, 1bar. In equation (I-9) the density of the rotameter float is much greater than that of the air, so $\rho_f - \rho \approx \rho_f$, and the flow rate, $G \propto \sqrt{\rho}$.

Now, from the ideal gas law,

$$\rho = \frac{p}{RT} \qquad \textbf{(I-10)}$$

and since the temperature (Kelvin) of the laboratory air supply deviates only slightly from 288°K, the flow rate is effectively proportional to $\sqrt{p}$.

So, finally, the required rotameter measurement needed to produce a mixture of mean temperature, T , relative saturation, ϕ, and mean channel velocity, u, is obtained from equations (I-2) and (I-7) to be

$$\dot{m}_{a+s}(rot) = \frac{(P - \phi p_g)Au}{R_a T}(1+\omega)\sqrt{P} \quad . \qquad \textbf{(I-11)}$$

I.2 *Orifice meter measurement*

The steam flow rate through the orifice meter necessary to produce the desired mixture is obtained from equations (I-1), (I-2), (I-3) and (I-6)

$$\dot{m}_s(orifice) = \frac{uA\phi}{v_g} - \left[\dot{m}_{a+s}(rot) - \frac{(P - \phi p_g)Au}{R_a T}\right] \qquad \textbf{(I-12)}$$

Having calculated the mass flow rate of steam through the orifice plate, the corresponding pressure difference across it, measured in millimetres of fluid with a manometer, is deduced from Figure I.1, below. This graph has been produced from the results of Appendix G, where a detailed explanation of the calibration of the orifice meter is given.

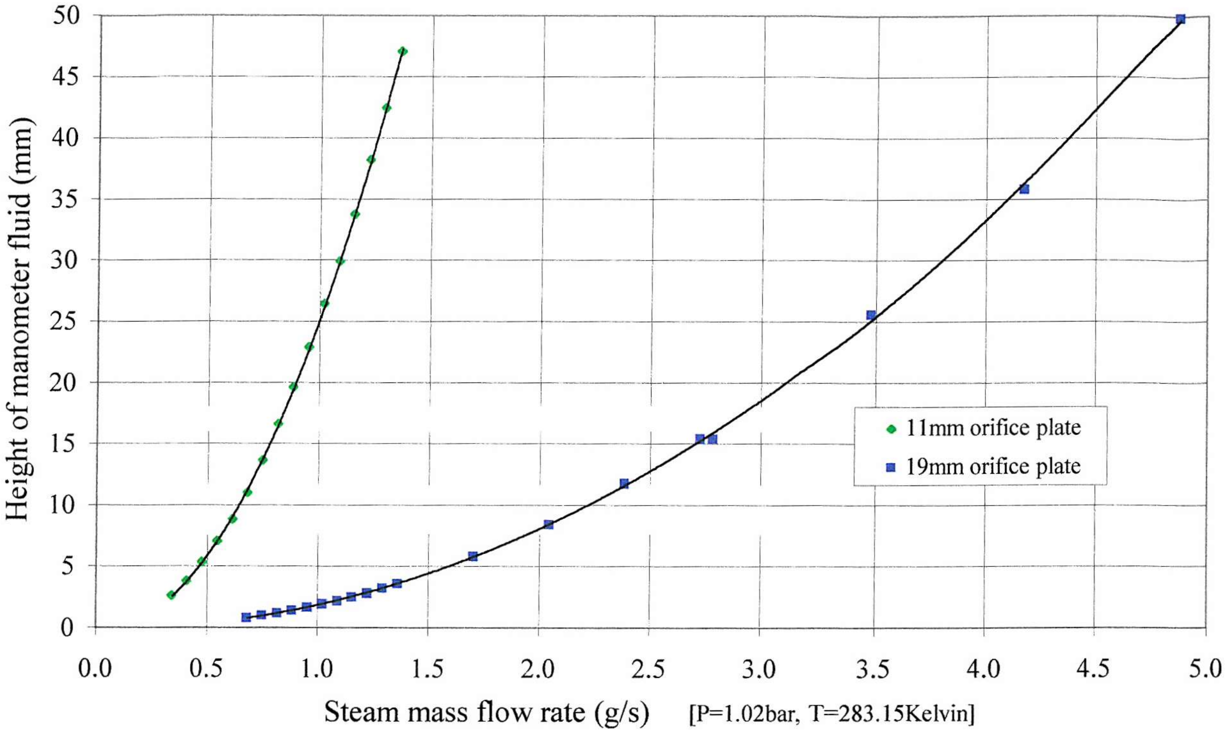

Figure I.1 Pressure difference across orifice meter, measured in mm head of fluid (SG=0.784) with a manometer, plotted against mass flow rate of steam flowing through it.

Again, a correction must be included for any difference in temperature or pressure of the steam from the values assumed in producing Figure I.1, i.e. 1.02bar, 110°C. Referring to equation (G-5), $\Delta P \propto 1/\rho \propto T/P$, therefore the correct height of manometer fluid, h, corresponding to the desired mass flow rate of steam through the orifice is given by

$$h = graphical\ value\ (fig.1.1) \times \frac{T}{273.15^{o}K} \times \frac{1.02bar}{P} \quad . \tag{I-13}$$

J Universal velocity and temperature distributions

The experimental test rig was designed to ensure fully developed turbulent flow within the condenser sections. As a result, a number of methods are available for predicting the form of the lateral velocity profile. One of the most commonly referred to is the universal velocity distribution, produced by von Kármán, and referred to in many heat transfer tests [70, 3].

Although developed for tubes, it also gives a good representation of the flow between parallel plates [71].

J.1 *Universal velocity distribution*

The turbulent shear stress of a fluid may be written [3]

$$\tau_t = -\rho\overline{v_x' v_y'} = \rho\varepsilon\frac{\partial v_x}{\partial y} \tag{J-1}$$

where v_x' and v_y' are the fluctuating component of the velocity in the x and y direction respectively, and ε is the eddy viscosity. Determination of this eddy viscosity produces the mean flow velocity, v_x, as a function of position, y, that is, the velocity distribution.

However, the eddy viscosity cannot be specified in a general manner [70]. A simplified, semi empirical model has to be used to quantify it, for example, Prandtl's mixing length model. This represents the eddy viscosity as

$$\varepsilon = l^2\left(\frac{\partial v_x}{\partial y}\right) \tag{J-2}$$

in which the characteristic mixing length, l, is zero at the surface and varies linearly with distance, thus

$$l = Cy \tag{J-3}$$

in which C is a constant. Substituting equations (J-2) and (J-3) into (J-1) gives

$$\tau_t = \rho C^2 y^2\left(\frac{\partial v_x}{\partial y}\right)^2 \tag{J-4}$$

which, taking the square root and integrating, assuming the shear stress to be constant at its wall value, τ_o, produces [70]

$$v_x = C_1\sqrt{\frac{\tau_o}{\rho}}\ln y + C_2 \tag{J-5}$$

This logarithmic velocity distribution is usually written in a dimensionless form by writing

$$\sqrt{\frac{\tau_o}{\rho}} = v_x^* \qquad \frac{v_x}{v_x^*} = v_x^+ \qquad \frac{y v_x^*}{\upsilon} = y^+ \tag{J-6}$$

where υ is the kinematic viscosity. Thus, equation (J-5) may be written

$$v_x^+ = C_1 \ln y^+ + C_3 \tag{J-7}$$

Now the total shear stress is given by the sum of the turbulent and laminar shear stresses. The laminar boundary layer shear stress is given by

$$\tau_l = \rho\upsilon\frac{\partial v_x}{\partial y} \tag{J-8}$$

so the total shear stress is

$$\tau = \tau_l + \tau_t = \rho(\upsilon + \varepsilon)\frac{\partial v_x}{\partial y} \tag{J-9}$$

which, introducing v_x^+ and y^+ and again assuming the shear stress in the boundary layer to be constant at the wall value τ_o, becomes

$$\frac{dv_x^+}{dy^+} = \frac{1}{1 + (\varepsilon/\upsilon)} \tag{J-10}$$

The university velocity distribution then results from representing the turbulent boundary layer as separable into three sublayers: the laminar sublayer, in which the eddy viscosity is negligible $(\varepsilon << \upsilon)$; a buffer zone in which the eddy viscosity and the kinematic viscosity are comparable $(\varepsilon \approx \upsilon)$; and a fully turbulent zone in which the eddy viscosity dominates $(\varepsilon >> \upsilon)$.

In the laminar sublayer, the fact that $\varepsilon << \upsilon$ means that $\varepsilon/\upsilon \approx 0$, hence from equation (J-10) the velocity distribution is linear, and $v_x^+ = y^+$. In the buffer and fully turbulent zones the velocity distribution is given by equation (J-7), where the constants C_1 and C_3 must be determined experimentally. The generally accepted representation for the universal velocity distribution, suggested by von Kármán is taken to be [3]

$$\begin{array}{lll} v_x^+ = y^+ & y^+ < 5 & \text{[Laminar sublayer]} \\ v_x^+ = 5.0\ln y^+ - 3.05 & 5 < y^+ < 30 & \text{[Buffer zone]} \\ v_x^+ = 2.5\ln y^+ + 5.5 & y^+ > 30 & \text{[Fully turbulent zone]} \end{array} \qquad \textbf{(J-11)}$$

For the calculation of the universal velocity distribution within a duct, the diameter of the duct, the density and the dynamic viscosity of the fluid and the wall shear stress must be known. The wall shear stress, τ_o, may be calculated using

$$\tau_o = \frac{1}{4}\frac{f\rho V^2}{2} \qquad \textbf{(J-12)}$$

obtained from the Fanning or D'arcy equation [3]. The friction factor f is obtained from the well known Moody diagram for pipe friction.

J.2 *Universal temperature distribution*

Because of the similarity of the transport equations of momentum and thermal energy, given by

$$\frac{\tau}{\rho} = (\upsilon + \varepsilon_M)\frac{dv_x}{dy} \qquad \textbf{(J-13)}$$

and

$$\frac{q''}{\rho c_p} = (\alpha + \varepsilon_H)\frac{dt}{dy} \qquad \textbf{(J-14)}$$

von Kármán suggested the temperature gradient be similar to the velocity gradient, given by the universal velocity distribution. Since momentum and heat are both carried about the turbulent flow by eddies, von Kármán assumed that the momentum and heat transfer diffusivities are equal $\left(\varepsilon_M = \varepsilon_H\right)$, and thereby produced the universal temperature distribution for the turbulent flow of a fluid through a hot or cold duct.

The transport equation for thermal energy may be written

$$\frac{q''}{\rho c_p} = \left(\alpha + \varepsilon_H\right)\frac{dt}{dy} = \upsilon\left(\frac{\alpha}{\upsilon} + \frac{\varepsilon_H}{\upsilon}\right)\frac{dt}{dy} \tag{J-15}$$

Now since it has been assumed that $\varepsilon_H = \varepsilon_M = \varepsilon$, then referring back to equation (J-10) gives

$$\frac{\varepsilon_H}{\upsilon} = \frac{1}{f'\left(y^+\right)} - 1 \tag{J-16}$$

where

$$f'\left(y^+\right) \equiv \frac{dv_x^+}{dy^+} \tag{J-17}$$

Thus,

$$\frac{q''}{\rho c_p} \approx \upsilon\left(\frac{\alpha}{\upsilon} - 1 + \frac{1}{f'\left(y^+\right)}\right)\frac{d\theta}{dy} \tag{J-18}$$

where θ is the temperature excess, that is, the temperature at point y less the temperature at the surface. The function $f'\left(y^+\right)$ can be obtained by differentiating the form of equation (J-11) that is applicable. In terms of the dimensionless location y^+ defined in equation (J-6),

$$d\theta \approx \left(\frac{q_o''}{\rho c_p}\right)\sqrt{\frac{\rho}{\tau_o}}\,\frac{dy^+}{\dfrac{1}{\Pr} - 1 + \dfrac{1}{f'\left(y^+\right)}}$$

Hence the universal temperature distribution is given by integrating the above equation, that is

$$\theta = \left(\frac{q_o''}{\rho c_p}\right)\sqrt{\frac{\rho}{\tau_o}}\Pr y^+ \qquad y^+ < 5 \qquad \text{[Laminar sublayer]}$$

$$\theta = \left(\frac{q_o''}{\rho c_p}\right)\sqrt{\frac{\rho}{\tau_o}}\left[5\Pr + 5\ln\left(1 - \Pr + \left(\frac{y^+}{5}\Pr\right)\right)\right]$$

$$5 < y^+ < 30 \qquad \text{[Buffer zone]} \tag{J-19}$$

$$\theta = \left(\frac{q_o''}{\rho c_p}\right)\sqrt{\frac{\tau_o}{\rho}}y^+ + \left(5\Pr - 1\right) + 5\ln\left(\frac{1 + 5\Pr}{6}\right)$$

$$y^+ > 30 \qquad \text{[Fully turbulent zone]}$$

K Bulk temperature estimation

K.1 *Introduction*

The most important property of a vapour – inert gas mixture with regard to fog formation is its relative humidity. The greater the relative humidity of such a mixture, the greater its propensity to form a fog. In order to specify the relative humidity of a mixture, it is necessary to know its bulk or mean cross-sectional temperature, and its mean vapour pressure. The relative humidity is then given by

$$\phi = \frac{p_s}{p_g} \tag{K-1}$$

where p_s is the actual vapour pressure and p_g is the saturation value of vapour pressure at the bulk mixture temperature t_b, and is obtained from tables.

The vapour pressure may be calculated from the vapour and inert gas flow rates, which were measured experimentally, and remain constant after measurement until the mixture enters the condenser. The bulk temperature, however, is more difficult to determine. To measure it experimentally would require an entire cross-sectional mixture sample to be taken from the point of condenser entry, the sample thermally isolated until the temperature is uniform throughout, and then a point measurement taken. This procedure was considered impractical. Alternatively, the bulk temperature at condenser entry could have been estimated from measurements of the separate vapour and inert gas flows prior to heating and mixing. However, the estimations would have to not only account for the energy added to the mixture using the heating tapes, but also the losses throughout the apparatus due to the imperfect nature of the insulation.

The method eventually chosen to estimate the bulk temperatures was to make use of the point temperature measurements obtained using thermocouples at 125mm throughout the length of the condenser. By performing a number of experiments to measure the lateral temperature profiles within the condenser under a range of different conditions, a reliable relationship between the point measurements and bulk temperature was to be obtained.

K.2 *Procedure for bulk temperature estimation*

From the temperature measurements presented in chapter 8, it soon became clear that there were four stages involved in estimating the bulk temperature from the point thermocouple measurements. These were:

- Estimate the true centre-line temperature from the thermocouple measurement
- Estimate the mean lateral temperature between the cold condenser walls
- Add a correction for the vertical temperature profile, parallel to the walls, giving the cross-sectional mean or bulk temperature
- Add a final correction relating to the flow dependent upon the axial condenser location.

K.2.1 Centre-line temperature

The thermocouples located in the condenser section were positioned mid way between the base and top of the condenser, and at the point of greatest temperature measurement laterally, as discussed in section 6.5. However, this was not at the centre of the condenser, as discussed in section 8.3, and illustrated in Figure K-1 below.

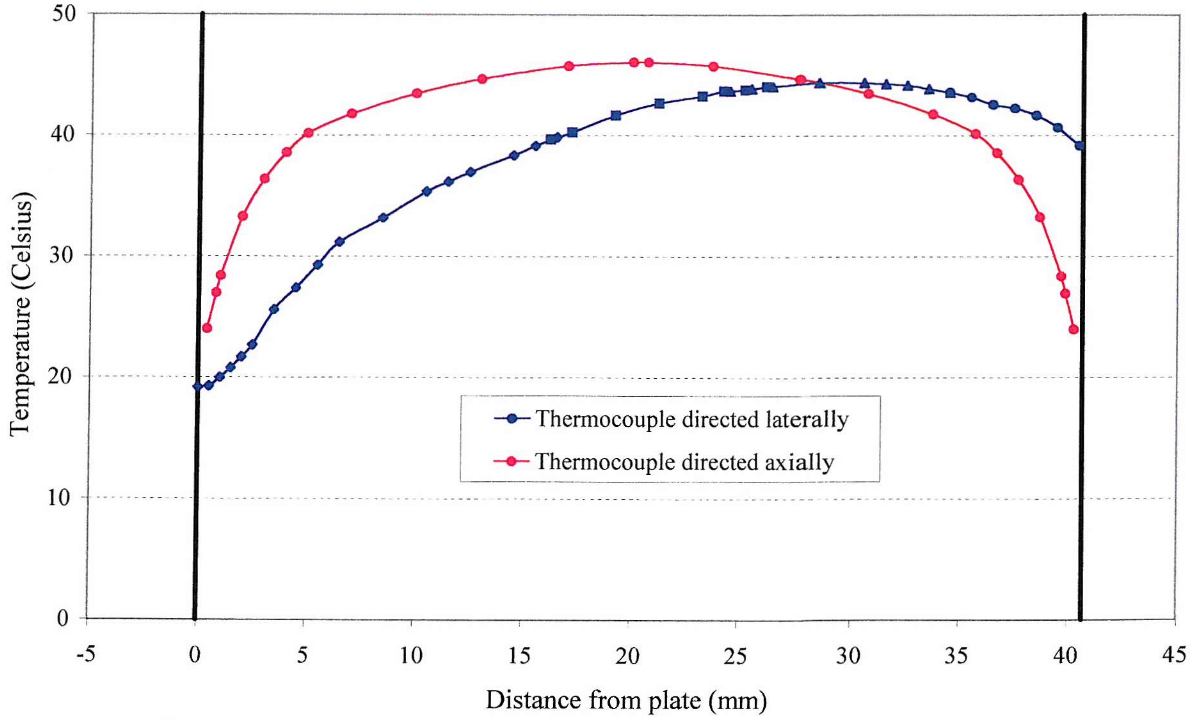

Figure K-1. Comparison of temperature distributions obtained using thermocouples directed laterally and axially within the condenser.

The maximum temperature measured with the thermocouples directed laterally was shown to be lower than the true value at the centre of the condenser (as measured accurately with a thermocouple directed axially – refer to section 8.3). By measuring the difference over a range of temperatures a simple correction was derived for calculating the centre-line temperature from the measured value,

$$t(centre-line) \approx t(measured) + 0.04[t(measured)-21] \quad \textbf{(K-2)}$$

K.2.2 Mean lateral temperature

Having estimated the centre-line temperature within the condenser, the next step was to estimate the mean lateral temperature between the plates. Towards the end of the two metre condenser, the temperature profile closely matches that of the universal velocity distribution, as indicated in Figure K-2 below.

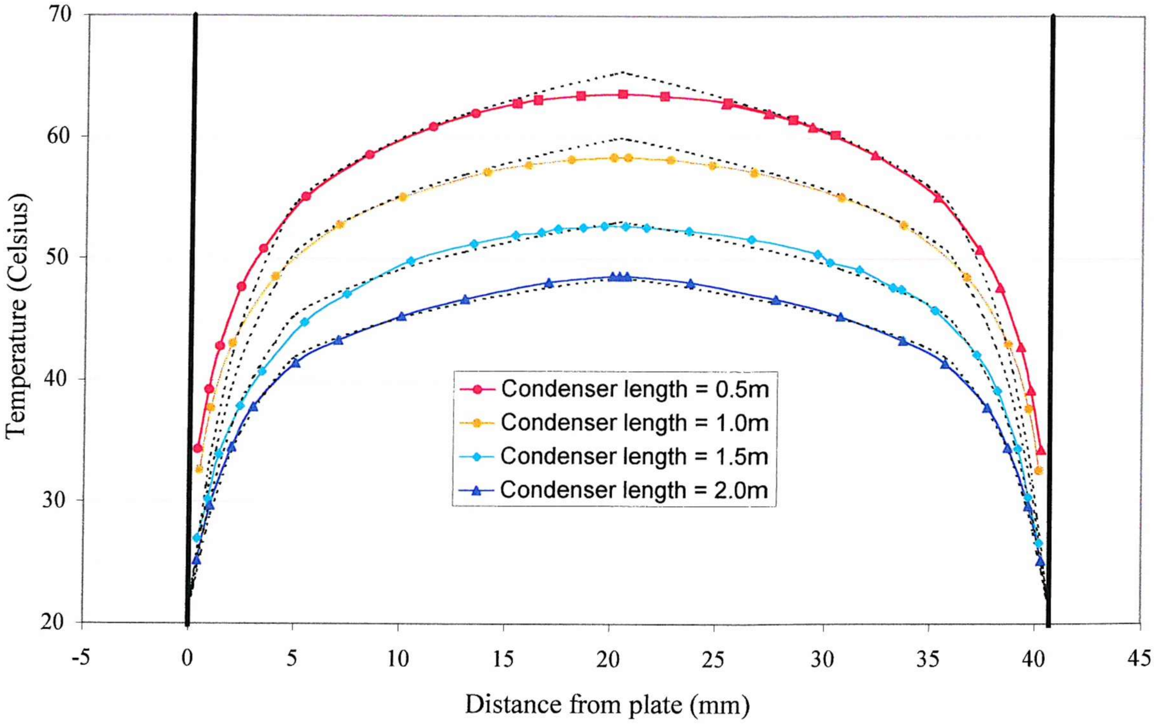

Figure K-2. Temperature profiles measured between the cold walls at condenser exit and the corresponding universal temperature distributions (dotted lines).

Hence, integrating the equations for the universal velocity distribution from one condenser wall to the centre and doubling the result may be expected to give a good estimation of the mean lateral temperature. Using the trapezium rule of integration with the experimental data, such as that plotted in Figure K-2, proved this was correct, the mean temperatures agreeing to within 0.2^{o}C on average. However, the complexity of the universal temperature distribution made this process somewhat cumbersome and time consuming. Stern and Votta [72] successfully used a much simpler formula to calculate the mean temperature, based in part on the universal velocity distribution. The formula used was of the form

$$t(mean) = X[t(centre-line) - t(wall)] + t(wall) \tag{K-3}$$

where X is a constant. Comparing the results of this formula with a range of experimental data obtained during experiments with hot air mixtures showed good agreement when the value of the constant was set at 0.81. However, the shape of the universal temperature profile changes with the Prandtl number of the fluid, as depicted in Figure K-3 where

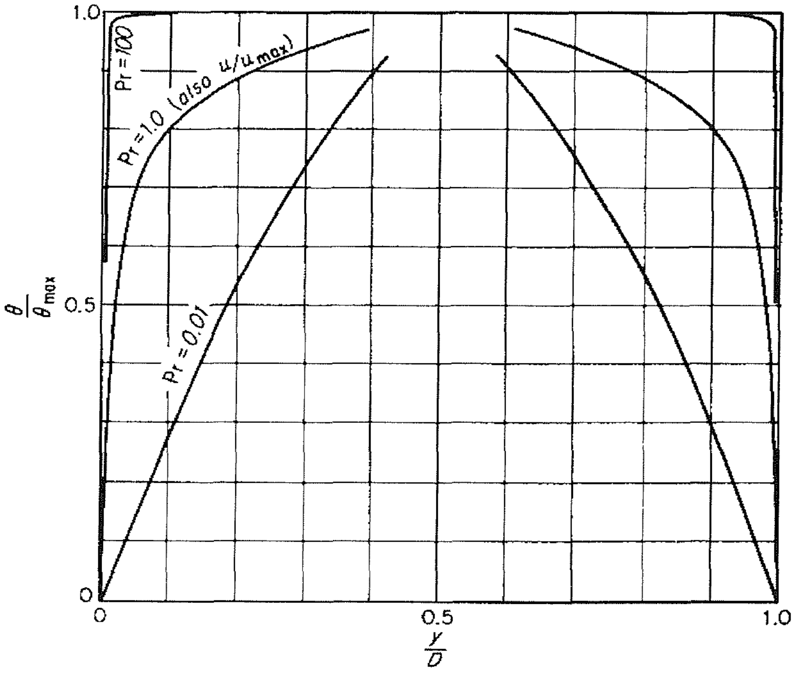

Figure K-3. Temperature distributions for fully developed turbulent flow [70]

The Prandtl number of air is approximately 0.71, while that of water vapour is slightly higher at around 0.95. Referring to the figure above, this implies a greater value of X for water vapour – air mixtures. This was confirmed by plotting the lateral temperature profiles of typical air and air – water vapour mixtures, as in Figure K-4 below.

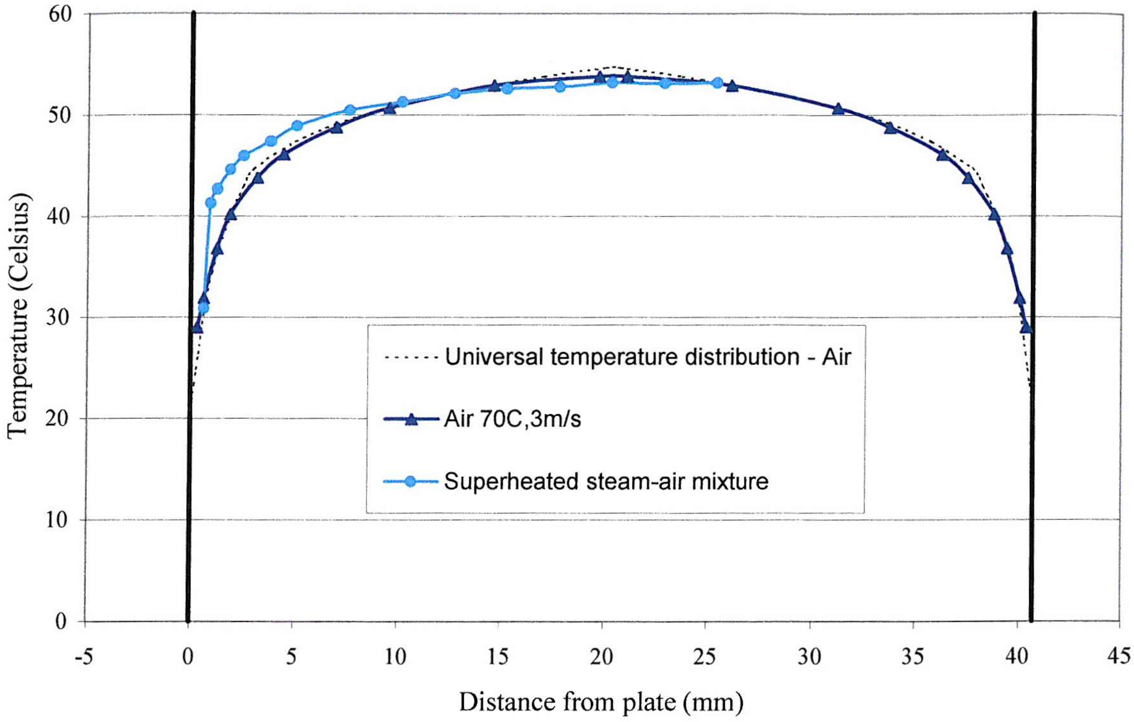

Figure K-4. Experimentally measured lateral temperature profiles for air and water vapour – air mixtures.

Again, using the trapezium rule of integration on a number of lateral temperature profiles obtained experimentally, this time with water vapour – air mixtures resulted in a value for X of approximately 0.86. When used with equation (K-3), and assuming a constant wall temperature of 21°C, this proved sufficiently accurate for all steam – air mixtures.

K.2.3 Mean cross-sectional (bulk) temperature

The next step was to assess the vertical variation of temperature within the duct. This was expected to be far less dramatic than the horizontal temperature gradients between the cold condenser walls. Example experimentally obtained vertical temperature profiles of an air and water vapour – air mixture are plotted in Figure K-5. Again the temperature profile of the air falls away more quickly as the condenser walls are approached. In both cases the temperature is approximately constant throughout the majority of the condenser height.

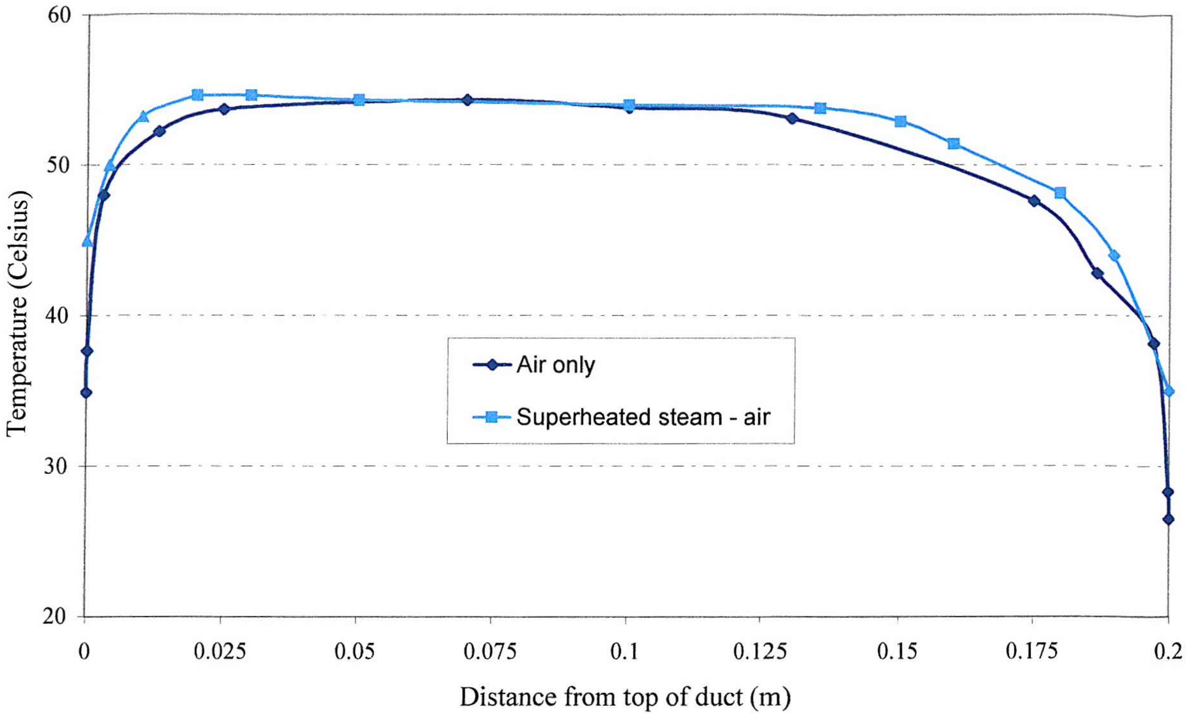

Figure K-5. Experimentally obtained vertical temperature profiles within the condenser.

From these and other experimental measurements a correction similar to that presented in equation (K-2) was adopted such that

$$t(cross-section) \approx t(lateral\ mean) - 0.05[t(lateral\ mean)-21] \tag{K-4}$$

K.2.4 Axial location correction

Finally, an additional correction is required should the axial location for which the bulk temperature is required not be sufficiently far along the condenser. This is due to the fact that the thermal boundary layer appears fully developed only after a condenser length of 1.5m (refer to Figure K-2). This was most easily accounted for using

$$t(bulk) = t(cross-section) + \frac{t(centre-line)}{60}(1.5-x) \tag{K-5}$$

when the axial condenser location, $x < 1.5$m.

REFERENCES

1. E. M. Sparrow, W. J. Minkowycz, and M. Saddy, Forced convection condensation in the presence of noncondensables and interfacial resistance, *J. Heat Mass Transfer*, **10**, 1829-1845, (1967).

2. A. L. Lydersen, Mass transfer in engineering practice, John Wiley & Sons, (1983).

3. A. J. Chapman, Heat transfer, 4th Ed., Macmillan Publishing Company, New York (1984).

4. D. E. Steinmeyer, Heat transfer : Fog formation in partial condensers, *Chemical Engineering Progress* **68**, 64-68 (1972).

5. N. A. Fuchs, The Mechanics of Aerosols, Pergamon Press, Oxford (1964).

6. R. H. Perry, Chemical Engineers' Handbook, 5th Ed., McGraw-Hill, New York (1973).

7. R. A. Smith, Vaporisers - Selection, Design & Operation, John Wiley & Sons, New York (1986).

8. K. Rietema and C. G. Verver (Eds.), Cyclones in Industry, Elsevier Publishing Company, Amsterdam (1961).

9. M. J. E. H. Muitjens, V. I. Kalikmanov, M. E. H. v.Dongen, A. Hirschberg and P. A. H. Derks, On Mist Formation in Natural Gas, *Revue de l'institut Francais du Petrole*, **49**, no.1, 63-72 (1994).

10. G. Cinar, B. S. Yilbas and M. Sunar, Study into nucleation of steam during expansion through a nozzle, *Int. J. Multiphase Flow* **23**, no.6, 1171-1188 (1997).

11. A. P. Colburn and A. G. Edison, Prevention of fog in cooler-condensers, *Ind. Engng Chem.* **33**, no.4, 457-458 (1941)

12. H. F. Johnstone, M. D. Kelley and D. L. McKinley, Fog formation in cooler-condensers, *Ind. Engng Chem.* **42**, 2298-2302 (1950)

13. H. Buttner and W. Denzer, Experiments on mist formation in static mixing of gases, *Ger. Chem. Eng.*, **6**, 282-287 (1983).

14. G. F. C. Rogers and Y. R. Mayhew, Engineering thermodynamics work and heat transfer (3rd. Ed), Longman, London (1980).

15. J. H. Keenan, F. G. Keyes, P. G. Hill and J. G. Moore, Steam Tables, John Wiley & Sons Inc., New York (1969).

16. Y. Hayashi, A. Takimoto and Y. Yamamoto, Heat and mass transfer with a mist formation in a laminar duct flow, *Heat Transfer Jap. Res.* **10**, 37-51 (1978).

17. H. J. H. Brouwers and A. K. Chesters, Film models for transport phenomena with fog formation : the classical film model, *Int. J. Heat Mass Transfer* **35**, 1-11 (1992).

18. D. P. Sekulic, Irreversible condensation conditions near the cryosurface, *Int. J. Heat Mass Transfer*, **28**, no.6, 1205-1214 (1985).

19. J. Korber and K. Schaber, Modelling of heat and mass transfer with fog formation, *Proc.10th Int. Heat Transfer Conf.* **3**, 341-346 (1994).

20. HTFS Handbook.

21. S. Twomey, Atmospheric Aerosols, Elsevier Scientific Publishing Company, Amsterdam (1977).

22. V. Ruth, J. P. Hirth and G. M. Pound, On the theory of homogeneous nucleation and spinodial decomposition in condensation from the vapour phase, *J. Chem. Phys.*, **88**, no.11, 7079-7087 (1988).

23. S. Heidenreich and F. Ebert, Condensational droplet growth as a preconditioning technique for the separation of submicron particles from gases, *Chemical Engineering and Processing*, **34**, 235-244 (1995).

24. J. B. Young, The condensation and evaporation of liquid droplets in a pure vapour at arbitrary Knudsen number, *Int. J. Heat Mass Transfer*, **34**, no.7, 1649-1661 (1991).

25. J. B. Young, The condensation and evaporation of liquid droplets at arbitrary Knudsen number in the presence of an inert gas, *Int. J. Heat Mass Transfer*, **36**, no.11, 2941-2956 (1993).

26. J. Lothe and G. M. Pound, Reconsiderations of Nucleation Theory, *J. Chem. Phys.*, **36**, no.8, 2080-2085 (1962).

27. A. Dillmann and G. E. A. Meier, A refined approach to the problem of homogeneous nucleation from the vapour phase, *J. Chem. Phys.*, **94**, no.5, 3872-3884 (1991).

28. C. Peters and J. Altmann, Monodisperse aerosol generation with rapid adjustable particle size for inhalation studies, *Journal of Aerosol Medicine*, **6**, no.4, 307-315 (1993).

29. L. Morawska, S. Thomas, M Jamriska and G. Johnston, The modality of particle size distributions of environmental aerosols, *Atmospheric Environment*, **33**, 4401-4411 (1999).

30. F. M. McGovern, An analysis of condensation nuclei levels at Mace Head, Ireland,

Atmospheric Environment, **33**, 1711-1722 (1999).

31. N. H. Fletcher, Size Effect in Heterogeneous Nucleation, *Journal of Chemical Physics*, **29**, no.3, 572-576 (1958).
32. O. H. Berg et al., Comparison of Observed and Modelled Hygroscopic Behaviour of Atmospheric Particles, *Contr. Atmos. Phys.*, **71**, no.1, 47-64 (1998).
33. P. Laj et al., The Size Dependent Composition of Fog Droplets, *Contr. Atmos. Phys.*, **71**, no.1, 115-130 (1998).
34. G. Frank et al., Droplet formation and Growth in Polluted Fogs, *Contr. Atmos. Phys.*, **71**, no.1, 65-85 (1998).
35. M. Wendisch et al., Drop Size Distribution and LWC in Po Valley Fog, *Contr. Atmos. Phys.*, **71**, no.1, 87-100 (1998).
36. J. Heintzenberg et al., Characteristics of Haze, Mist and Fog, *Contr. Atmos. Phys.*, **71**, no.1, 21-31 (1998).
37. B. G. Martinsson et al., Experimental determination of the connection between cloud droplet size and its dry residue size, *Atmospheric Environment*, **31**, no.16, 2477-2490 (1997).
38. I. Kanne-Dannetschek and D. Stauffer, Quantitative theory for time lag in nucleation, *J. Aerosol Sci.*, **12**, no.2, 105-108 (1981).
39. H. L. Toor, Fog formation in boundary value problems, *A. I. Ch. E. Journal*, **17**, no.1, 5-14, (1971).
40. H. J. H. Brouwers and C.W. M. Van der Geld, Heat transfer, condensation and fog formation in crossflow plastic heat exchangers, *Int. J. Heat Mass Transfer* **39**, 391-405 (1996).
41. J. G. Collier and J. R. Thome, Convective Boiling and Condensation, 3rd Ed., Clarendon Press, Oxford, (1994).
42. J. M. Coulson, J. F. Richardson, J. R. Backhurst and J. H. Harker, Chemical Engineering, Vol.1, 4th Ed., Pergamon Press, Exeter (1990).
43. G. S .H. Lock, Latent Heat Transfer - An Introduction to Fundamentals (1994).
44. T. K. Sherwood, R. L. Pigford and C. R. Wilke, Mass Transfer, McGraw-Hill (1975).

45. P. F. Peterson, V. E. Schrock and T. Kageyama, Diffusion layer theory for turbulent vapour condensation with noncondensable gases, *Trans. ASME Journal of Heat Transfer* **115**, 998-1003 (1991).

46. N. B. Vargaftik, Tables on thermophysical properties of liquids and gases, 2nd Ed., (1975).

47. H. J. H. Brouwers, An improved tangency condition for fog formation in cooler-condensers, *Int. J. Heat Mass Transfer* **34**, 2387-2394 (1991).

48. D. A. Frank-Kamenetskii, Diffusion and Heat Transfer in Chemical Kinetics, 2nd Ed., Plenum Press, New York (1969).

49. H. J. H. Brouwers, Film models for transport phenomena with fog formation : the fog film model, *Int. J. Heat Mass Transfer* **35**, 13-28 (1992).

50. S. H. Chan, D. H. Cho and D. W. Condiff, Heat transfer from a high temperature condensable mixture, *Int. J. Heat Mass Transfer* **23**, 63-71 (1980).

51. D. A. Sanchez, R. C. Allen (Jr.) and W. T. Kyner, Differential equations, 2nd Ed., Addison-Wesley Publishing Company, New York (1989).

52. R. M. Olsen, Essentials of engineering fluid mechanics (2nd. Ed), International text book company (1966).

53. Royal Dutch / Shell Group, Shell Flow Meter Engineering Handbook, Waltman Publishing Company, Delft, The Netherlands (1968).

54. N. J. Themelis, Transport and Chemical Rate Phenomena, Gordon and Breach Science Publishers SA (1995).

55. Aerometrics Phase Doppler Particle Analyser, 1-Component Operations Manual, Release 3.0 (1987).

56. University of Bath, BIRAL and TSI Inc., Laser Velocimetry Course Notes, (1995).

57. Metais and Eckert Forced, Mixed, and free convection regimes, *Trans. ASME Journal of Heat Transfer*, 295 (1964).

58. J. A. Wesselingh and R. Krishna, Mass Transfer, Ellis Horwood Limited (1990).

59. R. B. Bird, W. E. Stewart and E. N. Lightfoot, Transport Phenomena, John Wiley & Sons, New York (1960).

60. M. Epstein and G. M. Hauser, Simultaneous fog formation and thermophoretic droplet deposition in a turbulent pipe flow, *ASME Journal of Heat Transfer* **113**, 224-231 (1991).

61. Y. Hayashi, A. Takimoto and Y. Yamamoto, Mechanism of mist formation based on a critical supersaturation model in a turbulent convective field.

62. Numerical Algorithms Group Ltd., NAG Fortran Library - Mark 16, (1991).

63. A. P. Colburn and T. B. Drew, The condensation of mixed vapours, Trans. *A. I. Chem. Eng.*, **33**, 197-215 (1937).

64. A. P. Colburn and O. A. Hougen, Design of Cooler Condensers for Mixtures of Vapours and Noncondensing Gases, *Ind. Eng. Chem.* **26**, no.11, 1178-1182 (1934).

65. T. H. Chilton and A. P. Colburn, Mass Transfer (Absorption) Coefficients, *Ind. Eng. Chem.* **26**, no.11, 1183-1187 (1934).

66. J. T. Schrodt and E. R. Gerhard, Condensation of water vapour from a noncondensing gas on a vertical tubes in a bank, *Ind. Eng. Chem. Fundamentals* **4**, no.1, 46-49 (1965).

67. D. R. Olander, Design of Direct Contact Cooler Condensers, *Ind. Eng. Chem.* **53**, no.2, 121-126 (1961).

68. D. R. Coughanowr and E. O. Stensholt, Analog computer method for designing a cooler-condenser with fog formation, *Ind. Eng. Chem.* **26**, no.11, 1183-1187 (1934).

69. R. J. List (Smithsonian Institution), Smithsonian Meteorological Tables, 6th Ed., Smithsonian Institution Press, Washington D.C. (1971).

70. B. Gebhart, Heat Transfer 2nd Ed., McGraw Hill, New York (1971).

71. A. H. P. Skelland, Diffusional mass transfer, John Wiley & Sons, New York (1974).

72. F. Stern and F Votta Jr., Condensation from superheated gas-vapour mixtures, *A. I. Ch. E. Journal*, **14**, no.6, 928-933 (1968).